Search for Physics Beyond the Standard Model with a Shape Fit Method in Final States with Jets and Missing Transverse Energy at the ATLAS Experiment

Dissertation
zur Erlangung des Grades

Doktor der Naturwissenschaften

am Fachbereich Physik, Mathematik und Informatik
der Johannes Gutenberg-Universität Mainz

vorgelegt von
Katharina Jakobi

Juli 2019

Kurzfassung

Das Standardmodell (SM) der Elementarteilchenphysik ist eine Zusammenfassung aller bekannten Elementarteilchen und deren Wechselwirkungen und erlaubt enorm präzise Vorhersagen und Beschreibungen fast aller physikalischen Phänomene. Allerdings gibt es experimentelle Hinweise auf die Unvollständigkeit dieses Modells.
Zahlreiche Theorien jenseits des Standardmodells (BSM) wie beispielsweise Theorien der Dunklen Materie oder der Extra-Dimensionen bieten mögliche Erweiterungen des SM an. Eine sehr vielversprechende BSM-Theorie ist die Supersymmetrie (SUSY), die eine gebrochene Symmetrie zwischen Fermionen und Bosonen beschreibt und unter anderem die Existenz eines möglichen Dunkle-Materie-Kandidaten vorhersagt, des Neutralinos ($\tilde{\chi}_1^0$). Gemeinsam ist diesen Modellen, dass sie eine ähnliche Signatur mit Jets und fehlender Transversalenergie im Detektor hinterlassen würden. Der ATLAS-Detektor am Large Hadron Collider (LHC) ist als Vielzweckdetektor hervorragend geeignet, um die Existenz möglicher BSM-Teilchen nachweisen zu können. Die Daten, die in den Jahren 2015 und 2016 bei Proton-Proton-Kollisionen mit einer Schwerpunktsenergie von 13 TeV und einer integrierten Luminosität von insgesamt $36.1\,\mathrm{fb}^{-1}$ aufgenommen werden konnten, wurden nach BSM-Signaturen mit hochenergetischen Jets sowie hoher fehlender Transversalenergie durchsucht.

Diese Arbeit präsentiert die Analyse solcher Ereignisse mit BSM-ähnlicher Signatur mittels einer formsensitiven Methode, die ein vereinfachtes SUSY Modell ($\tilde{q} \to q + \tilde{\chi}_1^0$) als Bezugsmodell verwendet. Dieses sagt eine Paarproduktion von Squarks ($\tilde{q}$) vorher. Deren Zerfall führt zu einem Endzustand mit Jets aus den entstandenen Quarks sowie fehlender transversaler Energie durch die Neutralinos, welche den Detektor verlassen ohne detektiert zu werden. Der Endzustand entspricht daher vielen BSM-Signaturen. Die Analyse nutzt die Formunterschiede zwischen den erwarteten SM-Untergründen sowie verschiedener SUSY-Signale in sensitiven kinetischen Variablen. Unter Berücksichtigung der statistischen und dominanten systematischen Unsicherheiten werden die Verteilungen mit der Maximum-Likelihood-Methode an die Daten angepasst, um die Signal- und Untergrundanteile zu bestimmen. Für die Verbesserung der SM-Untergrunderwartungen sowie der damit verbundenen Unsicherheiten werden Daten-basierte Abschätzungen der Hauptuntergründe vorgenommen.
Da die Fitresultate eine gute Übereinstimmung der beobachteten Daten mit den erwarteten Untergründen zeigen, können neue Ausschlussgrenzen auf die Massen der supersymmetrischen Teilchen gesetzt werden. Neutralinos können bis zu einer Masse von 800 GeV und Squarks bis zu einer Masse von 1400 GeV ausgeschlossen werden.

Abstract

The Standard Model (SM) of Particle Physics is a summarising theory containing all elementary particles and their interactions and allows very precise predictions and descriptions of almost all known physical phenomena. Nevertheless, there are experimental findings which indicate that this theory is incomplete.
There are several theories beyond the Standard Model (BSM) that postulate the existence of new particles such as dark matter or even extra dimensions. The theory of Supersymmetry (SUSY) is one of the most promising extensions to the SM describing a broken symmetry between fermions and bosons. Amongst other things, it also predicts the existence of additional particles such as the neutralino ($\tilde{\chi}_1^0$), a suitable candidate for dark matter. The common feature of these BSMs is a similar signature in a particle detector containing jets and missing transverse energy. Being a multi-purpose detector, the ATLAS experiment at the Large Hadron Collider (LHC) is perfectly suited to search for evidences of various BSMs. In 2015 and 2016 ATLAS recorded data of the proton-proton collisions at a centre of mass energy of 13 TeV corresponding to a total integrated luminosity of $36.1\,\mathrm{fb}^{-1}$. These data events were searched for a BSM signature consisting of highly energetic jets and a significant amount of missing transverse energy.

This thesis presents an analysis of such events with a BSM like signature using a form sensitive method and a simplified SUSY model ($\tilde{q} \rightarrow q + \tilde{\chi}_1^0$) as a benchmark. The squarks ($\tilde{q}$) are assumed to be produced in pairs. Their decay would lead to a final state containing jets, produced by the emerging quarks as well as missing transverse energy due to the neutralinos, which escape the detector undetected. This final state is therefore equivalent to many BSM signatures. The analysis exploits the shape differences between the distributions of the SM backgrounds and the simulated SUSY signals in sensitive kinematic variables. The signal strength and background fractions are determined by a fit to the observed data based on the maximum likelihood method while considering the statistic and all dominant systematic uncertainties. To improve the SM background simulations and reduce uncertainties, a data driven estimation of the main backgrounds is performed.
Since the final fit results show a good agreement of observed data and expected standard model backgrounds, it is possible to determine new exclusion limits on the masses of the supersymmetric particles. Neutralino masses up to 800 GeV and squark masses up to 1400 GeV can be excluded.

Contents

Chapter 1.

Introduction

Since the beginning of human civilisation, the origin of the universe and the composition of matter have been among the most intriguing questions to be answered.
The search for new understanding regarding these questions motivated the development of high precision instruments in the fields of cosmology as well as elementary particle physics to investigate nature at the largest and smallest possible scales. Only by combining the findings of both disciplines it is possible to gain a complete picture of the development of our universe and the principles of nature.

The works of Copernicus, Kepler, Galilei and Newton [1–4] shaped our model of the cosmos until it was revolutionised by Einstein's general theory of relativity [5] at the beginning of the twentieth century, which marked the dawn of modern scientific cosmology.
In 1897, Thomson and others [6] found the first elementary particle by discovering the electron. He thereby falsified the model of atoms[1] as indivisible particles and paved the way for elementary particle physics.
At that time, only two fundamental forces were known: the electromagnetic and the gravitational interaction. Studies of radioactive decay processes (e.g. [7–9]) and the discovery of many other apparently fundamental particles throughout the following decades strongly motivated the development of a new model to accommodate these findings.

From the 1930s to the 1970s, the theoretical foundation for the strong interaction [10] and the quark model [11–13] were developed. The latter is an underlying concept which explains protons, neutrons and other so-called *hadrons* as composed of fundamental particles named *quarks*. Thus, it was possible to explain the variety of particles found in cosmic radiation and accelerator experiments as different bound states of two or three quarks, so-called *mesons* and *baryons*. Combined with the description and unification of the electromagnetic and weak forces [14–16] as well as the Higgs mechanism [17, 18], resulting in electroweak symmetry breaking and non-zero particle masses, these contributions form

[1] From ancient greek philosophers Leucippus and Democritus: atomos = indivisible.

a relativistic quantum field theory, the so-called *Standard Model* (SM).
While the development of today's universe, especially at large scales, is mainly induced by gravitation, physical processes in the early universe shortly after the Big Bang were dominated by the strong and electroweak interactions which led to nucleosynthesis and thereby to the formation of matter as we know it. These two forces as well as the constituents of matter and their behaviour are precisely described by the SM. It successfully explains a large variety of physical phenomena with high accuracy, making it the most important model of elementary particle physics. The discovery of the Higgs boson in 2012 [19, 20], which was predicted by the SM, is seen as its completion.

The SM does, however, have some major weaknesses such as the missing integration of the gravitational force into its theoretical framework or the fact that the particle masses along with other parameters are not determined by the theory. Furthermore, some experimental observations from cosmology cannot be explained by the SM, like the absence of antimatter in the universe [21] or the multiple indications for invisible matter, so-called *dark matter*. Space probe observations of the Cosmic Microwave Background (CMB) [22] in fact indicate that less than five percent of the energy content in the present universe is made of visible matter while more than one fourth consists of dark matter. The SM unfortunately does neither provide a possible particle candidate to account for these findings nor is there any hint to the nature of the remaining 70 percent of energy which is called *dark energy*. These are only some of the questions that are left unresolved by the SM and that motivate the extension of theories and experimental searches for new physics beyond the SM.

Alongside extra dimension theories, leptoquark models and others, the theory of *supersymmetry* (SUSY) was one of the most favoured enhancements of the SM. The smallest SUSY extension to the SM is given by the Minimal Supersymmetric Standard Model (MSSM) which postulates a super-partner to each particle of the SM. On the one hand it elegantly solves theoretical issues like the hierarchy problem [23]. On the other hand, it includes a suitable dark matter candidate since the lightest SUSY particle (LSP) is neutral and stable[2], providing motivation to search for new particles. If SUSY particles were produced in collider experiments, they would be expected to decay into SM particles and LSPs, leading to final states characterised by jets and missing transverse energy[3].

The analysis presented in this thesis was developed as a generic search for physics beyond the SM (BSM). It focuses on new heavy particles which could be produced in proton-proton-collisions and which could be identified by accompanying jets and missing transverse energy in the detector. Therefore, the MSSM can be used as a suitable bench-

[2]This applies in case of R-parity conservation.
[3]SUSY signatures including leptons are also possible, but are neglected in this work.

mark model. In contrast to other searches, which are mostly cut-based, a shape sensitive method was developed to maintain a high signal efficiency. The soft preselection used in the analysis enables it not only to be applied to SUSY searches but also to dark matter or leptoquark models.

The Large Hadron Collider (LHC) at the European Organization for Nuclear Research (CERN) is currently the world's most powerful collider. It provides high-energy beams for many different purposes and also made the discovery of the Higgs boson possible. The ATLAS experiment at the LHC, a multi-purpose detector, allows for the precise testing of SM predictions and, moreover, for searches for new particles with unknown properties. The present study uses ATLAS data recorded during the data-taking periods of 2015 and 2016. During this time, the two colliding proton beams provided a centre-of-mass energy of 13 TeV.

In the following chapter, the theoretical foundations of the SM and the supersymmetric theory, as an example for BSM models, are briefly described. The ATLAS experiment at the LHC is presented in chapter 3. Chapters 4 and 5 give a more detailed insight into the reconstruction of objects like jets, leptons and others in the detector and into the nature of the final state investigated. The analysis itself is then presented in chapter 6, the fit method used and the results obtained are shown in chapter 7 before chapter 8 finally summarises the concept of the analysis and its results and gives an outlook on future developments.

Chapter 2.

Theoretical Principles

This chapter briefly summarises the theoretical concept of elementary particles physics by introducing the Standard Model of Particle Physics, mainly following [24–27], its shortcomings and a selection of theories beyond the Standard Model with a special focus on the theory of Supersymmetry [28]. Natural units are used in this thesis, i.e. $\hbar = c = 1$.

2.1. The Standard Model of Particle Physics

The Standard Model of Particle Physics (SM) is a relativistic quantum field theory describing the most elementary building blocks of matter and their interactions as dynamic relativistic quantum fields. Since the SM is a re-normalisable theory, all physical observables are finite. The requirement of invariance under local gauge transformations of the gauge group

$$SU(3)_C \otimes SU(2)_L \otimes U(1)_Y \quad [1] \tag{2.1}$$

implies the description of the fundamental interactions. The theory of the strong interaction, described by quantum chromodynamics (QCD), is based on the symmetry group $SU(3)_C$ (see section 2.1.2). The electromagnetic interaction, described by quantum electrodynamics (QED), could be unified with the weak force. The theory of the resulting electroweak interaction is based on the $SU(2)_L \otimes U(1)_Y$ gauge group and briefly introduced in section 2.1.3.
The dynamics of the SM are described by the Lagrangian density:

$$\mathcal{L}_{\mathrm{SM}} = \mathcal{L}_{\mathrm{QCD}} + \mathcal{L}_{\mathrm{EW}} + \mathcal{L}_{\mathrm{Higgs}} + \mathcal{L}_{\mathrm{Yukawa}} \tag{2.2}$$

with $\mathcal{L}_{\mathrm{QCD}}$ representing quarks and gluons and their coupling and $\mathcal{L}_{\mathrm{EW}}$ summarising all electroweak interacting particles, also including the electroweak gauge bosons and their coupling. $\mathcal{L}_{\mathrm{Higgs}}$ and $\mathcal{L}_{\mathrm{Yukawa}}$ describe the Higgs sector of the Standard Model.

[1] The indices represent the corresponding couplings of the group: "C" for colour charge of the strong interaction, "L" for the weak coupling to left handed particles, "Y" for the weak hypercharge.

To this date, twelve fermions, the elementary building blocks of matter with spin $1/2$ [2], and four force mediating bosons with spin 1 have been detected. The Higgs boson with spin 0 plays a special role as evidence for the Higgs mechanism which allows particles to obtain mass. The particle content of the SM is described in section 2.1.1, the features of the Higgs mechanism in section 2.1.4.

2.1.1. The Particle Spectrum

The particle spectrum of the SM is based on three different types of fields:
Firstly, twelve *fermionic* fields with spin $1/2$ which are subject to the Pauli exclusion principle[3] and can be divided into *quarks* and *leptons* with different properties (see table 2.1). These are the fundamental building blocks of all visible matter in the universe. They are further divided into three generations or families according to their properties, whereby particles of the second and third generation are unstable and decay into first generation particles [4]. Only those are stable and account for the matter surrounding us. All leptons and quarks are characterised by quantum numbers like the weak isospin I (which depends on their helicity[5]) and the weak hypercharge Y[6] and participate in the electroweak interaction (see table 2.2).
Additionally, there are antiparticles to all fermions which are identical in all quantum numbers but have inverse charge.
Secondly, there are also twelve *bosonic* vector-like gauge fields with spin 1 which correspond to the so called *gauge bosons*. These act as mediators of three of the four fundamental forces: by exchanging photons, particles can interact electromagnetically while the weak force is mediated via charged W^+ and W^- bosons as well as neutral Z bosons and the strong interaction is transmitted by eight types of gluons (see table 2.3).
So far there is no quantum gravity theory that could be integrated into the SM nor are there experimental hints to the existence of gravitons, the hypothetical carrier of the gravitational force. However, this force is by thirty to forty orders of magnitude weaker than the other interactions - its contributions on the subatomic scale can therefore easily be neglected.

Finally, there is a doublet of scalar Higgs fields with spin 0 which enable quarks, leptons and the weak gauge bosons to carry mass whilst securing gauge invariance of the theory (see section 2.1.4).

[2] The intrinsic angular momentum carried by elementary particles is called spin.
[3] Any pair of indistinguishable fermions is described by an asymmetric state wrt exchange of the fermions.
[4] This does not apply to neutrinos.
[5] The helicity of a particle is defined as the projection of its spin along its direction of motion. Particles with positive helicity (when spin and momentum are parallel) are called right handed, left handed

	Name	Symbol	Mass [MeV]	electric charge [e]	color charge
Leptons	Electron	e	0.511	-1	–
	Electron Neutrino	ν_e	$< 2 \times 10^{-6}$	0	
	Muon	μ	105.658	-1	
	Muon Neutrino	ν_μ	< 0.19	0	
	Tau	τ	1776.86 ± 0.12	-1	
	Tau Neutrino	ν_τ	< 18.2	0	
Quarks	Up quark	u	$2.2^{+0.6}_{-0.4}$	$+\frac{2}{3}$	r, g, b
	Down quark	d	$4.7^{+0.5}_{-0.4}$	$-\frac{1}{3}$	
	Charm quark	c	1275 ± 25	$+\frac{2}{3}$	
	Strange quark	s	96^{+8}_{-4}	$-\frac{1}{3}$	
	Top quark	t	$173210 \pm 510 \pm 710$	$+\frac{2}{3}$	
	Bottom quark	b	4180^{+40}_{-30}	$-\frac{1}{3}$	

Table 2.1.: Leptons and quarks with their symbols (in the following often used as acronyms), recent mass measurements and their electric and colour charges [24, 25].

2.1.2. The Strong Interaction

The strong interaction is based on the symmetry group $SU(3)$ and described by the theory of quantum chromodynamics (QCD). Together with the quark model, QCD explains the properties and dynamics of all particles participating in the strong interaction, i.e. all quarks and gluons. On the one hand, they provide a regulatory scheme to categorise all hadronic particles according to their quark content into groups of baryons and mesons, and on the other hand, they explain the effect of the strong force as an exchange of massless gluons between these quarks.
The corresponding term of the Lagrangian density is given by:

$$\mathcal{L}_{\mathrm{QCD}} = \sum_q \bar{q} i \boldsymbol{D} q - \frac{1}{4} G^{\alpha}_{\mu\nu} G^{\mu\nu}_{\alpha}. \tag{2.3}$$

means negative helicity (spin and momentum have opposite directions)

[6] The weak hypercharge is defined by the electric charge Q and the third component of I as $Y = 2(Q - I_3)$.

	Generation			weak Isospin I	I_3	Y
Leptons	$\begin{pmatrix}\nu_e\\ e\end{pmatrix}_L$	$\begin{pmatrix}\nu_\mu\\ \mu\end{pmatrix}_L$	$\begin{pmatrix}\nu_\tau\\ \tau\end{pmatrix}_L$	1/2	$+1/2$ $-1/2$	-1
	e_R	μ_R	τ_R	0	0	-2
Quarks	$\begin{pmatrix}u\\ d\end{pmatrix}_L$	$\begin{pmatrix}c\\ s\end{pmatrix}_L$	$\begin{pmatrix}t\\ b\end{pmatrix}_L$	1/2	$+1/2$ $-1/2$	$+1/3$
	u_R	c_R	t_R	0	0	$+4/3$
	d_R	s_R	b_R	0	0	$-2/3$

Table 2.2.: The three generations of leptons and quarks with their respective quantum numbers weak isospin I, its third component I_3 and weak hypercharge Y. Right- and left-handed particles are marked with R and L respectively. So far, no right-handed neutrinos have been observed [24, 25, 27].

with q denoting the quarks, $\boldsymbol{D}$ the covariant derivative and $G^{\alpha}_{\mu\nu}$ the field strength tensor of the gluon field.
Quarks carry a charge called *colour charge*, which exists in three types named red, green and blue (r, g, b) while antiquarks hold the respective opposite charges, anti-red, anti-green or anti-blue, $(\bar{r}, \bar{g}, \bar{b})$. This additional quantum number ensures compliance with the Pauli principle.
Gluons carry one of eight combinations of colour and anti-colour and are able to interact not only with the colour-charged quarks but also with each other.
In protons, the only stable hadron and lightest baryon, the three constituents are two up quarks and one down quark, so-called *valence quarks* and are in combination colour neutral. They are bound together by fluctuating gluons which can produce quark-antiquark pairs, called *sea quarks*.

To this day, no free colour-charged particles have been observed, which represents an important feature of the QCD. All hadronic matter is colour neutral, which means that the colour and anti-colour charges of the partons within a bounding state have to cancel out. Furthermore, it is not possible to isolate single quarks, which is called *confinement*. The cause for this behaviour is the strong coupling constant: for low momentum transfers and larger distances the coupling strength becomes very large while for high energies and smaller distances it decreases logarithmically and gives an *asymptotic freedom* to quarks.

Name	Symbol	Mass [GeV]	electric charge [e]	Interaction	couples to
Gluon	g	0	0	strong	color charge
Photon	γ	0	0	electromagnetic	electric charge
$W^{\pm}$ Boson	$W^{\pm}$	80.385 ± 0.015	± 1	weak	weak charge
Z^0 Boson	Z^0	91.1876 ± 0.0021	0		
Higgs Boson	H^0	125.09 ± 0.2	0	Higgs field	Mass

Table 2.3.: The bosons of the Standard Model with their corresponding symbols (in the following often used as acronyms), recent mass measurements, electric charges and the interaction they mediate as well as the charge they couple to. [24, 26]

2.1.3. The Electroweak Interaction

The electromagnetic interaction is based on the $U(1)$ symmetry group and described by a quantum field theory called quantum electrodynamics (QED). This theory includes the dynamics of all electrically charged particles involved in the electromagnetic interaction, i.e. all quarks and charged leptons. Similar to the QCD, it comes with a force carrier, the photon. In contrast to gluons, photons themselves are electrically neutral and hence not self-interacting. Along with the fact that photons are massless, this allows the electromagnetic force to obtain an infinite range. Its coupling strength is given by the fine-structure constant α.
The weak interaction is the only force that couples to all particles of the Standard Model, especially to neutrinos, and includes two types of mediating bosons: the charged W^+ and W^- bosons as well as the neutral Z^0 boson. Unlike gluons or photons, both types are very massive and have a short lifetime which results in a short range and low strength, despite the coupling constant α_W being five times larger than α.
An important difference between the interactions of charged bosons (called *charged currents*) and neutral Z bosons (called *neutral currents*) is their impact on the involved particles: while neutral currents leave lepton and quark types, so called *flavours*, unchanged[7], charged currents can alter them not only within the same generation as in the decay of muons or the beta decay (see figure 2.1), but also across the three generations. The Cabibbo-Kobayashi-Maskawa matrix indicates the probability of a transition between flavours [24].
An interesting feature of the weak interaction is its violation of parity[8]. Unlike the other interactions, it distinguishes between different helicity states and its charged currents only couple to left-handed fermions and right-handed antifermions. There is also proof

[7] So far, no flavour changing neutral currents (FCNC) have been observed.
[8] The symmetry regarding the exchange of spatial coordinates (mirror symmetry) is broken.

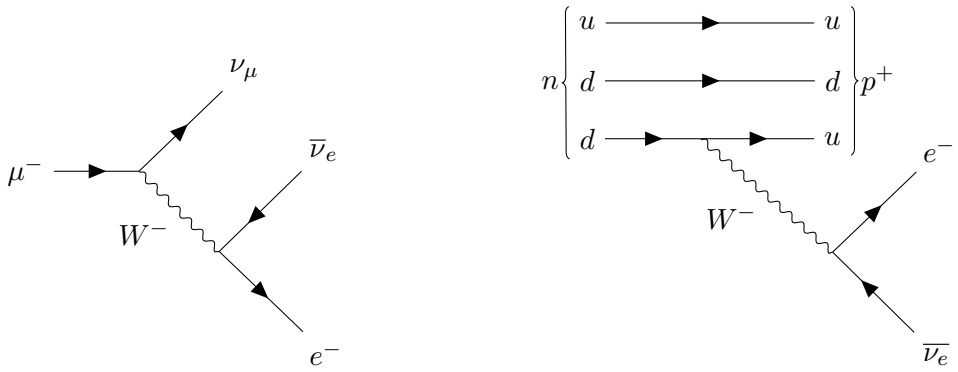

Figure 2.1.: Examples for charged currents changing the flavours of leptons as in the decay of muons (left) or quarks as in the beta decay (right).

that the electroweak interaction violates the combination of charge and space inversion, the so-called *CP invariance*. This behaviour is found in the decay of neutral K mesons as well as B mesons.
Similar to Maxwell's unification of electricity and magnetism it was shown that the electromagnetic and the weak interactions are two characteristics of the same fundamental force. This is called *electroweak unification*.
The Lagrange density for the electroweak interaction consists of two terms:

$$\mathcal{L}_{\text{EW}} = \mathcal{L}_{\text{Gauge}} + \mathcal{L}_{\text{Fermion}} \tag{2.4}$$

The first term refers to the Lagrange density of the gauge fields and includes the field strength tensors $W_i^{\mu\nu}$ of the $SU(2)$ group and $B^{\mu\nu}$ of $U(1)$:

$$\mathcal{L}_{\text{Gauge}} = -\frac{1}{4} W^i_{\mu\nu} W_i^{\mu\nu} - \frac{1}{4} B_{\mu\nu} B^{\mu\nu} \tag{2.5}$$

The second term represents the coupling of the left- (L) and right-handed (R) fermions to these gauge fields:

$$\mathcal{L}_{\text{Fermion}} = \sum_L \bar{L} i \boldsymbol{D} L + \sum_R \bar{R} i \boldsymbol{D} R \tag{2.6}$$

The requirement of gauge invariance of the theory implies that the gauge bosons have to be massless. Since the masses of Z and W bosons are different from 0, a new theory based on spontaneous symmetry breaking has to be introduced (see section 2.1.4).

2.1.4. The Higgs Mechanism

To ensure gauge invariance but to allow the gauge bosons of the weak force to obtain their masses at the same time, a new field Φ, called Higgs field, is introduced [29], denoted as

a doublet of scalar fields:

$$\Phi = \begin{pmatrix} \phi^+ \\ \phi^0 \end{pmatrix}. \tag{2.7}$$

The corresponding potential $V(\Phi)$ is given by

$$V(\Phi) = \mu^2 \Phi^\dagger \Phi + \lambda (\Phi^\dagger \Phi)^2 \tag{2.8}$$

and its shape depends on the parameters μ^2 and λ. While μ^2 is related to the mass of the associated boson, the Higgs boson, λ represents its self-interaction. If $\mu^2 > 0$ is chosen, the potential obtains a simple parabolic shape with a minimum at $v = 0$, while a choice of $\mu^2 < 0$ results in a so-called *Mexican hat potential* (see figure 2.2) with an infinite number of ground states with a non-zero *vacuum expectation value*

$$< \Phi >= \begin{pmatrix} 0 \\ v \end{pmatrix}, v = \frac{\mu}{\sqrt{\lambda}}. \tag{2.9}$$

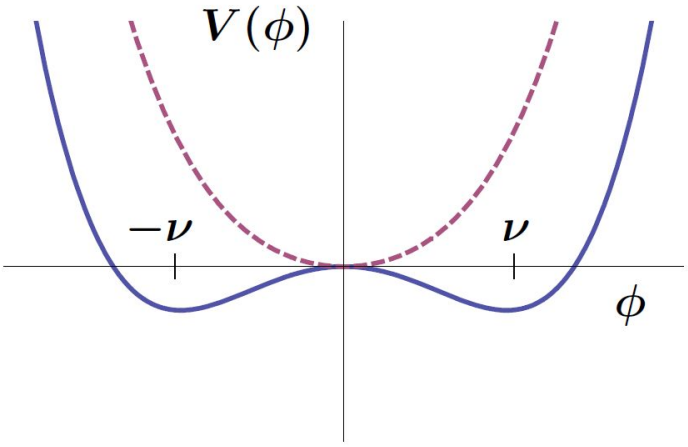

Figure 2.2.: The Higgs potential for $\mu > 0$ (dashed line) and $\mu < 0$ (solid line).[30]

In this case, the ground state is not invariant under $SU(2)_L \otimes U(1)_Y$ transformations any more but spontaneously breaks the symmetry by choosing one of the infinite number of vacuum states: $SU(2)_L \otimes U(1)_Y \rightarrow U(1)_{em}$[9].
This spontaneous symmetry breaking generates mass terms for the W and Z bosons while the photon remains massless:

$$m_\gamma = 0, \quad m_W = \tfrac{1}{2} v g, \quad m_Z = \tfrac{1}{2} v \sqrt{g^2 + g'^2} \tag{2.10}$$

[9]Since the vacuum v does not carry electric charge, the symmetry of $U(1)_{em}$ is not broken.

with g and g' denoting the coupling of the bosons to the Higgs field. The vacuum expectation value was experimentally determined to be $v = 2M_W/g \approx 246\,\text{GeV}$.
One degree of freedom of the Higgs field is identified with a new scalar particle, the Higgs boson, which does not couple to massless gluons or photons. The fermions, on the other hand, acquire their masses via so-called *Yukawa interactions* with the Higgs field. The interesting feature here is that the coupling strength is linearly proportional to the fermion mass, while it is proportional to the squares of the W and Z boson masses. The mass of the Higgs boson itself is given by $m_H = \sqrt{2\lambda}v$, but since the self-coupling λ is not predicted by theory, m_H has to be measured experimentally.
In July 2012, the two largest experiments at CERN's LHC, ATLAS [19] and CMS [20], announced their observations of a Higgs-like new particle at a mass of $m_H \approx 125\,\text{GeV}$.

2.1.5. Open Questions

The discovery of the Higgs boson is considered to be a fundamental confirmation of the Standard Model. In fact, its predictions and descriptions of almost all known physical phenomena have been proven to be highly accurate up to the TeV scale in countless precision measurements.
It is therefore seen as the ultimate theory of matter and the fundamental interactions. Hence, it is self-evident that any extension of this theory should include and build on the Standard Model.
Nevertheless, there are severe shortcomings and essential questions which remain unanswered, some of which are mentioned in the following.

Unification of interactions - gravitation
Amongst the most pressing issues is the missing implementation of general relativity describing gravitation into the theoretical framework of the Standard Model. It has not yet been possible to find a quantum field description to link gravitation to the other fundamental forces. In fact, at high energy scales like the Planck scale, at the order of $10^{19}\,\text{GeV}$, it becomes necessary to take gravitational effects into account which are neglected at the electroweak scale.

Unification of couplings
Since the unification of weak and electromagnetic interactions was successfully done, it is desirable to integrate the strong force as well into a *Grand Unified Theory (GUT)*. Moreover, as the coupling constants are dependent on the energy scale, approaching the order of $10^{16}\,\text{GeV}$, the so-called *grand unification scale*, the electromagnetic coupling increases with energy, while weak and strong couplings decrease. They might therefore merge at one point to build a universal coupling constant belonging to one underlying universal force which fragments at lower energies causing its components to appear separate. Unfortunately, this is not the case if the Standard Model alone is considered [31].

Hierarchy problem

Another more aesthetic problem that comes along with the requirement of renormalisability is the so-called *hierarchy* or *naturalness problem* [28]. The physical masses m_{phys} and couplings g_{phys} to be measured in experiments are renormalised, containing infinite contributions from loop diagrams:

$$m_{phys} = m + \Delta m; \qquad g_{phys} = g + \Delta g \tag{2.11}$$

Here, m and g describe the values at leading order or *tree level* while Δm and Δg denote the sum of all loop corrections from higher-order diagrams. In case of the Higgs mass, this leads to divergent contributions from all particles that couple to the Higgs boson (see figure 2.3).

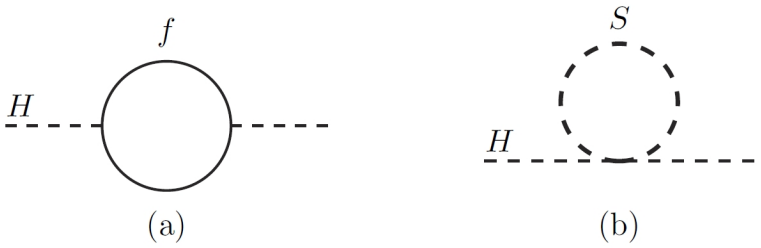

Figure 2.3.: The Feynman diagrams for the loop corrections to the Higgs mass due to the coupling to a fermion f (left) or a scalar particle S (right).[28]

For fermions f they can be written as:

$$\Delta m_H^2 = -\frac{|\lambda_f|^2}{8\pi^2}\Lambda_{UV}^2 + ... \tag{2.12}$$

and for scalar particles S the terms are given by:

$$\triangle m_H^2 = \frac{\lambda_S}{16\pi^2}[\Lambda_{UV}^2 - 2m_S^2 ln(\frac{\Lambda_{UV}}{m_S}) + ...] \tag{2.13}$$

They both increase the Higgs mass significantly and an unnaturally large fine tuning is required to keep it at the order of 100 GeV where it has been measured.

Dark Matter

The perhaps strongest indication for physics beyond the SM, however, arises from astrophysical and cosmological observations like collisions (see figure 2.4) and rotation curves of galaxies [32], gravitational lensing effects or the measurements of the cosmic microwave background (CMB).

They all imply that the visible matter described by the Standard Model only accounts for a minor fraction of the total mass in the universe and that there also exists an unknown type of matter, called *dark matter*, which is stable, massive and interacts gravitationally. Some models also suggest that these particles interact weakly and call them WIMPs (Weakly Interacting Massive Particles).

Figure 2.4.: Distribution of mass (blue), starlight of galaxies (orange) and hot gas (green) in the core of the galaxy cluster Abell 520, which was formed after the collision of massive galaxy clusters 2.4 billion light years from Earth. The mass content is dominated by dark matter, which was derived from gravitational lensing observations. The different positions imply different behaviour of visible and invisible matter. [33]

After the first measurement of the CMB in 1965 [36], it was subsequently analysed by NASA's COBE [37] and WMAP [38] satellites as well as ESA's Planck Surveyor with increased resolution [34] (see figure 2.5), showing that 4.9% of the energy density in the universe today is visible matter and almost 26.8% is made up of non-luminous matter. The remaining 68.3% of it is so-called *dark energy* [39], which is held responsible for the increasing expansion rate of the universe, but whose properties are otherwise unknown.

Further open questions

Another issue is for example the CP violation of the electroweak force being too small to account for the observed asymmetry between matter and antimatter in the universe[10].

[10]They should have been produced equally in the Big Bang, but since today's universe contains only matter, there must have been a significant surplus of matter which remained after the annihilation.

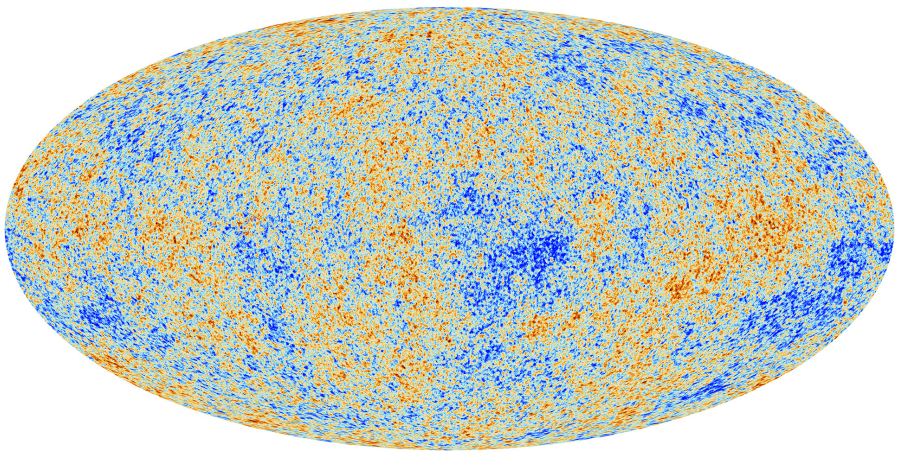

Figure 2.5.: The CMB as measured by Planck. It shows the tiny temperature anisotropies of $\pm 300\ \mu K$ which are remnants of the first freely expanding radiation 380,000 years after the Big Bang. [34, 35]

Also, neutrinos which, by oscillating between different flavour eigenstates, show clear evidence to have non-zero masses, contradict the SM predictions.
The number of generations in the SM is found to be 3 and there are also strong indications which forbid additional generations, but there is no inherent requirement from the theory. This is also the case with various other parameters of the SM: besides the masses of the neutrinos, all quark and lepton masses have to be determined by experiments. The same holds true for all coupling strengths and mixing angles and of course the Higgs mass and vacuum expectation value.

The variety of these unresolved issues strongly motivates the development of new theoretical frameworks as well as the search for new physics, so-called *physics beyond the Standard Model (BSM)* [40] and associated new particles of any kind. Some of these efforts, with a special focus on supersymmetry, will be presented in the next section.

2.2. Extensions to the Standard Model

There are several attempts to either extend the Standard Model by BSM theories to account for the unexplained observations or to solve theoretical shortcomings, some of which were mentioned in the previous section.
Searches for new particles are based on the assumption that a specific BSM model is realised in nature. The most encompassing categories of these models[11] are *large extra spatial*

[11] These categories are not mutually exclusive.

dimensions (LED) [40], leptoquarks[41], *weakly interacting massive particles* (WIMPs) [40] and *supersymmetry* (SUSY) [28]. Other models such as the little Higgs model [42], axions [43] or sterile neutrinos [44] will not be discussed here.

Large Extra Dimensions

The existence of extra spatial dimensions could explain the large difference between the electroweak scale at $\mathcal{O}(10^2\,\text{GeV})$ and the Planck scale at $\mathcal{O}(10^{19}\,\text{GeV})$ where gravitational effects become relevant.

In some models, spacetime is extended not only by one (as in the Kaluza-Klein proposal [45, 46]) but by n extra spatial dimensions. In these models, while SM particles and gauge interactions are confined to the usual 4 dimensional spacetime, gravity can propagate through the extended $4+n$ dimensional spacetime. According to Gauss's law, this would lead to a reduction of the gravitational force flux f and thereby its strength by $f \sim {}^{1}/_{r^{2+n}}$ (see equation 2.14).

$$f(r) = \begin{cases} -G_N \frac{m_1 m_2}{r^2} & \equiv -\frac{1}{M_{Pl}^2}\frac{m_1 m_2}{r^2}, \quad 4 \text{ dimensional spacetime} \\ -G_D \frac{m_1 m_2}{r^{2+n}} & \equiv -\frac{1}{M_D^{2+n}}\frac{m_1 m_2}{r^{2+n}}, \quad 4+n \text{ dimensional spacetime} \end{cases} \tag{2.14}$$

G_D and G_N are the respective fundamental gravitational constants, M_{Pl} is the Planck mass and M_D the corresponding fundamental scale of the $4+n$ dimensional theory. The fact that M_D could be of order 1 TeV as shown for example in [40] and thereby accessible at the LHC, motivates searches based on this theory.

If extra dimensions exist in nature, gravitons, possibly produced at the LHC, could propagate from our 4-dimensional spacetime into these extra dimensions and lead to missing transverse energy in the detector. In combination with the production of high-energy jets[12], this would lead to signatures like the one which was analysed with regard to LED models in [47].

Leptoquarks

Leptoquarks are hypothetical particles, scalar or vector bosons, that carry both lepton and baryon numbers [48, 49]. They could couple to both leptons and quarks, providing a connection and an exchange of information between both particle types. A pair of leptoquark and anti-leptoquark could be produced for example in gluon-gluon or quark-anti-quark fusion, but also single leptoquark production would be possible. They are expected to decay into pairs of leptons (or anti-leptons) and quarks (or anti-quarks), as shown in figure 2.6.

In case of both leptons being neutrinos, a signature with jets and missing transverse energy in the final state would be produced. Leptoquarks are part of many different BSMs, such as unification or SUSY models, and are expected to exist at the TeV scale.

[12] Objects reconstructed from parton showers in the detector, see section 4.5

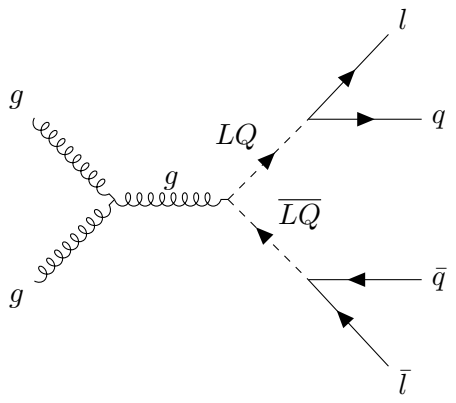

Figure 2.6.: Example of a pair production of Leptoquarks via gluon fusion and subsequent decay into pairs of leptons and quarks.

They could provide an explanation for the similarities between the quark and lepton sectors, for example the number of particle generations, which are not predicted by the SM.

Weakly Interacting Massive Particles
If the existence of WIMPs with masses in the GeV to TeV range and interaction cross sections at the electroweak scale is assumed, the matter content of the early universe could be correctly explained. In proton-proton collisions at the LHC, these WIMPs could be produced in pairs, possibly accompanied by jets (e.g. jets from radiated gluons) leading to the same signature as the LED and leptoquark models mentioned above. The simplified models used for the analysis of [47] predict the production of WIMPs via the exchange of a spin-1 mediator particle with axial-vector couplings (Z_A), a spin-1 mediator particle with vector couplings (Z_V) or a spin-0 pseudoscalar (Z_P).
The free parameters defining the models are the mass of the WIMP (m_χ), the mass of the mediator (m_{Z_A}, m_{Z_V} or m_{Z_P}, depending on the model), the flavour-universal coupling to quarks (g_q) and the coupling of mediator to WIMP (g_χ).
According to another model used in [47], WIMPs could also be produced by the exchange of scalar mediators carrying colour charge. Here, couplings with W/Z bosons are included, leading to new production mechanisms with direct couplings of DM and SM particles.
Since there are several models offering a suitable WIMP candidate, it is beneficial to perform searches as generically as possible and to aim for a broad applicability.

Among all BSM models coming with a dark matter candidate, the theory of supersymmetry, which was used as a benchmark model for the analysis presented in this thesis, is one of the most studied. It will be described in more detail in the next section mainly following

[28, 31, 40].

2.2.1. Supersymmetry

The popularity of SUSY models and the multiple efforts to find any hints of SUSY existing in nature are based on their capability to solve many problems at once while being simple and elegant.
SUSY unifies both types of particles, fermions and bosons, by introducing a new operator Q, which transforms fermion fields into boson fields and vice versa:

$$Q\,|\text{Boson}\rangle = |\text{Fermion}\rangle \qquad Q\,|\text{Fermion}\rangle = |\text{Boson}\rangle \tag{2.15}$$

The operator Q itself is a complex spinor, carrying spin 1/2 and is able to change the spin of the state it is applied to by the same value, transforming bosons into fermions and vice versa. This changes our understanding of fermions and bosons as two different particles: in SUSY, they are rather a particle doublet or one particle in two different states. If this was the case, every known particle would receive a superpartner ("sparticle") which would interact with other particles with the same coupling strength as their SM counterpart.
According to the Coleman-Mandula theorem [50], extensions to the relativistic quantum field theory framework of the SM introducing a new symmetry can only be done trivially and if the generators are direct products of the Poincaré group and the internal symmetry group.
The only possible exception to this, as shown in the Haag-Lopuszanski-Sohnius extension to the Coleman-Mandula theorem [51] by adding fermionic generators to the bosonic ones, is supersymmetry. The form of the possible extension is thereby strictly prescribed: the operators Q and $Q^\dagger$ together with the Poincaré group and the internal symmetry build the SUSY algebra and have to fulfil the (anti-) commutation rules described in equation (2.16) with P^μ being the four-vector generator of spacetime translations.

$$\begin{array}{rcccl} \left\{Q, Q^\dagger\right\} & = & P^\mu & & \\ \{Q, Q\} & = & \left\{Q^\dagger, Q^\dagger\right\} & = & 0 \\ [P^\mu, Q] & = & \left[P^\mu, Q^\dagger\right] & = & 0 \end{array} \tag{2.16}$$

In this notation, the indices of Q and $Q^\dagger$ are suppressed. Since the operator P^μ commutes with Q and $Q^\dagger$, both partners carry the same quantum numbers (except for the spin).
This would also apply to the particle masses, but since sparticles at the mass scale of the SM particles could not be found, their masses cannot be identical and therefore SUSY must be a broken symmetry (see section 2.2.4). Only if this symmetry breaking is small and the masses of the sparticles are about 1 TeV above those of their partners, SUSY can provide a viable solution to the hierarchy problem (see section 2.2.2).

2.2.2. Motivation

In section 2.1.5, some of the unresolved questions were presented, for which the SM alone cannot provide explanations. SUSY, on the other hand, provides simple solutions to some of these issues which is shown in the following.

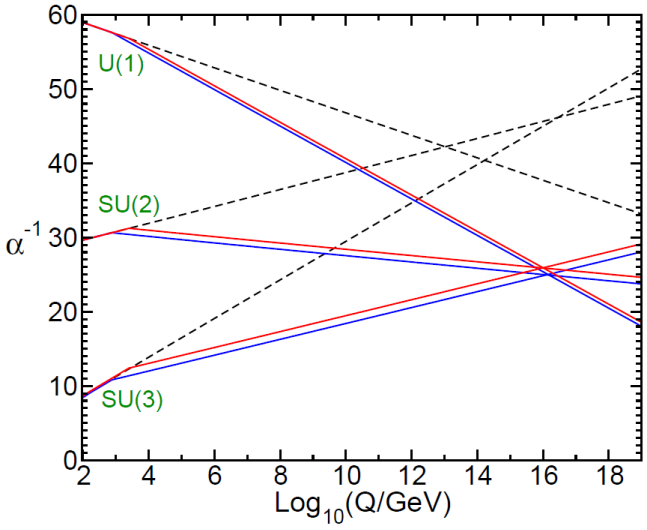

Figure 2.7.: Behavior of the inverse gauge couplings in the Standard Model (dashed lines) compared to the evolution in the MSSM (solid lines) with a SUSY threshold of the sparticles masses of 2.5 TeV.

Unification of couplings

The unification of the three couplings at high energy scales cannot be achieved by the SM alone, as the dashed lines in figure 2.7 clearly demonstrate. Nevertheless, with the Minimal Supersymmetric Standard Model (MSSM) (see section 2.2.3) introducing new heavier particles with masses above 1 TeV, their contributions to higher order diagrams must be considered. This way, the course of the energy dependent couplings is changed and, as the solid lines in figure 2.7 show, they can merge at the GUT scale at the order of 10^{16} GeV.

Hierarchy problem

Since the MSSM introduces a new set of particles, their contributions to the mass corrections must be taken into account. This can be applied to the Higgs mass corrections $\triangle m_H^2$ as the fermionic and scalar terms cancel each other out due to their inverse sign. In first order of corrections, the sum of all contributions is given by:

$$\triangle m_H^2 = -2\frac{|\lambda_f|^2}{16\pi^2}\Lambda_{UV}^2 + \frac{\lambda_S}{16\pi^2}\Lambda_{UV}^2 + ... \tag{2.17}$$

Spin 1/2		Spin 1		
Name	Symbol	Name	Symbol	Notes
gluino	$\tilde{g}$	gluon	g	both are color-octets
winos	$\tilde{W}^{\pm}$, $\tilde{W}^0$	W bosons	$W^{\pm}$, W^0	$\tilde{W}^0$ and $\tilde{B}^0$ mix to $\tilde{Z}^0$, $\tilde{\gamma}$
binos	$\tilde{B}^0$	B boson	B^0	

Table 2.4.: The gauge or vector super-multiplets of the MSSM.[24, 28]

An exact cancellation occurs if the couplings of fermionic and scalar particles fulfil $\lambda_S = |\lambda_f|^2$. All higher order corrections are cancelled out in the same way.

Dark Matter
In R-parity conserving SUSY models (see section 2.2.4), the lightest supersymmetric particle (LSP) is stable. Since it fulfils all requirements of WIMPS like zero electric charge and participation in weak and gravitational interaction only, it is a suitable candidate for Dark Matter.

2.2.3. The Minimal Supersymmetric Standard Model

Among all SUSY models, the Minimal Supersymmetric Standard Model (MSSM) adds the minimal number of new SUSY fields, i.e. new particles, to those of the Standard Model.
As the number of fermionic and bosonic degrees of freedom must be equal ($n_F = n_B$) within the MSSM, all SM spin-1 vector bosons ($n_B = 2$) receive a spin-½ SUSY partner called *gaugino* with whom they build a *gauge* or *vector super-multiplet*. All leptons and quarks, also having two helicity states, receive two spin-0 superpartners called *squarks* and *sleptons* and build *chiral* or *scalar super-multiplets*. The scalar Higgs boson with spin 0 should become a chiral super-multiplet, but in SUSY, this does not suffice to cancel out gauge anomalies and keep the theory consistent. This can only be achieved by adding another Higgs multiplet, a weak iso-doublet with hypercharge $Y = \pm 1/2$. This leads to a Higgs chiral super-multiplet containing four components, but since only a chiral super-multiplet with $Y = 1/2$ can give mass to up-type quarks via Yukawa coupling and down-type quarks are coupling only to a $Y = -1/2$ Higgs, there must be another differentiation. To account for this, another two super-multiplets are added, described by the indices u (for up-type) and d (for down-type), giving a total of eight components. The summary of these super-multiplets of the MSSM is shown in tables 2.4 and 2.5.

The gauge interactions of these squarks and sleptons are the same as for their SM partners. While left-handed squarks couple to the W boson, right-handed squarks do not.
Just like the W^0 and B^0 mix to build the mass eigenstates Z^0 and γ after electroweak sym-

Spin 0		Spin 1/2		
Name	Symbol	Name	Symbol	Notes
squarks	$\tilde{q}_L$, $\tilde{q}_R$	quarks	q_L, q_R	with $q = u, d, s, c, b, t$
sleptons	$\tilde{\nu}_e$, $\tilde{\nu}_\mu$, $\tilde{\nu}_\tau$ $\tilde{e}_L$, $\tilde{e}_R$, $\tilde{\mu}_L$, $\tilde{\mu}_R$, $\tilde{\tau}_L$, $\tilde{\tau}_R$	leptons	ν_e, ν_μ, ν_τ e_L, e_R, μ_L, μ_R, τ_L, τ_R	since only left-handed ν exist, there is no handedness for $\tilde{\nu}$
Higgsinos	$\tilde{H}_u^+$, $\tilde{H}_u^0$ $\tilde{H}_d^0$, $\tilde{H}_d^-$	Higgs	${H_u}^+$, ${H_u}^0$ H_d^0, H_d^-	$\tilde{H}_{u,d}^\pm$ mix with $\tilde{W}^\pm$ to $\tilde{\chi}_i^\pm$ $\tilde{H}_{u,d}^0$ with $\tilde{Z}^0$ and $\tilde{\gamma}$ to $\tilde{\chi}_j^0$

Table 2.5.: The chiral or scalar super-multiplets of the MSSM. Since sleptons are spin-0 particles their handedness refers to that of their superpartners. The indices u, d denote two types of Higgs giving mass to up- or down-type quarks, respectively.[24, 28]

metry breaking, the charged Higgsinos can mix with the charged winos $\tilde{W}^\pm$ to build the observable mass eigenstates called *charginos* ($\tilde{\chi}_i^\pm$ with $i = 1, 2$) while the superpositions of neutral Higgsinos with the neutral $\tilde{Z}^0$ and $\tilde{\gamma}$ result in *neutralinos* ($\tilde{\chi}_j^0$ with $j = 1, 2, 3, 4$).

2.2.4. R-Parity and Symmetry Breaking

The invariance of the Lagrangian density of SUSY models under gauge and SUSY transformations does not necessarily require lepton and baryon number conservation. While this has no consequences for theory, it is highly inconsistent with experimental findings. For instance, this would allow proton decays violating lepton and baryon number conservation, leading to a much shorter proton life time than what was experimentally determined.[13]
For this reason, a new discrete and multiplicative symmetry called *R-parity* is needed to assure a consistent theory extension which is compatible with the observed stability of the proton. It is defined as follows:

$$P_R = -1^{3(B-L)+2s} \tag{2.18}$$

with B denoting the baryon number, L the number of leptons and s the spin of the particle. In contrast to all SM particles carrying an even R-parity ($P_R = +1$), the SUSY particles have odd R-parity ($P_R = -1$).
From R-parity conservation some important consequences can be derived:

[13]The lower bound for the proton mean life is $t_{1/2} = 2.1 \times 10^{29}$ a in the p $\rightarrow$ invisible mode.[24]

- The lightest supersymmetric particle (LSP) must be stable because any decay into another SUSY particle is kinematically forbidden. Moreover, it carries $P_R = -1$, thus a decay into any SM particle would violate R-parity conservation. Furthermore, the LSP must not carry electric or colour charge, which means that it can only interact weakly and gravitationally because any other option would contradict the observable state of our universe. It is therefore a suitable Dark Matter candidate.

- Every supersymmetric particle, except the LSP, must decay into a final state with an odd number of LSPs, since the negative R-parity has to remain.

- In collider experiments, only even number of supersymmetric particles are expected to be produced. Since SM particles are collided which carry positive R-parity, the parity product of all final state particles must also be positive.

The SUSY model considered in this thesis assumes R-parity conservation. Nevertheless, there are many other searches based on R-parity violating models, which are able to set limits on R-parity violating coupling strengths.

Until the completion of this thesis, evidence for the existence of supersymmetric particles has not been found. This clearly contradicts the symmetry described in (2.16): if supersymmetry was an exact symmetry, then SM particles and their superpartners would have exactly the same masses and could already have been detected. This leads to the conclusion that supersymmetry must be a broken symmetry and that there must be a breaking mechanism included in the theory.
There are several possibilities to implement a breaking mechanism, like *minimum supergravity* (mSUGRA), *gauge-mediated symmetry breaking* (GMSB), or *anomaly-mediated symmetry breaking* (AMSB) which lead to different mass spectra of the sparticles.

2.2.5. SUSY Phenomenology

Supersymmetric particles can be produced in various processes which can be grouped into two categories: electroweak and strong production.
Electroweak channels are based on the annihilation of a quark-antiquark pair (in the initial state) producing neutralinos, charginos or sleptons (in the final state).
The strong production, on the other hand, comprises fusions of quarks with gluons as well as gluon-gluon fusion resulting in pairs of gluinos or squarks or a gluino-squark combination (see figure 2.8). Quark-antiquark annihilation or quark-quark scattering processes as shown in figure 2.9 are also able to contribute to the production of gluino or squark pairs.

The process considered as a benchmark signal is the pair production of squarks by gluon-gluon fusion. For both production channels the coupling strengths are the same as for SM processes, which is why sparticles are expected to be produced more likely by strong interaction processes than weakly in proton-proton collisions at the LHC.

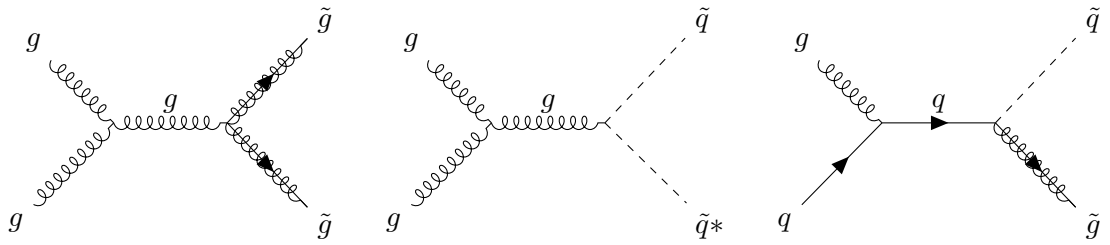

Figure 2.8.: Tree level Feynman graphs as examples for dominant gluon-gluon and gluon-quark fusion processes in the s-channel (based on [28]). The channel considered in this thesis is the one shown in the middle.

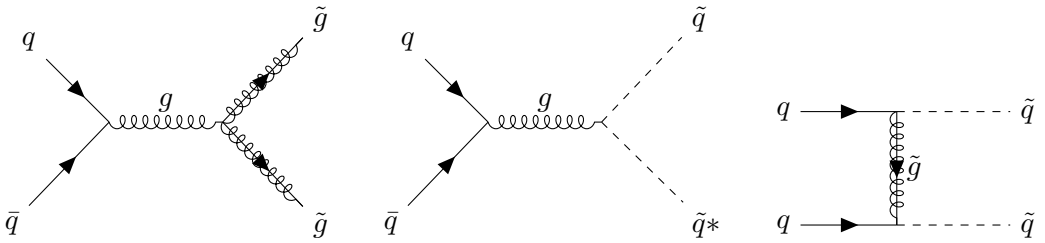

Figure 2.9.: Tree level Feynman graphs as examples for quark-antiquark annihilation and quark-quark scattering processes in the s-channel strongly producing pairs of gluinos or squarks. (based on [28])

The probability of SUSY processes occurring at the LHC strongly depends on the masses of the sparticles, which are free parameters and must be determined experimentally, and the available centre of mass energy (see section 3.1).

The sparticles which could be produced this way are expected to decay, under the assumption of R-parity conservation, into SM and SUSY particles with an odd number of LSPs in the final state as explained in section 2.2.4 . Figure 2.10 shows the possible decays for gluinos and squarks.
While squarks are expected to decay into a quark-gluino pair if kinematically allowed, they may also be able to decay into a quark and neutralino or chargino. In this case,

left-handed squarks are expected to prefer decaying into heavier charginos or neutralinos while right-handed squarks are expected to favour the direct decay to the LSP.
An example for the first case is the channel $\tilde{q} \rightarrow \tilde{\chi}_1^{\pm} + q \rightarrow \tilde{\chi}_1^0 + l + q$, a very well studied SUSY process leading to a final state containing a quark jet, a lepton and missing transverse energy due to the LSP escaping the detector without a trace. The latter decay channel $\tilde{q} \rightarrow q + \tilde{\chi}_1^0$ would lead to a final state containing a quark jet and missing transverse energy due to the escaping LSP, but without any leptons. This specific signal type matches the new physics signature of interest, thus it is used as a benchmark model in the analysis of this thesis, as chapter 5 describes in more detail.

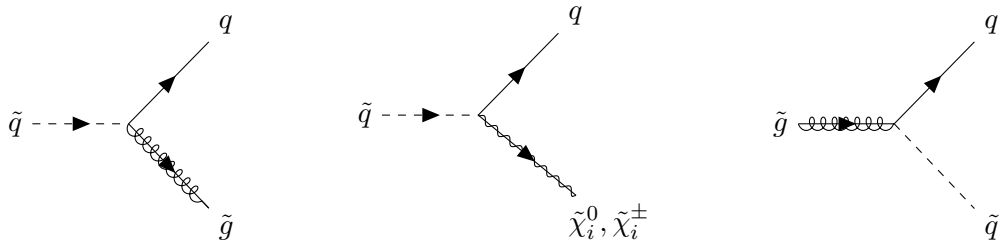

Figure 2.10.: The diagrams on the left and in the middle show the strong and weak decay channels of the squarks while the diagram on the right illustrates the strong decay of gluinos into a squark-antisquark pair. (based on [28])

2.3. Current Searches and Exclusion Limits

This section summarises the most important milestones on the path of searches for new physics with focus on SUSY searches until the beginning of this thesis.
To this day, no hints of the existence of supersymmetric particles, other WIMP candidates or any other BSM physics have been found in any of the variety of BSM searches performed all over the world for the last decades. A summary of different BSM searches with ATLAS is given in figure 2.11. Comparable results from the CMS experiment can be found in [52].

From 1989 to 2000, CERN operated the Large Electron-Positron (LEP) Collider with a centre-of-mass energy ranging from 91 GeV at the beginning to 209 GeV before the shutdown. During this time, the four experiments ALEPH, DELPHI, L3 and OPAL collected data and tested different SUSY models.
Simultaneously, a proton-antiproton collider called Tevatron with the two detectors CDF and DØ run by Fermilab reached an even higher centre-of-mass energy of up to 1 TeV. The combined results for the SUGRA based search for squarks and gluinos are shown in figure 2.12.

Starting in 2008, a new accelerator called the *Large Hadron Collider* (LHC) succeeded LEP, accelerating and colliding protons with a centre-of-mass energy of 7 TeV and 8 TeV in 2011 and 2012 (Run-1) and later from 2015 until the end of 2018 with 13 TeV (Run-2). The two experiments ATLAS (A Toroidal LHC ApparatuS) and CMS (Compact Muon Solenoid) have recorded data that was used in multiple SUSY searches. The ATLAS results for Run-1 are summarised in figure 2.13. Corresponding CMS results can be found in [56]. The accelerator and the ATLAS detector, which were also used for the analysis of this thesis, will be presented in more detail in chapter 3.

As a reference analysis the 0-lepton search is used, whose results based on the data sets from Run-1 are interpreted in the context of simplified models where squarks and gluinos are pair-produced and directly decay into quarks and neutralinos (i.e. the LSP). [57]. These results obtained by both the ATLAS and CMS 0-lepton groups are presented in figures 2.14 and 2.15.
By considering these broad exclusions, it appears unlikely that there is a possible SUSY discovery below the TeV range. Nevertheless, it is crucial to examine the remaining parameter spaces very thoroughly and to optimise and compare the existing methods of analysis.

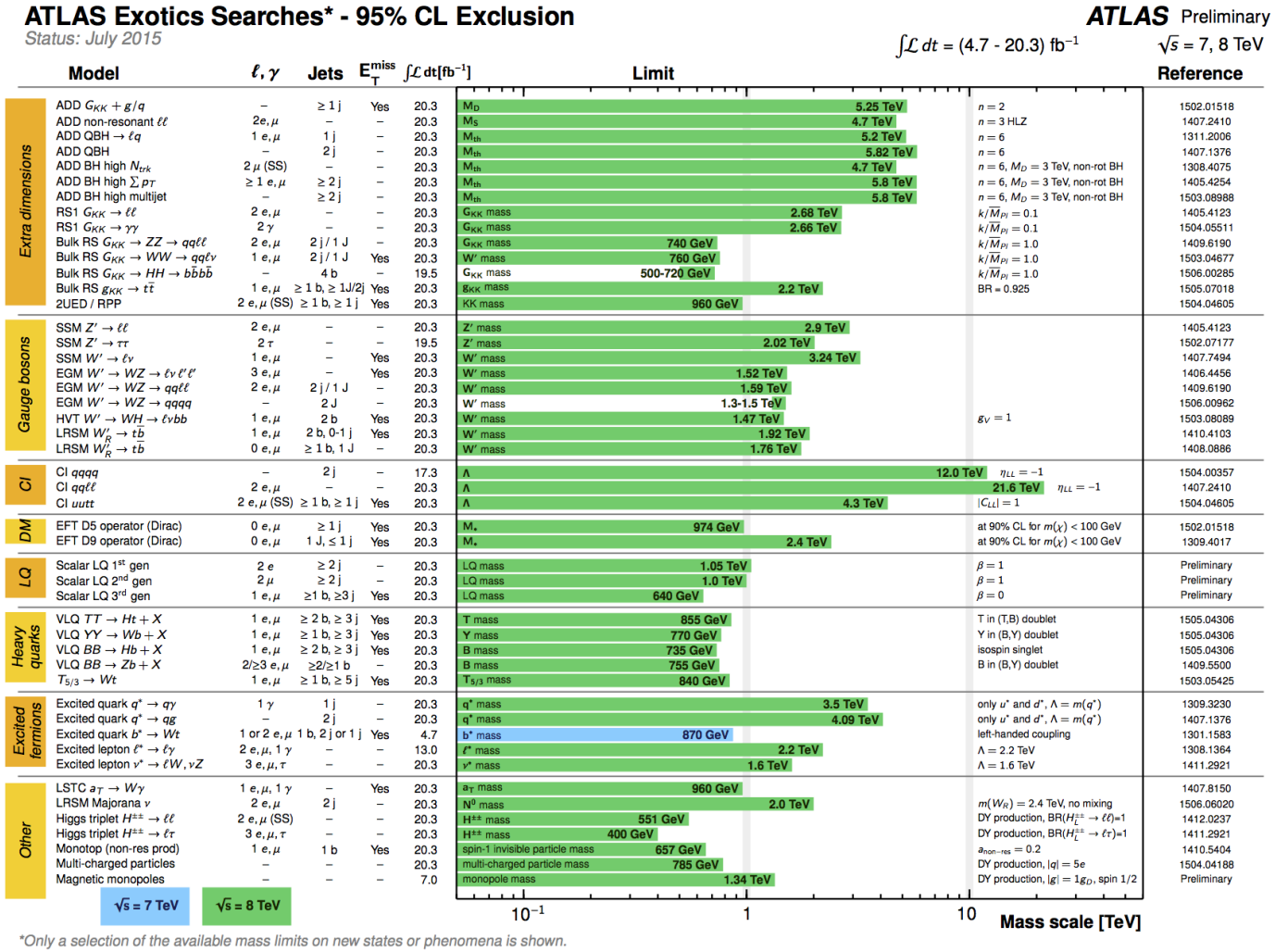

Figure 2.11.: Summary of multiple searches performed at the ATLAS experiment based on the 7 TeV (blue bars) and 8 TeV (green bars) data sets.[53]

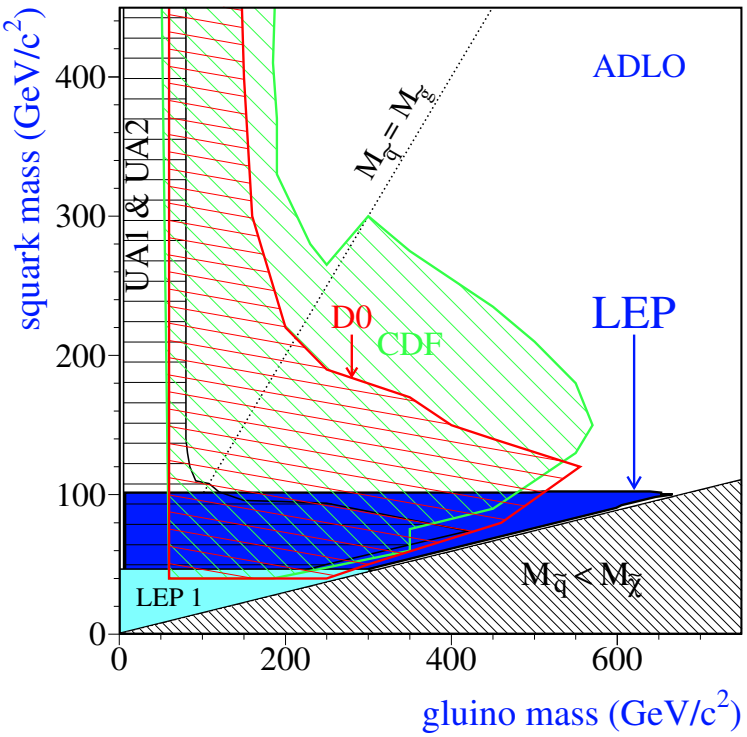

Figure 2.12.: Combination of SUSY searches by LEP and Tevatron.[54] The plane of the squark and the gluino mass is shown. The light and dark blue areas mark the parameter ranges excluded by LEP experiments, the green and red shaded sectors could be excluded by the Tevatron experiments. The black striped area on the left could be excluded by previous experiments. The black shaded area is kinetically forbidden.

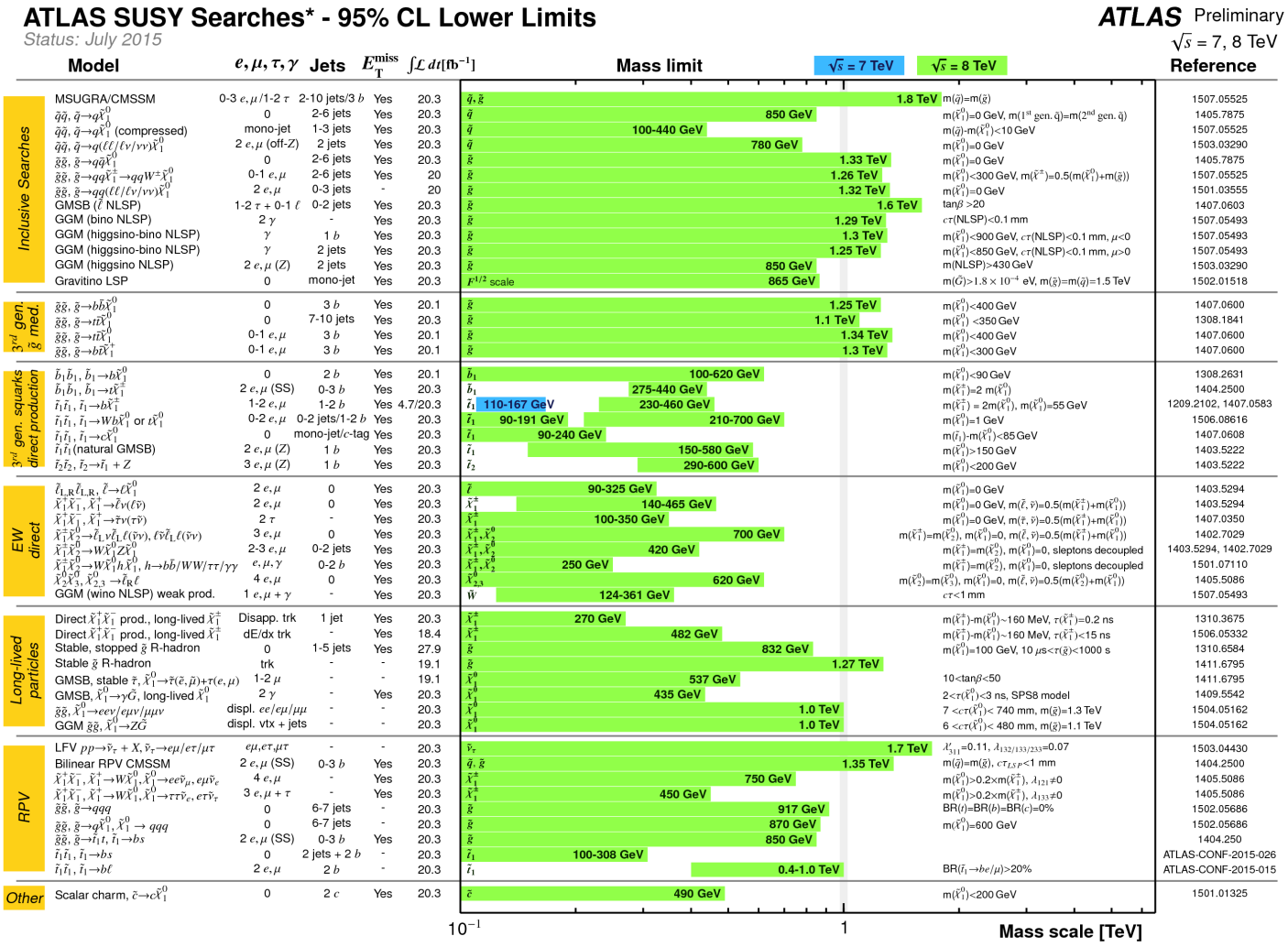

*Only a selection of the available mass limits on new states or phenomena is shown. All limits quoted are observed minus 1σ theoretical signal cross section uncertainty.

Figure 2.13.: Summary of ATLAS SUSY search results based on various different models and obtained with multiple analysis strategies. The green bars show the exclusion range for different sparticle masses gained from the 8 TeV data sets while those from 7 TeV data are shown in blue.[55]

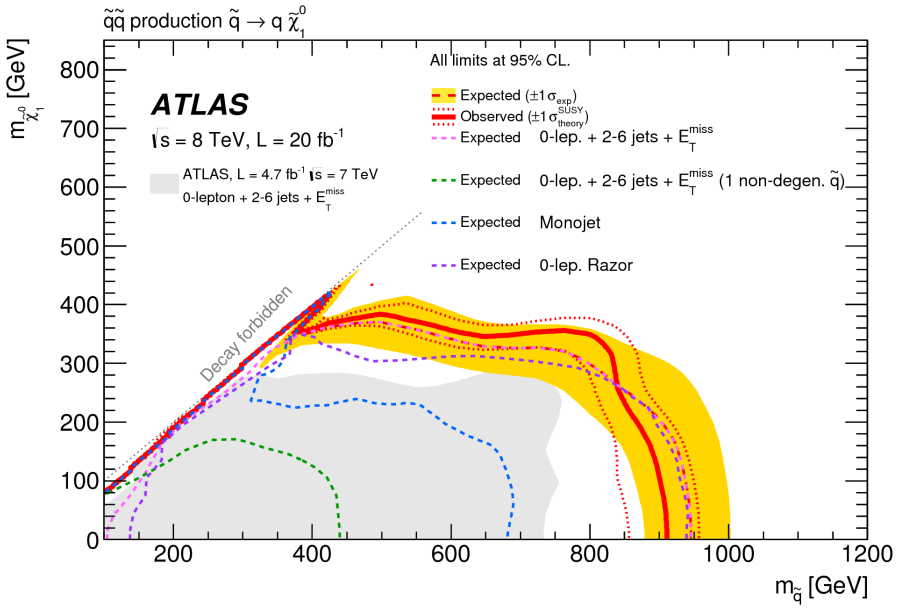

Figure 2.14.: Exclusion limit of the 0-lepton analysis at ATLAS performed with the full data set of 2011 (grey area as a comparison) and 2012. The expected exclusion limits of different search methods are marked with dashed lines, the combined one in red with a yellow uncertainty band, and the solid red line shows the observed limit.[57].

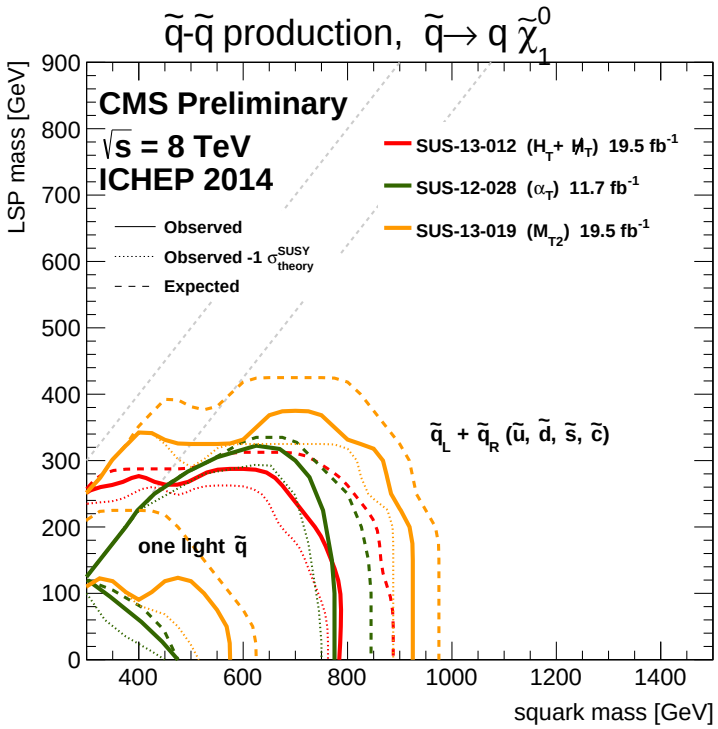

Figure 2.15.: Exclusion limit of the 0-lepton analysis of CMS performed with the data set of Run-1. The dashed lines mark the expected limit while the solid lines show what was observed with data.[58]

Chapter 3.

Experimental Facilities

The European Organization for Nuclear Research (CERN)[59], an international research organisation founded in 1953, currently operates the world's most powerful accelerator, the Large Hadron Collider (LHC). Until today, 23 member states have joined this unique European project involving nine accelerators and more than 20 different experiments.
Chapter 3.1 gives an overview of CERN's accelerator facilities focusing on the LHC, which provides the high energy proton beams for the experiments ATLAS, CMS, ALICE and LHCb. They are located at four intersection points of the two beam tubes contained in the LHC's accelerator ring.
The ATLAS detector[60], one of the two multi purpose detectors at the LHC, records proton-proton collisions and delivers data for many studies, amongst others for a wide range of BSM searches (see chapter 2.3) as well as for the analysis presented in this thesis. It is introduced therefore in more detail in chapter 3.2, where the most relevant components for this search are explained.

3.1. The Large Hadron Collider

After the Large Electron-Positron (LEP) Collider was shut down in 2000, its facilities, including the circular tunnel with a circumference of 27 km, were reused for a more powerful successor, the LHC [61][62].
The LHC was designed to accelerate and collide protons and lead ions with a centre-of-mass energy of maximum 14 TeV and 1150 TeV, respectively. It is defined as $\sqrt{s}$ with $s = (p_1 + p_2)^2$, where p_1 and p_2 are the four-momenta of the colliding protons.

This record energy becomes accessible to the hadrons, in this case protons[1], by undergoing two stages.

[1] The experiments with heavy ions are not relevant for the analysis presented in this thesis and will therefore be neglected in the following.

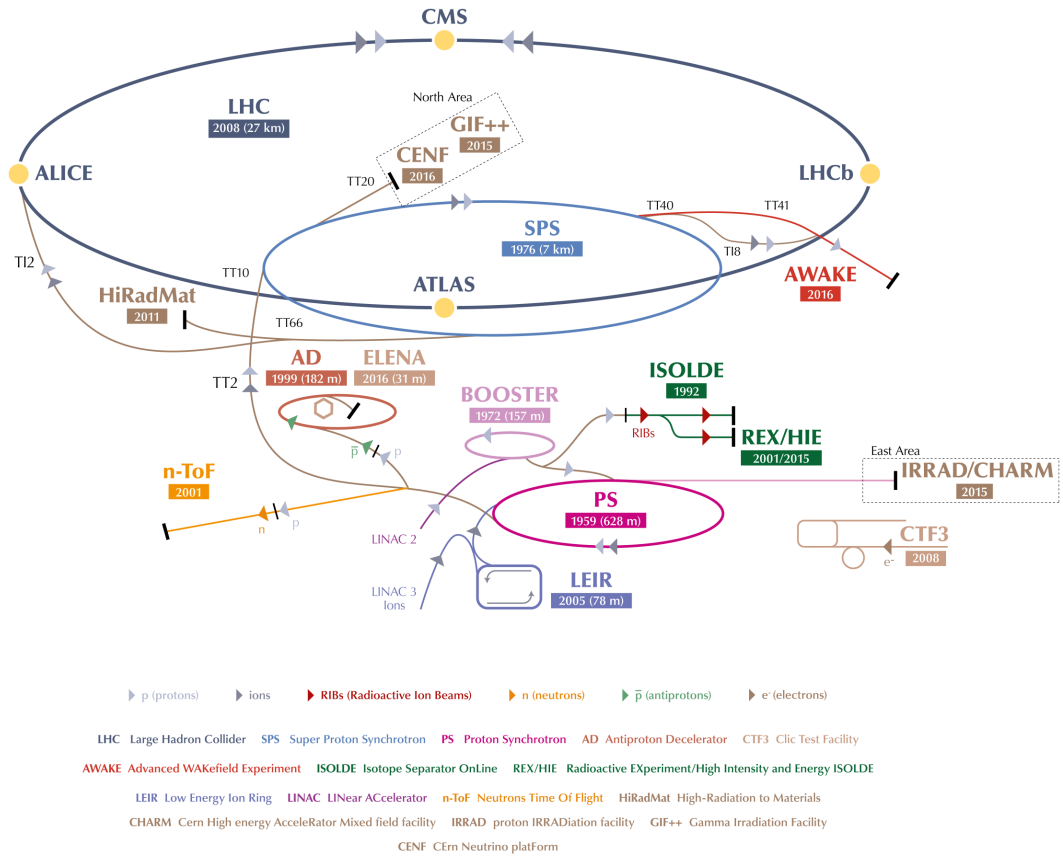

Figure 3.1.: CERN's accelerator complex including LINAC2, Booster, PS and SPS which act as pre-accelerators for the LHC. [63]

First, the protons are inserted into CERN's accelerator complex and accelerated in different steps to a velocity of more than $0.9999 \times c$ and a kinetic energy of 450 GeV. It is shown in picture 3.1 and acts as an accelerator chain by passing the protons from one accelerator to the next, increasing their velocity during each step.
The protons, obtained by ionising hydrogen atoms, are first inserted into a linear accelerator, LINAC2, then further into the first circular accelerator called Proton Synchrotron Booster (PSB), followed by the Proton Synchrotron (PS) and then to the Super Proton Synchrotron (SPS) before they finally enter the LHC.

Second, while being filled into the LHC, the protons are split over two separate beam pipes, which run parallel but in opposite directions. They are further accelerated to a maximum of 7 TeV per beam, providing a centre-of-mass energy at the collision points of 14 TeV. The LHC did not run with this design centre-of-mass energy yet but rather

increased the value from 7 TeV to 8 TeV during Run-1. For the data taking period of Run-2, it was increased to 13 TeV and only the next run will be conducted at the maximum centre-of-mass energy.
Head-on collisions can be conducted at four intersection points making the maximum centre-of-mass energy available in these precise areas.

To increase the collision probability, each of the two beams consists of 2808 bunches, containing about 1.2×10^{11} protons. The time gap between the bunches was set to 50 ns in Run-1 and then decreased to 25 ns in Run-2 which corresponds to a frequency of 40 MHz. To be able to keep the protons on a circular trajectory, the accelerator rings are equipped with powerful superconducting dipole magnets, cooled down with superfluid helium to only 1.9 K, whose magnetic fields force the charged particles on a curved path. Furthermore, superconducting quadrupole magnets are used in order to compensate for the repulsion between the protons, to focus the beams in the transversal plane to the beam direction and thus increase their intensity.

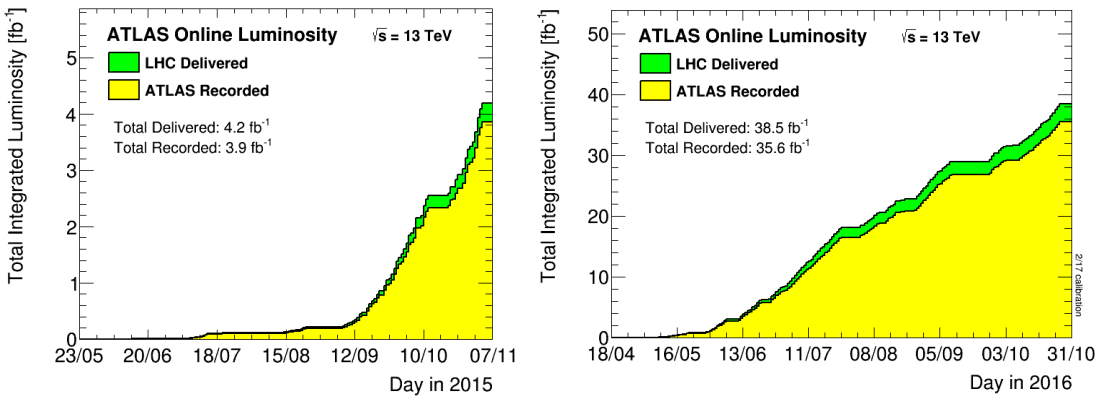

Figure 3.2.: Integrated luminosity delivered by the LHC (green) and recorded by the ATLAS detector (yellow) during the data taking periods of 2015 and 2016 [64]

To measure the intensity of the proton beams, a quantity called *luminosity* is used which measures the number of proton interactions per area and time and is defined as follows:

$$\mathcal{L} = \frac{N_p^2 n_b f}{4\pi\sigma_x\sigma_y}. \tag{3.1}$$

Here, N_p is the number of protons per bunch and n_b the number of bunches collided with frequency f. The bunches are assumed to have Gaussian distributed x- and y-widths σ_x and σ_y. The number of events, i.e. how often a specific process is expected to occur

during a period of data taking, is then given by the luminosity integrated over time and the *cross section* σ of the process:

$$N_{\text{process}} = \sigma_{\text{process}} \times \int \mathcal{L}\, dt \tag{3.2}$$

Figure 3.2 shows the integrated luminosity for the data taking periods of 2015 and 2016.

The cross section of a process is a measurable quantity to describe the probability of this process occurring in particle collisions, which, according to the factorisation theorem by Drell and Yan [65] and under consideration of leading corrections from gluon emission, can be defined as follows:

$$\sigma_{AB} = \int dx_a\ f_{a/A}(x_a, Q^2) \int dx_b\ f_{b/B}(x_b, Q^2)\ \hat{\sigma}_{ab\to X} \tag{3.3}$$

Here, the total cross section for the scattering of two hadrons A and B is normalised with $f_{a/A}$ and $f_{b/B}$ being the *parton distribution functions* (PDFs) of the two interacting partons a and b (see chapter 2.1.2), while $\hat{\sigma}_{ab}$ denotes the cross section on parton level. Since the proton momentum is divided among all its partons, the probability density to observe a parton carrying a specific momentum fraction is given by experimentally determined PDFs $f_i(x_i, Q^2)$. The *Bjørken variable* x_i is equivalent to the momentum fraction of parton i and Q^2 represents the energy transfer between the interacting partons. Figure 3.3 gives a schematic impression of such a scattering process. The different production cross sections for sparticle pairs at a centre-of-mass energy of 13 TeV are compared in figure 3.4.

Obviously, a high number of protons per bunch and a small bunch spacing are beneficial for the study of rare processes but they also lead to increased additional interactions, called *pileup*. Two effects can be distinguished: on one hand, in addition to the hard scattering process of interest, other proton collisions can appear during the same bunch crossing and leave traces with different points of origin, called *vertices*, in the detector. This effect is known as *in-time pileup*. On the other hand, *out-of-time pileup* can occur when detector measurements of remnants of a previous bunch crossing are delayed so that they are assigned to the following bunch crossing. The average number of interactions per bunch crossing for the 2015 and 2016 data is presented in figure 3.5.

3.2. The ATLAS Experiment

The ATLAS detector [69–71] is one of the two largest experiments at the LHC and serves as a general-purpose detector. Its main functions are to contribute to the discovery of new particles, like the Higgs boson in 2012, but also to enable precision measurements of SM

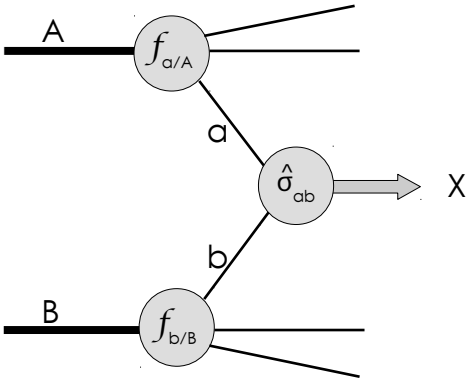

Figure 3.3.: Schematic illustration of hadronic scattering processes in which e.g. sparticles could be produced. (based on [66])

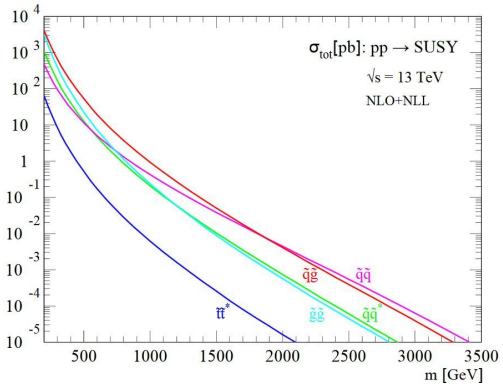

Figure 3.4.: Different production cross sections as functions of the sparticle masses considering higher order corrections.[67]

processes. Searches for dark matter candidates and other new physics objects particularly rely on ATLAS.
In order to detect a variety of particles with different properties, it has a cylindrical form with six concentric layers of detecting material (see figure 3.6). These components are optimised for recording different types of particles with the highest possible resolution and are described in sections 3.2.1 to 3.2.3 following [71].

The collision point of the two proton beams is positioned in the centre of ATLAS to maximise the coverage of solid angle in the forward regions close to the beam pipe. The products of the scattering processes, which are spread in all directions, can be identified by measuring their trajectory, charge, momentum and energy. The measurements of charge and momentum additionally require a strong magnetic field which is generated by solenoid and toroid magnets inside ATLAS.
The collision point is also used to define the origin of a coordinate system and the spherical coordinates ϕ and θ are used to describe the geometry of objects within the detector as shown in figure 3.7.
Additionally, a variable called *pseudo-rapidity* η is defined as $\eta = -\ln(\tan(\frac{\theta}{2}))$, since differences in η are invariant under Lorentz boosts along the z-axis. Distances between objects can now be described as $\Delta R = \sqrt{(\Delta\phi)^2 + (\Delta\eta)^2}$. As the exact z-components of the momenta of the colliding particles are unknown and cannot be measured, their parameters are only considered in the transversal plane which is perpendicular to the beam axis. The transverse momentum and the transverse energy for example are defined as

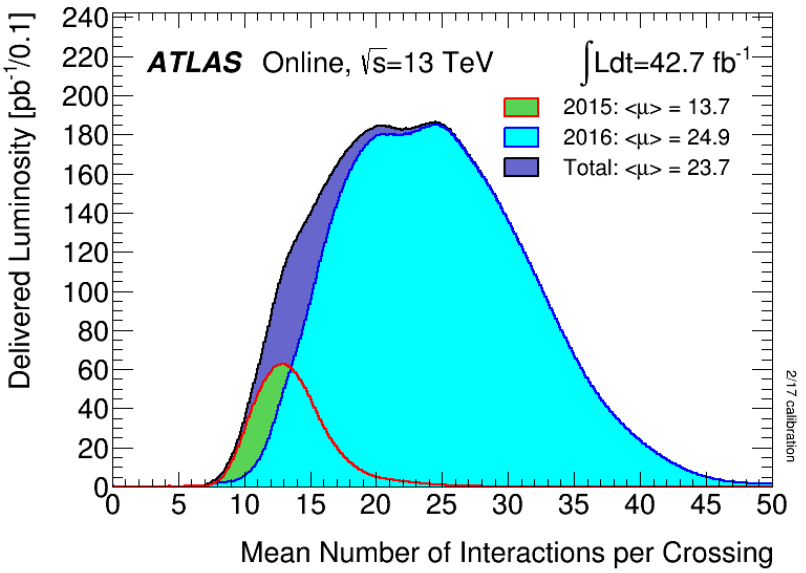

Figure 3.5.: Left: mean number of interactions per bunch crossing (μ) for the 2015 and 2016 collision data. The value of μ was considerably increased, mainly due to an increase in the number of protons per bunch.[64]

$$p_T = \sqrt{(p_x)^2 + (p_y)^2} \tag{3.4}$$

$$E_T = \sqrt{(E_x)^2 + (E_y)^2} \tag{3.5}$$

Under ideal circumstances, if all emerging particles could be exactly measured by the detector, the vectorial sum of all transverse momenta and energies would be zero due to momentum and energy conservation. However, most important, especially for signatures of new physics like SUSY processes, are the electrically neutral particles which escape undetected, just like neutrinos.
In events, where such particles are created, their momenta and energies cannot be accounted for, thus both variables will differ from zero. This missing energy in the transverse plane, called *missing transverse energy* ($E_{\mathrm{T}}^{\mathrm{miss}}$), is one of the most frequently used variables in searches for BSM physics. It is given by the sum of the missing energy in the transverse plane in the calorimeter and in the myon spectrometer.
Another quantity frequently used as a discriminating variable is the *effective mass* (M_{eff}), which is defined as the scalar sum of the transverse momenta of all jets together with the missing transverse energy in an event.

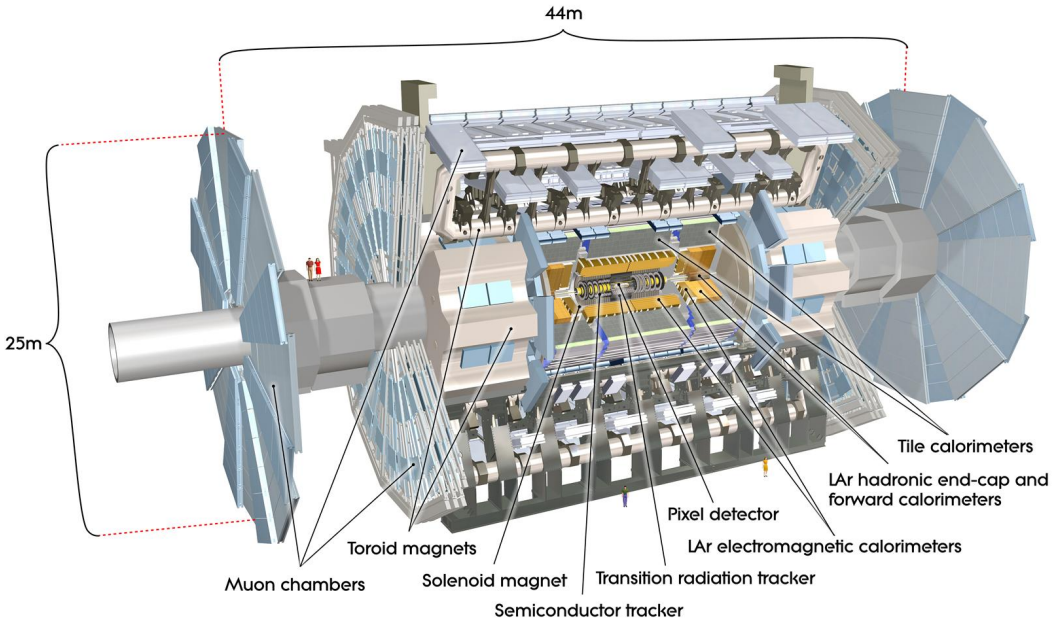

Figure 3.6.: Computer generated image of the ATLAS detector. Its main components are individually labelled and persons are shown for scale. [68]

For the exact determination of both variables, a high detector resolution, especially in the calorimeter (see section 3.2.2), is crucial.

3.2.1. The Inner Detector

The detector component closest to the beam pipe and the interaction point is the inner detector (ID) shown in figure 3.8. Its main task is the detection of particle tracks and their curvatures for the reconstruction of the vertices and the momenta of electrically charged particles. Thus, it uses a solenoidal magnetic field of 2 T.
It consists of three sub-detectors with a total length of 6.2 m and an outer radius of 1.15 m, covering a pseudorapidity range of $|\eta| < 2.5$: the pixel detector, the semi-conductor tracker (SCT) and the transition radiation tracker (TRT), as presented on the right of figure 3.8.

From 2013 to 2014, the pixel detector was upgraded with an additional pixel layer called insertable B-layer (IBL)[73], so that since Run-2 it contains four layers with 46080 pixels per pixel module in the barrel region. Moreover, both end-caps contain three discs with additional pixel modules, leading to a total of 92 million pixels, which are the smallest read-out units with a size of $50\times\ 400\,\mu m^2$ (90% of the pixels) or $50\times\ 600\,\mu m^2$ (10% of

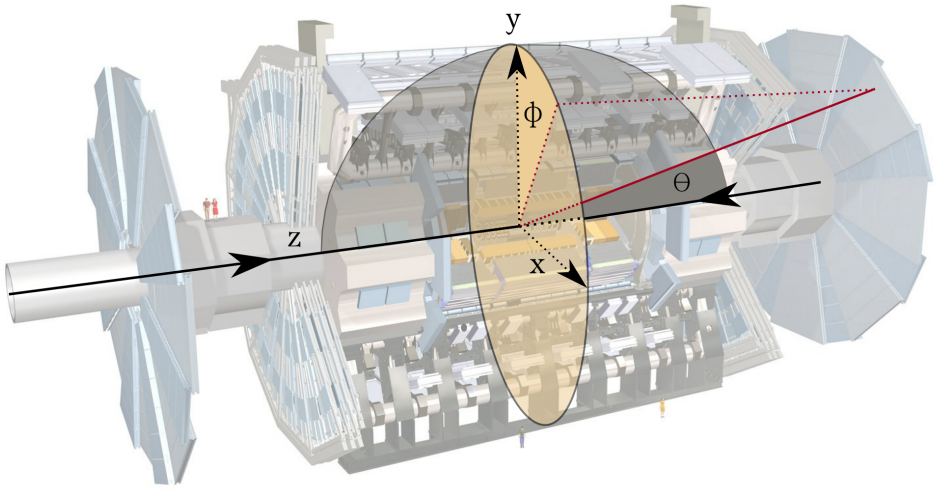

Figure 3.7.: The geometry of ATLAS: The origin of the coordinate system is positioned at the collision point, its z-axis is aligned with the beam axis and the x-y-plane is perpendicular to the beam direction. The position of any object can be described using the two spherical coordinates $\theta \in [0, \pi]$ and $\phi \in [-\pi, \pi]$ (based on [68]).

the pixels) and an intrinsic accuracy of 10 µm in $(R - \phi)$ and 115 µm in z for the barrel region (10 µm in $(R - \phi)$ and 115 µm in R for the end-caps). Hence, they are mainly responsible for the high granularity of the pixel detector.
The SCT is built similarly to the pixel detector with four double layers of silicon micro-strip modules in the barrel region and nine in each end-cap. Due to the positioning of the strips, particles can be detected with an accuracy of 17 µm in $(R - \phi)$ and 580 µm in z for the barrel region (17 µm in $(R - \phi)$ and 580 µm in R for the end-caps).
The outermost sub-detector is the TRT, which consists of gas-filled tubes called straw tubes functioning like proportional counters. If highly relativistic particles pass the tube walls made of inhomogeneous dielectric media, the emitted transition radiation photons will lead to electrical signals. The signal amplitudes depend on the intensity of the absorbed photons which is proportional to the Lorentz factor of the particles. Therefore, by using separate low and high thresholds on a straw-by-straw basis, a distinction between particle types can be achieved to compensate for the lower resolution of 130 µm in $(R - \phi)$ direction. Thus, the TRT is used to identify particles with the same charge but different

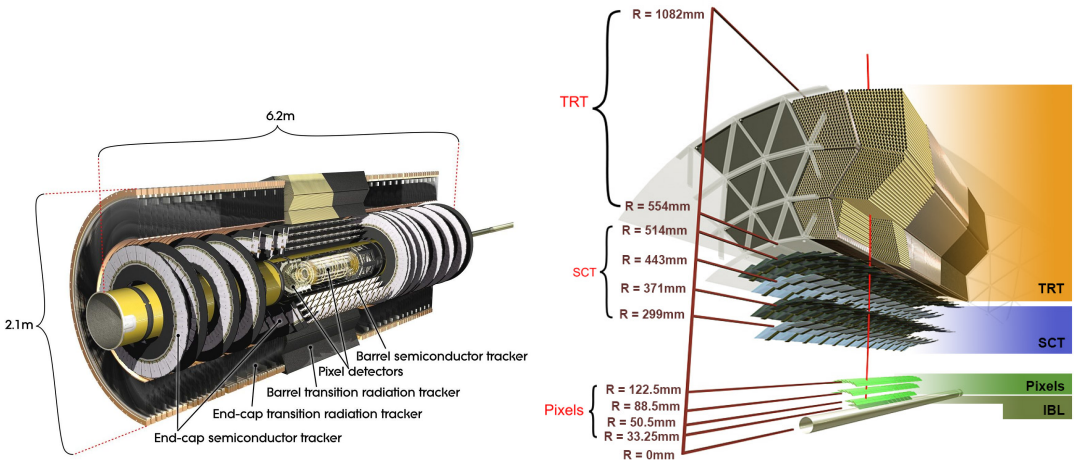

Figure 3.8.: Structure of the inner detector in a cut-away view (left) and a section of the barrel region (right).[72][73]

masses like pions and electrons and also to measure their momenta using the bending of their trajectories due to the magnetic field.

3.2.2. The Calorimeter System

The calorimeter allows the energy measurement of charged and neutral particles which enter it after passing the inner detector. It is also crucial for the reconstruction of jets and missing transverse energy.
Until they are fully absorbed, particles produce electromagnetic or hadronic showers when interacting with the calorimeter material which have to be contained and measured as completely and precisely as possible. The calorimeter system consists of two sub-detectors, the electromagnetic (EMCal) and hadronic calorimeters (HCal), providing a coverage up to $|\eta| < 4.9$. Both are built as sampling calorimeters and contain absorbing lead plates to cause interaction and showering in alternation with liquid argon as active material to ensure a stable measurement of the deposited energy. They are cylindric and consist of a barrel surrounding the inner detector, end-caps and extended barrels enclosing the end-caps as shown in figure 3.9. In addition to the large η-coverage, a thickness of at least 22 radiation lengths will ensure precise measurement of the missing transverse energy, which is important especially for many BSM physics signatures.
The EMCal is optimised to measure electron and photon energies or electromagnetically interacting particles in general. These cause ionisation in the liquid argon leading to secondary particles (showers of low-energy electrons, positrons and photons), which are recorded by electrodes. The accordion-shaped geometry of electrodes and absorber guarantees a full ϕ-symmetry and coverage. While the barrel region ($|\eta| < 1.475$) is

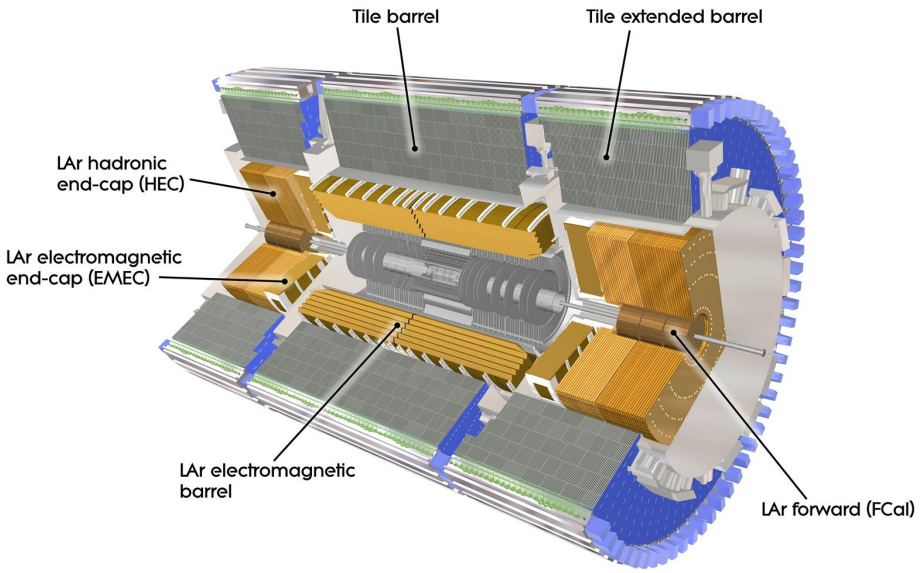

Figure 3.9.: The calorimeter system [74]

equipped with three active layers, the end-caps ($1.375 < |\eta| < 3.2$) and the overlap regions between barrel and end-caps only have two in depth, each layer with a different granularity $\Delta\phi \times \Delta\eta$.
The HCal is suited to measure the energies of hadrons such as neutrons, protons or pions whose interactions with the detector lead to hadronisation and the formation of jets. Since they have a longer radiation length, it is positioned concentrically around the EMCal. It is built analogously to the EMCal, but uses a different sampling material, which consists of steel absorber and plastic scintillator tiles as active material in the barrel ($|\eta| < 1.0$) and extended barrels ($0.8 < |\eta| < 1.7$) and liquid argon in the end-caps ($1.5 < |\eta| < 3.2$). Additionally, a forward calorimeter (FCal) is used, built of liquid argon as active and copper and tungsten as passive materials, since the high-η regions must sustain higher energy radiation.

The energy resolution for reconstructed objects such as jets in the calorimeter strongly depends on the object's energy. It can be described by equation 3.6.

$$\frac{\sigma E}{E} = \frac{N}{E} \oplus \frac{S}{\sqrt{E}} \oplus C \tag{3.6}$$

At lower energies, it is dominated by the noise term (N), containing electronics and detector noise as well as pile-up. At medium energies, the stochastic term (S) is most

limiting, which includes statistic fluctuations. At higher energies, the constant term (C) predominates which takes into account fluctuations that are a constant fraction of the energy like signal loss in passive material [75].
The values of these terms in the case of jets in the central region ($0.2 < |\eta| < 0.4$) were determined to be $S \approx 60\,\%\sqrt{\mathrm{GeV}}$, $C \approx 3\%$ and $0.5\,\mathrm{GeV} < N < 1.5\,\mathrm{GeV}$ going from the barrel to the end-cap region.[76]
Since for this analysis jets are the most important objects to be reconstructed from calorimeter data (described in more detail in chaper 4.5), their energy resolution as a function of η is shown in figure 3.10.

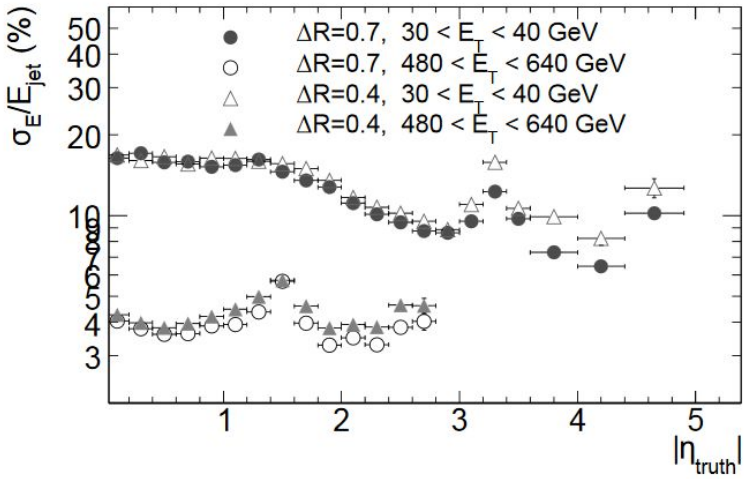

Figure 3.10.: Jet energy resolution of QCD di-jets as a function of η. Different jet energies (E_T) and sizes (ΔR) are compared[76]

3.2.3. The Muon Spectrometer

The muon spectrometer is the outermost component of the ATLAS detector and surrounds the calorimeter. This order is necessary since muons are minimum-ionising particles and therefore lose only a small amount of energy in the calorimeter. The calorimeter systems are designed to contain the complete energy deposits of particles like electrons or photons as well as hadronic particles. This also avoids punch-throughs into the muon system, thus muons are the only charged particles to enter the muon spectrometer. Their energy and momentum can be measured using a toroidal magnetic system to deflect their tracks: a large barrel toroid provides a magnetic field of 0.5 T mostly orthogonal to the trajectories in the range of $|\eta| < 1.4$ and two end-cap magnets with 1 T in the $1.6 < |\eta| < 2.7$ region (see figure 3.11). Therefore, combined with the tracking information from the inner

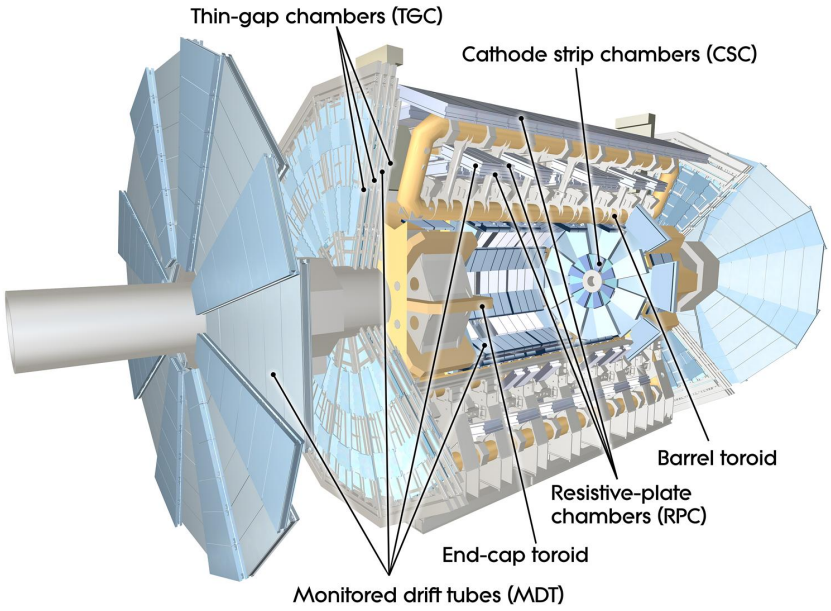

Figure 3.11.: Muon spectrometer [77]

detector, the muon system allows the reconstruction of muon tracks.
The operating principle is analogous to the TRT: there are three cylindrical layers of monitored drift tubes (MDTs) in the barrel region and also three layers of cathode strip chambers (CSCs)[2] perpendicular to the beam axis in the end-caps. To enable fast triggering on high-energy muons, resistive plate chambers (RPCs) and thin gap chambers (TGCs) are used in the barrel region and end-caps, respectively. These trigger chambers do not only provide bunch-crossing identification, but also well-defined energy thresholds and additional muon coordinates.
The resolution of the muon spectrometer strongly depends (alongside the momentum of the muons) on the η-range as is shown in figure 3.12.

3.2.4. The Trigger System and Data Acquisition

Given the technical possibilities, the recording and storage of data produced by collisions in the ATLAS detector at a rate of 40 MHz can only be achieved if the quantity is reduced. Only interesting events must be efficiently selected and stored for further processing and analysis.
This can be accomplished by the ATLAS trigger and data acquisition (TDAQ) system. Since increased event sizes were expected for Run-2 due to pile-up effects and more

[2] CSCs are multi-wire proportional chambers with cathodes segmented into strips.

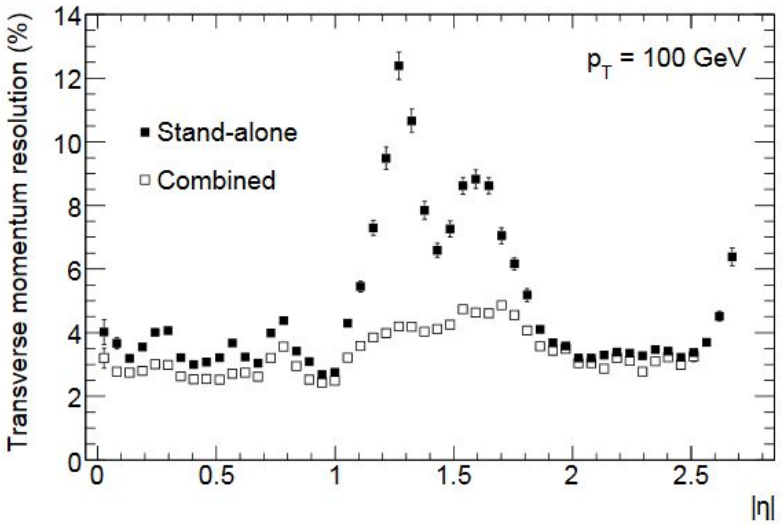

Figure 3.12.: Expected fractional momentum resolution for muons with $p_T = 100\,\text{GeV}$ as a function of $|\eta|$ for stand-alone and combined reconstruction. In the $1.1 < |\eta| < 1.7$ region the resolution is decreased due to several reasons (absence of middle muon stations in the barrel/end-cap transition region for the initial data-taking, low bending power of the magnetic field in the transition region between barrel and end-cap toroids, material of the coils of the end-cap toroids). [76]

efficient technology was available, the TDAQ system received major improvements during the long shutdown 2013-2014 between Run-1 and Run-2, described and summarised in [78].
The TDAQ system consists of the two level trigger (Level 1 (L1) and High-Level-Trigger (HLT)) on the one hand and the data acquisition on the other hand as shown in figure 3.13.
Their main task is to process the detector information from 160 million readout channels, to identify potentially interesting events based on different criteria in real time and to subsequently reduce the event rate for storage.
The hardware-based L1 trigger selects events containing high-energy objects like muons, electrons, photons or hadronically decaying τ-leptons and jets as well as missing transverse energy. Thus, L1 uses reduced-granularity information from RPCs and TGCs for the muons and from all calorimeter sub-systems. Taking less than 2.5 µs for its decisions, the L1 leaves an event rate of 100 kHz.
The detector regions, where objects of interest were identified by the L1 trigger, are stored as *Regions of Interest* (RoI) and used later on by the HLT.

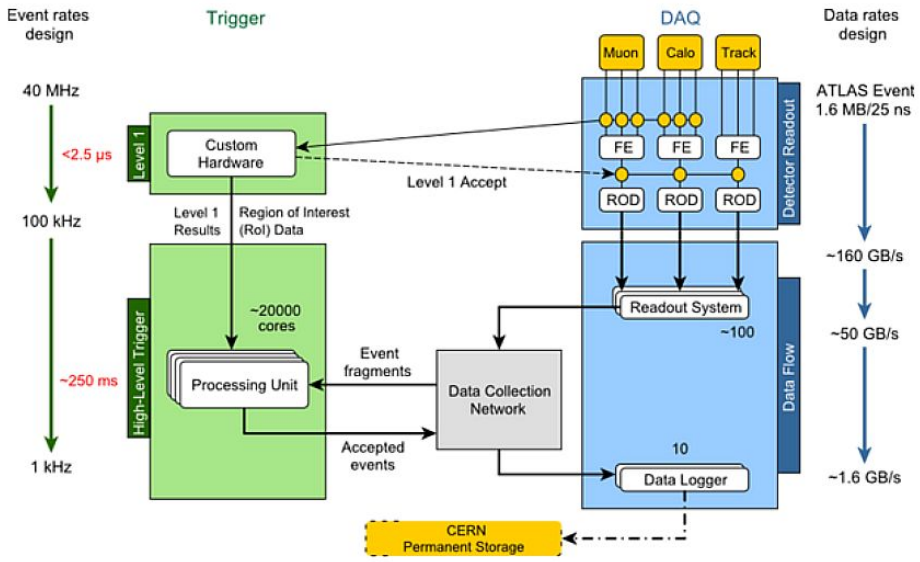

Figure 3.13.: The ATLAS Trigger and DAQ system for Run-2 [78]

The HLT is a software-based trigger which uses algorithms to select the RoI information on coordinates, energy and type of signature as well as off-line analysis procedures for the selection within 250 ms. It thereby reduces the event rate to less than 1 kHz.
In contrast to L1, the HLT can additionally access the full granularity and precision of the calorimeter and muon systems as well as information from the inner detector.
The data acquisition system (DAQ) fulfils many tasks like receiving and buffering event information from the detector readout at the L1 trigger rate into read-out drivers (RODs). It also transmits the requested RoI data in form of event fragments from the read-out system (ROS) to the HLT. Finally, if events have passed all selection criteria, they are moved to permanent storage. Only then, the events are fully reconstructed on the Tier-0 cluster at CERN, and distributed to the worldwide computing grid: first to Tier-1 and the smaller Tier-2 computer centres and finally to local Tier-3 centres at universities and institutes to ensure a parallel usage.

Chapter 4.

Object Reconstruction

To identify the objects produced in proton-proton collisions within the ATLAS detector, the information from its components is used to perform a reconstruction of their respective point of origin (the so called *vertex*), trajectory (named *track*) and energy. Figure 4.1 gives a schematic overview of tracks and showers of different particle types within the ATLAS detector. For BSM searches, a special focus lies on the quality of jets and missing transverse energy, since their qualities have great impact on the corresponding uncertainties and consequently the significances of the analyses. In this chapter, the reconstruction of jets, leptons (electrons, muons and taus[1]) and missing transverse energy is presented. Additionally, tracks, vertices and the treatment of overlapping objects are explained.

4.1. Tracks and Vertices

As described in chapter 3.1, due to pile-up effects several points of interaction can emerge during one bunch crossing (see figure 4.2). These so called *vertices* can not be detected directly, but are reconstructed from the tracks (at least two tracks with $p_T > 0.4\,\text{GeV}$ are required) of the emerging particles [80] [81]. The vertex with the highest $\sum p_T^2$, the squared sum of transverse momenta of all associated tracks, is generally defined as the *primary vertex* (PV) of the hard scatter process. Other, so called *secondary vertices* can be created by particles like tau leptons and many hadrons[2], with a lifetime long enough (order of ps) to decay at a small distance from the PV.
The tracks used for reconstructing the vertices are themselves build based on trajectory information from the pixel detector (including the IBL), SCT and TRT. It is obtained from charged particles passing through the inner detector. These *hits* are clustered together to form three-dimensional objects as described in [83].

[1] In the following, these terms refer to the lepton as well as the respective anti-particle.
[2] Especially mesons containing bottom or charm quarks are of high importance for the identification of the resulting jets, the so called *heavy flavour tagging*, exemplary shown in [82].

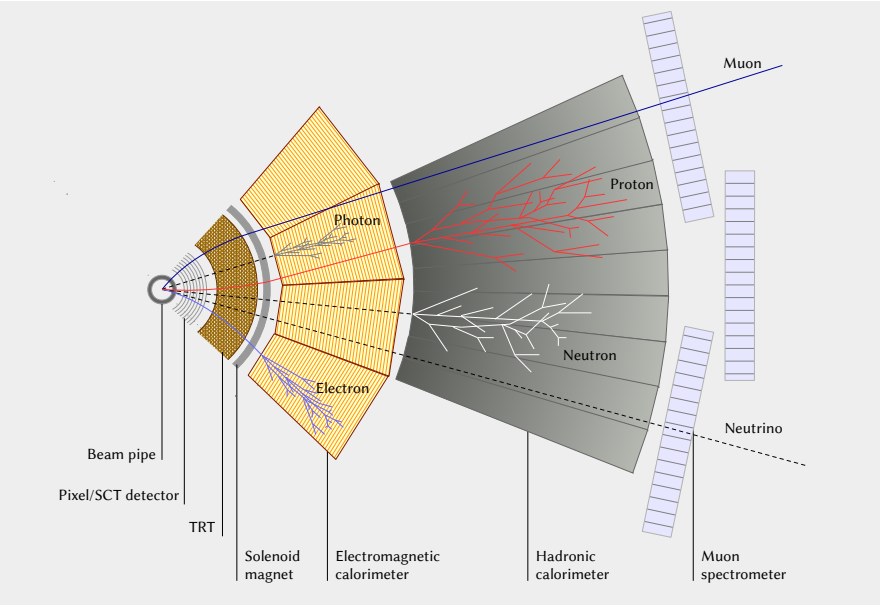

Figure 4.1.: Schematic overview of different types of particle tracks and showers as they are reconstructed based on information from the different detector components (based on [79]).

4.2. Electrons

To reconstruct and identify electrons that are produced in the event, information from the electromagnetic calorimeter is used together with the track information from the inner detector.
The energy depositions in the EMCal are analysed by a so-called *sliding window algorithm* [85], searching for cells in both η and ϕ direction of the calorimeter (only the barrel region, $|\eta| < 2.47$, is considered) with an energy deposit of $> 2.5\,\text{GeV}$, identifying them as *seed clusters* and using them as an input for the reconstruction and track matching [86]. The energy of the electron candidate is derived from the total energy of the resulting cluster, its momentum and charge from the curvature of the track.
The quality of the reconstructed electrons is specified with three divisions, called *Loose*, *Medium* and *Tight*, following the recommendations of the ATLAS e/gamma group [87]. They differ in the rejection of background (e.g. jets are often misidentified as electrons), quality of track reconstruction, quality of the track-cluster matching or the shape of the electromagnetic showers in the EMCal. Further information on the reconstruction efficiency of electrons can be found in [88]. Recent public plots show the electron

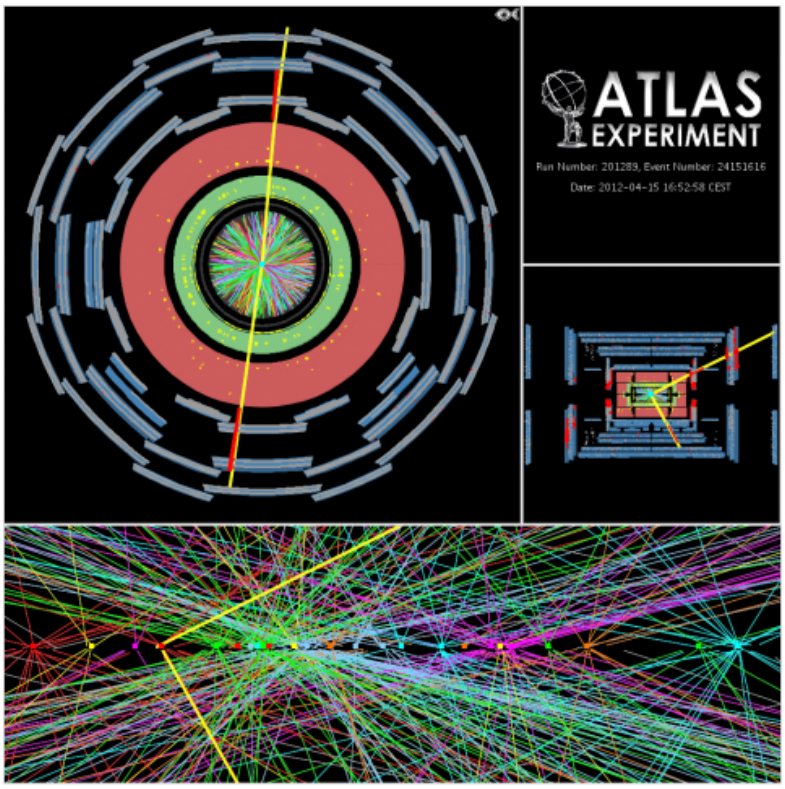

Figure 4.2.: Exemplary event display showing a hard scattering process resulting in two jets with the same primary vertex (yellow) and the simultaneously occurring interactions with multiple adjacent secondary vertices [84].

identification efficiency in $Z \to ee$ events based on 2016 data ($8.8\,\mathrm{fb}^{-1}$) as a function of transverse energy E_{T} and the pseudo-rapidity η, see figure 4.3.
The two sets of requirements which are applied to the electrons objects used in this analysis are explained in more detail in chapter 6.4. Additionally, isolation of the electron is required, demanding no further energy deposits close to those associated with the electron.

4.3. Muons

Muons are reconstructed in the ID analogously to electrons. As described in chapter 3.2.3, in contrast to electrons, they pass through all detector layers with only slight loss of energy. Hence, the track information from the ID has to be combined with those from the muon spectrometer (MS) to reconstruct a complete trajectory. The reconstruction of track candidates in the MS is done by a fitting algorithm aligning hits from segments in

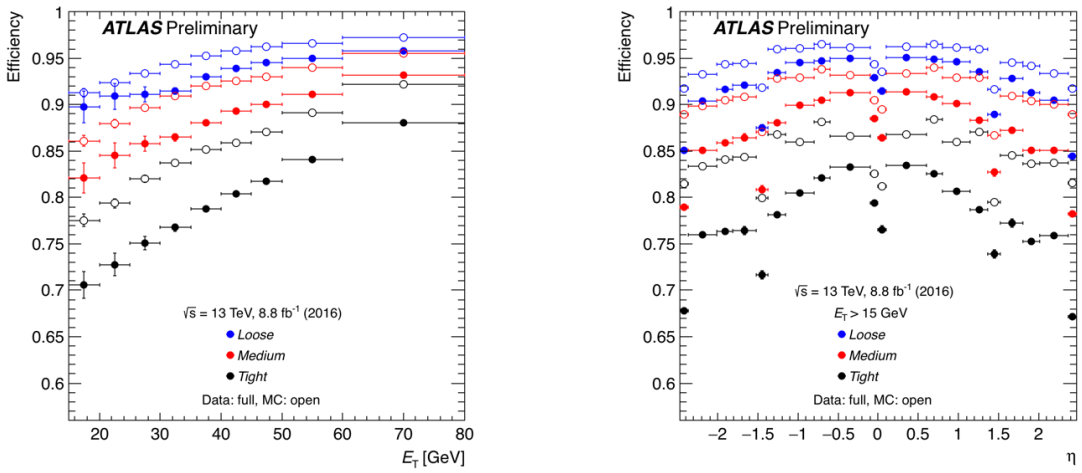

Figure 4.3.: Electron identification efficiencies in $Z \to ee$ events as a function of transverse energy E_{T} (left), integrated over the full pseudo-rapidity range and as a function of pseudo-rapidity η (right). The efficiencies were measured based on 2016 data (with $8.8\,\mathrm{fb}^{-1}$ integrated luminosity) and are compared to MC simulation[89].

different layers to a trajectory. These segments are built by searching for hit patterns and combining them inside each MDT chambers. A track candidate requires at least two matched segments, except for the barrel-endcap transition region where one can suffice. There are different possibilities to combine the independently created track reconstructions from the ID and MS and even considering information from the calorimeters. Depending on which subdetectors are used for the combined reconstruction, four different types of muons are defined:

- Combined (CB) muons: A global fit combines hits from ID and MS following a given pattern: Mostly the outside-in pattern is used, firstly reconstructing muons in the MS, then extrapolating inward to match to an ID track. Also an inside-out pattern is possible, which extrapolates the ID tracks outward to match them with MS tracks and build the combined track. This approach provides the most precise muon reconstructions.

- Segment-tagged (ST) muons: A track in the ID is extrapolated to at least one local track segment in the MDT or CSC chambers. This approach can be used even if only a few chambers in the MS are hit by the muon.

- Calorimeter-tagged (CT) muons: A track in the ID is matched to an energy deposit in the calorimeter which is compatible with a muon. This muon type has the lowest purity, but the method enables reconstruction even in those regions where the MS has poor or no acceptance due to construction conditions.

- Extrapolated (ME) muons: A track in the MS is extrapolated to a compatible vertex, without further information from the ID or calorimeter. This method is used for reconstruction of muons in the forward region which is not covered by the ID.

Similar to the electron quality classification, reconstructed muons are divided into *Loose*, *Medium*, *Tight* and *High-p_T* identification criteria, according to the ATLAS muon group's definitions [90]. They differ in the number of hits in the MS, the quality of reconstructed hits in the ID and MS and the chosen combination method. In this analysis, the *Loose* identification criterion was chosen, which provides maximum reconstruction efficiency while keeping a high muon track quality. Being an inclusive category, it uses all muon types, including CB muons which fulfill the *Medium* ID. In the $|\eta| < 2.5$ region, the composition is 97.5% CB, 1.5% CT and 1% ST muons. Additional requirements analogous to those for electrons have to be fulfilled, which is explained in more detail in chapter 6.4.

This description is based on [91], where further information on the reconstruction of muons can be found. This paper also presents the most recent measurements of the reconstruction efficiency for muons in $Z \to \mu\mu$ events based on 2015 data (see figure 4.4).

4.4. Taus

Tau leptons are unstable, as described in chapter 2, and after a mean length of $87\mu m$ [24] will decay either leptonically or hadronically, creating a secondary vertex. In the first case, the emerging electrons or muons are reconstructed as described before. The corresponding neutrinos leave the detector material without interaction and are thereby contributing to the total missing transverse energy. In the case of a hadronic decay, the emerging particle shower is reconstructed as a jet in the hadronic calorimeter. Tau jets are characterised by a smaller radius compared to those created by protons or other hadrons and a trajectory matching the secondary vertex. However, the misidentification rate of tau jets is high, leading to a lower reconstruction efficiency than those of muons or electrons. Further information on the tau reconstruction and trigger efficiency measurements performed with 2015 data ($3.2\,\mathrm{fb}^{-1}$) can be found in [92].

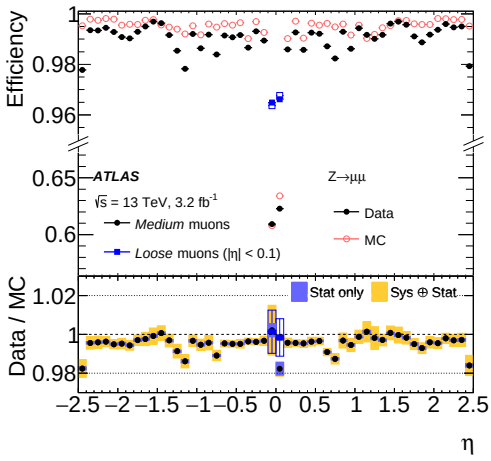

Figure 4.4.: Identification efficiencies for muons with $p_T > 10\,\text{GeV}$, fulfilling the *Medium* (black) or *Loose* (blue) criteria, in $Z \to \mu\mu$ events as a function of the pseudo-rapidity η. The efficiencies were measured based on 2015 data (with $3.2\,\text{fb}^{-1}$ integrated luminosity) and are compared to MC simulation[91].

4.5. Jets

Jets are created when hadrons or single gluons or quarks pass through the calorimeter, where they interact with the detector material and create particle showers through hadronisation until they have deposited their complete energy. These energy deposits in topologically connected calorimeter cells are then used for the reconstruction of jet objects [93]. If they pass certain quality and energy thresholds, these cells are combined to so called *topological clusters*. These are three dimensional objects used by jet reconstruction algorithms, which apply different techniques to form jet objects.
The anti-k$_t$ algorithm [94] for example selects the cluster with highest energy and then adds neighbouring cells with lower energies until the resulting jet is a cone-shaped object with radius R. This algorithm is most commonly used in ATLAS analyses. The resulting object can then be associated to the corresponding tracks reconstructed in the ID.
To further improve the jet quality, reduce the uncertainty of the jet energy resolution (JER) and apply corrections on the jet energy scale (JES), a calibration of the jets in several steps is necessary [95]:
The origin of the jet is required to be the primary vertex, correcting the orientation and improving the η-resolution of the jet. In-time and out-of-time pile-up contributions must be subtracted, for which different methods can be applied to reduce the excess energy, a jet-area-based density subtraction and a residual correction based on MC simulations [95, 96]. Following these steps, an absolute JES calibration is used to correct the four-momenta

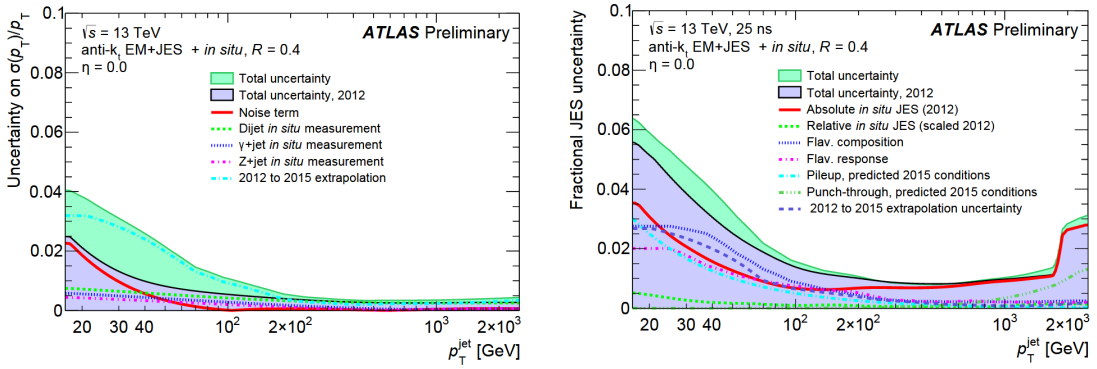

Figure 4.5.: Estimations of the jet energy resolution (left) and jet energy scale (right) uncertainties for the 2015 data as a function of the transverse momentum p_T [97].

of the jets, using truth jets in MC dijet events. Also, a correction of flavour-dependencies[3] is applied and finally a residual in-situ calibration is used for jets in data, based on well-measured reference objects.
Consequently, all these corrections lead to a large set of systematic uncertainties, which can be reduced to a smaller set of nuisance parameters with minimal loss of correlations [97]. These include pile-up corrections, p_T- and η-dependent corrections and corrections from in-situ studies (main contribution). The composition of these nuisance parameters, their origin and absolute values are described in more detail in [98].
The most relevant uncertainties of the JES and JER and their total size were estimated with 2015 data and are shown as a function of the jet transverse momentum in figure 4.5. A more recent analysis of the uncertainties of the JES based on the full 2015 data set can be found in [95]. More details on the experimental uncertainties accounted for in this analysis can be found in section 6.7.1.
To suppress pile-up jets in the jet selection of the analysis, a so called *jet vertex tagger* (JVT)[99] is used. This discriminant, based on a 2-dimensional likelihood, enables the rejection of jets which do not originate from the hard-scatter vertex. It uses two track-based variables as input:
The first is corrJVF, a jet vertex fraction (JVF) variable, that is corrected for pile-up track contributions. The JVF itself is defined as the summed p_T of all tracks matched to a given jet, associated with the PV relative to the total p_T sum of all tracks matched to the jet [100].
The second variable is R_{pT}, which uses information from the ID and calorimeter to calculate the sum of transverse momenta of all tracks which originate from the hard-

[3] Quark or gluon initiated jets will lead to different calorimeter responses.

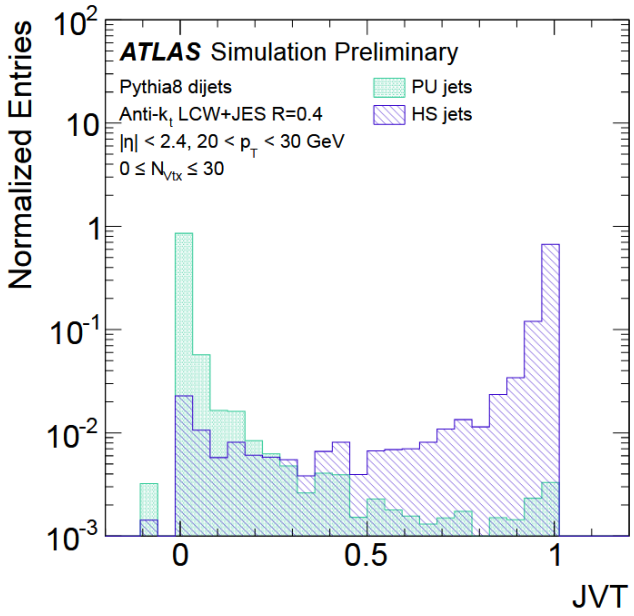

Figure 4.6.: JVT distributions for hard-scatter (HS) and pile-up (PU) jets (with 20 GeV $<$ p_T $<$ 30 GeV). The value of -0.1 was given to jets without associated tracks. [99].

scatter vertex and are associated with the jet. This sum is then divided by the total jet p_T, after calibration and pile-up subtraction. The JVT distributions for hard-scatter and pile-up jets is shown in figure 4.6 which illustrates its discrimination power.

For jets selected in this analysis a medium JVT working point was chosen (JVT$>$ 0.59), following the recommendations of the ATLAS Jet and Etmiss Combined Performance Group [101]. It provides an average efficiency of 92%.

Other quality criteria, ensuring that the selected jets are not misidentified or produced by background noise in the calorimeters, beam-induced background or cosmic ray showers, are combined into two selection criteria called *Loose Bad* and *Tight Bad*. Their detailed definitions are given in [102]. For this analysis, a veto on *Loose Bad* jets was chosen, aiming for a high efficiency rather than a high purity of the jets. If a jet is flagged as *Loose Bad*, that means it fulfils at least one out of a set of six criteria, the event containing it is rejected. For the leading jet of an event, a veto on *Tight Bad* was applied, meaning that leading jets must not be *Loose Bad* and must fulfil additional requirements for the event to be retained.

Finally, in addition to the JVT criterion and the bad jet veto, jets are required to have at least $p_T > 20$ GeV and $|\eta| < 2.8$ to be considered as *baseline jets* and used in the overlap removal. Only if they pass the even tighter thresholds of $p_T > 30$ GeV and $|\eta| < 2.5$, they

are used as *signal jets* for the analysis. In the following chapters, jet refers to *signal jets*. The overlap removal method is used to eliminate objects that are reconstructed multiple times. There are different possibilities of reconstructing the same object twice, most of which are ruled our by the described object definitions. The remaining cases are scanned by the overlap removal procedure, searching for two overlapping objects, meaning they are reconstructed within a given ΔR. There are three combinations that are searched for in this analysis:

Jet-Electron overlap
Jets could be reconstructed from an electromagnetic shower caused by electrons. If they are located within $\Delta R < 0.2$ of a reconstructed electron, the jets are removed. On the other hand, if an electron is reconstructed within $\Delta R < 0.4$ of a jet, is is assigned to the jet and is removed as an electron object.

Jet-Muon overlap
Jets could also be reconstructed from muon tracks, therefore they are removed if they occur within $\Delta R < 0.2$ of a muon and have less than three tracks. If a muon is reconstructed within $\Delta R < 0.4$ of a jet, the same assumption is made as for electrons and the muon is removed.

Electron-Muon overlap
If electrons and muons are reconstructed sharing tracks in the ID ($\Delta R < 0.01$), the electrons are removed. However, if the muons are CT type muons, which do not have additional hits in the MS to verify it, the muon is removed instead.

These requirements are following the recommendations in [103] and must be fulfilled by all reconstructed objects used in the analysis.

4.6. Missing Transverse Energy

As briefly mentioned in section 3.2, the missing transverse energy ($E_{\mathrm{T}}^{\mathrm{miss}}$) is defined as the the vectorial sum of all transverse energies. It is a common and frequently used variable to account for particles such as neutrinos or other only weakly or non-interacting BSM particles, that leave the detector unrecorded. Its calculation and uncertainties are also taken into account in the analysis of this thesis and are described in more detail in [104]. The basis of the $E_{\mathrm{T}}^{\mathrm{miss}}$ determination is the vectorial sum of transverse momenta of all objects reconstructed in the calorimeters and MS, the so called *hard term*, as well as the so called *soft term*. The latter can be built by taking into account all tracks from charged-particles reconstructed in the ID, that are associated with the hard-scatter vertex, but not with any hard object. This option is referred to as the track-based version. For

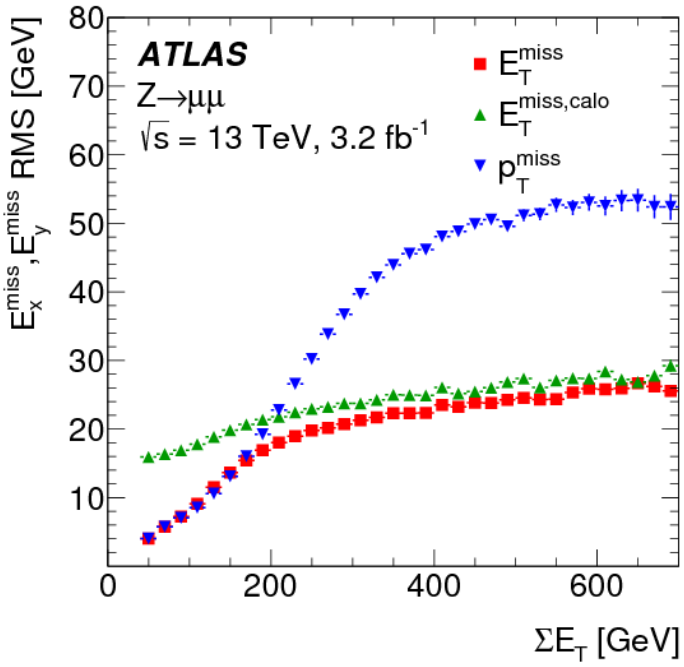

Figure 4.7.: Comparison of the $E_{\mathrm{T}}^{\mathrm{miss}}$ resolution as a function of energy sum ($\sum E_{\mathrm{T}}$) for the track-based option (red), the calorimeter-based option (green) and a track-only option (blue), which is neglected here [104].

the alternative calorimeter-based version, the soft-term is calculated using calorimeter clusters produced by soft neutral particles. The latter is a more inclusive option, but also more dependent on pile-up and therefore has a poorer reconstruction quality than the track-based version. Additionally, the resolution of the resulting $E_{\mathrm{T}}^{\mathrm{miss}}$ is suffering from the missing consideration of muons, which leave tracks but hardly energy depositions in the calorimeter (see figure 4.7). Therefore, the track-based option was chosen for the calculation of $E_{\mathrm{T}}^{\mathrm{miss}}$ in this analysis.

Chapter 5.

Phenomenology

The analysis presented in this work was developed as a generic search for BSM signatures and focuses on events with final states containing jets and missing transverse energy, often depicted as $X \rightarrow$ jet + invisible.
In section 2.2, different BSM models that could lead to a final state like this, were presented, among them leptoquark models ($LQ \rightarrow q + \nu$), Dark Matter processes containing an ISR jet or the MSSM (as presented in section 2.2.3 and following). They are addressed by different, specialised analyses (see [47, 49, 105]). One MSSM process, $\tilde{q} \rightarrow q + \tilde{\chi}_1^0$, was chosen as a benchmark model for the analysis and is referred to as *signal* in the following. The investigated signal final state is presented in more detail in section 5.1.
Due to trigger requirements and improved identifiability, boosted scenarios containing *initial state radiation* (ISR) jets were selected. Their influence on the kinematics of the final state is explained in section 5.2.
However, some SM processes lead to very similar or even undistinguishable final states, so called *reducible* and *irreducible backgrounds*, respectively. As irreducible backgrounds cannot be removed sufficiently by selection criteria, a very precise estimation of their expected fractions and shape has to be conducted (see section 6.6). To extract this information, so called *control regions* (CRs) are used. They are combinations of selection requirements (cuts) optimised to select a specific background as purely as possible while maintaining sufficiently high statistics (see section 6.6). The dominant backgrounds with regard to the analysed final state are outlined in section 5.3.
In order to distinguish the signal signature from these backgrounds, different methods can be used:
A *cut-based approach* is often suitable, meaning the implementation of tight selection criteria to strongly reduce background contamination and thereby enhance the signal-to-background ratio. The obvious disadvantage of losing signal efficiency while increasing the statistical uncertainty can be avoided by keeping a selection with very loose criteria instead. A set of selection cuts was optimised to create a suitable *signal region* (SR) (see chapter 6.5).

In this analysis, a *shape fit method* was used to distinguish between signal and backgrounds, thus, suitable kinematic variables had to be chosen (see section 5.5). Different Monte Carlo generators were used to simulate signal as well as SM background events, which are presented in section 5.4.

5.1. Signal Final State

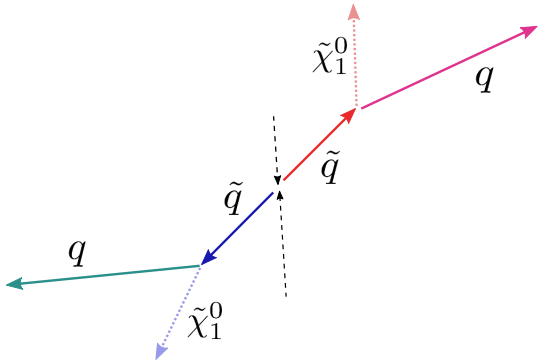

Figure 5.1.: Schematic illustration of two squarks being pair-produced back-to-back and decaying into SM quarks and neutralinos (LSPs).

According to the production and decay channels presented in section 2.2.5, there are multiple ways SUSY particles might be pair-produced in proton-proton collisions, and they have different decay channels leading to SM particles and LSPs.
The signal process of interest is shown in figure 5.1. Given the assumption that no initial state radiation occurs, both SUSY particles, in this case light flavoured[1] squarks, are produced back-to-back in the transverse plane due to energy and momentum conservation. A decay channel was chosen where both squarks $\tilde{q}$ decay into an SM quark q accompanied by the lightest SUSY particle, $\tilde{\chi}_1^0$. This leads to the desired final state with two jets, since both quarks would form hadrons that produce jets in the calorimeter. Meanwhile, the two LSPs would leave the detector unrecorded, thus causing missing transverse energy, as defined in chapter 4.6. Due to momentum conservation, both squarks $\tilde{q}$ transmit their energy and momenta to their respective decay products, leading to the following relations: A low mass difference between the two SUSY particles, $\Delta m = m_{\tilde{q}} - m_{\tilde{\chi}_1^0}$ of 0 GeV to 100 GeV, leads to low momentum jets and low $E_{\mathrm{T}}^{\mathrm{miss}}$. A medium mass difference of 100 GeV to 450 GeV leads to medium energy jets and a medium amount of $E_{\mathrm{T}}^{\mathrm{miss}}$, while

[1] This means that only $\tilde{u}, \tilde{d}, \tilde{s}, \tilde{c}$ flavours are considered.

a high mass difference of more than 450 GeV leads to high energy jets and high $E_{\mathrm{T}}^{\mathrm{miss}}$[2]. Since there are no incisive objects like electrons or muons in the final state, the difficulty to identify this process increases with lower jet energies and lower amounts of missing transverse energy.

5.2. Initial State Radiation

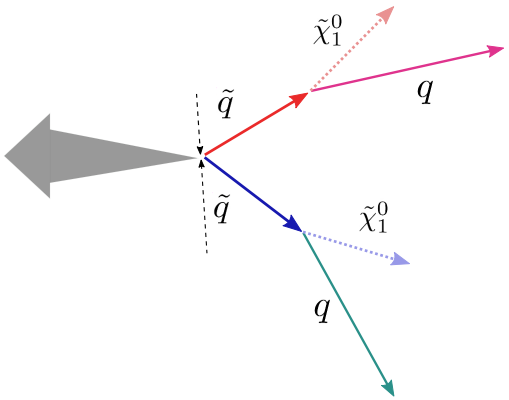

Figure 5.2.: Different kinematics of two pair-produced squarks through ISR jet boost.

A boosted scenario, characterised in this case by an energetic ISR jet, is needed to increase recognisability of the signal process of interest and to fulfil the trigger requirements. It occurs when a high energy gluon is radiated from the initial state gluons or quarks (see section 2.2.5). Due to momentum conservation, the total transverse momentum of the other particles will be increased (boosted) by the amount of the transverse ISR momentum, but in opposite direction. As a consequence, the squarks are no longer back-to-back and the angle between their decay products is reduced, resulting in increased missing transverse energy. This can be observed as a shift to higher values in the missing transverse energy distribution of the signal process. It was also observed, that in some kinematic variables this boost can increase the shape differences between signal and background distributions (see section 5.5). Additionally, the effects of the boost on the signals are different, depending on the mass difference between squark and neutralino. This is demonstrated for six different signals in the $E_{\mathrm{T}}^{\mathrm{miss}}$ distribution in figure 5.3.
It can be observed that signals with higher Δm feature a high amount of $E_{\mathrm{T}}^{\mathrm{miss}}$ and can therefore pass the $E_{\mathrm{T}}^{\mathrm{miss}}$-trigger criterion, regardless of the ISR jet momentum. In

[2] This division of the phase space is necessary to account for the different kinematic behaviour of the signals depending on Δm. The limits were estimated based on the results of previous optimised analyses.

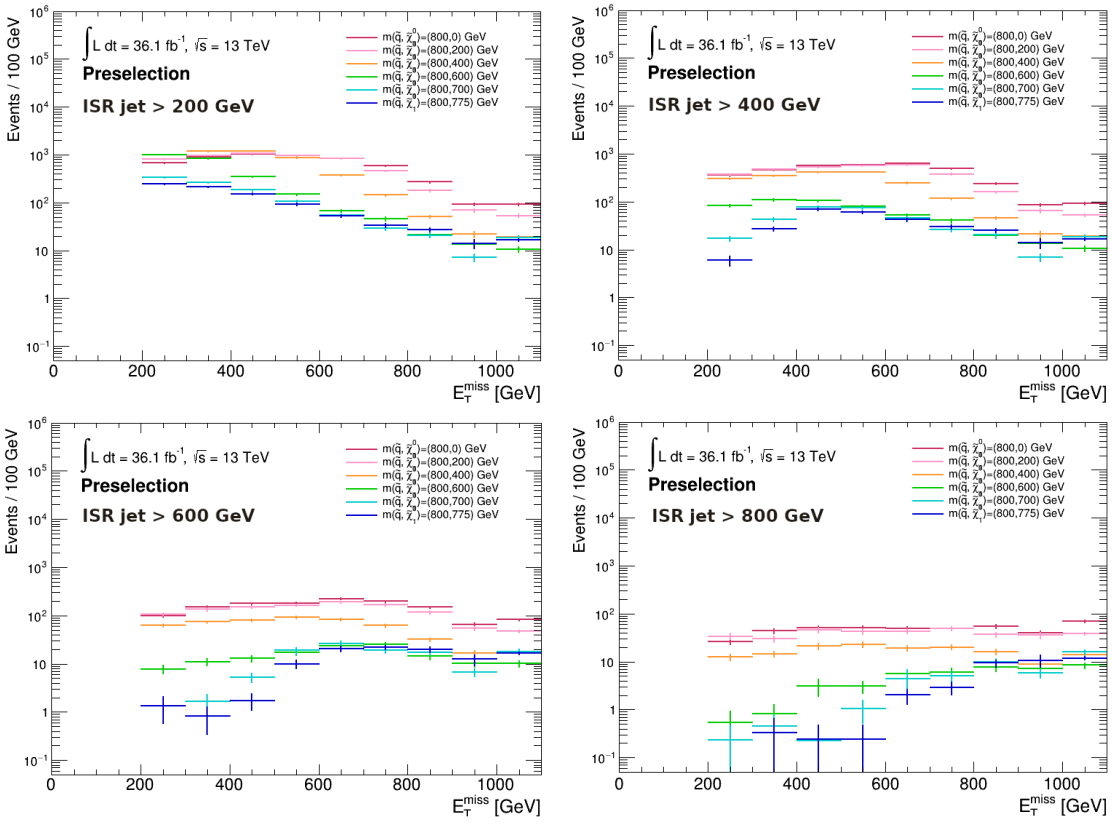

Figure 5.3.: Effect of ISR jets with different transverse momenta on six signals with different mass difference between squark and neutralino

contrast, the signal distributions with smaller Δm are shifted towards higher $E_{\mathrm{T}}^{\mathrm{miss}}$: the higher the ISR momentum, the stronger the effect (despite an expected loss of events).

5.3. Standard Model Backgrounds

Final states which are very similar to the signal can be created through different SM processes, characterised by the same signature with jets and missing transverse energy in the final state. Additionally, some background processes feature a high cross section and are hard to suppress. The event selection presented in section 6.4 was designed to reduce the occurring SM backgrounds as effectively as possible. It is referred to as *preselection* in the following and includes for example a lower bound on missing transverse energy in the events, which reduces effectively almost every SM background. In the following, the most relevant backgrounds for the investigated final state are briefly outlined.

Z boson events

Depending on their decay channel, Z bosons can produce a signature similar to the signal. The most dominant background arises from the $Z \to \nu\bar{\nu}$ decay channel in combination with ISR jets. Corresponding to the ISR jet momenta, a high amount of missing transverse energy emerges due to the undetected neutrinos. If a quark pair is produced through the ISR, the final state is similar to the signal as shown in figure 5.4. These processes are denoted as $Z \to \nu\nu$ in the following.
Another possibility is a hadronically decaying Z, but since the amount of $E_{\mathrm{T}}^{\mathrm{miss}}$ in these events is small, they can easily be sorted out by an $E_{\mathrm{T}}^{\mathrm{miss}}$ cut. Finally, events with leptonically decaying Z bosons and additional jets from gluon radiation where one or both leptons are measured incorrectly. Additionally to the $E_{\mathrm{T}}^{\mathrm{miss}}$ cut, they can be suppressed effectively by a veto on leptons. Due to their minor contribution, they are combined with other minor background processes into a background denoted with *Other*.

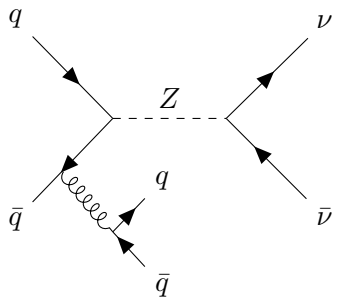

Figure 5.4.: A Z boson, produced by quark-antiquark annihilation, decaying into neutrinos. An additional quark-antiquark pair from ISR leads to the same signature as the signal process.

W boson events

Another important background results from W bosons decaying into a charged lepton and its corresponding neutrino (see figure 5.5). The behaviour of this process regarding an ISR jet is analogue to that of $Z \to \nu\nu$. In events with tau-leptons ($W \to \tau\nu_\tau$) in particular, the final state includes even more jets (arising from the hadronically decaying tau, $\tau \to W\bar{\nu}_\tau \to q\bar{q}'\bar{\nu}_\tau$) and missing transverse energy (due to tau neutrinos) and thus imitates the signal. This process is denoted as $W \to \tau\nu$ in the following.
Background processes like $W \to e\nu_e$ and $W \to \mu\nu_\mu$ (denoted as $W \to e\nu$ and $W \to \mu\nu$) are easier to identify due to the electron and muon, respectively.

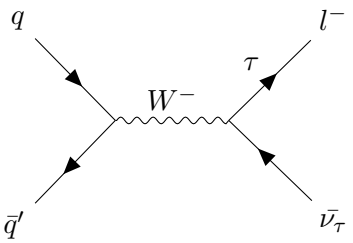

Figure 5.5.: Feynman diagram of a W boson decaying into a charged lepton and a neutrino.

Top quark events
Finally, another main background is produced by top- anti-top pairs as presented in figure 5.6. The signature features at least two b-jets and further jets or leptons and missing transverse energy depending on the weak decay of the W bosons, just as described before. From semi- and di-leptonic decays, especially with hadronically decaying τ leptons, a final state similar to the signal is produced. This background, indicated by $t\bar{t}$ in the following, becomes more dominant if events with a high jet multiplicity are selected.

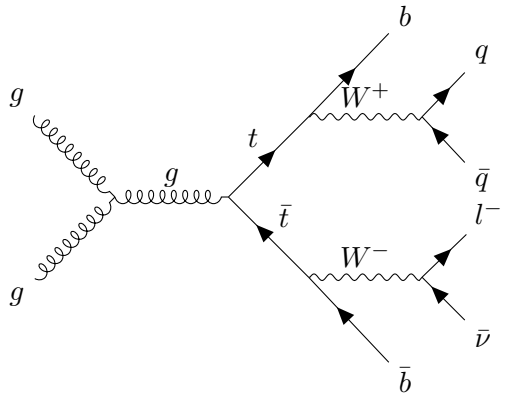

Figure 5.6.: An exemplary semi-leptonic $t\bar{t}$ decay leading to a final state with four quark jets and missing transverse energy due to the neutrino.

Minor backgrounds
The background with the highest cross section arises from simple quark and gluon scatterings, called *multijet* events. It can reach high jet multiplicities from hadronising parton showers. Through mismeasurement of the jet energies an artificial missing transverse energy can occur. Nevertheless, this background can easily be reduced by demanding a minimal spatial distance between jets and $E_{\mathrm{T}}^{\mathrm{miss}}$ ($\Delta\phi > 0.4\,\mathrm{rad}$), since misidentified ob-

jects are usually found within small distances from $E_{\mathrm{T}}^{\mathrm{miss}}$. This background has therefore only small influence on the total number of events.
Furthermore, W bosons can produce a single top quark when decaying hadronically, leading to single top events. W and Z bosons can also be produced in pairs, called a diboson event. However, these processes have a very low cross section, which means that the contribution to the total background expectation is small. To improve clarity, these processes are combined into one, denoted as *Other*.

5.4. Monte Carlo Simulation

In order to interpret the data measured by the ATLAS detector, simulations of both background and signal processes are needed. They are generated using multiple Monte Carlo (MC) generators with different benefits and drawbacks, depending on the type of process, but the underlying principle is always the same.
First, the MC generators calculate the matrix element of the respective process[3] either at leading order (LO) or at next-to-leading order (NLO) (including additional loop corrections). Increasing the simulation accuracy through additional perturbation corrections would exponentially increase the required computing capacity. The hadronisation of quarks and gluons in the final state as well as the underlying event is then simulated in the parton shower.
This is followed by the detector simulation[106][4], in which the output of the generators is taken and the interaction of all produced particles with the ATLAS detector is simulated. A toolkit called GEANT4[107, 108] is used to accesse databases containing information on all detector components such as their geometry and response. The results have the same format as the recorded data, so that they can be processed equally by the reconstruction (see chapter 4).
All simulated processes used in this analysis belong to the SUSY12 derivation which is based on the official Monte Carlo simulation MC15. It uses a chosen subset of available variables and information about the events which is most relevant for this SUSY analysis to reduce computing time. The MC simulations of all considered background processes are specified in the following. They are summarised in table 5.1 and shown in more detail in appendix A.

[3] This includes the four-momenta of incoming and outgoing particles of the collision and is used to calculate the cross section of the process. It also takes into account the substructure of the proton by a given PDF (see section 3.1). Nevertheless, the cross section used to normalise each MC sample in the analysis (see list of MC samples in appendix A) is calculated separately to higher orders.
[4] Samples without full detector simulation are called *truth-samples*. The truth-level data is still available in fully simulated samples.

Process	MC generator	Slicing and Filter
$Z\nu\nu$ or Z+jets	Sherpa 2.2.1	max($H_T, p_T(Z)$): 0-70, 70-140, 140-280, 280-500, 500-1000 MeV, filter: ISR flavour (light, charm, bottom)
$W\tau\nu$ or W+jets	Sherpa 2.2.1	max($H_T, p_T(W)$): 0-70, 70-140, 140-280, 280-500, 500-1000 MeV, filter: ISR flavour (light, charm, bottom)
Diboson	Sherpa 2.2.1	decay channel
$t\bar{t}$, singletop	Powheg + Pythia 6	decay channel, amount of $E_{\mathrm{T}}^{\mathrm{miss}}$
$t\bar{t}$W, $t\bar{t}$Z, $t\bar{t}$WW	MadGraph + Pythia 8	decay channel
3 top, 4 top	MadGraph + Pythia 8	-

Table 5.1.: Overview of MC simulations used in this analysis with their respective generators and slicing.

Background samples

The main backgrounds ($Z \rightarrow \nu\nu$, Z+jets, $W\tau\nu$, W+jets)[5] were produced using SHERPA[109], version 2.2.1, which calculates the matrix elements at LO or NLO, depending on the process and especially, the jet multiplicity. For the production of the Z and W samples, Sherpa calculates Feynman diagrams with up to 3 additional jets at NLO, all others at LO, and then combines them. For these processes, the PDF set NNPDF3.0NNLO is used.
These samples were produced in slices (depending on the maximum of transverse momentum of the boson and the total transverse energy (H_T)) and with application of filters to reduce computation power while maintaining a high statistic in chosen regions of the phase space, especially in regions with high $E_{\mathrm{T}}^{\mathrm{miss}}$ or jet energies. For the simulation of $t\bar{t}$ as well as single top events, the Powheg[110] generator was used to calculate the matrix element at NLO. It is applied in combination with Pythia 6 [111] for the generation of the parton shower and hadronisation. For both processes, the CT10 PDF set is used with the PERUGIA tune P2012.
The minor background arising from diboson events was generated using SHERPA version 2.2.1 with the same configuration as for the Z and W processes. Other top processes were produced with MadGraph[112], a multileg generator, using QCD corrections at NLO, to calculate and combine different matrix elements and Pythia 8[113] for the showering.

Signal samples

The MC simulations of signal processes were produced using MadGraph for the matrix element and Pythia 8 for the showering. They consider only pair produced squarks with light flavours: $\tilde{u}$, $\tilde{d}$, $\tilde{c}$, $\tilde{s}$. Various points of the parameter space of the free mass

[5] V+jets summarises all other decay processes of the boson V.

parameters $m_{\tilde{q}}$ and $m_{\tilde{\chi}_1^0}$ were chosen with regard to a broad coverage for multiple analyses. The produced mass points cover a range of 200 - 2200 GeV for the squark mass and 0 - 1100 GeV for the neutralino mass. A part of the mass plane with produced mass points is shown in figure 5.7. The grey line represents the border of kinematically allowed mass combinations ($m_{\tilde{q}} = m_{\tilde{\chi}_1^0}$). Mass points above this diagonal are kinematically forbidden[6].

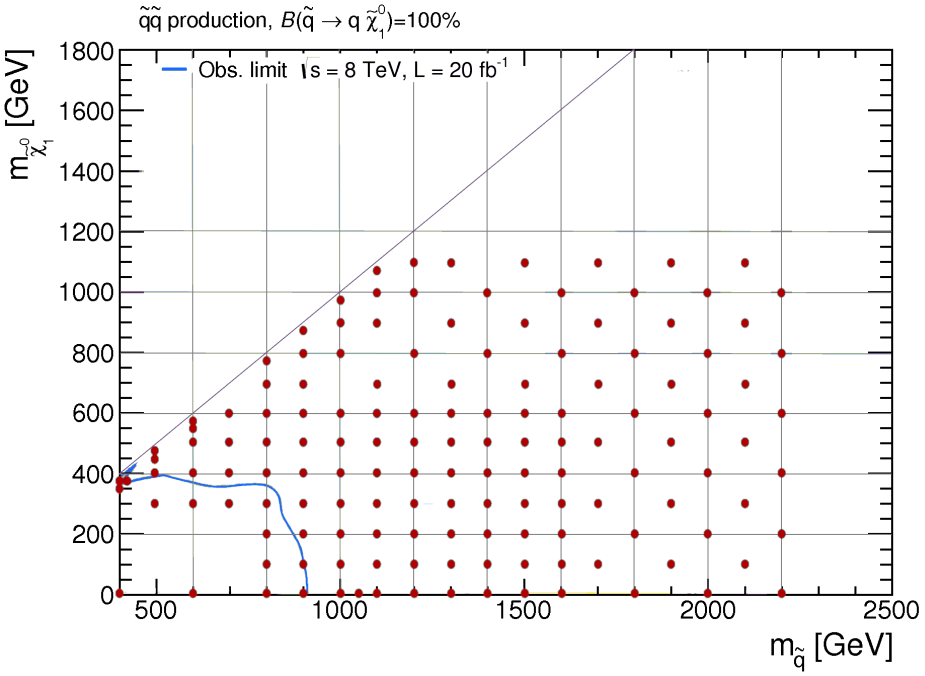

Figure 5.7.: A section of the $m_{\tilde{q}}$ and $m_{\tilde{\chi}_1^0}$ mass plane: The red dots indicate the simulated mass points (signals) and the exclusion limit (blue line) shows the range excluded by the 8 TeV 0-lepton ATLAS analysis as presented in [57].

5.5. Kinematic Variables

Since the background processes mentioned before can produce similar final states and thus look like the signal process of interest, it is crucial to choose suitable kinematic variables for the analysis. The approach used in this case is a shape fit analysis, which relies on shape differences between signal and background, as explained in detail in section 6.1. Different variables such as $E_{\mathrm{T}}^{\mathrm{miss}}$ and M_{eff} (as defined in section 3.2) have been analysed

[6] This is because the used MSSM model assumes that the neutralino is the lightest stable SUSY particle.

with regard to their discrimination power between signal and background. These previous studies focussing on the shape differences between the distributions, are shown in [114]. Another variable which was considered here, is M_{T2} as presented in [115]. It is particularly useful for final states where heavy particles are pair-produced (in this case squarks) and decay into one visible and one invisible particle (in this case the neutralino), which leads to missing transverse energy.
From four-momentum conservation $p_{\tilde{q}}^2 = (p_q + p_{\tilde{\chi}_1^0})^2$ and the energy-momentum relation $m^2 = E^2 - |\vec{p}|^2$ for a two-body decay of one particle in the transverse plane[7] it can be followed that:

$$M^2 \geq M_{\mathrm{T}}^2 = m_{T,q}^2 + m_{T,\tilde{\chi}_1^0}^2 + 2(E_{T,q} \times E_{T,\tilde{\chi}_1^0} - |\vec{p}_{T,q}| \times |\vec{p}_{T,\tilde{\chi}_1^0}|) \tag{5.1}$$

with M being the mass of the mother particle, $m_{T,q}$ and $m_{T,\tilde{\chi}_1^0}^2$ denoting the masses of the quark and neutralino, respectively and $\vec{p}_{T,q}$ and $\vec{p}_{T,\tilde{\chi}_1^0}$ being their momenta. This transverse mass gives a lower bound on the rest mass of a single decaying mother particle. Both pair-produced mother particles (indicated with 1,2) have equal mass, therefore the higher of both lower bounds is taken as the lower bound of both mother particle masses: $M_0^2 \geqslant \max(M_{\mathrm{T},1}^2, M_{\mathrm{T},2}^2)$.
Since only the total sum of missing traverse energy can be measured and the neutralino mass is unknown, the minimal value fulfilling the requirement $\vec{p}_{T,\tilde{\chi}_1^0}^{(1)} + \vec{p}_{T,\tilde{\chi}_1^0}^{(2)} = \vec{p}_{T,\mathrm{miss}}$ is chosen. This is done by scanning all possible values of $\vec{p}_{T,\tilde{\chi}_1^0}^{(i)}$ and calculating the vector sum. The minimal value leading to the given amount of $\vec{p}_{T,\mathrm{miss}}$ is kept.

The definition of M_{T2} as a function of the neutralino mass $m_{\tilde{\chi}_1^0}$ is then given as:

$$M_{\mathrm{T2}}^2(m_{\tilde{\chi}_1^0}) = \min_{\vec{p}_{T,\tilde{\chi}_1^0}^{(1)} + \vec{p}_{T,\tilde{\chi}_1^0}^{(2)} = \vec{p}_{T,\mathrm{miss}}} [\max(M_{\mathrm{T},1}^2, M_{\mathrm{T},2}^2)] \tag{5.2}$$

The variable is calculated using the two leading jets and assuming a neutralino mass of zero. This generic calculation is not ideal, since signal points with different neutralino masses are investigated, but it is a feasible simplification. The behaviour of different signals with small, medium and large Δm in this variable is shown in figure 5.8.
The comparison shows that the shape and peak of the distributions strongly depend on the mass difference between $\tilde{q}$ and $\tilde{\chi}_1^0$. Higher Δm signals are positioned more on the right side, smaller Δm are shifted more to the left.

Figure 5.9 shows a comparison of the backgrounds and two exemplary signals in the $E_{\mathrm{T}}^{\mathrm{miss}}$, M_{T2}, and M_{eff} distributions after application of the preselection. The two signals with mass differences Δm of 200 GeV and 400 GeV were chosen as benchmark points outside

[7] The momentum component in the direction of the beam (z-axis) is unknown and neglected.

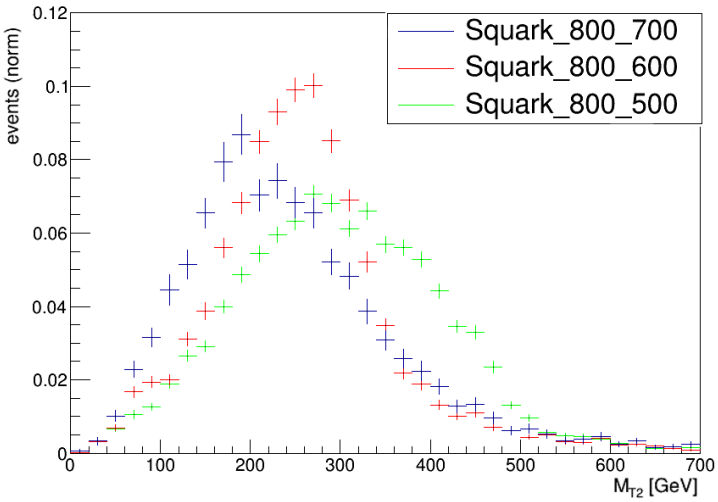

Figure 5.8.: Different signals (normalised) with small, medium and large Δm are compared in the M_{T2} variable (after application of the preselection).

the excluded area of the mass plane (see figure 6.1).

The shape differences between signal and background distributions vary from one signal to another. As expected, signals with smaller Δm (and therefore smaller amounts of $E_{\mathrm{T}}^{\mathrm{miss}}$) have fewer events since they are harder to reconstruct. The reason for this are the softer jets of these signals, which are harder to identify. As observed before, their distributions are shifted more to the left (lower values) and their shapes are more similar to the background shape than signal distributions with higher Δm. Thus, they rely more on an ISR boost for increased sensitivity.
Splitting up the distributions into bins with different jet multiplicities could take into account the various phenomenologies of signals in different Δm regions. In consequence, the sensitivity of the shape fit would be increased compared to fitting an inclusive region and treating all signals equally. This method is therefore used in the analysis as described in section 6.2.
Furthermore, it can be observed, that shape differences in the M_{eff} distribution slowly increase towards higher values. Thus, can be concluded that the M_{eff} variable can be used in tail analyses with hard cuts which disregard shape information as performed in [105]. In contrast, both $E_{\mathrm{T}}^{\mathrm{miss}}$ and M_{T2} are suitable variables for a shape fit method since they show clear shape differences in form of a bump, especially at medium range. For signals with higher Δm one can expect a better performance from the shape fit of the M_{T2} distribution[8]. Searches for signals with smaller Δm should focus on fewer, softer

[8]With regard to the application to Dark Matter processes, the M_{T2} variable will not be suitable due to

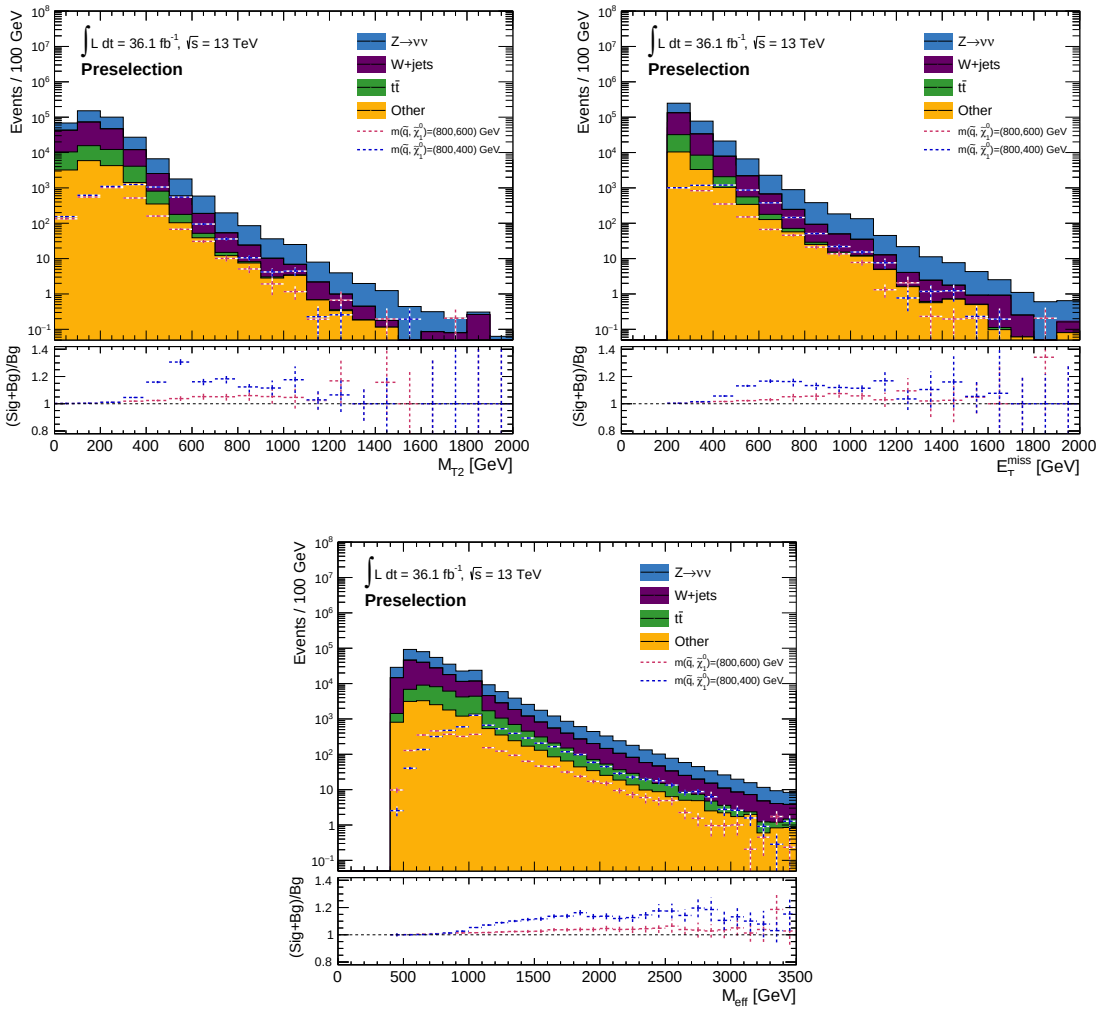

Figure 5.9.: A comparison of the considered kinematic variables M_{T2}, $E_{\mathrm{T}}^{\mathrm{miss}}$ and M_{eff} with regard to their discrimination power due to shape differences between signal and background distributions. All distributions are shown after the preselection. The backgrounds are drawn stacked.

jets, while signals with higher Δm are better analysed by selecting multiple jets with higher momenta.
Since the shape differences are rather small (of the order of 1% to 10%), especially for signals with small Δm it is essential to ensure small enough uncertainties.

low mass differences. Thus, it is reasonable to use both variables for the shape fit.

Chapter 6.

Analysis

In this chapter, the features of the analysis are presented. In section 6.1, the concept and strategy of the analysis are motivated. In order to clearly work out the different concept of a shape fit analysis and to evaluate its results, a comparison is made to another analysis also focussing on events without leptons to search for the same signal process, the ATLAS 0-lepton analysis (see section 6.2).
In sections 6.3 and 6.4, the data sets, trigger and event selection used are described in more detail. The signal region selections are then presented in section 6.5. Section 6.6 focusses on the backgrounds and their treatment to estimate the background expectations. Moreover, a replacement method to improve the simulated expectations of the two main backgrounds is introduced. Finally, section 6.7 discusses the systematic uncertainties considered in the analysis.

6.1. Motivation

The final state $\tilde{q} \rightarrow q + \tilde{\chi}_1^0$ (or in general jets + invisible) used as a benchmark signal in this thesis is of high interest among SUSY searches and is investigated by various groups with different methods. As discussed in section 5.5, it is useful to divide the mass plane of $m_{\tilde{q}}$ and $m_{\tilde{\chi}_1^0}$ into regions with small, medium and large Δm and to consider them separately (see figure 6.1).

For a comparison, the expected exclusion limits of different ATLAS analyses, the monojet analysis and the 0-lepton analysis are shown [57]. The final observed limit gained by their combination is shown with a solid red line. The area within these limits, i.e. all considered signal points in this range, were excluded by the analyses at a 95% confidence level.
The two expected limits show clear differences. The monojet approach is optimised to gain high sensitivity for signals with small Δm, requiring at least one jet and making

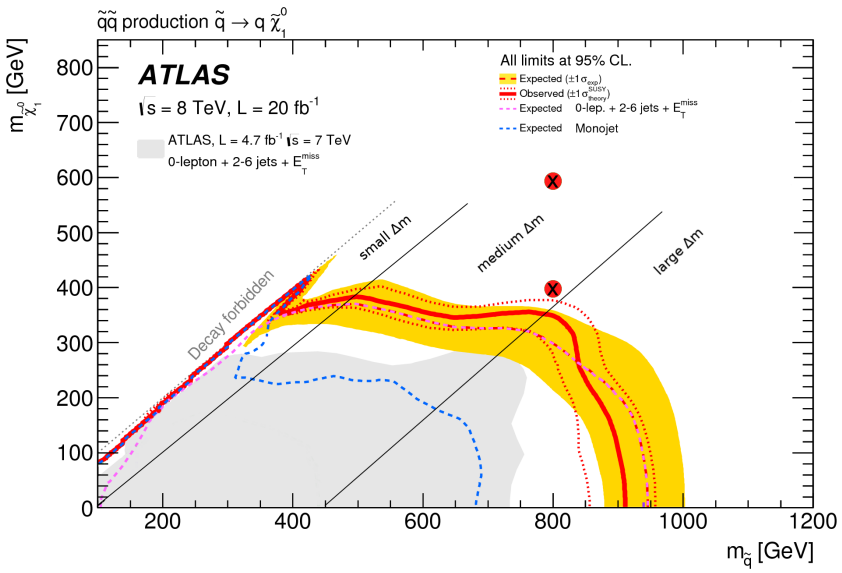

Figure 6.1.: Exclusion limits in the mass plane of the squark mass $m_{\tilde{q}}$ and neutralino mass $m_{\tilde{\chi}_1^0}$. Different analysis methods show different performances depending on the Δm region. The grey dashed line separates the kinematically forbidden area from the allowed mass range. The expected exclusion limit of the 8 TeV 0-lepton analysis (pink dashed line) is compared with the one of the monojet analysis (blue dashed line). The combination of both results in the expected limit (red dashed line) and observed limit (red solid line). Both analyses use the full 2012 data set (using [57]).

use of an ISR boost. The other approach used in the 0-lepton analysis leads to a high sensitivity in the region of large Δm, by applying very tight selection criteria and gaining the sensitivity from signal to background comparisons in the tail regions of kinematic distributions, in particular M_{eff} (see section 5.5).
It can be expected that extensions of the sensitivity will be obtained more easily in those areas the analyses are optimised for, respectively. Meanwhile, neither of the two approaches is optimised for the region of medium Δm. It is in general not very well covered by the conventional analysis methods, since the signal-to-background discrimination is difficult for cut-based analyses.

To deliver a suitable completion, the analysis of this thesis is optimised for high sensitivity in the medium Δm region. Its aim is to either detect a possible signal within this Δm range or to increase the exclusion-sensitivity and thereby extend the excluded area of the mass plane.
The concept of this analysis is based on a shape fit method and keeps the event selection

as soft[1] and generic as possible to be applicable to other signal models as well. This approach is explained in more detail by comparing it to the one used in the 0-lepton analysis in the following section.

6.2. Comparison with 0-lepton Analysis

Based on the 8 TeV results, the two approaches described above were extended to the data set recorded in 2015 and 2016 at 13 TeV centre of mass energy [47, 105]. The monojet and the 0-lepton analyses both select events containing missing transverse energy and jets, but no leptons, which makes their results comparable with those of the analysis presented in this thesis. In this case, the 0-lepton approach and its results (as presented in [105]) are used as a comparison and reference.
The approach, also referred to as M_{eff}-based search, uses the effective mass variable as a discriminant between signal and backgrounds. Different inclusive SRs are applied which are optimised for a signal yield (or signal-to-background ratio) as high as possible. In these SRs events are selected with two or more to six or more jets featuring a transverse momentum of $p_T > 50\,\text{GeV}$, respectively. Also different lower bounds of 1000 GeV up to 3600 GeV are set on the effective mass variable.
To estimate the background expectation in these SRs, orthogonal selections are used for each of the primary backgrounds (which are the same as those outlined in section 5.3). These CRs are optimised to maintain statistical precision while minimising the systematic uncertainties on the background expectation arising from the extrapolation from control to signal regions. A detailed description of the CR and SR selection criteria can be found in chapters 7 and 8 of [105].
Three types of likelihood fits (explained more detailed in section 7.2) are then applied to these regions (each region is treated as one bin):

- a *background-only* fit to estimate the background yields in the SRs and to determine the scale factors of the background components,
- a *model-independent* fit to quantify the level of agreement between predicted and observed yields (see figure 6.2) and to set upper limits on the number of signal events in the SRs,
- and a *model-dependent* fit, additionally taking into account the signal contamination in the CRs.

[1] In this context, *soft* refers to low thresholds on p_T and mass variables of various objects in the selected events.

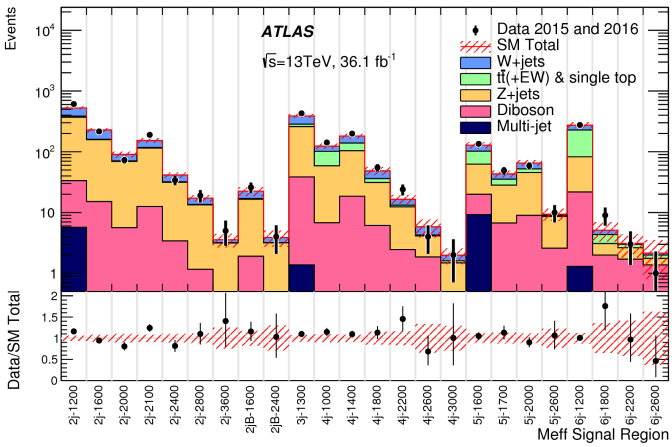

Figure 6.2.: Summary of all SRs used in the 0-lepton analysis. The ratio below shows a comparison of observed and expected event yields per signal region. The background predictions are extracted from background-only fits. [105]

The fit results of those regions with the best expected sensitivity at each point are then used to create the expected and observed exclusion limits.
The approach used in the analysis presented in this thesis is quite different to the M_{eff}-based search. Instead of selecting many signal regions with tight criteria to gain a high sensitivity, this analysis focuses on the differences in shape between the signal and background distributions. It uses the best suitable kinematic variables, $E_{\text{T}}^{\text{miss}}$ and M_{T2}, in a few dedicated regions to exploit a high amount of shape information.
All of the selection criteria are optimised to obtain bump-like shape differences as high as possible at the centre of the distributions to avoid a tail analysis[2].
They are then used to perform a shape fit based on the maximum likelihood method (see chapter 7). This way, systematic uncertainties can be controlled more easily.
Further, an enhancement of sensitivity is achieved by dividing the distributions into three bins according to their jet multiplicity. In this case the three bins are selecting events which contain exactly two jets, exactly three jets and four or more jets, respectively. In addition to the reasons given in section 5.5, using these three jet bins simultaneously leads to an increased amount of shape information at hand which is beneficial for the shape fit. This was already exploited in a very similar approach in previous studies presented in [114].
The results of the 0-lepton multi-bin-fit are compared to the ones of the shape fit from this analysis in chapter 7.

[2]This means that contributions from the high-end of the distribution are dominant.

year	$\int Ldt$	period	run numbers	MET trigger
2015	$3.9\,\text{fb}^{-1}$	D	263962-276954	HLT_xe70_mht (D3-D6)
		E	278727-279928	HLT_xe70_mht
		F	279932-280422	HLT_xe70_mht
		G	280423-281075	HLT_xe70_mht
		H	281130-281411	HLT_xe70_mht
		I	281662-282482	HLT_xe70_mht
		J	282625-284484	HLT_xe70_mht
2016	$35.6\,\text{fb}^{-1}$	A	296939-300287	HLT_xe90_mht_L1XE50
		B	300345-300908	HLT_xe90_mht_L1XE50
		C	301912-302393	HLT_xe90_mht_L1XE50
		D	302737-303560	HLT_xe90_mht_L1XE50 (D1-D3), HLT_xe100_mht_L1XE50 (D4-F1)
		E	303638-303892	HLT_xe100_mht_L1XE50
		F	303943-304494	HLT_xe100_mht_L1XE50 (F1), HLT_xe110_mht_L1XE50 (F2-L)
		G	305291-306714	HLT_xe110_mht_L1XE50
		H	305359,309314,309346,310216	HLT_xe110_mht_L1XE50
		I	307124-308084	HLT_xe110_mht_L1XE50
		J	308979-309166	HLT_xe110_mht_L1XE50
		K	309311-309759	HLT_xe110_mht_L1XE50
		L	310015-311481	HLT_xe110_mht_L1XE50

Table 6.1.: The data sets of the years 2015 and 2016 with their corresponding data taking periods, run numbers and integrated luminosities. The right column shows the $E_{\text{T}}^{\text{miss}}$ triggers used during each period.

6.3. Data Set and Trigger

The data sets used in the analysis presented in this thesis were recorded by the ATLAS detector during the data taking periods of 2015 (periods D to J)[3] and 2016 (periods A to L). Every data taking period is divided into runs with specific settings, each contributing to the total integrated recorded luminosity of $3.9\,\text{fb}^{-1}$ for 2015 and $35.6\,\text{fb}^{-1}$ in 2016, respectively (figure 3.2 in section 3.1). All data sets used, their corresponding run numbers and the integrated luminosities are listed in table 6.1.
These raw data events are then analysed by the ATLAS data quality team which provides good run lists (GRL)[4]. These contain information on which data sets fulfil the quality requirements and should be used and which must be excluded. All runs with unstable beam conditions or problems in any sub-detectors (such as unresponsive cells or magnets still in commissioning mode) are thereby excluded. Thus, the final integrated luminosity for 2015 and 2016 usable in analyses is reduced from $39.5\,\text{fb}^{-1}$ (recorded) to $36.1\,\text{fb}^{-1}$ (good for physics). The uncertainty of this luminosity measurement is 2.1% and is considered as a systematic uncertainty in the fit (section 6.7).

[3] At the beginning of 2015, the bunch spacing was 50 ns, which was changed to 25 ns in period D.
[4] The GRLs used in this analysis are:
data15_13TeV.periodAllYear_DetStatus-v73-pro19-08_DQDefects-00-01-02_PHYS_StandardGRL_All_Good_25ns.xml,
data16_13TeV.periodAllYear_DetStatus-v88-pro20-21_DQDefects-00-02-04_PHYS_StandardGRL_All_Good_25ns.xml

Additionally, the events selected for this analysis must fulfil the trigger requirements of different missing transverse energy triggers. On the one hand, this choice was made due to the high amount of $E_{\mathrm{T}}^{\mathrm{miss}}$ which is typical for the BSM signals of interest. On the other hand, other available triggers like lepton triggers or jet triggers are unsuitable since there are no leptons in the analysed final state and the thresholds of jet triggers are above 260 GeV[5].
Depending on the corresponding data taking periods, $E_{\mathrm{T}}^{\mathrm{miss}}$ triggers with different thresholds were used (see table 6.1). For the 2015 data, the lowest unprescaled trigger[6] `HLT_xe70_mht` using high level jet-based $E_{\mathrm{T}}^{\mathrm{miss}}$ algorithms was applied, selecting only events containing $E_{\mathrm{T}}^{\mathrm{miss}} > 70\,\mathrm{GeV}$. Its efficiency turn-on curve is shown in figure 6.3.
For the 2016 data, three different $E_{\mathrm{T}}^{\mathrm{miss}}$ triggers were applied, `HLT_xe90_mht_L1XE50`, `HLT_xe100_mht_L1XE50` and `HLT_xe110_mht_L1XE50`. They calculate the amount of $E_{\mathrm{T}}^{\mathrm{miss}}$ using level 1 objects, which are based on information from the calorimeter cells and pass a threshold of 50 GeV (`L1_XE50`). The triggers set a nominal threshold of 90 GeV or 100 GeV, respectively. Their efficiencies are shown in figure 6.3.
The efficiency curves show that the usage of these $E_{\mathrm{T}}^{\mathrm{miss}}$ triggers at a trigger efficiency of more than 95% demands a threshold of $E_{\mathrm{T}}^{\mathrm{miss}} > 160\,\mathrm{GeV}$ for 2015 data and above 170 GeV for 2016 data in the selected events. To fulfil the trigger requirements and to operate on the trigger efficiency plateaus, the amount of $E_{\mathrm{T}}^{\mathrm{miss}}$ in events selected for this analysis is chosen to be above 200 GeV. To ensure an increased amount of $E_{\mathrm{T}}^{\mathrm{miss}}$ while keeping energetic jets and thus improve sensitivity, boosted scenarios are selected, demanding an energetic ISR jet as discussed in section 5.2.

6.4. Event Selection

Beside the restriction of the GRLs and the necessary threshold on $E_{\mathrm{T}}^{\mathrm{miss}}$ by the trigger, the selected events have to fulfil other criteria as well (collectively referred to as preselection) to reduce the number of events from background processes while maintaining a signal efficiency as high as possible. This is especially relevant for signals with smaller Δm and lower amounts of $E_{\mathrm{T}}^{\mathrm{miss}}$, as explained in section 5.5.
These include event cleaning cuts to guarantee good data quality as well as analysis based selection criteria adjusted to the needs of the shape fit. They are summarised in the following and listed in table 6.2. Their respective effect on the distributions are visualised in figures 6.4 and 6.5.

Event cleaning
A so called *event cleaning* rejects all events recorded shortly before or after a noise burst in the liquid argon calorimeter and those containing incomplete event information. If the

[5] For the CRs, suitable lepton triggers could be used instead, but were not available at the time.
[6] Unprescaled triggers do not have any additional requirements that reduce the trigger output rates.

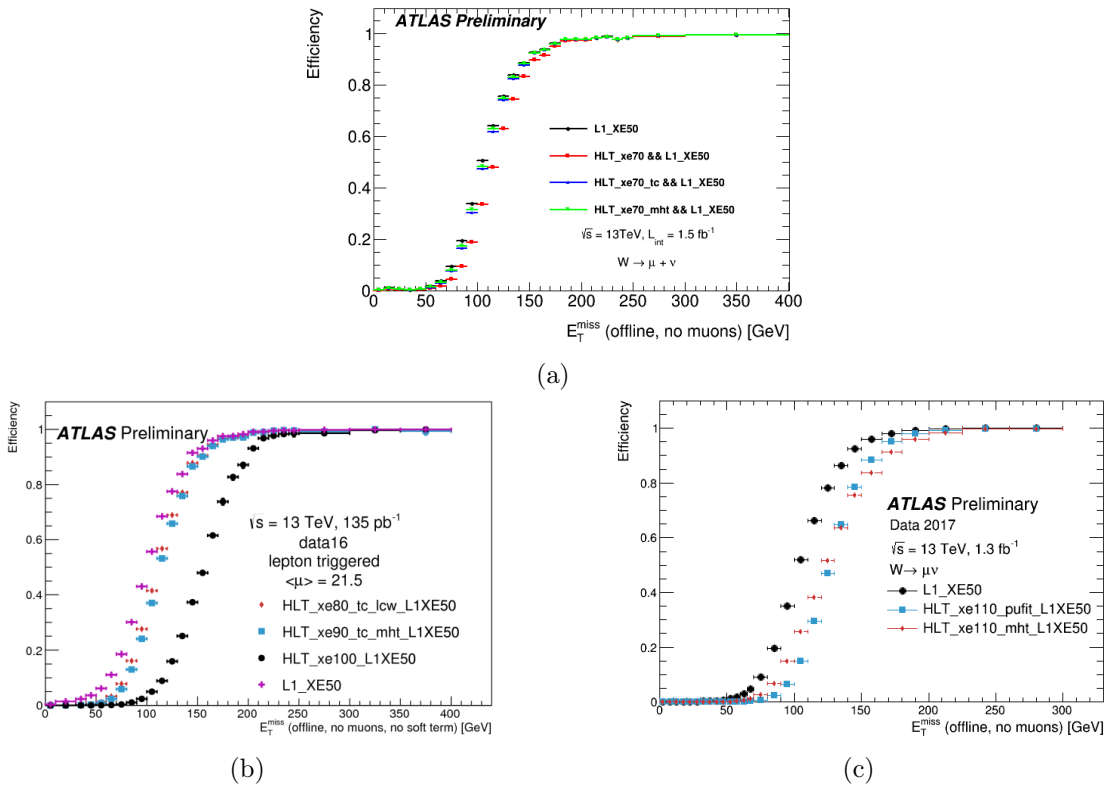

Figure 6.3.: Efficiency curves of the used $E_{\mathrm{T}}^{\mathrm{miss}}$ triggers during the data taking periods of 2015 (a) and 2016 (b),(c).[116]

selection criteria	variable	cause
trigger	MET $> 70 - 110\,\mathrm{GeV}$	MET trigger
event cleaning	GRL, no bad jet or bad muon, primary vertex	good quality
analysis based selection	MET $> 200\,\mathrm{GeV}$	trigger plateau
	$\Delta\phi$(MET, jets)$> 0.4\,\mathrm{rad}$	QCD suppression
	$N_{\mathrm{ele}} = 0$, $N_{\mathrm{muon}} = 0$ (lepton veto)	$Wl\nu$, $t\bar{t}$ suppression
	$n_{\mathrm{jets}} \geq 2$	quark jets and optionally ISR jet
	p_T(jet1) $> 200\,\mathrm{GeV}$	hard gluon radiation

Table 6.2.: Event selection criteria of the trigger, event cleaning and analysis based selection.

events are corrupted due to tile calorimeter or semi-conductor tracker issues, they are also removed.
Events containing a jet or muon which is flagged as bad are deleted as well. In case of bad jets, this could mean for example that noise from the hadronic calorimeter or pile-up effects have caused a fake jet signal. In case of bad muons this means that events containing a baseline muon before overlap removal is applied satisfying $\frac{\sigma(p/q)}{|q/p|} > 0.2$ (with p being the momentum and q the charge of the particle, σ is the corresponding uncertainty) are deleted. Additionally, every event must have one primary vertex with at least two tracks with a transverse momentum of at least 500 MeV assigned to it. These quality requirements follow the SUSY object definitions of the ATLAS SUSY Tools package tag 00-08-60 [117, 118].

Analysis based selection
After the clean-up and $E_{\mathrm{T}}^{\mathrm{miss}}$ trigger are applied, a lepton veto is included in the preselection within the analysis. Especially in the SRs, this is a very effective requirement which rejects all events containing electrons or muons. Electrons considered for this criterion must fulfil the *Loose* quality criterium (see chapter 4) and additionally feature a transverse momentum of $> 10\,\mathrm{GeV}$, eta range of $|\eta < 2.47|$ and an origin from the primary vertex. For muons a transverse momentum of more than 10 GeV, an eta range of $|\eta < 2.7|$ as well as an isolation criterion analogue to that of electrons is demanded. These requirements are best suited for a conservative lepton veto, which is needed to guarantee a high signal efficiency in the SRs. By applying this selection criterion, all background processes leading to final states with leptons are strongly reduced (for example semi- and dileptonic $t\bar{t}$ events with electrons or muons), leaving $Z \to \nu\nu$ and $W \to \tau\nu$ (with τ decaying hadronically) to be dominant (see figure 6.4).
For the control regions on the other hand, where, instead of the lepton veto, one electron or one muon is selected, the same requirements are used, except for the higher quality criteria *Medium* and an increased transverse momentum of more than 25 GeV.

Additionally to the $E_{\mathrm{T}}^{\mathrm{miss}} > 200\,\mathrm{GeV}$ requirement mentioned in section 6.3, $E_{\mathrm{T}}^{\mathrm{miss}}$ must have a minimal spatial distance of $\Delta\phi > 0.4\,\mathrm{rad}$ to all jets in the event to reduce multijet events as explained in section 5.3 (see figure 6.5).
Finally, only events which contain at least two jets are selected. Since the analysis focuses on a boosted scenario as explained in section 5.2, a hard ISR jet[7] emerging from the gluon radiation or a hard quark jet is required. Therefore, it is demanded that the hardest jet must have a transverse momentum of $p_T > 200\,\mathrm{GeV}$[8].

[7] In this context, *hard* refers to the high p_T of the object.
[8] This value was determined by performing a cut optimisation.

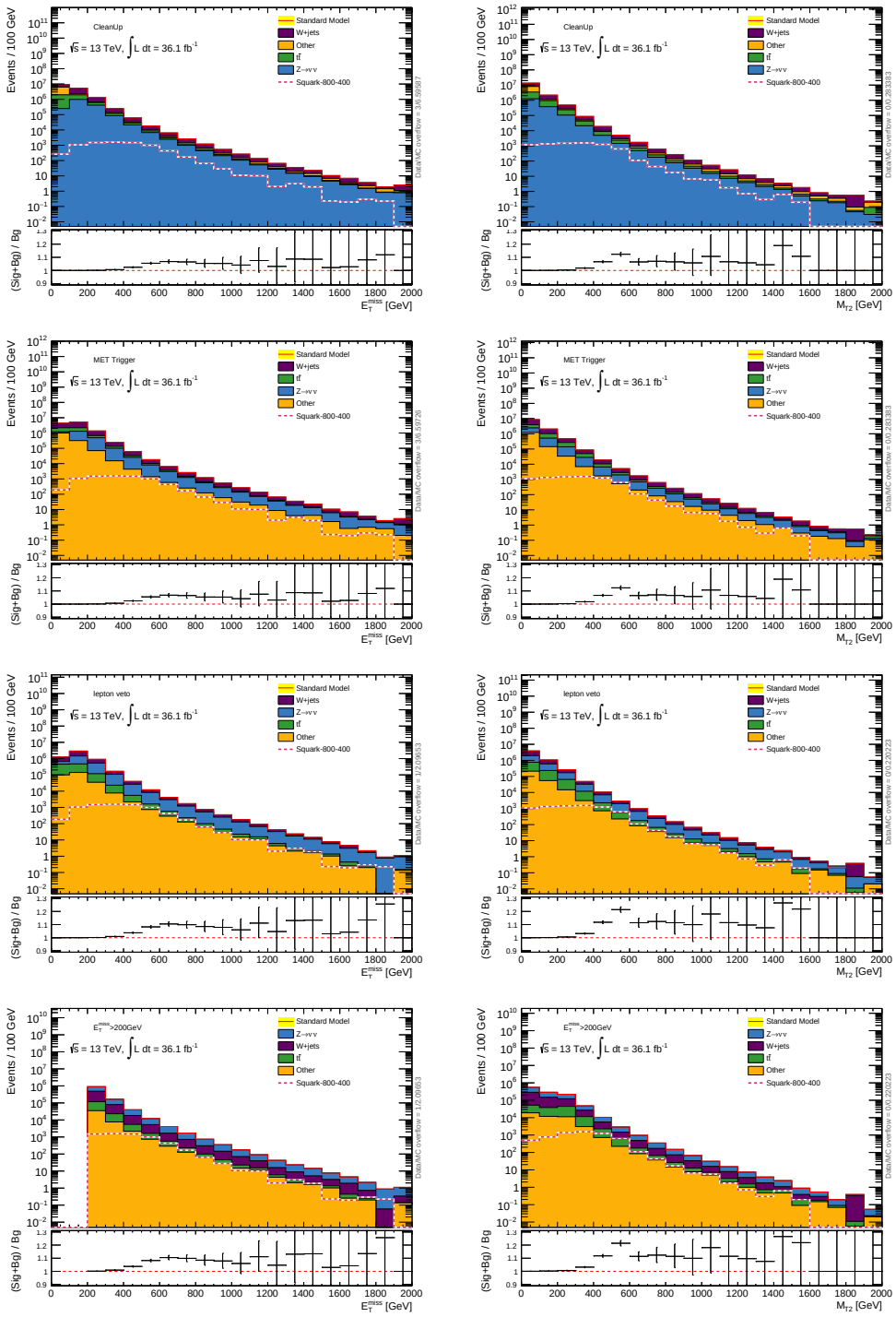

Figure 6.4.: Effect of the event selection criteria on the $E_{\mathrm{T}}^{\mathrm{miss}}$ (left) and M_{T2} (right) distributions.

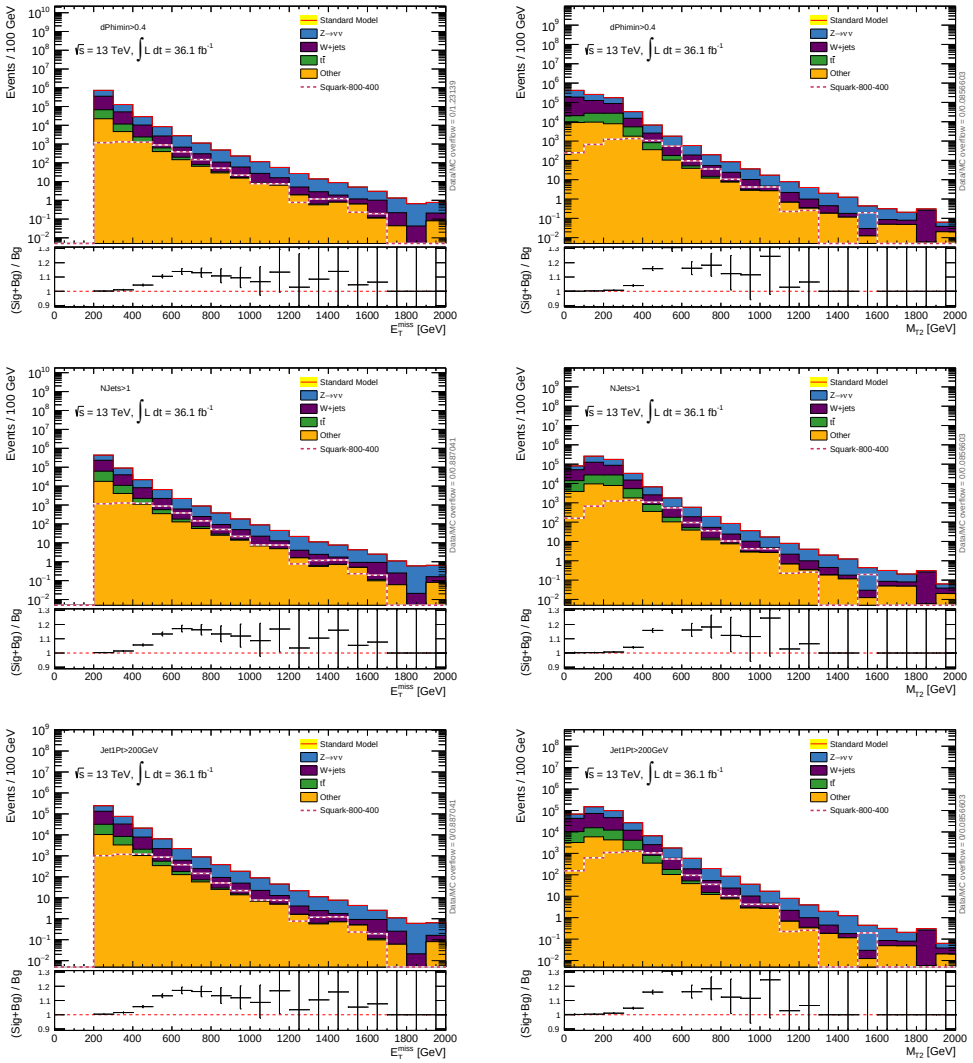

Figure 6.5.: Effect of the event selection criteria on the $E_{\mathrm{T}}^{\mathrm{miss}}$ (left) and M_{T2} (right) distributions (continuation of figure 6.4).

6.5. Signal Region Selection

Based on the preselection, a signal region optimisation was performed to find combinations of cuts leading to the best possible sensitivity and discrimination power between signal and background. Thereby, the focus was set on gaining high sensitivity from shape differences in the low and medium range of the distribution and thus avoiding a tail analysis.

Variable	Step size	Minimum	Maximum	Optimised cut value
p_T(jet1) [GeV]	50	0	2000	> 200
p_T(jet2) [GeV]	50	0	1000	> 100
p_T(jet3) [GeV]	50	0	1000	> 50
p_T(jet4) [GeV]	5	0	1000	> 30
$\Delta\phi(E_{\mathrm{T}}^{\mathrm{miss}}, \mathrm{jets})_{\mathrm{min}}$ [rad]	0.05	0	1	> 0.4
$E_{\mathrm{T}}^{\mathrm{miss}}$ [GeV]	80	200	1000	> 200
M_{T2} [GeV]	50	0	2000	> 50
M_{eff} [GeV]	200	400	4000	> 600

Table 6.3.: Variables considered in the cut optimisation for the SR with their respective value ranges, step sizes and final optimised values.

The optimisation was done for distributions in the kinematic variables $E_{\mathrm{T}}^{\mathrm{miss}}$ and M_{T2} as presented in section 5.5, since they show the best discrimination power between the signal and background shapes. Other variables like p_T of the four hardest jets, $\Delta\phi(E_{\mathrm{T}}^{\mathrm{miss}}, \mathrm{jets})_{\mathrm{min}}$ and M_{eff} were varied in pre-defined steps. Table 6.3 summarises all variables that were included in the optimisation as well as the scan ranges and step sizes that were applied. The scan ranges were chosen to be quite large to perform a complete scan, even if the maximum values would lead to a tail analysis. Nevertheless, the results show a better performance of the fit at lower cut values.

To perform the optimisation, a final integrated luminosity of $36.5\,\mathrm{fb}^{-1}$ for the complete data set of 2015 + 2016 was assumed. The optimisation was conducted for a set of benchmark signal points outside the already excluded area (as shown in figure 6.1) and with mass differences of $\Delta m < 200\,\mathrm{GeV}$.

In the first step of the optimisation, all three jet multiplicity bins were analysed separately and the best cut combinations were determined with regard to the expected sensitivity. For each possible cut combination[9] a simple hypothesis test was used and the sensitivity Z^0[119] was calculated. It is a simple integrated sensitivity, based on the number of signal and background events, without consideration of shape differences. Instead of including all systematics directly, a flat systematic of 1% was assumed for the sensitivity calculation. This low estimation was only used for these preliminary studies, but has no impact on the predications and further proceeding.

[9] Only logical combinations were considered, in the 2 jet bin for example no cut on the momenta of a third or fourth jet was used.

Figure 6.6 exemplarily shows the n-1 distributions[10] produced by the optimisation for the $N_{\text{jet}} = 3$ bin and the cut combination with the highest sensitivity. Additionally, the Z^0 curve is shown. It depicts the integrated sensitivity that would be gained by cutting on the respective bin value, not the sensitivity per bin.

The optimised cuts on the individual variables (drawn as vertical, dashed red line) were then manually fine tuned, so that they are not always positioned at the bin with the highest sensitivity. They were in some cases allowed to stay below the maximum yield with the intention of keeping the sensitivity from lower bins instead of cutting them away. This procedure is used here exceptionally, since a tail analysis is to be avoided and instead the applied shape fit relies on the sensitivity from the bins in the lower and medium range.

In the second step of the optimisation, a maximum likelihood fit was used to fit all three jet multiplicity bins simultaneously with the same cut combination. Thereby, only the three best performing cut combinations of the previous step, one for each jet multiplicity, were tested. The fit was done separately for both discriminating variables ($E_{\text{T}}^{\text{miss}}$ and M_{T2}). All available signal points were scanned successively and an expected exclusion limit was produced for each variable.
The two final cut combinations which were identified as the best performing for the two variables individually, leading to the largest excluded area, were similar enough to be merged so that only one cut combination was kept for both variables. It is given in the right column of table 6.3. Figure 6.7 shows the resulting expected exclusion limits for $E_{\text{T}}^{\text{miss}}$ and M_{T2} using this optimised cut combination.
The effects of these optimised cuts on the number of remaining events in the SR can be seen in table 6.4.

An important aspect of a shape fit analysis is the binning of the distributions. In contrast to cut-and-count analyses like the 0-lepton search [105], the SRs cannot be reduced to one bin, but are divided into several bins to maintain their shape information. On the one hand, the shape differences between signal and background should be emphasised by choosing a sufficient number of bins. On the other hand, statistical fluctuations should be avoided by choosing sufficiently large bins, especially at the high-end of the distributions. Bins containing no background events but some signal events would lead to infinite sensitivity[11]. Additionally, a large number of bins to be fitted simultaneously would push any fitting tool to its performance limits.
Various binnings were tested, including a variable binning with increasing bin widths

[10] They show the respective distributions with all cuts applied except the one on the shown variable.
[11] This is not realistic, but caused by the technical shortcomings of the fitting tool.

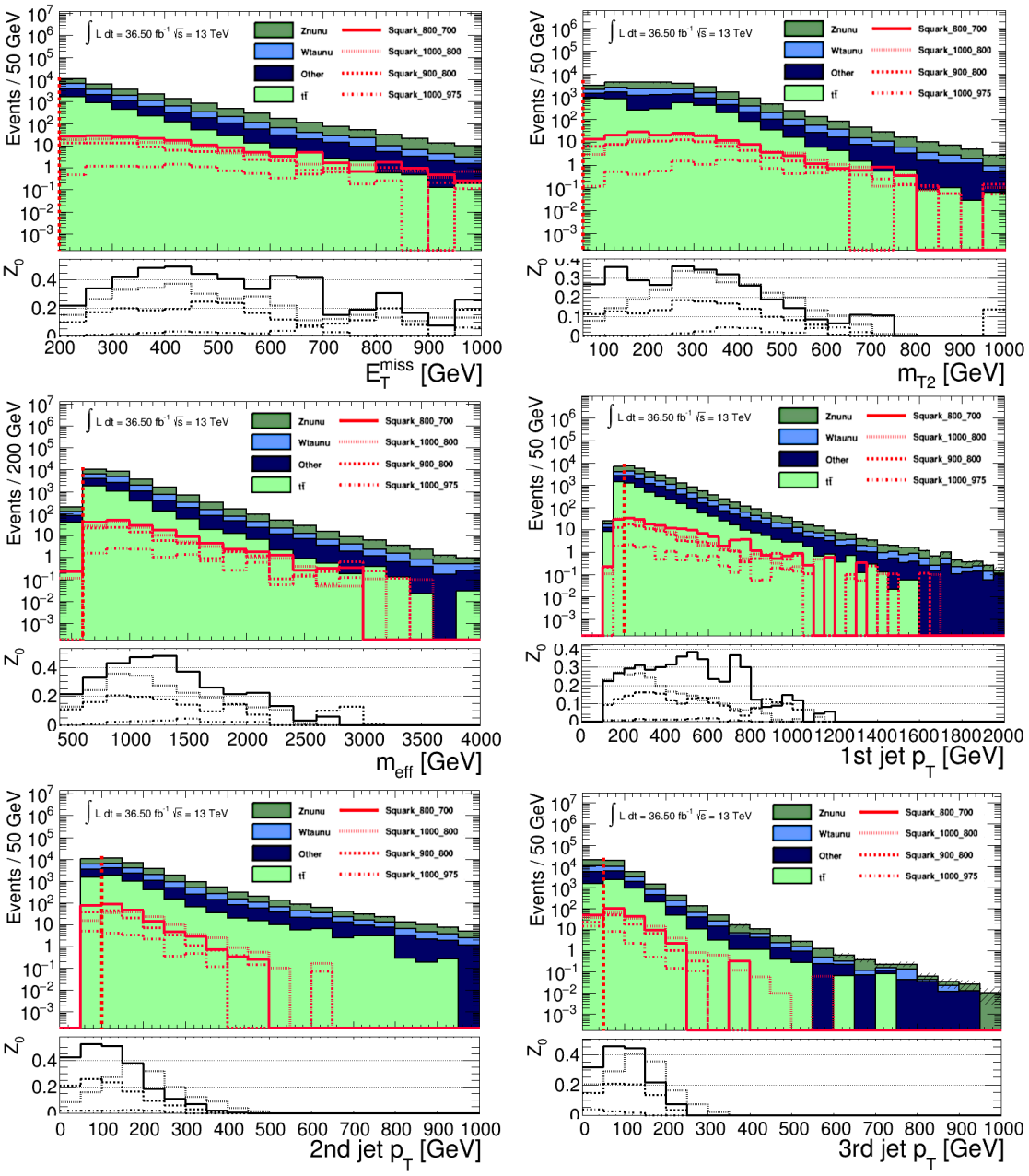

Figure 6.6.: N-1 distributions of the best cut combination for the 3 jet bin. They show the distribution and sensitivity if all other cuts are applied except the one on the variable displayed. The sensitivity is not drawn per bin, but shows the estimated integrated sensitivity if the cut is set on the corresponding bin.

Cut	Cut Name	$Z \to \nu\nu$	$W \to \tau\nu$	$t\bar{t}$	$W \to \mu\nu$	$W \to e\nu$	Diboson	single top
0	All	1.8014e+06±1746	2.10844e+06±2963	3.2503e+06±1385	2.67986e+06±4025	1.94557e+06±8825	237851±217	408929±381
1	Clean Up	1.77843e+06±1733	2.08099e+06±2911	2.96385e+06±1343	2.64538e+06±3941	1.91512e+06±8790	234939±215	381679±369
	SR							
2	$E_{\mathrm{T}}^{\mathrm{miss}}$ Trigger	1.7294e+06±1700	1.96154e+06±2803	2.15903e+06±1113	2.46618e+06±3756	1.48403e+06±5250	173836±192	300521±326
3	lepton veto	1.72008e+06±1697	1.55087e+06±2456	790273±827	467806±1357	449828±1536	64922±120	110098±200
4	$E_{\mathrm{T}}^{\mathrm{miss}}$ >200 GeV	533567±963	282613±1062	103349±145	89427±454	70943±473	19790±67.8	16450±64.7
5	$\Delta\Phi_{min} > 0.4$	477501±949	196900±1017	53531±101	78859±439	61342±408	14756±57.3	9030±49.2
6	NJets>1	275814±522	124799±848	52194±100	45207±261	37299±256	12371±50.9	7928±45.1
7	Jet1Pt> 200 GeV	176753±427	83021±785	28107±69.8	27285±174	23776±179	8056±41.1	5209±37.6
8	M_{eff} >600 GeV	116593±337	50540±715	23742±62.6	16588±99.6	14651±102	6207±31.4	3851±31.1
9	M_{T2} >50	115901±337	49674±715	23340±61.5	16461±99.2	14518±101	6159±31.3	3791±30.8
10	NJet=2	19657±72.7	6919±82.1	654±8.82	2606±35.2	2294±35.3	641±10.4	375±11.4
11	NJet=3	11482±45.9	4963±93.1	2271±20.2	1723±24.6	1528±21.8	692±9.88	428±11
12	NJet≥ 4	17266±45.5	8942±45.3	10776±43.5	2772±25.4	2624±30.2	1559±14.4	1133±15.1

Cut	Cut Name	$Z \to \tau\tau$	$t\bar{t}V$	$Z \to \mu\mu$	$Z \to ee$	Total MC	Data	Data/MC
0	All	205981±7761	14080±10.6	1.24213e+06±2128	2.85402e+06±10149	1.68516e+07±16614	1.5665e+08±12516	9.3±0.00919
1	CleanUp	201580±7756	13920±10.5	1.18456e+06±1887	2.79972e+06±10105	1.63019e+07±16502	1.40013e+08±11833	8.59±0.00872
	SR							
2	$E_{\mathrm{T}}^{\mathrm{miss}}$ Trigger	164445±7751	11135±9.48	692070±1194	77260±608	1.12992e+07±10763	blinded	blinded
3	lepton veto	87535±336	4533±6.23	16818±190	2764±69.4	5.29255e+06±3751	blinded	blinded
4	$E_{\mathrm{T}}^{\mathrm{miss}}$ >200 GeV	6808±71.5	1126±3.17	2103±34.5	8.64±3.22	1.13174e+06±1592	blinded	blinded
5	$\Delta\Phi_{min} > 0.4$	2596±47.1	602±2.31	1856±33.1	0.518±0.136	900615±1524	blinded	blinded
6	NJets>1	1665±30.9	600±2.3	1036±20.8	0.4±0.0938	561983±1072	blinded	blinded
7	Jet1Pt> 200 GeV	1110±25.6	368±1.82	574±13.3	0.339±0.0869	356173±935	blinded	blinded
8	M_{eff} >600 GeV	661±16.7	356±1.8	310±7.5	0.264±0.0743	234901±809	blinded	blinded
9	M_{T2} >50	649±16.6	351±1.78	307±7.48	0.264±0.0743	232536±808	blinded	blinded
10	NJet=2	92.4±4.18	3.64±0.163	48.8±2.65	0.0315±0.0236	33400±123	blinded	blinded
11	NJet=3	67±2.86	17.2±0.377	33.1±2.74	0.00744±0.00744	23342±113	blinded	blinded
12	NJet≥ 4	113±3.01	244±1.52	47.8±1.8	0.105±0.0432	45830±92.8	blinded	blinded

Table 6.4.: Breakdown of all selection criteria of the SR. The effect of each selection criterion on the number of remaining events in each background process can be seen. The event numbers are shown with their statistical uncertainties. The data events in the SR are not shown to avoid any bias.

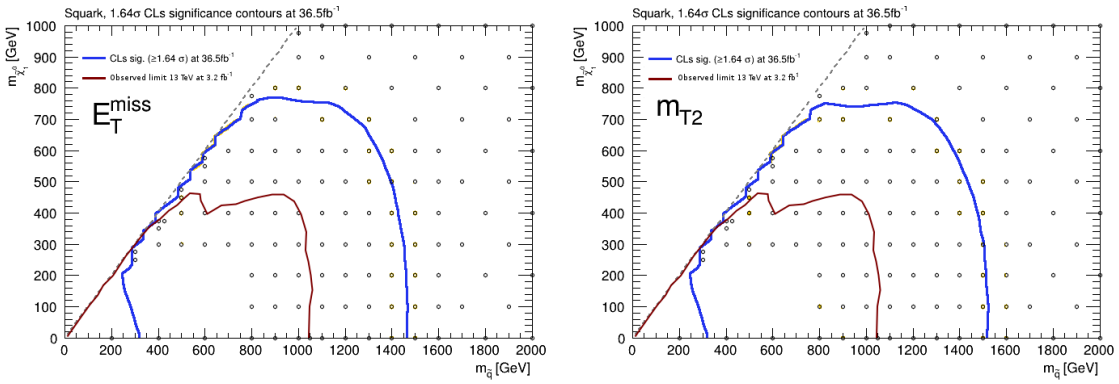

Figure 6.7.: Expected exclusion limits for $E_{\mathrm{T}}^{\mathrm{miss}}$ (left) and M_{T2} (right) using the optimised cut combination. They were produced by conducting a profile likelihood fit, fitting the three jet multiplicity bins simultaneously. Systematic uncertainties are not included. The previous limit of the 0-lepton analysis performed with 2012 data at $\sqrt{s} = 8\,\mathrm{TeV}$ is shown as a reminder. A direct comparison is not legitimate due to different data sets and because systematic uncertainties have not yet been considered.

towards higher values. Finally, an equal binning was chosen using 10 bins with a width of 100 GeV each in the range from 0 to 1000 GeV and an additional overflow bin to include the information of all events in higher bins without the disadvantage of poor statistics[12]. The distributions of the SR in all jet multiplicity bins ($N_{\mathrm{jet}} = 2, N_{\mathrm{jet}} = 3, N_{\mathrm{jet}} \geqslant 4$) are shown for the two variables $E_{\mathrm{T}}^{\mathrm{miss}}$ and M_{T2} in figures 6.8 and 6.9, respectively. The backgrounds are drawn stacked, the signals are overlaid separately. To improve clarity, all W processes in the SRs are combined into one denoted as W + jets.
Shape differences between signal and background distributions can be observed in the medium range and partly at the high-end of the range and are, as discussed in section 5.5, especially pronounced for the signal with larger mass difference.

[12]The plots therefore are slightly different from those shown in section 6.6

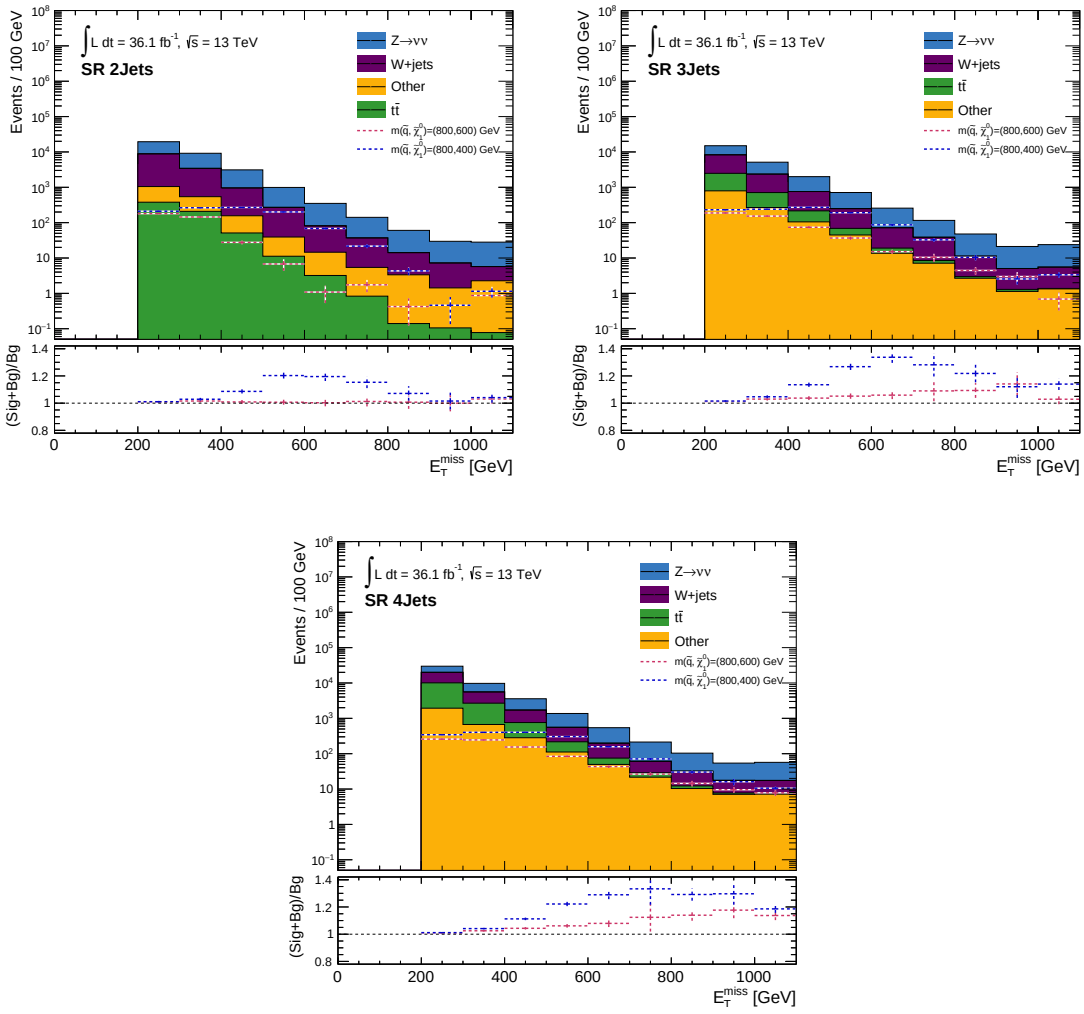

Figure 6.8.: The distributions of $E_{\mathrm{T}}^{\mathrm{miss}}$ in the SRs. The three jet multiplicity bins selecting events with 2 jets, 3 jets and $\geqslant 4$ jets, respectively, are shown.

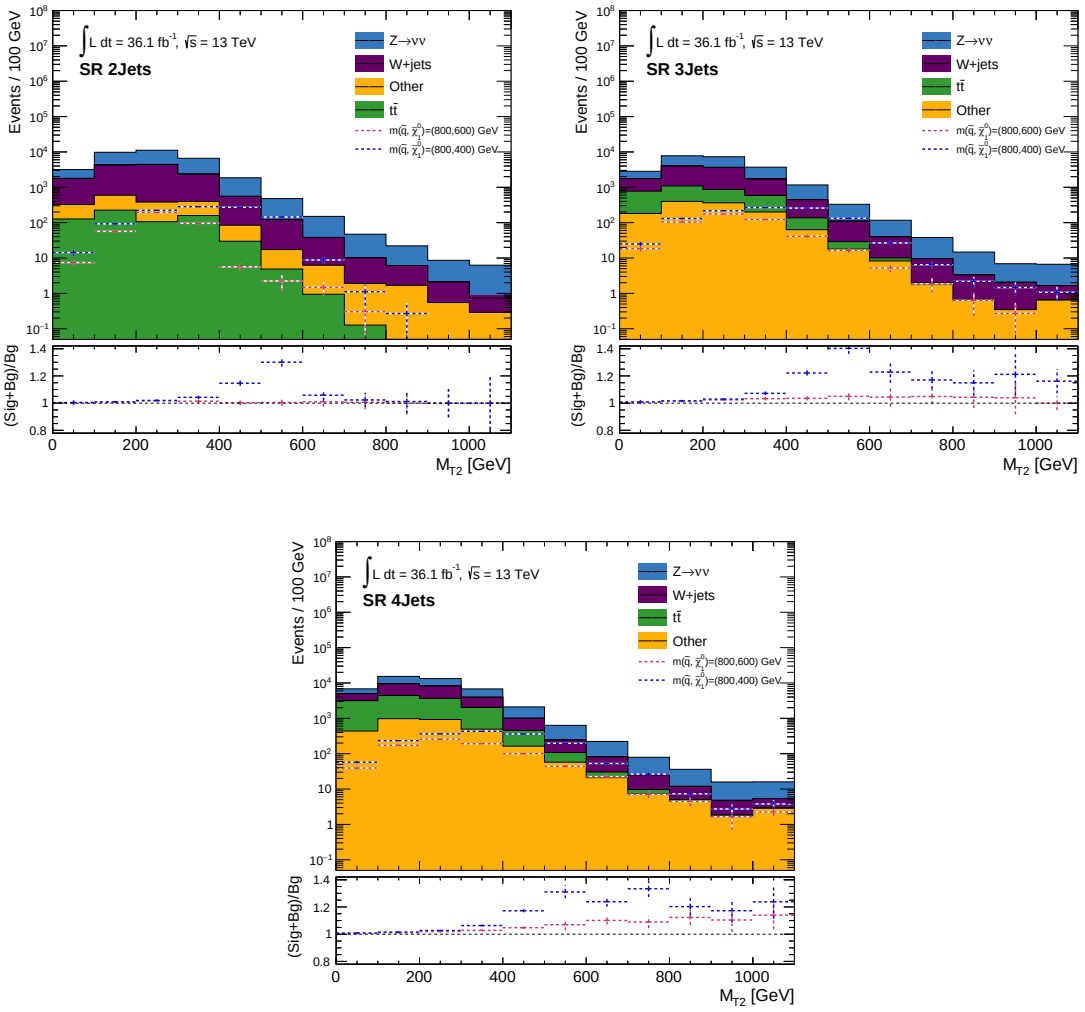

Figure 6.9.: The distributions of M_{T2} in the SRs. The three jet multiplicity bins selecting events with 2 jets, 3 jets and $\geqslant 4$ jets, respectively, are shown.

6.6. Control Region Selection

The CRs were created corresponding to the SR selection presented in the previous section. They serve multiple purposes like the reduction of background shape uncertainties or the calculation of normalisation factors[13] during the fit (see chapter 7). Therefore, the CRs have to select one specific background as purely as possible while being orthogonal to the SR and having similar kinematic characteristics. These properties allow the normalisation factors obtained from the background estimations in the CRs to be applied in the SR.

As the distributions after the preselection (figure 5.9) and in the SR (figures 6.8 and 6.9) show, the dominant standard model backgrounds arise from $Z \to \nu\nu$ and W + jets processes (as the breakdown in table 6.4 shows, dominant contributions are $W \to \tau\nu$ with hadronically decaying taus). Unfortunately, in case of these two processes, the events are very hard to select cleanly, making it impossible to design reasonable CRs for them. They do not contain electrons or muons in the final state, which could be used for the selection, only missing transverse energy and jets. Any CR would be contaminated with signal and contributions from other backgrounds with similar final states.
Since the shape differences between signal and background are small (as shown in section 5.5), it is required to reduce the uncertainty of the background as far as possible to maintain a high sensitivity. Especially the two main backgrounds, $Z \to \nu\nu$ and $W \to \tau\nu$, which dominate the distributions in the observed variables, must be very well understood. The best way would be to determine the shapes of the background distributions from data in dedicated CRs. Since these two processes cannot be purely selected, they are replaced by processes which are similar but easier and cleaner to select. In order to obtain shape uncertainties for the original processes, single objects are replaced to simulate the original background process.
The two approaches for $Z \to \nu\nu$ and $W \to \tau\nu$ are explained in more detail in the following. The effects of each selection criterion finally used for both CRs on the number of remaining events can be seen in tables 6.5 and 6.6.

6.6.1. Estimation of $Z \to \nu\nu$

The first main background, $Z \to \nu\nu$ features no leptons in the final state, but only jets (in case of ISR) and $E_{\mathrm{T}}^{\mathrm{miss}}$. As explained in chapter 5, it is an irreducible background and cannot be distinguished from signal events. To create a pure CR, selecting this process alone is not possible due to contamination, but instead, a suitable substitute process could be used. Instead of selecting $Z \to \nu\nu$ events, it would be an obvious choice to select

[13] These factors are obtained by fitting the background distributions to the observed data in dedicated CRs. They are then used to scale the respective backgrounds in the SRs accordingly to improve the accuracy of background expectations and reduce shape uncertainties.

Cut	Cut Name	$Z \to \nu\nu$	$W \to \tau\nu$	$t\bar{t}$	$W \to \mu\nu$
	Wenu CR				
22	$E_{\mathrm{T}}^{\mathrm{miss}}$ Trigger	1.7294e+06±1700	1.96154e+06±2803	2.15903e+06±1113	2.46618e+06±3756
23	p_{T} (Ele)>25 GeV	426±17.8	80521±831	293981±338	393±39.8
24	$E_{\mathrm{T}}^{\mathrm{miss}}{}_{\mathrm{corr}} > 200$ GeV	79.7±3.16	27575±240	67698±136	102±11.1
25	$\Delta\Phi_{\mathrm{min}} > 0.4$	46.1±2.58	12632±171	23675±76.6	38.2±8.93
26	$\mathrm{NJets}_{\mathrm{corr}}>1$	40.8±2.37	8241±96.2	23167±75.9	27.3±4.77
27	$\mathrm{Jet1Pt}_{\mathrm{corr}}>200$ GeV	27.3±1.84	5713±76	12339±53.1	21.9±3.59
28	$M_{\mathrm{eff\ corr}}$ >600 GeV	25.6±1.7	4241±53.9	11347±50.4	16.6±2.97
29	$M_{\mathrm{T2\ corr}}>50$	24.6±1.68	4120±48.8	11045±49.4	15.6±2.94
30	$\mathrm{NJet}_{\mathrm{corr}}=2$	1.25±0.264	591±15.9	241±5.89	1.75±0.604
31	$\mathrm{NJet}_{\mathrm{corr}}=3$	2.89±1.03	331±9.24	668±11.7	1.28±0.325
32	$\mathrm{NJet}_{\mathrm{corr}}\geq 4$	4.51±0.483	572±10.3	4262±32	2.1±0.57

Cut	Cut Name	$W \to e\nu$	Other	Total MC	Data	Data/MC
	Wenu CR					
22	$E_{\mathrm{T}}^{\mathrm{miss}}$ Trigger	1.48403e+06±5250	1.41927e+06±7875	1.12195e+07±10755	7.91152e+07±8895	7.05±0.00681
23	p_{T} (Ele)>25 GeV	739378±4024	90281±300	1.20498e+06±4134	851052±923	0.706±0.00254
24	$E_{\mathrm{T}}^{\mathrm{miss}}{}_{\mathrm{corr}} > 200$ GeV	178733±658	21216±92.3	295404±719	273856±523	0.927±0.00287
25	$\Delta\Phi_{\mathrm{min,corr}} > 0.4$	81506±454	7692±52.8	125589±494	127793±357	1.02±0.00491
26	$\mathrm{NJets}_{\mathrm{corr}}>1$	60204±344	6746±46.6	98426±368	97846±313	0.994±0.00489
27	$\mathrm{Jet1Pt}_{\mathrm{corr}}>200$ GeV	43564±290	4576±32.7	66240±306	66858±259	1.01±0.00609
28	$M_{\mathrm{eff\ corr}}$ >600 GeV	33964±198	3958±29.4	53553±213	53692±232	1±0.00588
29	$M_{\mathrm{T2\ corr}}>50$	28834±159	3774±28.3	47813±176	48061±219	1.01±0.00589
30	$\mathrm{NJet}_{\mathrm{corr}}=2$	2544±35.1	230±7.61	3609±39.7	4025±63.4	1.12±0.0214
31	$\mathrm{NJet}_{\mathrm{corr}}=3$	1777±25	264±7.51	3044±30.1	3135±56	1.03±0.021
32	$\mathrm{NJet}_{\mathrm{corr}}\geq 4$	4264±36.1	949±13	10052±51	9383±96.9	0.933±0.0107

Table 6.5.: Breakdown of all selection criteria of the electron CR. The effect of each selection criterion on the number of remaining events in each background process can be seen. The event numbers are shown with their statistical uncertainties. The data events in the SR are not shown to avoid any bias.

Cut	Cut Name	$Z \to \nu\nu$	$W \to \tau\nu$	$t\bar{t}$	$W \to \mu\nu$
	Wmunu CR				
42	$E_{\mathrm{T}}^{\mathrm{miss}}$ Trigger	1.7294e+06±1700	1.96154e+06±2803	2.15903e+06±1113	2.46618e+06±3756
43	p_{T} (Mu)>25 GeV	45.6±3.42	117258±657	484439±442	1.65289e+06±3346
44	$E_{\mathrm{T}}^{\mathrm{miss}}{}_{\mathrm{corr}} > 200$ GeV	11.8±1.79	43008±478	149418±230	538776±2636
45	$\Delta\Phi_{\mathrm{min}} > 0.4$	9.43±1.58	39101±369	105322±194	484949±2626
46	$\mathrm{NJets}_{\mathrm{corr}}$>1	6.63±1.1	22936±166	101956±190	278684±1137
47	$\mathrm{Jet1Pt}_{\mathrm{corr}}> 200$ GeV	4.24±0.861	14872±119	50944±130	179272±522
48	$M_{\mathrm{eff\ corr}}$ >600 GeV	3.35±0.723	12873±95.1	49223±128	166005±459
49	$M_{\mathrm{T2\ corr}}$>50	3.33±0.723	12754±94.4	48590±127	164201±457
50	$\mathrm{NJet}_{\mathrm{corr}}$=2	0.38±0.115	1829±28.6	1696±22.5	22230±132
51	$\mathrm{NJet}_{\mathrm{corr}}$=3	0.139±0.0596	1016±17.5	4435±38.2	12006±62.6
52	$\mathrm{NJet}_{\mathrm{corr}} \geq 4$	0.395±0.184	1511±16.5	17190±74.8	17691±61.6

Cut	Cut Name	$W \to e\nu$	Other	Total MC	Data	Data/MC
	Wmunu CR					
42	$E_{\mathrm{T}}^{\mathrm{miss}}$ Trigger	1.48403e+06±5250	1.41927e+06±7875	1.12195e+07±10755	7.91152e+07±8895	7.05±0.00681
43	p_{T} (Mu)>25 GeV	16.6±18.9	229735±468	2.48438e+06±3470	2.20412e+06±1485	0.887±0.00138
44	$E_{\mathrm{T}}^{\mathrm{miss}}{}_{\mathrm{corr}} > 200$ GeV	6.68±2.3	60663±208	791883±2697	804327±897	1.02±0.00364
45	$\Delta\Phi_{\mathrm{min,corr}} > 0.4$	6.88±2.22	49558±199	678946±2667	700129±837	1.03±0.00423
46	$\mathrm{NJets}_{\mathrm{corr}}$>1	2.12±0.835	38154±112	441740±1170	445805±668	1.01±0.00307
47	$\mathrm{Jet1Pt}_{\mathrm{corr}}> 200$ GeV	1.37±0.696	23566±83.4	268660±557	273336±523	1.02±0.00287
48	$M_{\mathrm{eff\ corr}}$ >600 GeV	1.15±0.632	22290±79.6	250395±493	254071±504	1.01±0.00284
49	$M_{\mathrm{T2\ corr}}$>50	1.04±0.623	21998±78.8	247548±490	251133±501	1.01±0.00285
50	$\mathrm{NJet}_{\mathrm{corr}}$=2	0.0681±0.0681	2059±22.3	27814±138	31854±178	1.15±0.00858
51	$\mathrm{NJet}_{\mathrm{corr}}$=3	0.273±0.248	1874±20.7	19331±78.1	19766±141	1.02±0.00836
52	$\mathrm{NJet}_{\mathrm{corr}} \geq 4$	0.00848±0.00848	4282±29.5	40676±103	38014±195	0.935±0.00534

Table 6.6.: Breakdown of all selection criteria of the muon CR. The effect of each selection criterion on the number of remaining events in each background process can be seen. The event numbers are shown with their statistical uncertainties. The data events in the SR are not shown to avoid any bias.

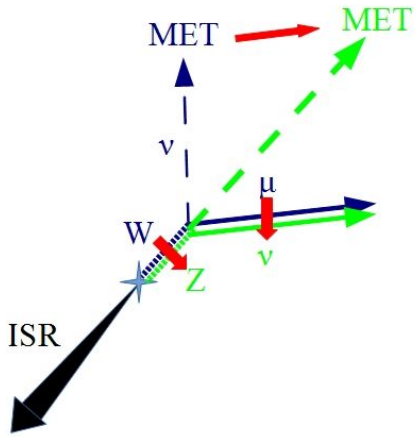

Figure 6.10.: Replacement of a muon from a $W \to \mu\nu$ process (blue) by a neutrino to simulate a $Z \to \nu\nu$ process (green). Due to the additional neutralino, the amount of missing transverse energy has to be recalculated.

$Z \to ll$ events and replace the leptons with neutrinos by adding their momenta to the $E_{\mathrm{T}}^{\mathrm{miss}}$. Since the branching ratio of this process is only 6.7%[14] (compared to 20% for $Z \to \nu\nu$)[24], the MC sample and especially the collected data only have limited statistics.

Therefore, $W \to \mu\nu$ events are selected instead by requiring them to contain a muon with $p_T > 25\,\mathrm{GeV}$ as the only lepton. The momentum of the muon is then added to $E_{\mathrm{T}}^{\mathrm{miss}}$, leading to a recalculation of all jet and $E_{\mathrm{T}}^{\mathrm{miss}}$ related variables (see figure 6.10). All other selection criteria for this CR can be adopted from the SR optimisation, but are defined on the recalculated variables (see table 6.7).
A closure test is performed comparing the original distribution (in the SR) and the replaced distribution (in the CR) to show the validity of this method. The comparison is made for the 2 jet, 3 jet and 4 or more jet selections and in both discriminating variables $E_{\mathrm{T}}^{\mathrm{miss}}$ and M_{T2}. The results are presented in figures 6.11 and 6.12.

[14]The ratio describes the probability of a particle decaying via a given decay channel into a specific final state. In this case, the ratios of $Z \to ee$ and $Z \to \mu\mu$ are added.

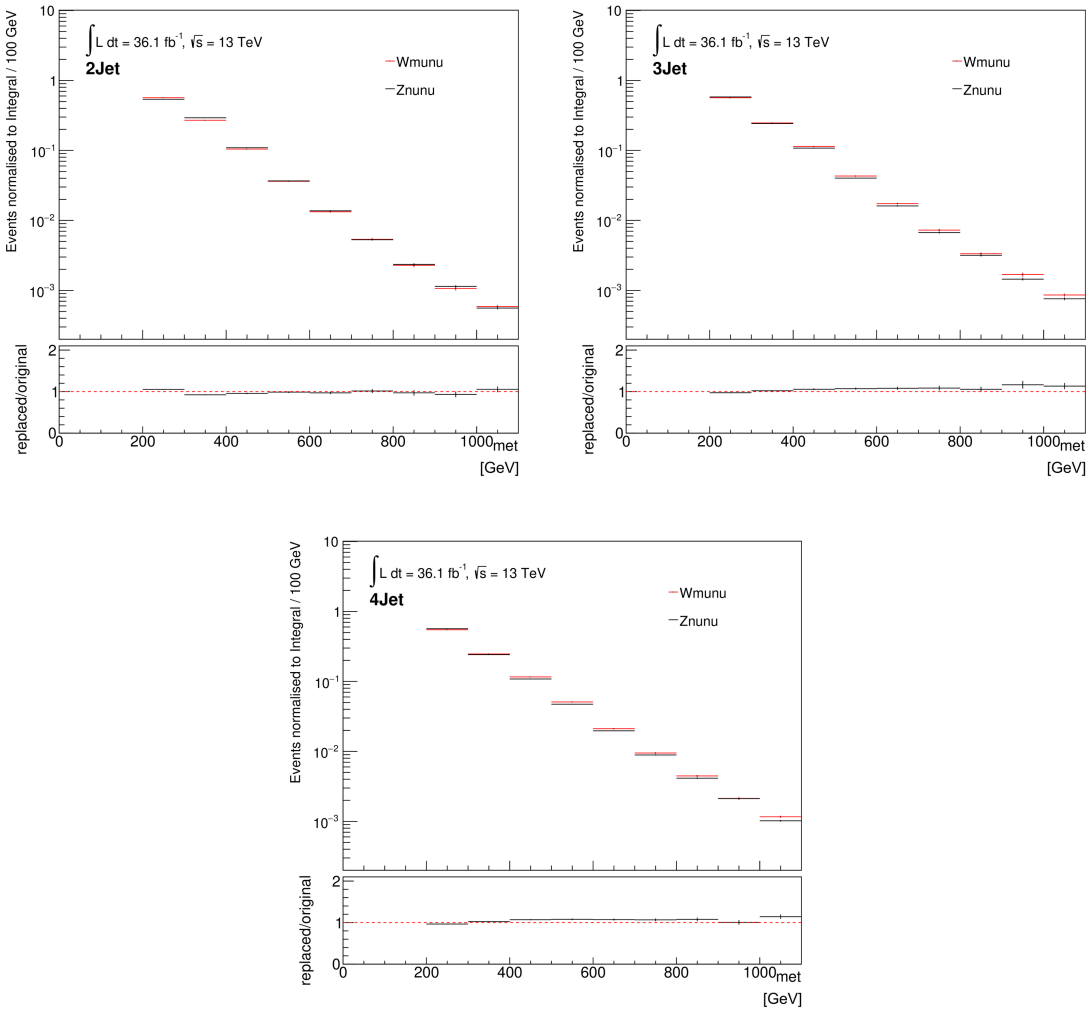

Figure 6.11.: Closure test for the $Z \to \nu\nu$ background replacement. The original process $Z \to \nu\nu$ in the SRs is compared to the substitute process $W \to \mu\nu$ in the corresponding CRs where the muon was added to $E_{\mathrm{T}}^{\mathrm{miss}}$. The deviations between both processes are used as uncertainty on $Z \to \nu\nu$ for the fit in the SRs. The results are shown for the $E_{\mathrm{T}}^{\mathrm{miss}}$ distribution.

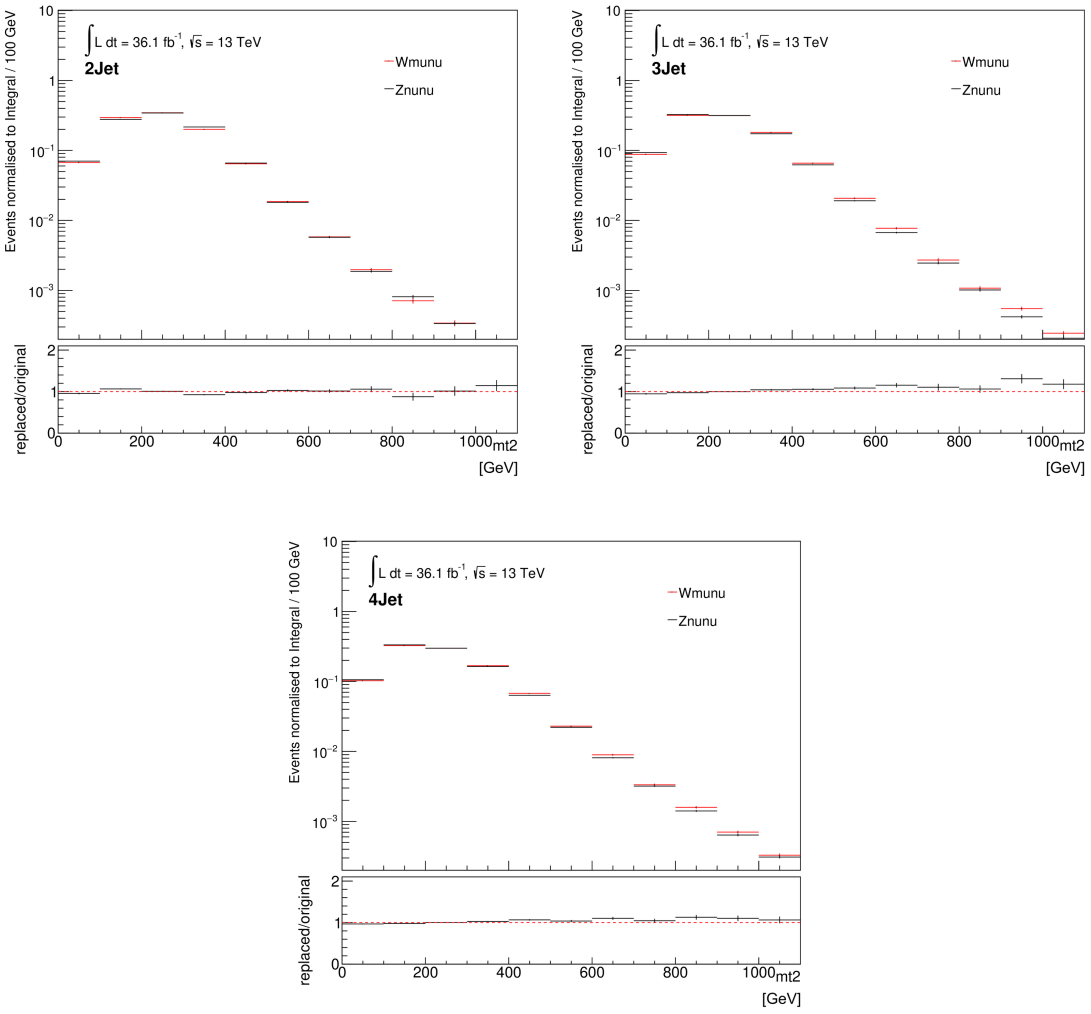

Figure 6.12.: Closure test for the $Z \to \nu\nu$ background replacement. The original process $Z \to \nu\nu$ in the SRs is compared to the substitute process $W \to \mu\nu$ in the corresponding CRs where the muon was added to $E_{\mathrm{T}}^{\mathrm{miss}}$. The deviations between both processes are used as uncertainty on $Z \to \nu\nu$ for the fit in the SRs. The results are shown for the M_{T2} distribution.

The closure test for $Z \to \nu\nu$ shows good agreement between the original and the replaced processes in both variables. Despite the fact that no compensation for the mass difference between Z and W boson was implemented, both variables show flat ratio plots in all jet multiplicity bins. Thus, it can be concluded that the replacement method works very well and the replaced $W \to \mu\nu$ process can be used further to determine shape uncertainties and scale factors for $Z \to \nu\nu$.
The differences between the original and the replaced processes are considered in the fit as an uncertainty of the original process in the SRs.

Variable	$W\mu\nu$ CR	$We\nu$ CR
leptons	1 muon, $p_T > 25\,\text{GeV}$	1 electron, $p_T > 25\,\text{GeV}$
$p_T(\text{jet1})$	>200 GeV	
$p_T(\text{jet2})$	>100 GeV	
$p_T(\text{jet3})$	>50 GeV	
$p_T(\text{jet4})$	>30 GeV	
$\Delta\phi(E_{\text{T}}^{\text{miss}}, \text{jets})_{\text{min}}$	>0.4 rad	
$E_{\text{T}}^{\text{miss}}$	>200 GeV	
M_{T2}	>50 GeV	
M_{eff}	>600 GeV	

Table 6.7.: Selection criteria of the CRs for $W \to \mu\nu$ and $W \to e\nu$. They are identical to the SR cuts except for the inverted lepton veto. The variables were recalculated after the replacement method was applied.

6.6.2. Estimation of $W \to \tau\nu$

The approach for the second main background process, $W \to \tau\nu$, is similar. To create a CR for $W \to \tau\nu$ events and thereby separate them from signal events is difficult due to their identical final states. Thus, as a substitute, $W \to e\nu$ events are selected by requesting a single electron with $p_T > 25\,\text{GeV}$ as the only lepton. Since the tau lepton of the original process decays hadronically ($\tau \to \nu_\tau + W \to \nu_\tau + q + \bar{q}'$), the electron must be replaced with the corresponding tau-jet and tau-neutrino as depicted in figure 6.13.
To determine which transverse momentum fraction of the electron has to be substituted by a tau-jet and which corresponds to the tau-neutrino and has to be added to $E_{\text{T}}^{\text{miss}}$, a p_T mapping is used based on truth-level information. This map (figure 6.14, left) shows the fraction of the neutrino p_T as a function of the total tau p_T in the SR, without separation into jet multiplicity bins[15]. The profile of this p_T-map (figure 6.14, right) shows the

[15]That is the SR with two or more jets.

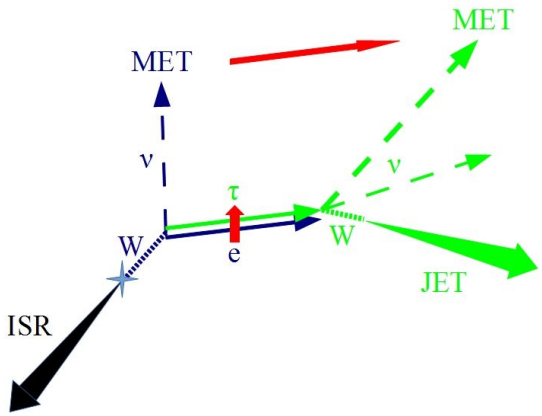

Figure 6.13.: Replacement of the electron in a $W \to e\nu$ process (blue) by a τ to simulate a $W \to \tau\nu$ process (green). Since the τ decays further and leads to an additional neutrino, the amount of missing transverse energy has to be recalculated.

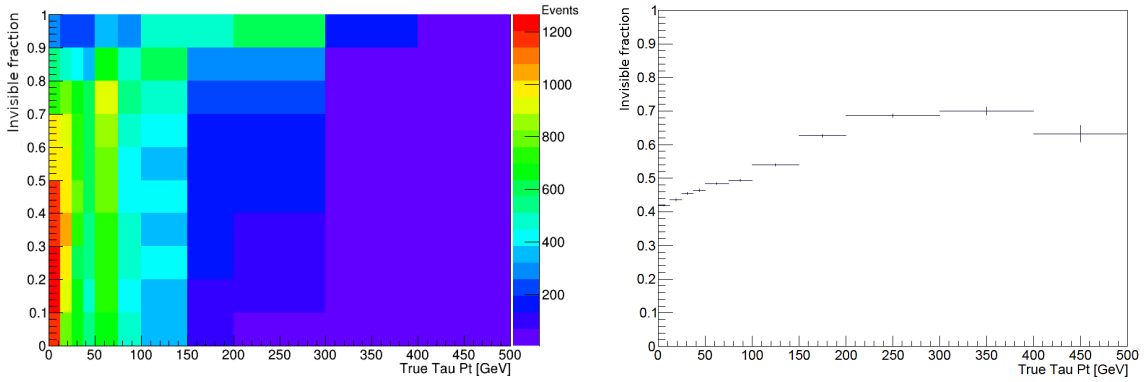

Figure 6.14.: Left: p_T-map showing the p_T fraction of the invisible tau-neutrino from the total tau p_T as a function of the total tau p_T,
Right: Profile of the p_T-map illustrating the mean value for each bin.

resulting mean value along the y-axis in each bin (with the standard error of the mean). This profile is then used to determine the correct fractions of neutrino and jet p_T for each electron momentum[16].
The invisible fraction (corresponding to the neutrino's p_T) is then added to the $E_{\mathrm{T}}^{\mathrm{miss}}$ which is recalculated, as well as all related variables. The visible fraction (corresponding to the τ-jet's p_T) is used to create a new jet object, which has to fulfil the regular jet requirements.

[16]The transverse momenta of electron and tau are set equal.

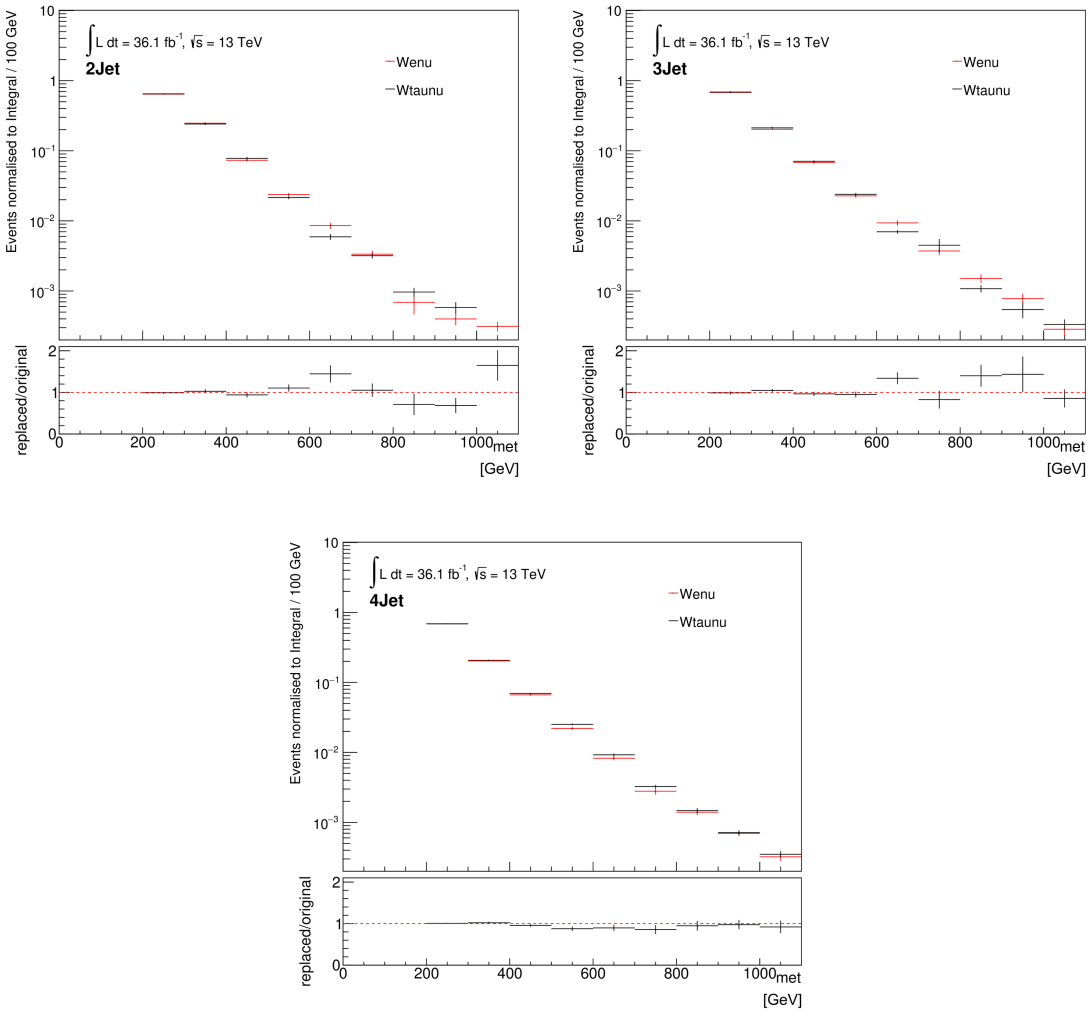

Figure 6.15.: Closure test for the $W \to \tau\nu$ background replacement. The original process $W \to \tau\nu$ in the SRs is compared to the substitute process $W \to e\nu$ in the corresponding CRs where the electron was replaced by a tau jet. The deviations between both processes are used as uncertainty on $W \to \tau\nu$ for the fit in the SRs. The results are shown for the $E_{\mathrm{T}}^{\mathrm{miss}}$ distribution.

A closure test was used here as well to validate the method. The results are shown in figures 6.15 and 6.16.
The closure test for $W \to \tau\nu$ shows some shortcomings at higher values of $E_{\mathrm{T}}^{\mathrm{miss}}$ as well

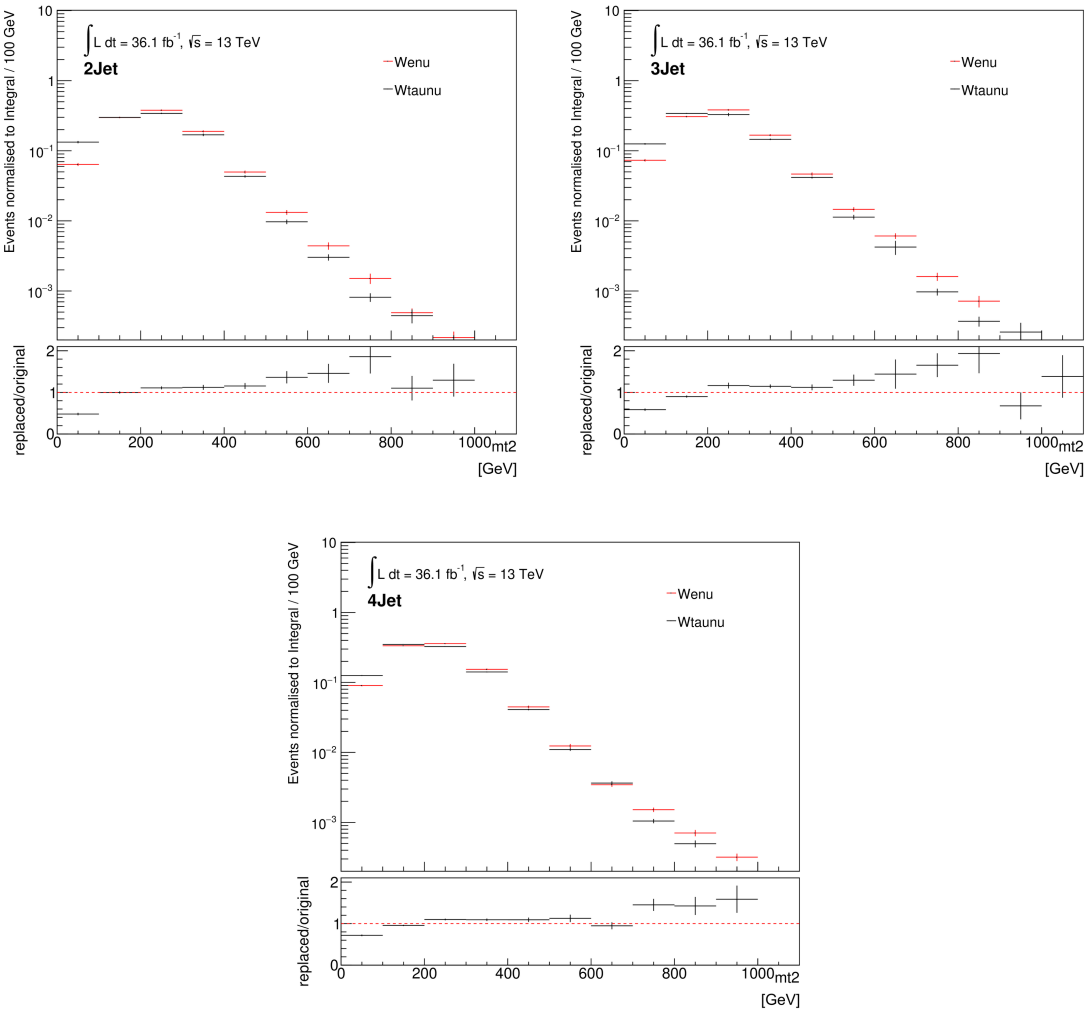

Figure 6.16.: Closure test for the $W \to \tau\nu$ background replacement. The original process $W \to \tau\nu$ in the SRs is compared to the substitute process $W \to e\nu$ in the corresponding CRs where the electron was replaced by a tau jet. The deviations between both processes are used as uncertainty on $W \to \tau\nu$ for the fit in the SRs. The results are shown for the M_{T2} distribution.

as M_{T2}. However, the statistical errors in these bins are quite large. While the ratio plots display a good agreement for lower values of $E_{\mathrm{T}}^{\mathrm{miss}}$ in the 2 jet and 3 jet bins, the 4 jet bin shows an overall accordance. For the M_{T2} distribution, the accordance of replaced and original process is worse, especially for higher values. This might occur due to

differences regarding the angles of the substituted objects, which are not considered in this method. It is necessary to account for these deviations in form of a systematic uncertainty.

The distributions of $E_{\mathrm{T}}^{\mathrm{miss}}$ and M_{T2} in the two CRs for $W \to e\nu$ and $W \to \mu\nu$ are shown in figures 6.17 to 6.20. Hereby, the W processes which were combined into W + jets in the SRs for clarity are now drawn individually.
It can be seen that there are slight deviations from one in the data to background ratio throughout all distributions and regions. Especially in the highest jet multiplicity the MC simulations seem to overestimate the data, while there is a slight MC deficit in the 2 jet bin towards the top end of the distributions.
Since those regions with lower jet multiplicity, which are dominated by W-processes, show a slight data excess, it can be deduced that the fit will try to compensate for it by increasing the normalisation for these backgrounds. In regions with high jet multiplicity, $t\bar{t}$ is the dominant background process. The deficit in data is likely to be compensated by the fit by scaling down $t\bar{t}$ (normalisation factor of < 1).

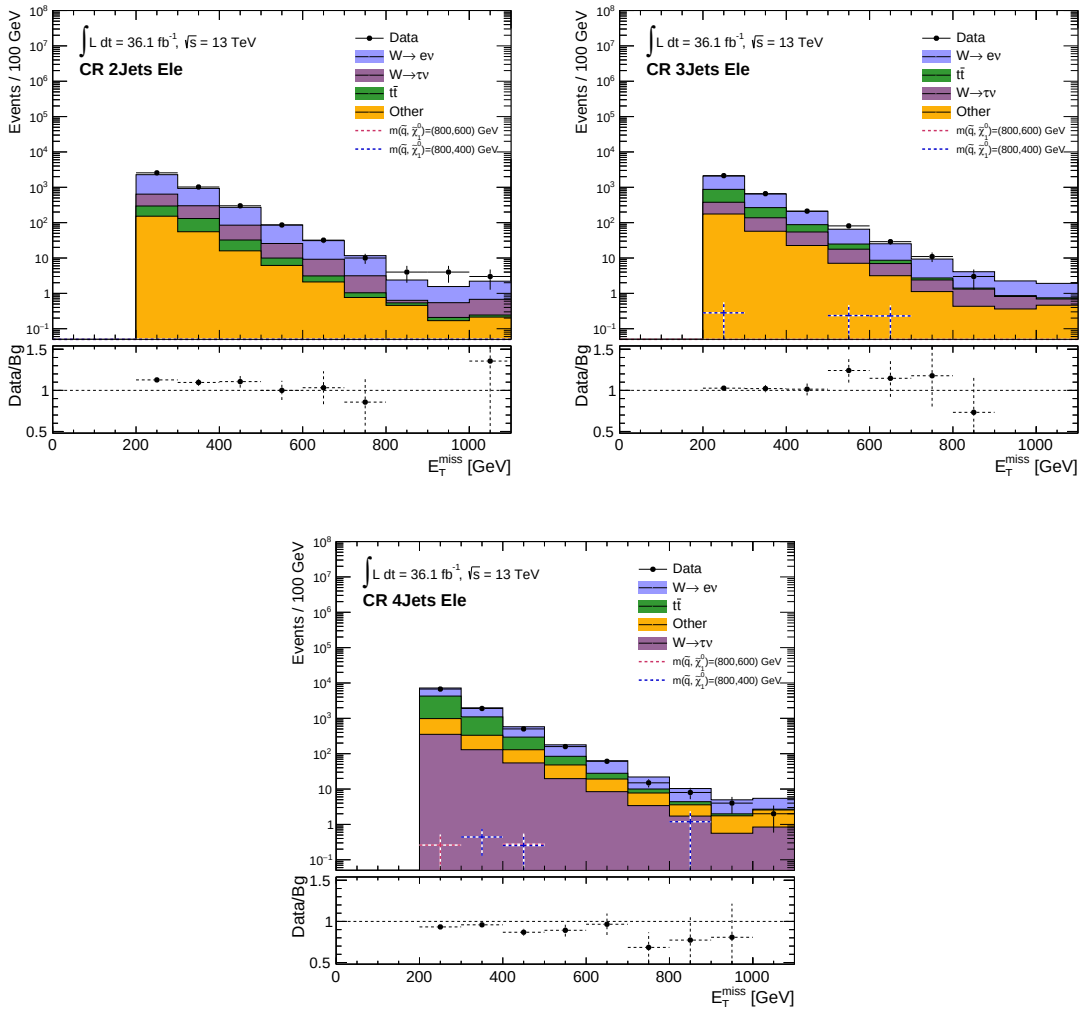

Figure 6.17.: The distributions of $E_{\mathrm{T}}^{\mathrm{miss}}$ in the $W \to e\nu$ CRs. The three jet multiplicity bins selecting events with 2 jets, 3 jets and $\geqslant 4$ jets respectively are shown.

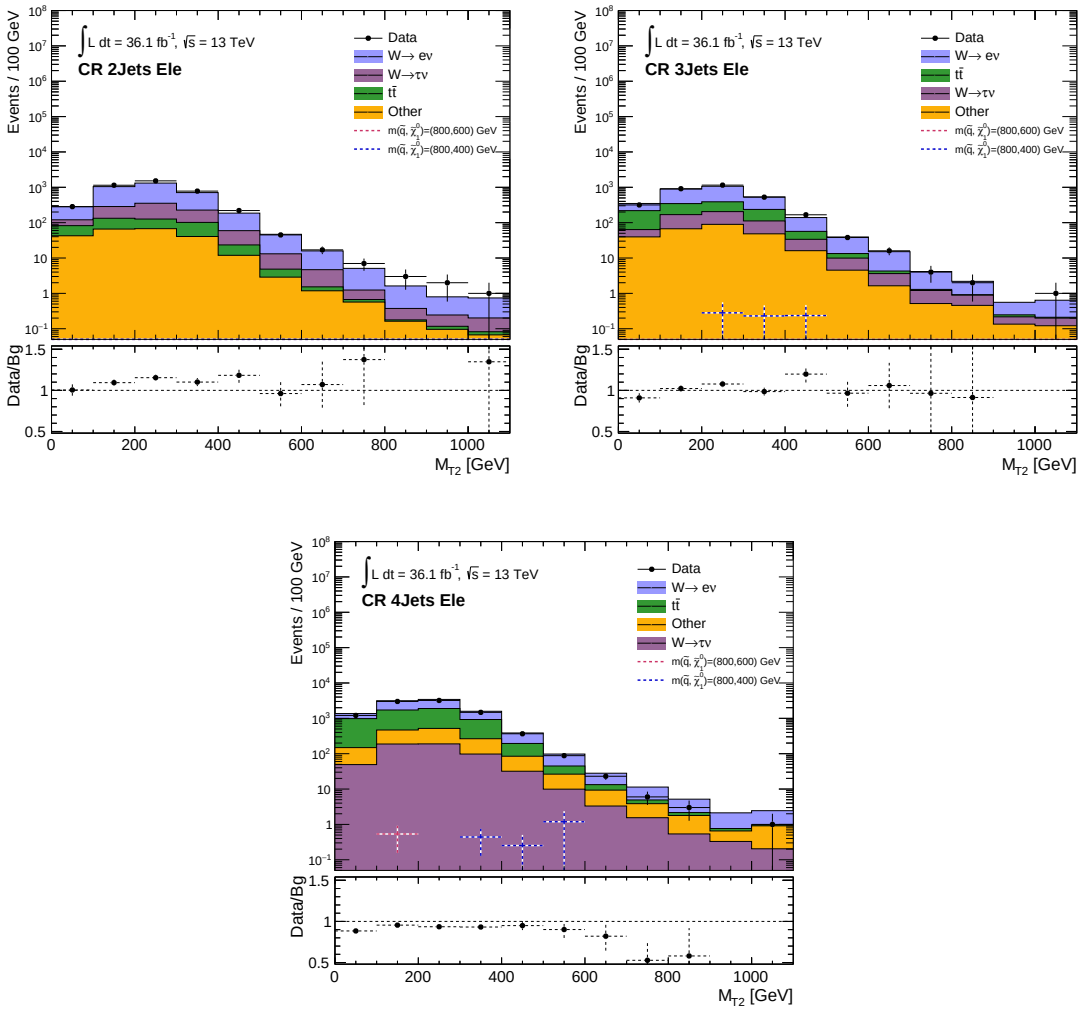

Figure 6.18.: The distributions of M_{T2} in the $W \to e\nu$ CRs. The three jet multiplicity bins selecting events with 2 jets, 3 jets and $\geqslant 4$ jets respectively are shown.

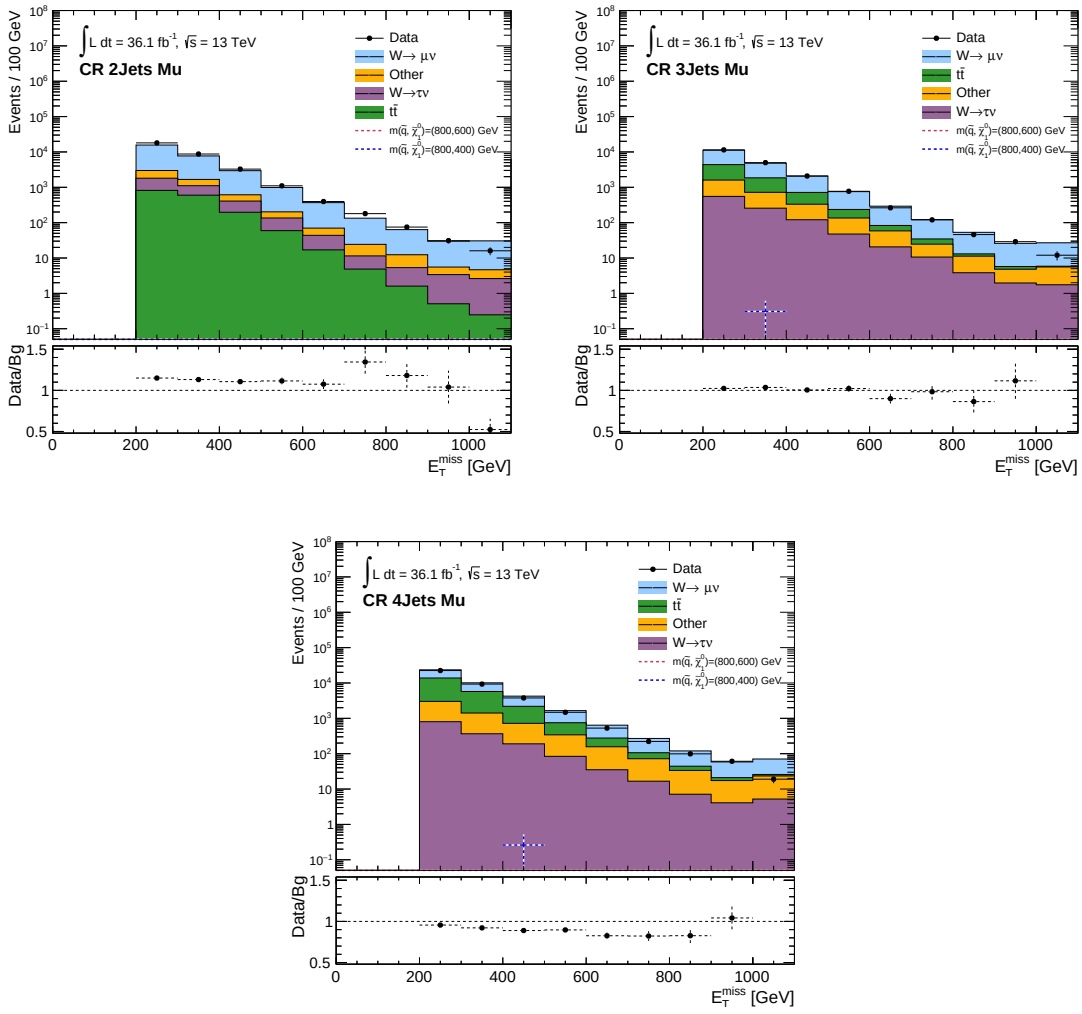

Figure 6.19.: The distributions of $E_{\mathrm{T}}^{\mathrm{miss}}$ in the $W \to \mu\nu$ CRs. The three jet multiplicity bins selecting events with 2 jets, 3 jets and $\geqslant 4$ jets respectively are shown.

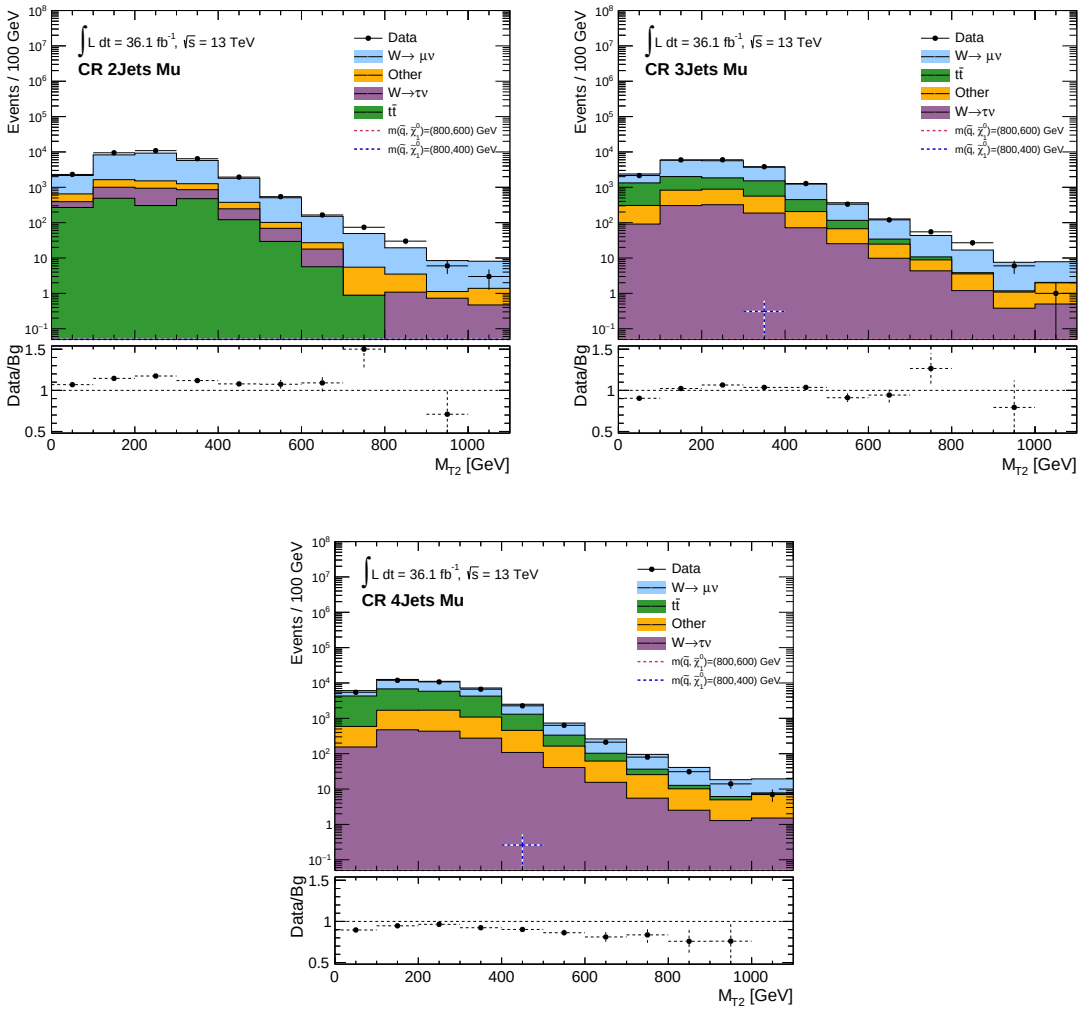

Figure 6.20.: The distributions of M_{T2} in the $W \to \mu\nu$ CRs. The three jet multiplicity bins selecting events with 2 jets, 3 jets and $\geqslant 4$ jets respectively are shown.

6.7. Systematic Uncertainties

Alongside the uncertainties arising from statistical fluctuations, a variety of systematic uncertainties have to be taken into account. On the one hand, these can emerge from experimental sources such as the limited energy resolution of the calorimeter as shown in section 3.2.2 or a faulty object reconstruction as discussed in chapter 4.
On the other hand, they can be connected to theoretical insufficiencies like the modelling of processes in the MC generators, particularly regarding the shapes of their distributions in the observed variables. Both types of uncertainties can affect the sensitivity of the shape fit by blurring the exact shape and making it harder for the fit to make precise estimations.

In the following sections, the main systematics considered in this analysis, as summarised in table 6.8, are described. Their individual and total impact is shown in chapter 7.

6.7.1. Experimental Uncertainties

Jet energy scale and resolution
Since the calculation of $E_{\mathrm{T}}^{\mathrm{miss}}$ strongly depends on the transverse momenta of objects like jets and leptons, being visible in the detector (see section 3.2), their energy scale and resolution are limiting factors on the accuracy of the $E_{\mathrm{T}}^{\mathrm{miss}}$.
A systematic deviation of the measured jet energies (*jet energy scale*, JES) in the hadronic calorimeter leads to a shift in the $E_{\mathrm{T}}^{\mathrm{miss}}$ distribution; a low energy resolution of the jets (*jet energy resolution*, JER) will cause a low $E_{\mathrm{T}}^{\mathrm{miss}}$ resolution. A deviation of the measured jet numbers would result in events being shifted from one N_{jet} region to another, thereby changing the distribution shapes.
The consideration of these uncertainties was done according to the recommendations of the ATLAS Jet and Etmiss combined performance group. They provide estimations for the JES and JER uncertainties in form of grouped nuisance parameters (see section 4.5).

Lepton energy scale and resolution
Although a lepton veto is applied in the SR, leptons are relevant for the selections of the CRs. Therefore, the uncertainties regarding their energy scale and resolution must be considered in the CRs nevertheless. These systematics can arise for example from similar detector shortcomings as the jet energy resolution and scale systematics, but in this case the responsible components are the electromagnetic calorimeter or the muon spectrometer, respectively. Furthermore, the identification and reconstruction of the leptons are subject to uncertainties. The uncertainties of the electron energy resolution, electron energy scale as well as the muon energy scale and identification are applied in the analysis according to the recommendations of the ATLAS electron-gamma group and the ATLAS muon combined performance group similar to the documentation in [120] and [121].

Systematic Type	Systematic Name
Jet energy scale	Jet_EtaIntercalibration_NonClosure_Up/Down
	Jet_GroupedNP_1_Up/Down
	Jet_GroupedNP_2_Up/Down
	Jet_GroupedNP_3_Up/Down
Jet energy resolution	Jet_JER_Single_NP_Up
Missing transverse energy scale	MET_SoftTrk_ScaleUp/Down
Missing transverse energy resolution	MET_SoftTrk_ResoPara
	MET_SoftTrk_ResoPerp
Electrons	EG_Scale_All_Up/Down
	EG_Resolution_All_Up/Down
Muons	Muon_ID_Up/Down
	Muon_Scale_Up/Down
	Muon_MS_Up/Down
	Muon_Sagitta_Resbias_Up/Down
	Muon_Sagitta_Rho_Up/Down
Pile-up	PileupReweighting
Luminosity	LumiError

Table 6.8.: Experimental systematic uncertainties considered in the analysis.

Missing transverse energy scale and resolution
As mentioned above, the calculation of the missing transverse energy strongly depends on the energies and momenta of all other objects in the events, i.e. jets and leptons. Thus, uncertainties of these variables are directly transferred to uncertainties of the resolution and scale of the missing transverse energy. They are calculated using the soft term as explained in section 4.6.

Others
The uncertainties on the pile-up dependence on the average number of interactions μ (see section 3.2) are considered in form of errors on the corresponding re-weighting factors. This compensates for the lack of total pile-up information in the generated MC in comparison to the data as described in [122].

Systematic Type	Systematic Name	applied to sample
shape uncertainty	ShapeSyst	$Z\nu\nu$, all $W + jets$
CKKW	VPt_ckkw_Syst	$Z\nu\nu$, all $W + jets$
resummation	VPt_qsf_Syst	$Z\nu\nu$, all $W + jets$
replacement uncertainty	ClosureSyst	$Z\nu\nu$, $W\tau\nu$
hard scattering	ttbar_hardscatterSyst	$t\bar{t}$
parton shower	ttbar_showerSyst	$t\bar{t}$
radiation	ttbar_RadFlatSyst	$t\bar{t}$
cross section uncertainty	BgXSec	Other (only fixed backgrounds)
	SigXSec	signal

Table 6.9.: Theoretical systematic uncertainties considered in the analysis.

The uncertainty of the combined integrated luminosity of the 2015 and 2016 data sets is 2.1%. It is derived using a method similar to the one described in [123].

6.7.2. Theoretical Uncertainties

Since the available MC generators only consider the first two or three leading orders of perturbation to simulate background and signal processes, incorrect modelling occurs, depending on the respective generator and process. Thus, theoretical uncertainties on the calculated hard scattering process as well as the showering and radiation must be taken into account.
These uncertainties are usually estimated for every background process by comparing a variety of generators and by using different methods for parts of the modelling to extract scale variation uncertainties [17] and PDF uncertainties [18]. The analysis presented here used a different, more conservative approach: instead of applying these individual theoretical uncertainties, a systematic uncertainty on the distribution shapes was extracted from the comparison of signal and background distributions in the SRs.

[17] These arise from variation of renormalisation and factorisation scales in the simulation. Other sources are the resummation and matching scales, varying parameters of the parton shower.
[18] These arise from varying the used PDF set.

Shape Systematic

The shape systematic is created to simulate a worst case scenario. It has the same size and form as the shape difference between signal and background distributions, thus blurring the distributions at exactly those positions where the shape differences occur and the fit extracts its sensitivity from. Figure 6.21 exemplarily shows the distributions for $E_{\mathrm{T}}^{\mathrm{miss}}$ and M_{T2} in the SR with 2 jets[19]. For a comparison of signal and total background shapes, the ratio $\frac{\text{signal+background}}{\text{background}}$ is plotted in each SR, which is also used as the upwards shape uncertainty (see middle row of figure 6.21). The downward uncertainty was generated by inverting the bin contents of these ratios (bottom row of figure 6.21). This shape uncertainty is then applied to $Z \to \nu\nu$, $W \to \mu\nu$, $W \to \tau\nu$ and $W \to e\nu$ in all SRs and CRs [20], sufficiently estimating the theoretical uncertainties for these background processes.

Since every signal shows a different shape, the systematic was extracted for all signals separately, i.e. each signal point received its individual shape uncertainty.

Closure Systematic

Another uncertainty that must be taken into account arises from the inaccuracy of the replacement method. The closure tests presented in sections 6.6.1 and 6.6.2 show slight deviations between $Z \to \nu\nu$ and replaced $W \to \mu\nu$ on the one hand and larger deviations between $W \to \tau\nu$ and replaced $W \to e\nu$ on the other hand. These deviations are illustrated as ratios of $\frac{\text{replaced process}}{\text{original process}}$ below the comparisons in figures 6.11, 6.12, 6.15 and 6.16.

The replacement method for $Z \to \nu\nu$ shows deviations of the order of 5%, therefore a flat symmetric uncertainty of the same size was applied to $Z \to \nu\nu$ in the SRs. The deviations from the replacement method for $W \to \tau\nu$ are more diverse, which is why the ratios are used as an upward uncertainty and the downward uncertainty is generated by inverting the bin contents. These are then applied to $W \to \tau\nu$ in the SRs (exemplarily shown for $E_{\mathrm{T}}^{\mathrm{miss}}$ in figure B.1 of appendix B).

$t\bar{t}$

The theoretical uncertainties on the $t\bar{t}$ background were applied according to the recommendations given by the ATLAS background forum and top groups [124, 125].

For the uncertainty on the modelling of the *hard scattering* process, the nominal $t\bar{t}$ MC sample (produced by Powheg with Pythia6) should be compared to another sample using a different event generator, e.g. aMcAtNLO with Pythia6. Since this suffers from poor statistics, the comparison was made using samples produced by Powheg with Herwig on the one hand and aMcAtNLO with Herwig on the other hand instead. Both use a different generator for the parton shower (Herwig instead of Pythia), which makes the

[19] The corresponding plots in the SRs with 3 and 4 jets are shown in figures C.1 and C.2 of appendix C.
[20] The $t\bar{t}$ background was left out, since there are special uncertainties applied to it.

uncertainties independent from the hard scattering generator.
For the *parton shower* uncertainty, the nominal sample was directly compared to the sample produced by Powheg with Herwig.
These two comparisons are illustrated in figure 6.22. It shows the distributions of $E_{\mathrm{T}}^{\mathrm{miss}}$ and M_{T2} in the SRs. The ratio $\frac{\text{aMcAtNLO+Herwig}}{\text{Powheg+Herwig}}$, shown in light green, is used to estimate a hard scattering uncertainty. The comparison of Powheg+Herwig and the nominal sample (Powheg+Pythia) is illustrated in red and used to estimate the parton shower uncertainty.

Since both samples with varied generators suffer from poor statistics, which becomes especially severe in the tail region, the binning was adjusted accordingly (one wider bin in the tail region). The generator comparison was also performed in the CRs and the results were compared to those from the SRs. Since both results are sufficiently similar, the same uncertainty was applied in the CRs as in the corresponding SRs. The generator comparisons in the electron and muon CRs are shown in E.1 and E.2 of appendix E.

For the estimation of the *radiation* uncertainty, two samples are used which were produced by the same generators as the nominal sample, but using a different tuning [21]. Since both samples are only available on truth level, a direct comparison to the nominal would not be correct. Instead, they were compared to each other and the variation was determined as $\frac{\text{radHigh-radLow}}{\text{radHigh+radLow}}$.
Figure 6.23 shows the comparison of the radiation samples in the SRs for $E_{\mathrm{T}}^{\mathrm{miss}}$ and M_{T2}. The same variable binning was used here due to low statistics in the tail regions. The corresponding comparisons in the electron and muon CRs are shown in E.3 and E.4 of appendix E.
Since the comparison shows different results in all regions (also if SRs and CRs are compared), the ratios were used to extract an individual uncertainty for each region.

Other

To take into account the uncertainty emerging from the matching scale used in the generation of the W and Z processes, the so called *CKKW matching* systematic is considered for them, following the recommendations of the ATLAS physics modelling group [126]. The nominal value (20 GeV), deciding which particles are generated in the matrix element and which in the parton shower, is varied from 15 GeV to 30 GeV. Additionally, a variation of the resummation scale is considered for these processes which is decisive for the parton showers and is varied from 0.5 times to 2 times its value. Both uncertainties have only small contributions, as figure D.1 in appendix D shows.
Uncertainties on the modelling of other background processes were neglected, since table

[21] The parameters affecting the radiation modelling were varied up and down, thus the samples are indicated with radiation high and low

6.4 shows that they have a small enough contribution in the SRs [22].

Cross section
The uncertainty of the cross section was assumed to be 30% for background and 10% for signal processes. These uncertainties were only applied to the combined Other background and the signals respectively. This conservative estimation should compensate for the fact that no other theoretical uncertainties were considered for these processes.

[22] The largest of these background processes arises from diboson events. It is known to be very well modelled and to have small uncertainties

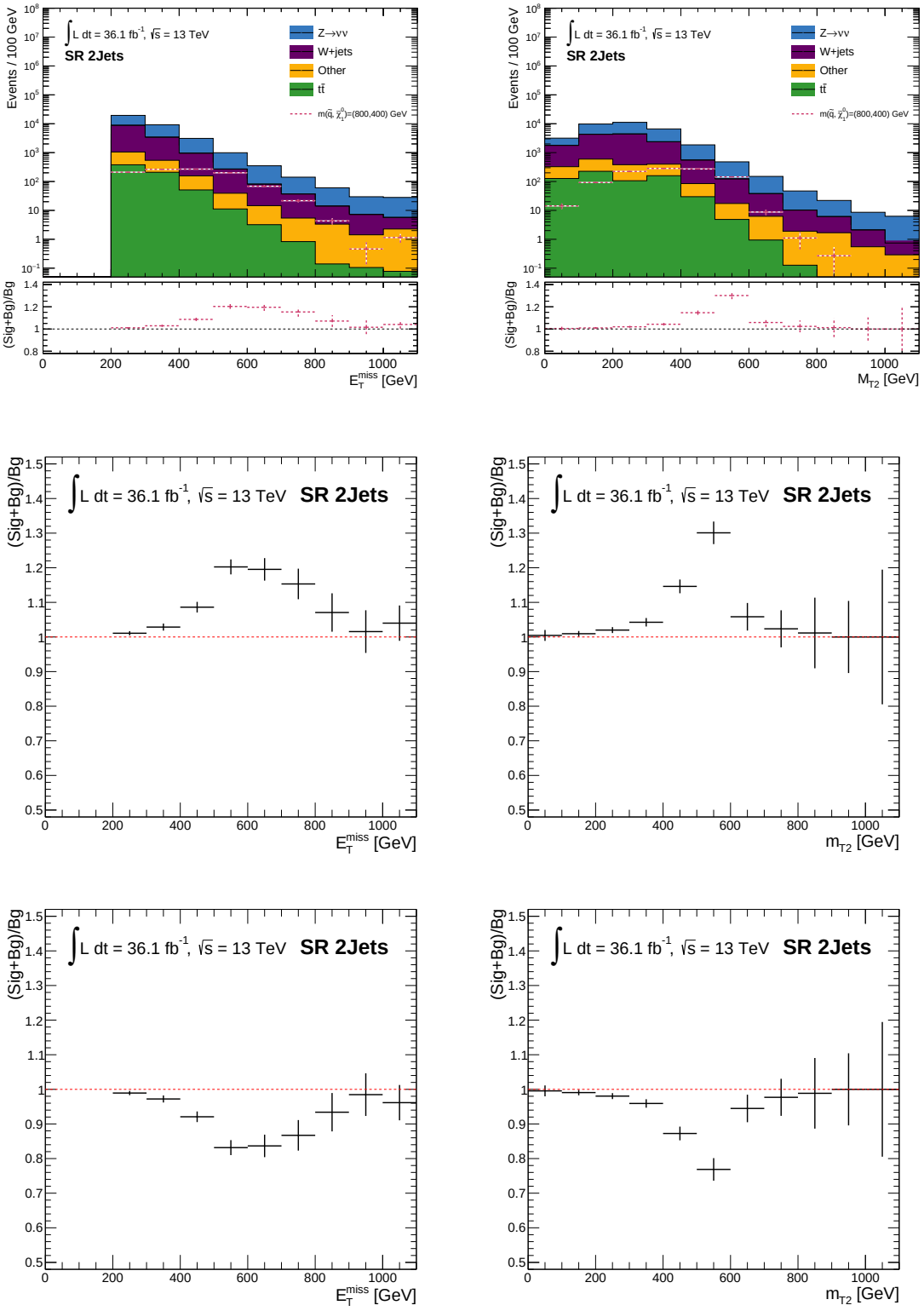

Figure 6.21.: Shape systematics extracted from the SR distributions (top row). The upward uncertainty is gained from the ratio of $\frac{\text{signal+background}}{\text{background}}$ (middle row), the downward uncertainty is produced by inverting the bin contents of the upward uncertainty (bottom row).

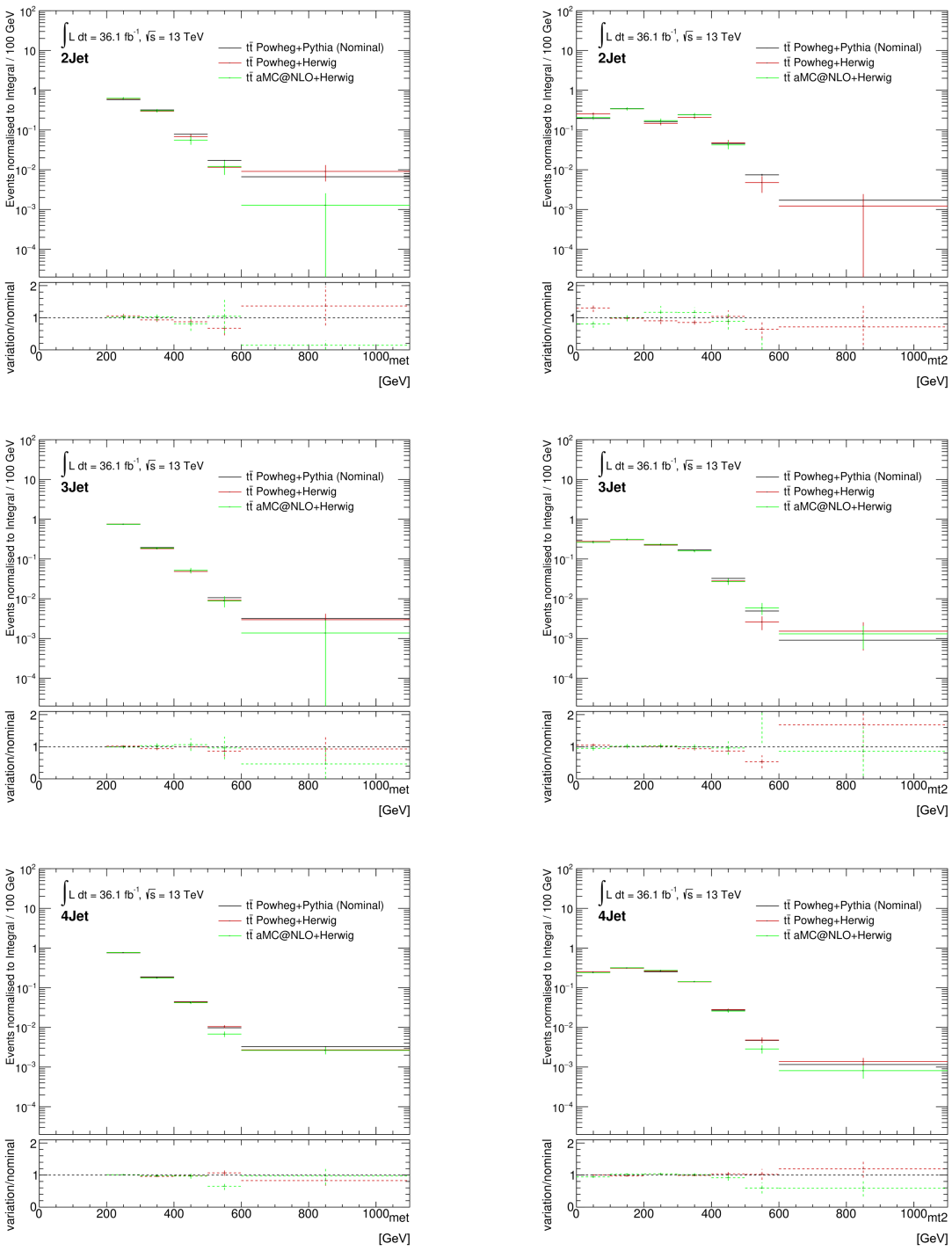

Figure 6.22.: Comparison of different event generators and parton shower generators for $E_{\mathrm{T}}^{\mathrm{miss}}$ (left column) and M_{T2} (right column) in the SRs to estimate the theoretical uncertainties for the nominal $t\bar{t}$ sample.

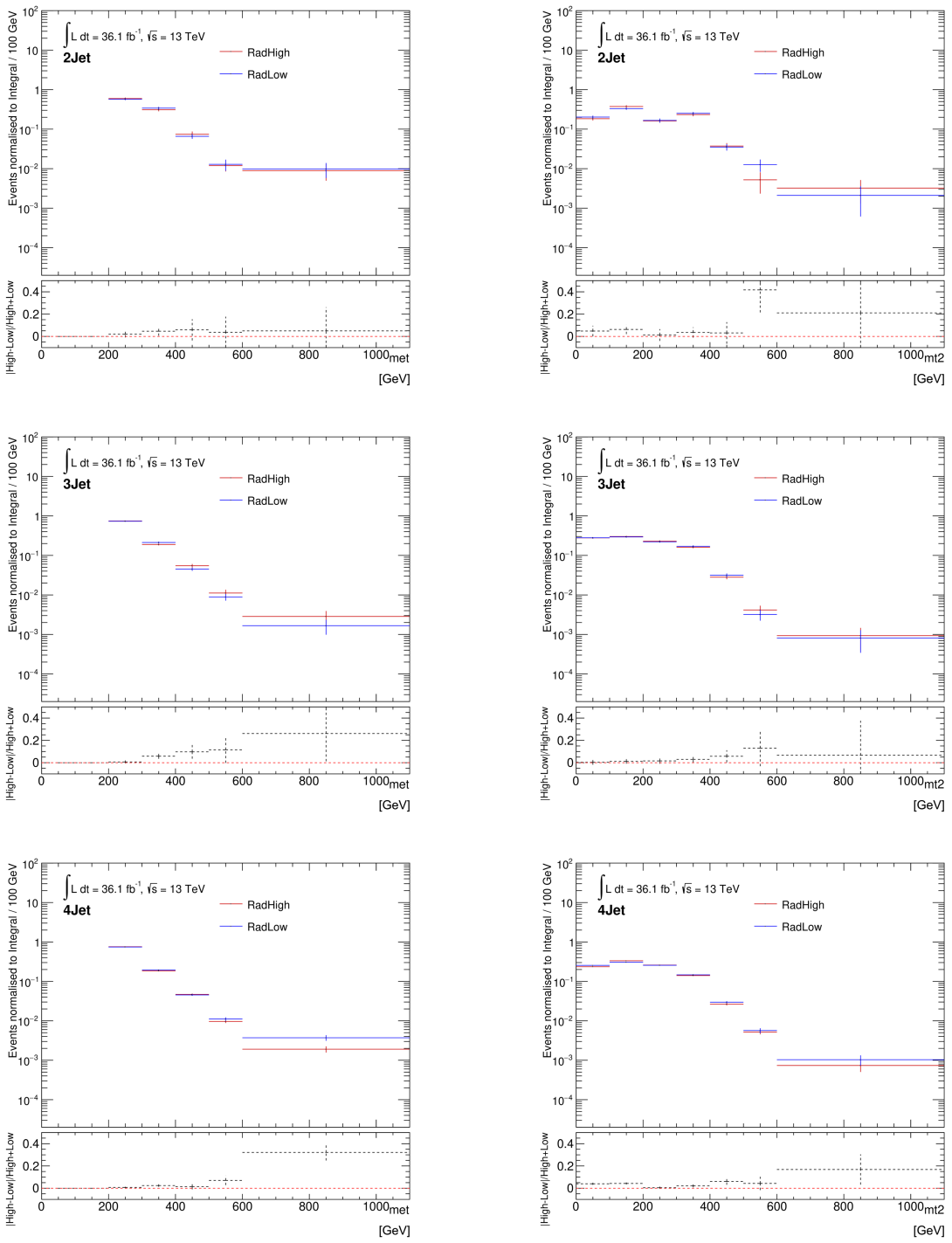

Figure 6.23.: Comparison of different tunings in the Powheg+Pythia samples for $E_{\mathrm{T}}^{\mathrm{miss}}$ (left column) and M_{T2} (right column) in the SRs to estimate the radiation uncertainties for the nominal $t\bar{t}$ sample.

Chapter 7.

Fit Method and Results

As presented before, the analysis presented in this thesis uses a shape fit based on the maximum likelihood method and aims for a high sensitivity using a benchmark signal model. To determine whether the measured data can be described by the simulated background processes alone (and a signal process can be significantly excluded) or whether there is significant evidence of a signal contribution in the data, the previously defined signal region and control region distributions are fitted simultaneously. This fit is performed using the HistFitter tool [127][1], which is based on the statistics packages RooStats [128] and HistFactory [129].
In this chapter, the statistical principles of the fit method used and the different fit configurations are described (see sections 7.1 and 7.2) based on [130] and [131]. The results obtained for the respective fit configuration are presented in section 7.3 and their interpretation and comparison to the results of the 0-lepton group is given in section 7.4.

7.1. Statistical Principles

The fit is performed simultaneously in all three N_{jet} bins of the CRs and the SR under consideration of statistic and systematic uncertainties. Thereby the best agreement between the MC expectations for the SM backgrounds and the signal model on the one hand and the observed data on the other hand is determined. This is done by maximising the likelihood function:

$$L(n, \theta^0 | \mu_{\text{sig}}, \mu_{\text{bkg}}, \theta) = \prod_{i \in SR} P_i(n_i | \lambda_i(\mu_{\text{sig}}, \mu_{\text{bkg}}, \theta)) \times \prod_{i \in CR} P_i(n_i | \lambda_i(\mu_{\text{sig}}, \mu_{\text{bkg}}, \theta)) \times P_{\text{syst}}(\theta^0, \theta) \tag{7.1}$$

[1] The HistFitter version v0.60.0 was used.

In this case, the likelihood function consists of three terms: the first denotes the Poisson probabilities in the SRs for the observation of n_i events, given the expectation of λ_i events, using the assumption of a signal strength μ_{sig} and the background normalisation factors μ_{bkg}. The second term represents the analogous Poisson probabilities in the CRs. Hereby, θ parametrises the Poisson distributed statistic uncertainties in form of nuisance parameters (subsequently indicated with γ).
The third term takes into account the systematic uncertainties in form of Gaussian probabilities. The nuisance parameters θ denote the systematic uncertainties (subsequently also indicated with α). The fit is allowed to vary θ around a given central value θ^0, this is referred to as *pulling*. In cases of overestimated systematic uncertainties, the fit is able to reduce them, which is called *profiling*.

The results of the maximum likelihood fit are further used to perform a hypothesis test. In case of an exclusion fit, the CLs method is applied. Thereby, the two hypotheses *background-only* and *signal+background* are tested, meaning the data can either be described by the expected SM background alone or a signal contribution can be identified in the data. To test a hypothesised μ, the profile likelihood ratio is used, defined as:

$$q_{\mu_{\text{sig}}} = -2log(\frac{L(\mu_{\text{sig}}, \hat{\hat{\theta}})}{L(\hat{\mu}_{\text{sig}}, \hat{\theta})}) \tag{7.2}$$

Hereby, $\hat{\mu}_{\text{sig}}$ and $\hat{\theta}$ maximise the likelihood function globally, while $\hat{\hat{\theta}}$ leads to maximisation for the given signal strength μ_{sig}. This ratio is used to calculate the corresponding p-value of the test, which quantifies the agreement between observed data and the assumed hypothesis. For the background-only hypothesis, μ_{sig} is set to 0. For the background-only and the signal+background hypotheses, the p-value is given by:

$$1 - p_b = \int_{q_{\text{obs}}}^{\infty} f(q|b)dq, \qquad p_{s+b} = \int_{q_{\text{obs}}}^{\infty} f(q|s+b)dq, \tag{7.3}$$

respectively (see figure 7.1).
The CLs value is then calculated from the ratio of both p-values:

$$CL_s = \frac{p_{s+b}}{1 - p_b} \tag{7.4}$$

By definition, a CLs value of < 0.05 (or 95% confidence level) is necessary to exclude a signal.

7.2. HistFitter Configuration

As briefly mentioned in section 6.2, there are three different types of fit configurations available in HistFitter: the background only, the exclusion and the discovery fit set-up,

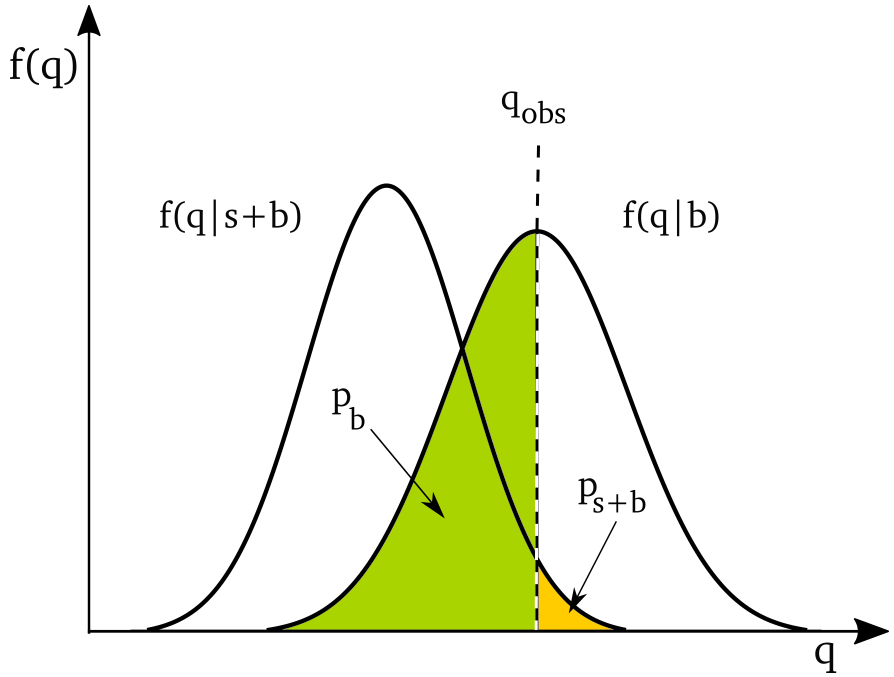

Figure 7.1.: Schematic illustration of the probability density functions and p-values for the signal+background and the background only hypotheses.

each serving a different purpose.

Background only fit
A background only fit solely considers the CRs to determine the expectation of the backgrounds by fitting them to data[2] and calculating their respective normalisation factors. Since the background only hypothesis is tested, the signal scale factor is set to 0. The background only fit is therefore independent from any signal model. The background only fit was performed under consideration of all systematic uncertainties.
The expected and fitted[3] background events in the CRs are presented in section 7.3. The total numbers of fitted background events are then applied in the SRs to test if there is an excess observable. Depending on the outcome, an exclusion or discovery test is performed.

Exclusion fit
The exclusion fit considers CRs and SRs simultaneously. It fits all backgrounds and the signal distribution to data in the CRs and SRs. The fit then determines the signal

[2]The observed data events are unblinded in the CR since the signal expectation is 0. Thus, there is no danger of bias.
[3]*Fitted* refers to the up-scaled or down-scaled distributions by their respective normalisation factors.

strength of a given signal (thus is model-dependent) and the background normalisation factors under consideration of all systematic uncertainties.
A hypothesis test is then performed to calculate a p-value for each given signal model based on the CLs method and (if applied to several signal points in the mass plane) an exclusion limit can be produced for the interpretation of the fit results.

Discovery fit
The discovery fit also considers CRs and SRs simultaneously, but can only be conducted with a single bin in each region. Just like before, the signal expectation in the CRs is neglected, but in contrast to the exclusion fit, the discovery fit does not consider a specific signal model in the SRs. It is model-independent and uses a dummy with the total signal expectation as a free fit parameter. A hypothesis test will determine the discovery sensitivity if data excess is observed in the SRs. Since the analysis is optimised to be shape sensitive, it is not expected to demonstrate sensitivity in this fit configuration. The assumption of zero signal contribution in the CRs is conservative, since a possible signal contamination would lead to an overestimated background expectation in the SRs.

For all fit set-ups, the $Z \to \nu\nu$, $W \to \tau\nu$ and $t\bar{t}$ backgrounds were fitted individually with separate normalisation factors $\mu_{Z\nu\nu}$, $\mu_{W\tau\nu}$, $\mu_{t\bar{t}}$. These are the same in all jet multiplicity regions, since it is assumed that the modelling of jet multiplicities for each process is done correctly by the MC generators. All other background processes in the SRs were combined into *Other* and given a fixed value.
$W \to e\nu$ receives the same normalisation factor as $W \to \tau\nu$. This is necessary, since the $W \to e\nu$ events, selected in the dedicated CR (indicated as CRele), have undergone the replacement method and are now used to extract a data driven background estimation for $W \to \tau\nu$. Thus, they are treated as if they were the same process.
The same holds true for $W \to \mu\nu$ and $Z \to \nu\nu$, which also share the same normalisation factor. The data driven background estimation of $W \to \mu\nu$, extracted from the corresponding CR (indicated as CRmu), is then applied on $Z \to \nu\nu$ in the SR. In the CRs, the dominating $W \to e\nu$ and $W \to \mu\nu$ backgrounds were drawn separately and only the remaining backgrounds were combined in Other.

7.3. Fit Results

7.3.1. Background Only Fit

The results of the background only fit setup are presented in the following. First, the fit results of the $E_{\mathrm{T}}^{\mathrm{miss}}$ fit are shown, followed by the results obtained with the M_{T2} variable.

$E_{\mathrm{T}}^{\mathrm{miss}}$

The normalisation factors of the three main backgrounds were fitted to:

$$\begin{aligned} \mu_{Z\nu\nu}\ (\equiv \mu_{W\mu\nu}) &= 1.2285 \pm 0.0193 \\ \mu_{W\tau\nu}\ (\equiv \mu_{We\nu}) &= 1.2157 \pm 0.0244 \\ \mu_{t\bar{t}} &= 1.0377 \pm 0.0506 \end{aligned}$$

The $E_{\mathrm{T}}^{\mathrm{miss}}$ distributions in all SRs and CRs before and after the fit are shown in figures 7.2, 7.3 and 7.4, where the ratio plots illustrate the total uncertainty (grey shaded band). In the SRs, a data excess can be observed in the 800 GeV-900 GeV bin of the 3 jet region which is analysed further in the following. In all CRs, the after-fit ratios show a good over-all agreement between data and the MC expectations, except for a few bins with slight data excess. This indicates that they can be sufficiently normalised by the fit, although only one normalisation factor is determined for each fitted process. As expected from the data excess in the CRs with lower jet multiplicity, the fit increases those backgrounds, which are dominant in these regions, by 20% to compensate for the MC deficit. Additionally, the systematic uncertainties are profiled by the fit, which can be observed as a reduction of the error band in all regions, especially in the 4 jet region. Figure 7.5 gives an overview of the final values of all normalisation factors and the pulled and profiled systematic uncertainties after the fit, showing the strength of the pulling (deviation from the nominal value) in units of σ.
Tables F.1, F.2 and F.3 in appendix F show the number of expected events from the MC prediction, the number of fitted events and the observed events in data for each process in each bin[4] for the SRs with 2 jets, 3 jets and 4 or more jets, respectively. Tables F.4, F.5 and F.6 show the number of expected, fitted and observed events for the electron CRs. The corresponding values for the muon CRs are presented by tables F.7, F.8 and F.9.
The systematic uncertainties were applied as explained in section 6.7, except for the shape uncertainty which is linked to the usage of a signal model. Tables G.1 to G.9 in appendix G show the after-fit uncertainties for each process in each SR and CR for the $E_{\mathrm{T}}^{\mathrm{miss}}$ distributions. Since some of them are correlated, the total uncertainty is not necessarily the sum of the squares. The correlations are shown in figure H.1 in appendix H.

M_{T2}

In the analogous fit, using the M_{T2} distributions, the normalisation factors of the three main backgrounds were determined as:

[4] Bins 0 and 1 are not shown, since they are empty for the $E_{\mathrm{T}}^{\mathrm{miss}}$ distribution.

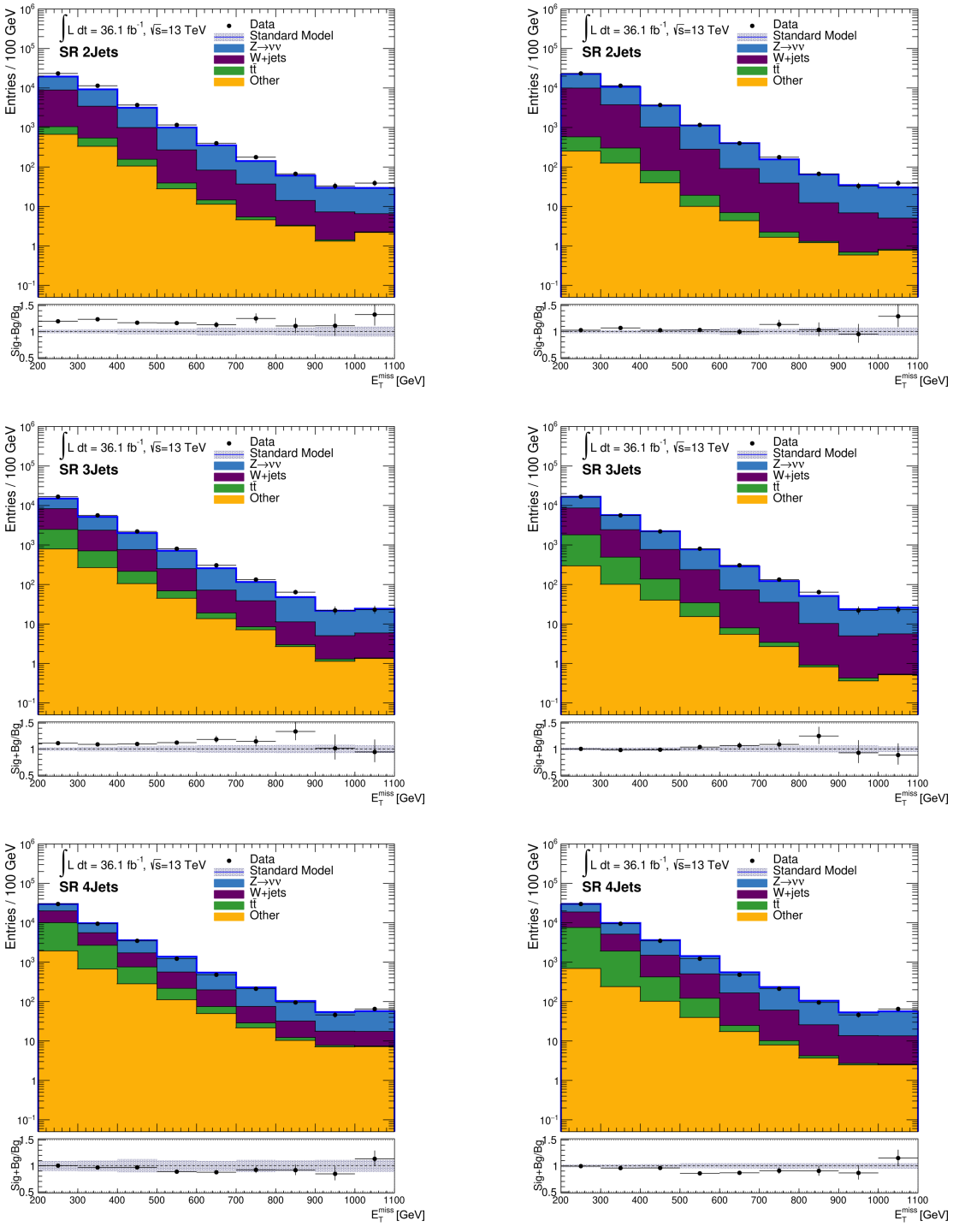

Figure 7.2.: Comparison of the $E_{\mathrm{T}}^{\mathrm{miss}}$ distributions before (left) and after fit (right) for the 2jet, 3jet and $\geqslant$ 4jet SRs.

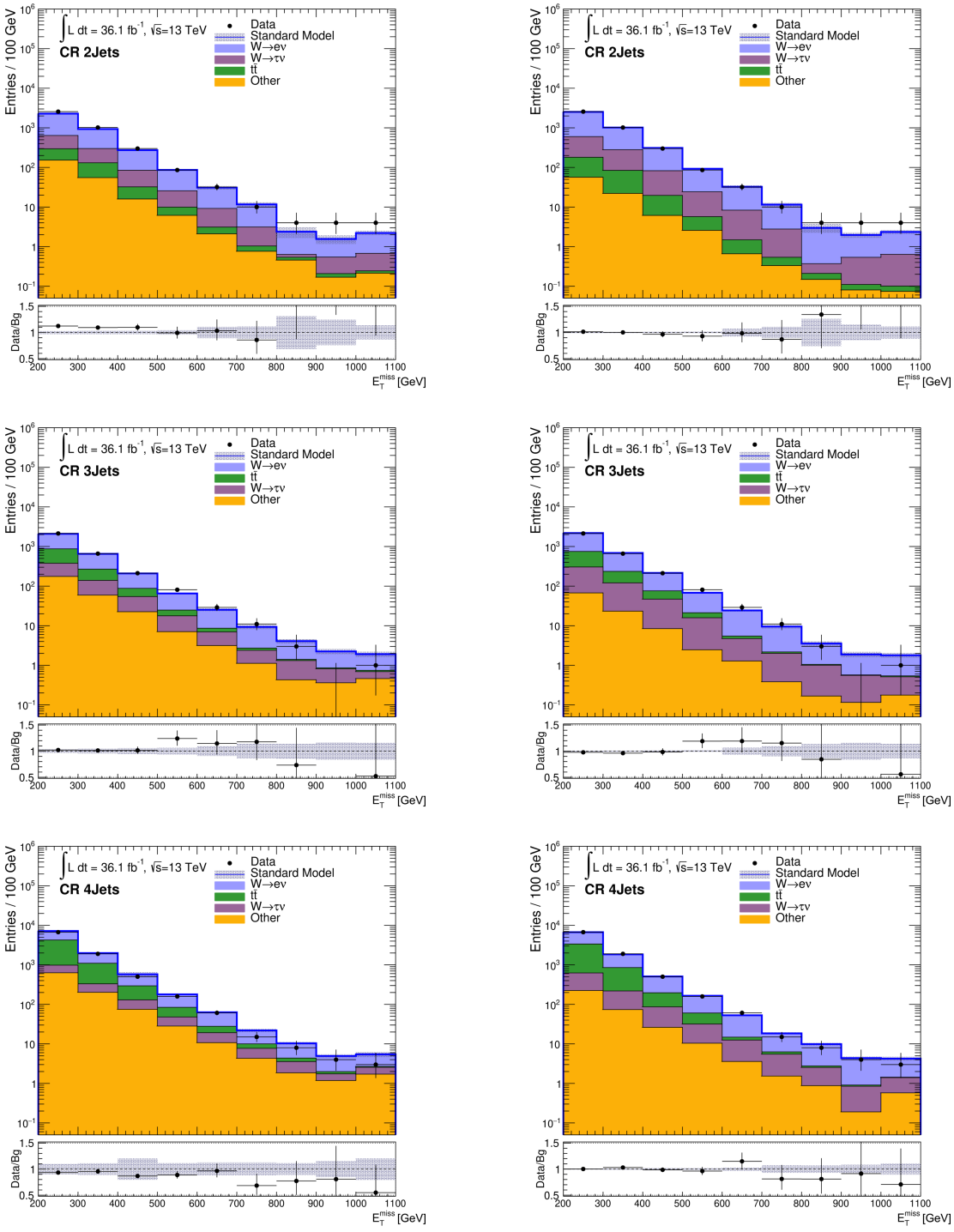

Figure 7.3.: Comparison of the $E_{\mathrm{T}}^{\mathrm{miss}}$ distributions before (left) and after fit (right) for the 2jet, 3jet and $\geqslant$ 4jet electron CRs.

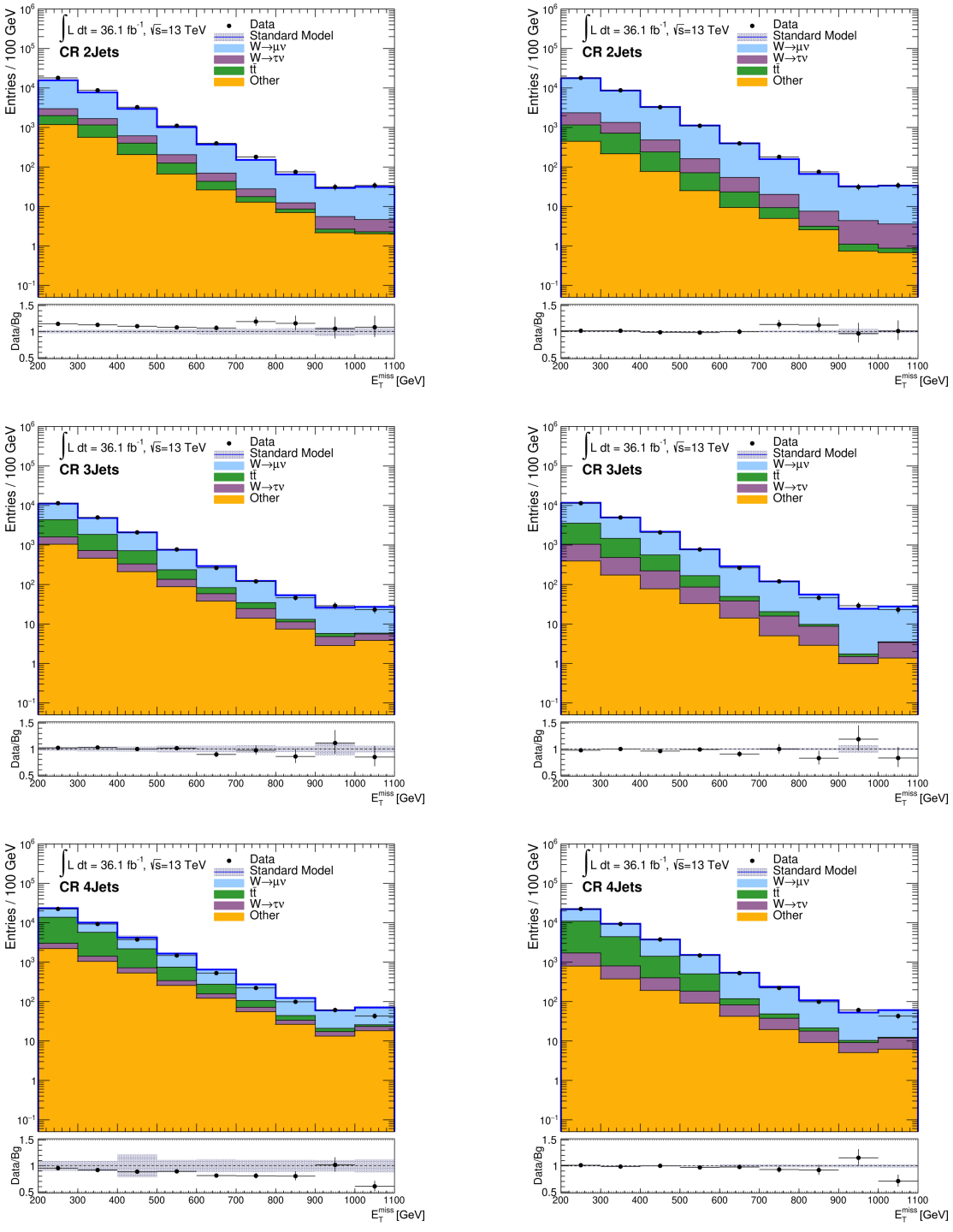

Figure 7.4.: Comparison of the $E_{\mathrm{T}}^{\mathrm{miss}}$ distributions before (left) and after fit (right) for the 2jet, 3jet and $\geqslant$ 4jet muon CRs.

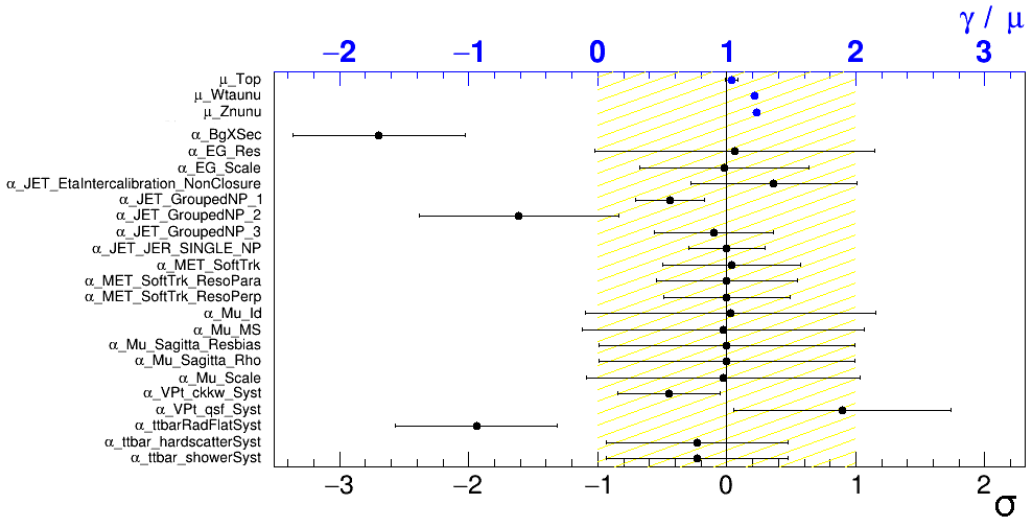

Figure 7.5.: Overview of the final fit parameters after the background only fit in $E_{\mathrm{T}}^{\mathrm{miss}}$. The normalisation factors are shown on top, below the deviation from the nominal values of the systematic uncertainties can be seen (in units of σ) as they were pulled by the fit.

$$\mu_{Z\nu\nu}\ (\equiv \mu_{W\mu\nu}) = 1.2050 \pm 0.0189$$
$$\mu_{W\tau\nu}\ (\equiv \mu_{We\nu}) = 1.1986 \pm 0.0249$$
$$\mu_{t\bar{t}} = 0.8712 \pm 0.0484$$

The M_{T2} distributions in all SRs and CRs before and after fit are shown in figures 7.6, 7.7 and 7.8, where the ratio plots illustrate the total uncertainty (grey shaded band). In the SRs, a slight data excess in the 700 GeV-800 GeV and 800 GeV-900 GeV bins of the 2 jet region can be observed, and also in the CRs some bins feature as slight data excess. They are investigated further in the following.
In this case, the effect observed previously with $E_{\mathrm{T}}^{\mathrm{miss}}$ is even stronger: the fit reduces the $t\bar{t}$ background by 13% while increasing the others by 20%. The reasons are the same: the MC deficit in the 2 jet (and partly the 3 jet) regions is compensated by enlarging $W \to e\nu$ and $W \to \tau\nu$ (the dominant backgrounds in these regions). The MC excess in the 4 jet regions is eliminated by reducing the strong $t\bar{t}$ background, in order to achieve a good agreement with the observed data. In comparison to the results of the $E_{\mathrm{T}}^{\mathrm{miss}}$ fit, it can be observed that the normalisation factor for $t\bar{t}$ is clearly different, which can be explained by the shortcoming of the MC modelling of this process. The samples available for the analysis showed deficiencies especially in high $E_{\mathrm{T}}^{\mathrm{miss}}$ and p_{T} regions which can lead to

severe consequences if the fit compensates this by varying the nuisance parameters. The systematic uncertainties are profiled by the fit which can be observed as a reduced error band in all regions. Figure 7.9 shows the corresponding final values of all normalisation factors and systematic uncertainties after the fit.
Tables F.13, F.14 and F.15 in appendix F show the number of expected events from the MC prediction, the number of fitted events and the observed events in data for each process in each bin for the electron CRs with 2 jets, 3 jets and 4 or more jets, respectively. The corresponding values for the muon CRs are presented by tables F.16, F.17 and F.18 The systematic uncertainties were applied as explained in 6.7, except for the shape uncertainty which is linked to the usage of a signal model. Tables G.13 to G.18 in appendix G show the corresponding after-fit uncertainties for the M_{T2} fit. The correlations of the uncertainties are shown in figure H.2 in appendix H.

Comparison

In both variables a data excess can be observed in the 700 GeV - 800 GeV and 800 GeV - 900 GeV bins of the muon CR (see figures 7.4 and 7.8) as well as in the 800 GeV - 900 GeV bin of the SR (see figure 7.2). It should be noted that these regions are designed to be orthogonal and are thus independent from each other. Since the considered squark signals do not lead to leptons in the final state (and are therefore negligible in the CRs, as shown in section 6.6, other signal models could be tested.
One possibility could be leptoquarks (LQ), which are expected to decay into quark-lepton pairs (see section 2.2), thus possibly leading to a final state with jets, missing energy (in case of a neutrino) and one lepton (for example a muon). To investigate whether such LQ signals could match the data excesses in the muon CRs, distributions like the invariant mass of the final state particles (different combinations of jets and leptons) can be used. Figure 7.10 shows two examples, the transverse mass of the jet (m_T^j) and the invariant mass of the jet and the muon (m_{lj}), both in the muon CR[5]. If such a leptoquark signal was present, a clear data excess at the same position could be observed in both. A scan through all possible combinations of final state particles and the examination of different variables (m_{jll}, m_{jjll}, $m_T^{jl\nu}$, $m_T^{jjl\nu}$,...) did not show consistent excesses, meaning no excesses around the same mass point in corresponding plots like the two shown in figure 7.10. As a result, no significant indication to the presence of leptoquark signals could be found.

The data driven normalisation factors from both background only fits were then used in the respective SRs to obtain improved background estimations for the fitted processes.

[5]For the calculation, the pairs with the smallest mass difference were chosen.

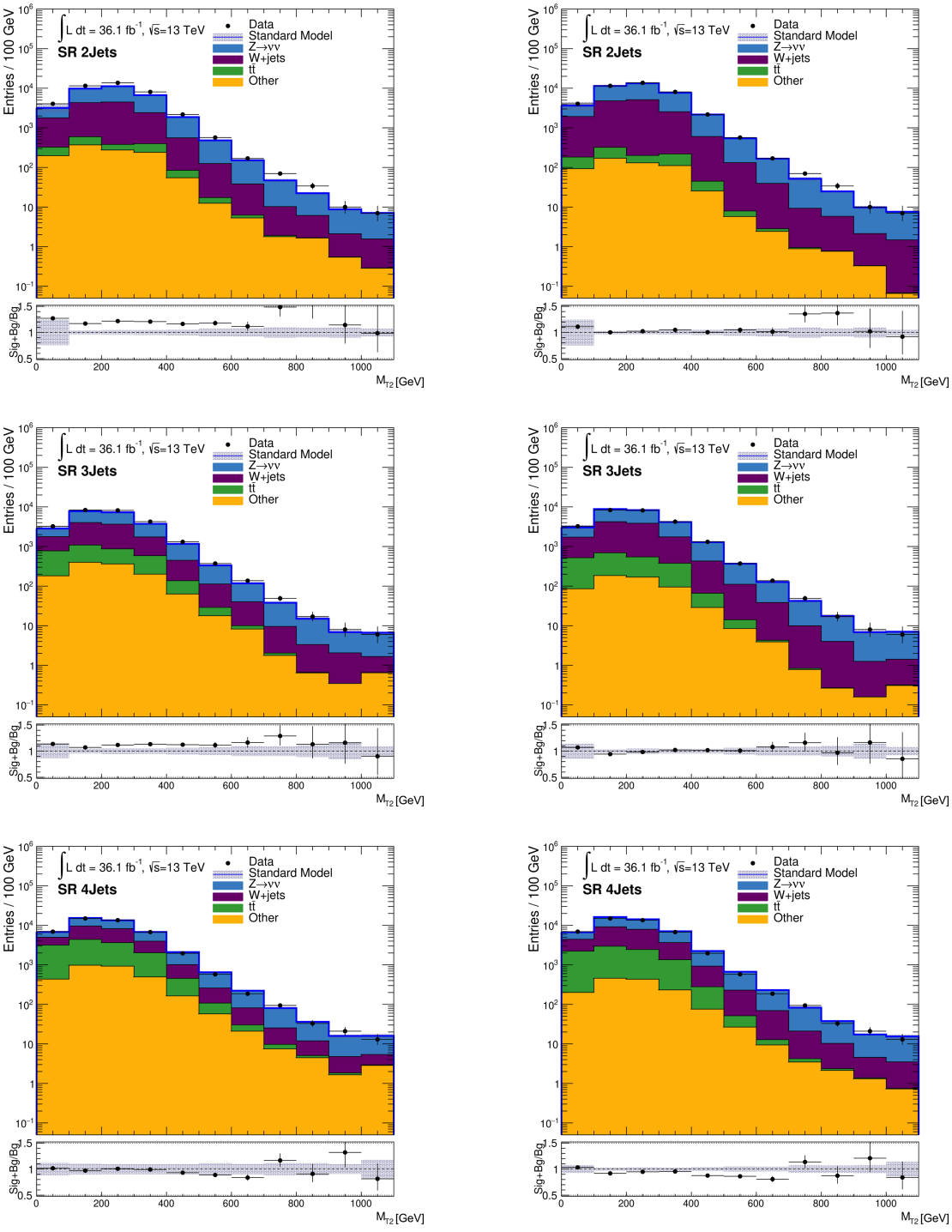

Figure 7.6.: Comparison of the M_{T2} distributions before and after fit for the 2jet, 3jet and $\geqslant$ 4jet SRs.

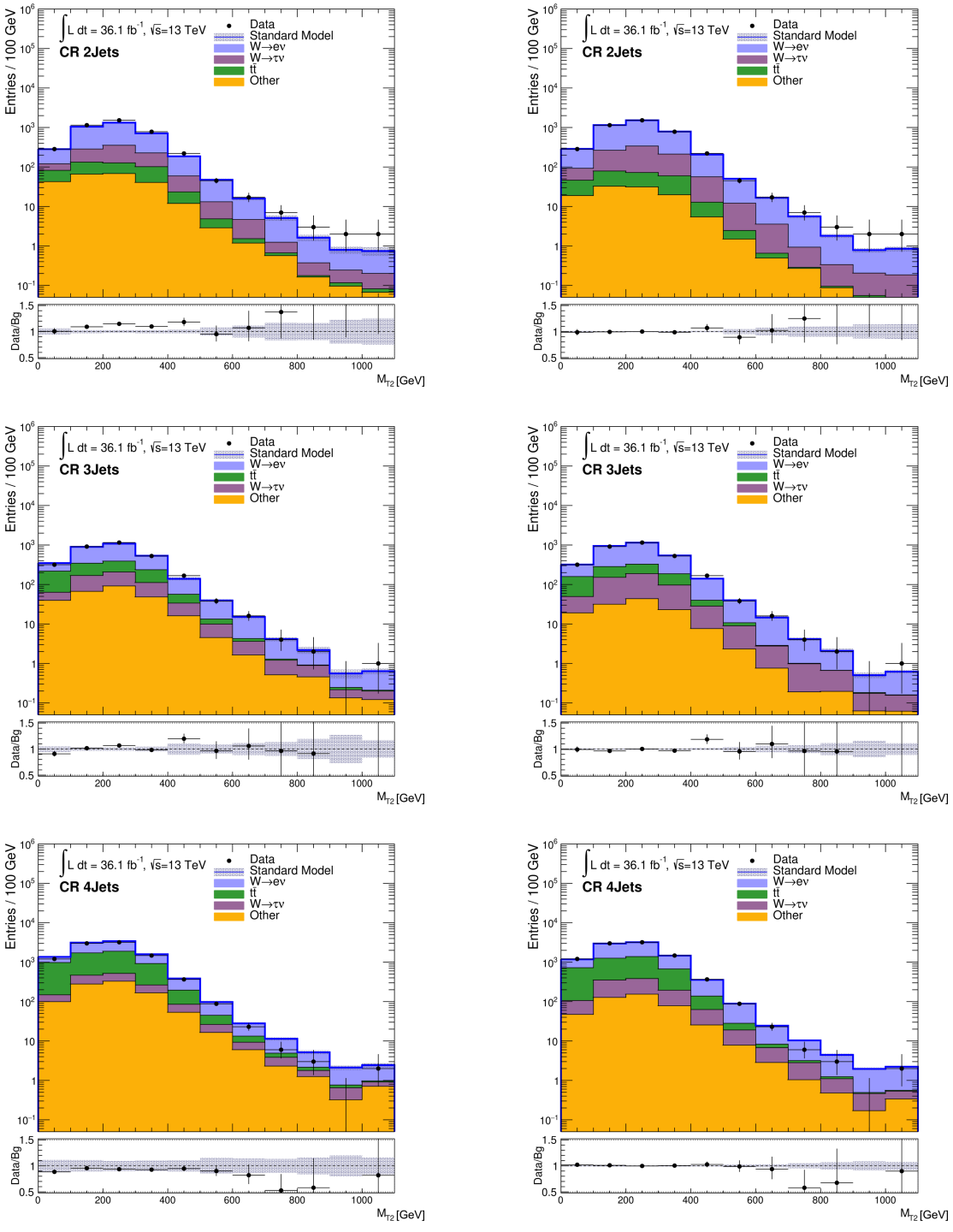

Figure 7.7.: Comparison of the M_{T2} distributions before (left) and after fit (right) for the 2jet, 3jet and $\geqslant$ 4jet electron CRs.

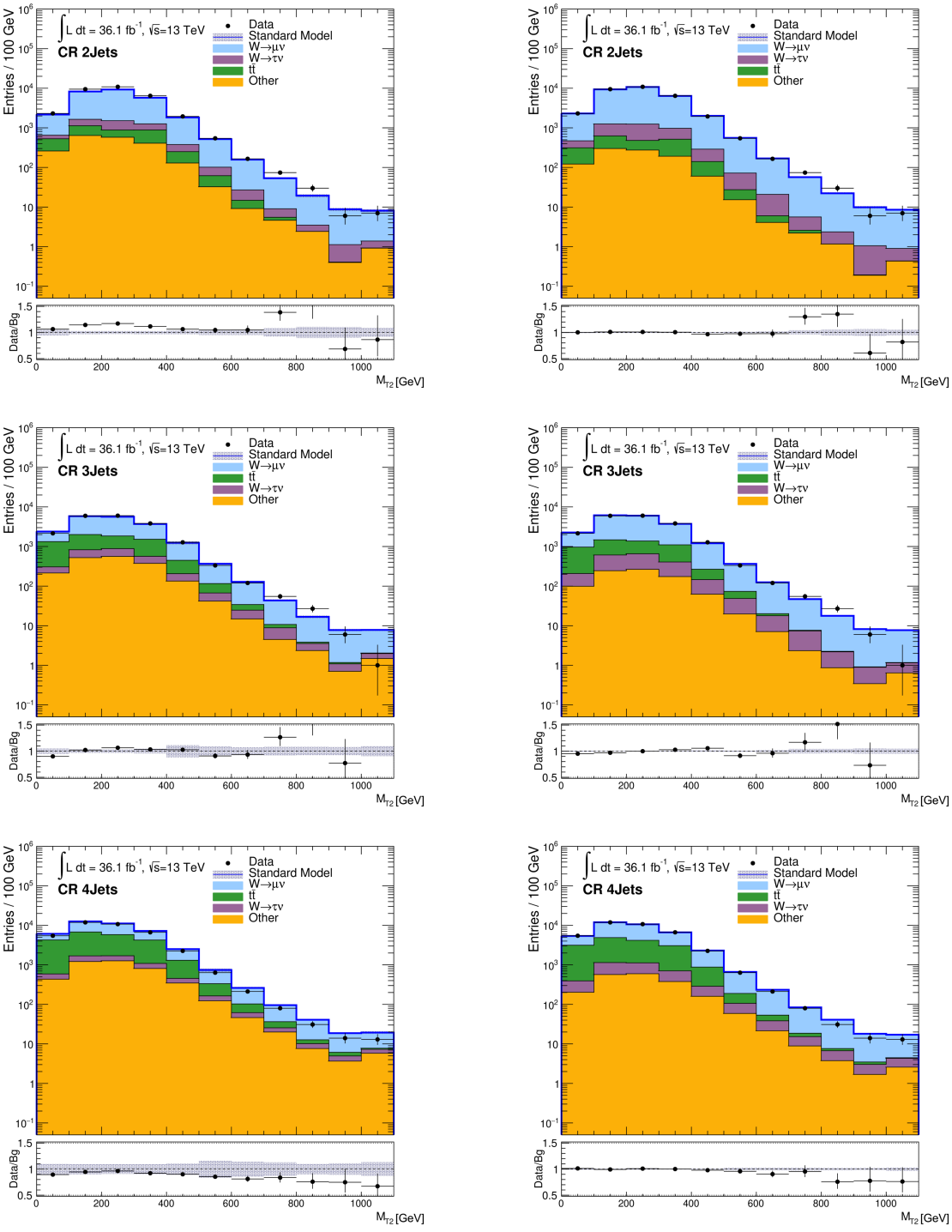

Figure 7.8.: Comparison of the M_{T2} distributions before (left) and after fit (right) for the 2jet, 3jet and $\geqslant$ 4jet muon CRs.

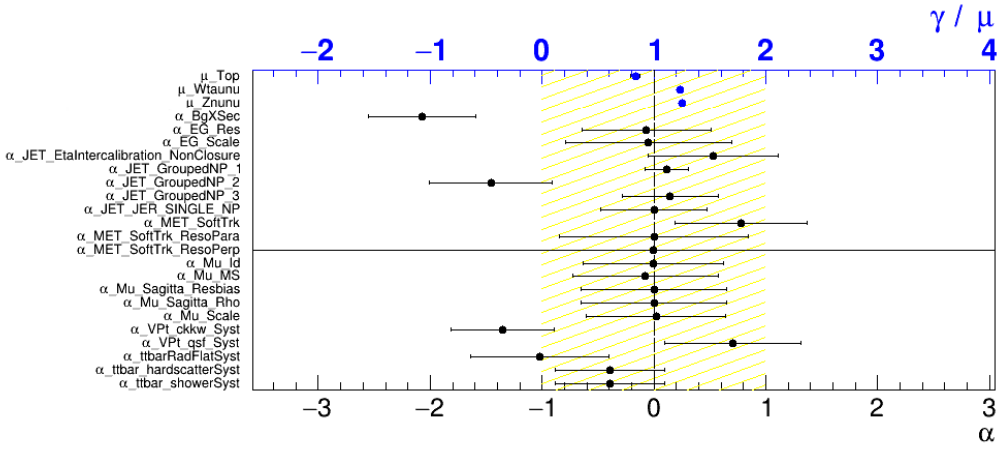

Figure 7.9.: Overview of the final fit parameters after the background only fit in M_{T2}. The normalisation factors are shown on top, below the deviation from the nominal values of the systematic uncertainties can be seen (in units of σ) as they were pulled by the fit.

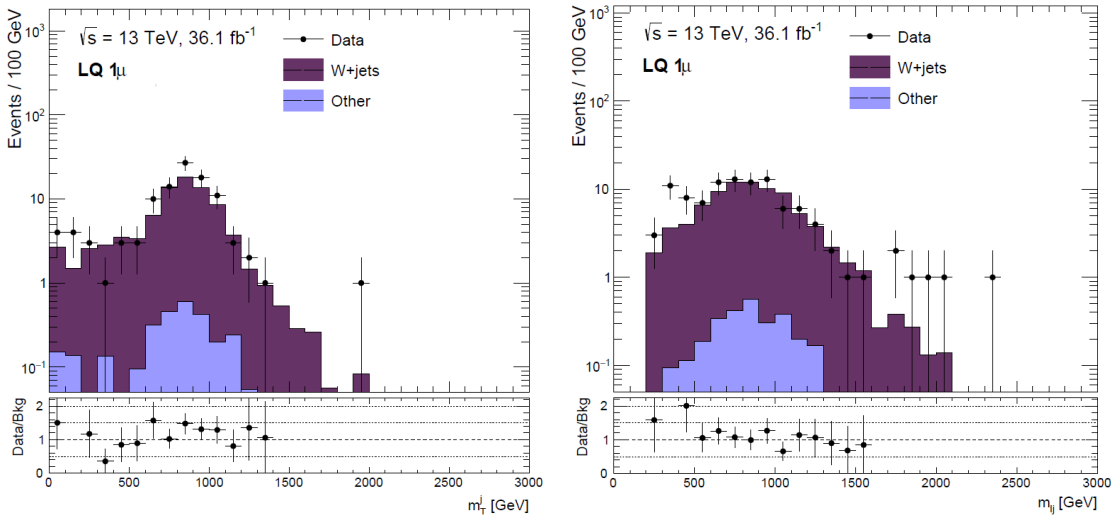

Figure 7.10.: Transverse mass of the jet (left) and invariant mass of the jet and the muon (right) in the muon CR. Both show no significant data excess, which would be observed in case of a present leptoquark contribution[132].

7.3.2. Exclusion Fit

In the final step, the exclusion fit, the CRs and SRs are fitted simultaneously, as described in section 7.3.1. To obtain the expected exclusion limit, the signal and backgrounds are compared to the total number of expected background events after the background-only fit in the SRs (pseudo data). Subsequently, the SRs are unblinded and the fit is conducted with the observed data instead. The results are then used to draw the observed exclusion limits. In the following, the results obtained in both fit variables are presented.

$\boldsymbol{E_{\mathrm{T}}^{\mathrm{miss}}}$

The normalisation factors of the backgrounds and the signal strength (for one exemplary signal with $m_{\tilde{q}} = 800\,\mathrm{GeV}$ and $m_{\tilde{\chi}_1^0} = 400\,\mathrm{GeV}$) were calculated as:

$$\begin{aligned} \mu_{Z\nu\nu} &= 1.1308 \pm 0.0261 \\ \mu_{W\tau\nu} &= 1.1298 \pm 0.0312 \\ \mu_{t\bar{t}} &= 1.1389 \pm 0.0427 \\ \mu_{\mathrm{sig}} &= 6.6854 \times 10^{-11} \pm 0.0207 \end{aligned}$$

This result differs from the corresponding background-only fit which was expected since the SRs are considered as well. They feature a higher statistic (about an order of magnitude larger) compared to the CRs, thus the fit uses the additional event information for profiling and constraining. This can change the value of the resulting normalisation factors.
The distributions in the SRs before and after fit are shown in figure 7.11 and the corresponding yields per bin are shown in tables 7.1 to 7.3. Again, a data excess in the 800 GeV-900 GeV bin of the 3 jet region can be observed. Furthermore, it can be seen that the fit achieves a good agreement between backgrounds and observed data in all three jet multiplicity regions by increasing the MC expectations of the three freely fitted processes by 13%. The signal predictions are reduced to almost 0.
The breakdown of the most significant systematic uncertainties in the SRs are presented in tables 7.4 to 7.6 and their correlations are shown in figure H.3 in appendix H. The biggest uncertainty contributions arise from the theoretical uncertainties, in this case the shape and closure systematic on $Z \to \nu\nu$. For $t\bar{t}$, the shower and hard scattering systematics are dominant. Additionally, the jet energy scale uncertainty strongly contributes in all three regions. Other experimental uncertainties are negligible.
The total uncertainty can clearly be reduced in all three bins, leading to a high sensitivity and allowing an exclusion with high significance. Figure 7.14 gives an overview of the final values of the normalisation factors and the uncertainties. It can be observed that all

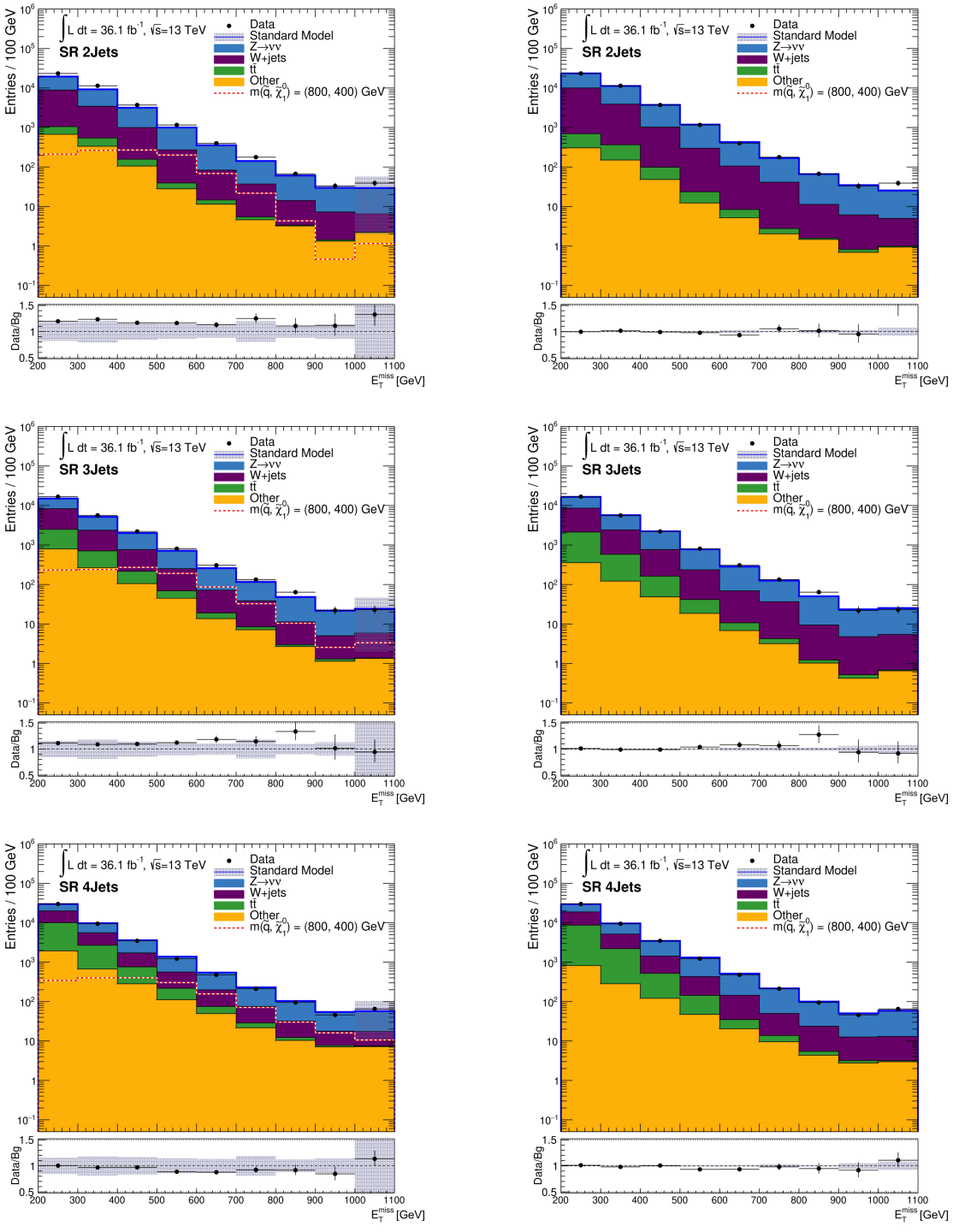

Figure 7.11.: Comparison of the $E_{\mathrm{T}}^{\mathrm{miss}}$ distributions before (left) and after fit (right) for the 2jet, 3jet and $\geqslant$ 4jet SRs.

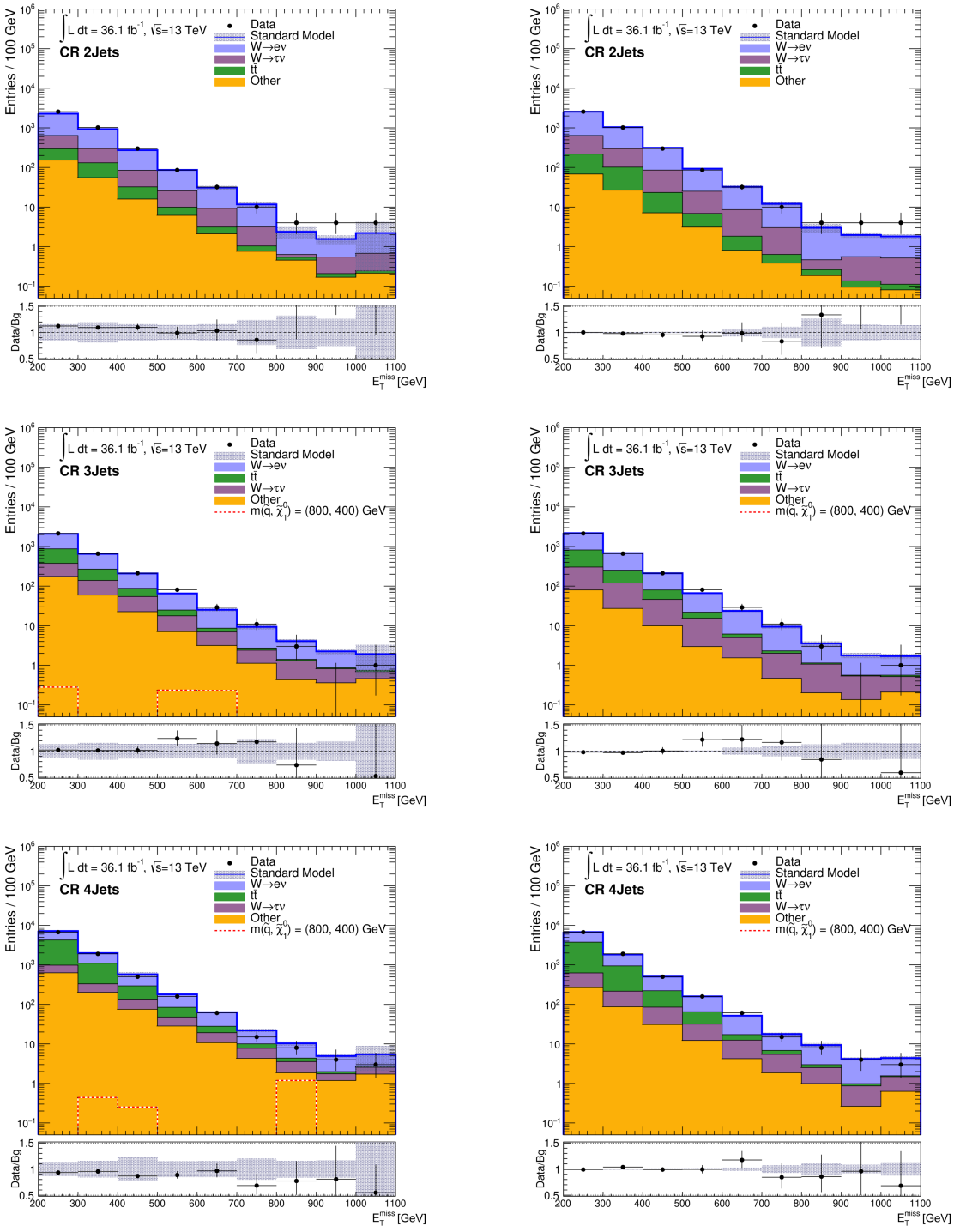

Figure 7.12.: Comparison of the $E_{\mathrm{T}}^{\mathrm{miss}}$ distributions before (left) and after fit (right) for the 2jet, 3jet and $\geqslant$ 4jet electron CRs.

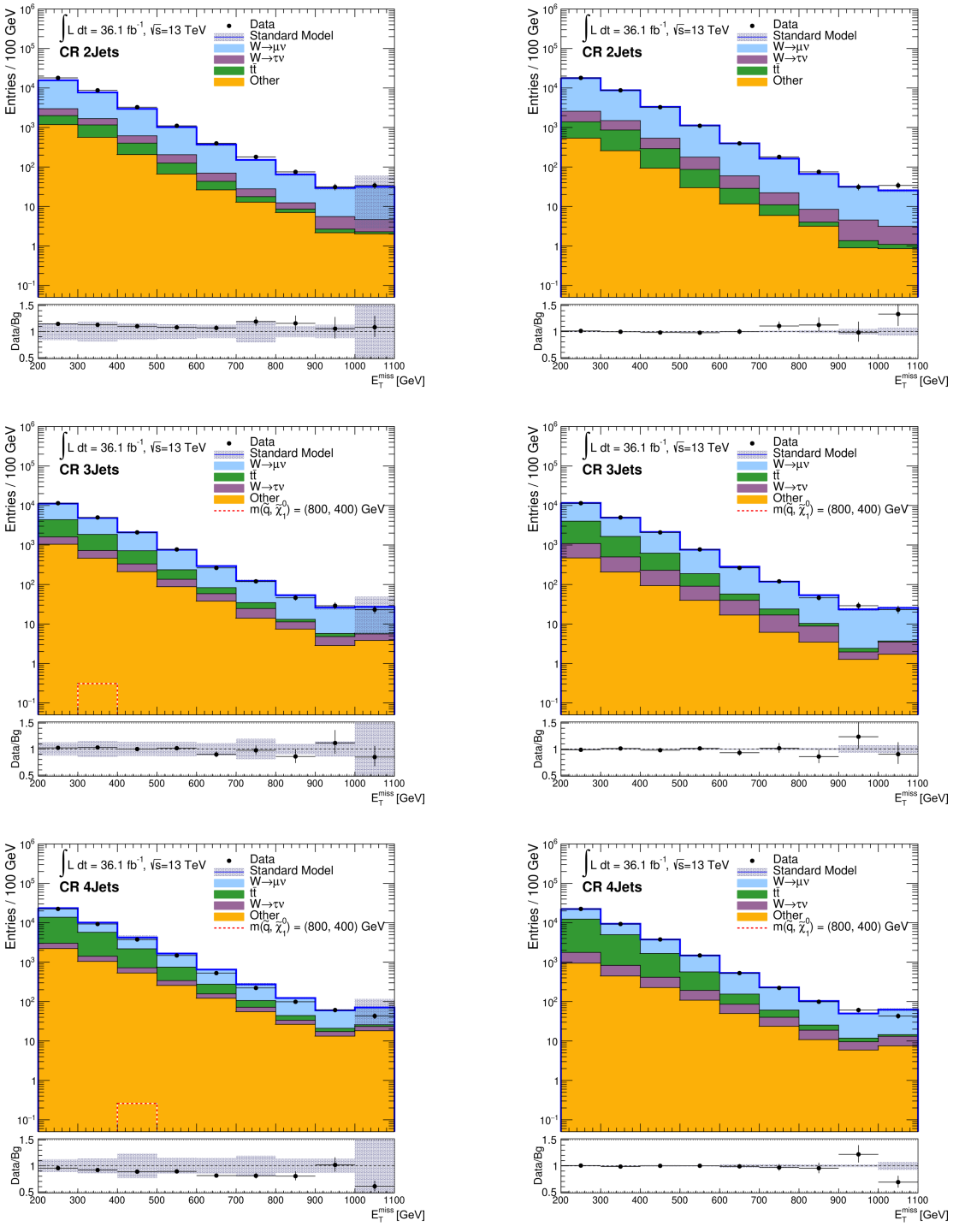

Figure 7.13.: Comparison of the $E_{\mathrm{T}}^{\mathrm{miss}}$ distributions before (left) and after fit (right) for the 2jet, 3jet and $\geqslant$ 4jet muon CRs.

SR 2Jet Bin E_T^{miss}	total	bin2	bin3	bin4	bin5	bin6	bin7	bin8	bin9	bin10
Observed events	40332	23345	11412	3701	1159	399	177	67	33	39
Fitted bkg events	40350.90 ± 188.21	23460.5 ± 115.7	11245.3 ± 72.3	3737.0 ± 32.6	1185.5 ± 13.8	428.7 ± 12.1	167.9 ± 2.9	66.0 ± 1.9	34.7 ± 1.1	25.3 ± 2.0
Fitted Znunu events	24910.04 ± 214.99	13422.0 ± 117.0	7338.6 ± 69.9	2709.2 ± 24.6	886.9 ± 9.0	322.9 ± 4.0	126.7 ± 2.4	54.7 ± 1.0	28.6 ± 0.7	20.3 ± 1.5
Fitted Wtaunu events	8420.72 ± 118.11	5410.9 ± 81.9	2132.4 ± 42.0	591.5 ± 25.6	178.2 ± 10.4	69.9 ± 12.1	27.2 ± 1.0	4.8 ± 1.3	3.4 ± 0.8	2.5 ± 1.2
Fitted ttbar events	672.35 ± 31.57	392.1 ± 18.4	214.5 ± 10.3	50.3 ± 2.3	11.2 ± 0.6	3.2 ± 0.1	0.7 ± 0.1	0.1 ± 0.0	0.1 ± 0.0	0.1 ± 0.0
Fitted Wmunu events	3077.64 ± 47.65	2044.5 ± 33.5	753.6 ± 11.6	195.2 ± 2.5	56.1 ± 1.3	15.4 ± 1.0	7.3 ± 0.3	3.0 ± 0.2	1.3 ± 0.1	1.1 ± 0.1
Fitted Wenu events	2744.66 ± 38.89	1886.2 ± 26.5	656.2 ± 9.7	142.6 ± 3.8	40.8 ± 0.8	12.0 ± 0.4	4.0 ± 0.3	1.9 ± 0.1	0.6 ± 0.0	0.4 ± 0.0
Fitted Other events	525.49 ± 126.25	304.9 ± 73.3	150.0 ± 36.0	48.2 ± 11.6	12.2 ± 2.9	5.2 ± 1.2	2.0 ± 0.5	1.5 ± 0.4	0.7 ± 0.2	0.9 ± 0.2
MC exp. SM events	34563.02	19718.50	9502.55	3433.68	1197.74	421.87	163.13	64.83	30.16	30.57
MC exp. Znunu events	19746.23	10607.76	5778.39	2167.98	725.93	270.19	104.37	46.31	22.44	22.87
MC exp. Wtaunu events	7033.88	4525.98	1733.47	547.81	148.48	42.71	22.05	6.69	4.04	2.65
MC exp. ttbar events	654.57	378.95	208.92	51.11	11.22	3.21	0.83	0.14	0.11	0.08
MC exp. Wmunu events	2620.58	1742.33	638.64	164.45	48.35	16.18	5.56	2.69	1.36	1.02
MC exp. Wenu events	2306.19	1581.64	545.44	127.95	34.88	9.71	4.06	1.47	0.44	0.61
MC exp. Other events	1161.49	671.25	333.95	105.59	28.00	11.37	4.59	3.21	1.32	2.19

Table 7.1.: Summary of expected and fitted background event numbers in the 2 jet SR for the exclusion fit in $E_{\mathrm{T}}^{\mathrm{miss}}$.

SR 3Jet Bin E_T^{miss}	total	bin2	bin3	bin4	bin5	bin6	bin7	bin8	bin9	bin10
Observed events	25891	16706	5629	2204	804	306	133	64	22	23
Fitted bkg events	25722.71 ± 132.99	16525.2 ± 90.2	5688.8 ± 53.4	2227.3 ± 18.4	774.3 ± 8.5	283.5 ± 8.4	124.9 ± 4.4	50.1 ± 1.6	23.4 ± 1.4	25.1 ± 1.9
Fitted Znunu events	13602.86 ± 136.31	7941.5 ± 80.6	3281.3 ± 37.4	1459.8 ± 15.2	538.6 ± 6.0	214.4 ± 2.9	88.2 ± 1.8	40.7 ± 0.8	18.7 ± 1.0	19.7 ± 1.5
Fitted Wtaunu events	5613.98 ± 91.11	3888.9 ± 71.3	1135.7 ± 43.0	388.4 ± 12.6	127.8 ± 5.7	37.8 ± 7.8	24.0 ± 3.7	5.1 ± 1.4	3.0 ± 0.8	3.2 ± 0.5
Fitted ttbar events	2369.11 ± 79.25	1768.5 ± 59.0	458.6 ± 15.6	113.8 ± 3.8	23.0 ± 1.0	3.9 ± 0.7	1.1 ± 0.2	0.2 ± 0.1	0.1 ± 0.0	0.0 ± 0.0
Fitted Wmunu events	1890.49 ± 34.31	1339.2 ± 23.0	371.4 ± 9.4	123.9 ± 2.2	35.6 ± 0.7	11.4 ± 0.2	5.2 ± 0.2	2.0 ± 0.1	0.8 ± 0.0	1.2 ± 0.1
Fitted Wenu events	1688.88 ± 28.65	1230.8 ± 20.8	320.0 ± 6.4	92.8 ± 1.9	30.7 ± 0.6	9.3 ± 0.3	3.2 ± 0.2	1.1 ± 0.1	0.5 ± 0.0	0.4 ± 0.0
Fitted Other events	557.39 ± 133.82	356.3 ± 85.5	121.9 ± 29.4	48.6 ± 11.7	18.5 ± 4.4	6.8 ± 1.7	3.2 ± 0.8	1.0 ± 0.2	0.4 ± 0.1	0.7 ± 0.2
MC exp. SM events	24432.79	15237.74	5405.10	2279.59	906.53	345.08	148.48	58.29	24.25	27.72
MC exp. Znunu events	11529.89	6694.82	2793.46	1242.23	464.19	186.39	77.16	36.54	16.64	18.47
MC exp. Wtaunu events	5066.57	3502.21	1019.85	355.96	120.50	34.70	22.33	5.36	2.70	2.96
MC exp. ttbar events	2272.81	1690.11	440.91	110.41	24.12	5.43	1.34	0.30	0.16	0.04
MC exp. Wmunu events	1724.23	1212.66	348.33	111.15	33.39	10.47	4.71	1.73	0.69	1.11
MC exp. Wenu events	1532.21	1112.40	294.26	83.94	28.64	7.70	3.20	1.26	0.37	0.45
MC exp. Other events	1237.96	793.91	268.08	105.22	44.81	13.65	7.13	2.68	1.14	1.34

Table 7.2.: Summary of expected and fitted background event numbers in the 3 jet SR for the exclusion fit in $E_{\mathrm{T}}^{\mathrm{miss}}$.

SR 4Jet Bin E_T^{miss}	total	bin2	bin3	bin4	bin5	bin6	bin7	bin8	bin9	bin10
Observed events	45028	29959	9459	3487	1226	479	212	95	46	65
Fitted bkg events	45010.82 ± 200.38	29637.2 ± 128.5	9654.0 ± 63.3	3465.3 ± 30.8	1315.5 ± 21.1	513.3 ± 8.3	216.3 ± 5.6	100.2 ± 1.6	50.3 ± 2.6	58.7 ± 4.7
Fitted Znunu events	18865.11 ± 223.54	10763.7 ± 130.1	4489.8 ± 56.3	2033.8 ± 23.9	883.5 ± 10.5	368.5 ± 5.9	166.2 ± 4.4	76.5 ± 1.4	37.6 ± 2.0	45.5 ± 3.8
Fitted Wtaunu events	9066.56 ± 182.48	6327.1 ± 128.1	1884.5 ± 46.6	576.4 ± 23.3	166.3 ± 20.3	68.3 ± 6.3	21.0 ± 3.0	11.5 ± 0.6	5.8 ± 0.4	5.6 ± 0.6
Fitted ttbar events	10328.56 ± 272.24	7891.4 ± 199.1	1920.2 ± 51.2	399.9 ± 25.7	96.7 ± 3.6	14.4 ± 4.2	4.2 ± 1.2	1.1 ± 0.3	0.4 ± 0.1	0.2 ± 0.1
Fitted Wmunu events	2784.88 ± 60.35	1937.6 ± 41.7	568.9 ± 13.1	170.2 ± 4.7	67.4 ± 1.5	22.4 ± 0.7	9.1 ± 0.3	4.2 ± 0.2	2.2 ± 0.1	2.8 ± 0.4
Fitted Wenu events	2651.59 ± 54.33	1895.1 ± 38.4	507.3 ± 11.7	164.0 ± 3.4	54.4 ± 1.3	19.1 ± 0.5	6.2 ± 0.7	2.6 ± 0.1	1.5 ± 0.1	1.5 ± 0.1
Fitted Other events	1314.11 ± 313.43	822.4 ± 196.2	283.4 ± 67.6	121.0 ± 28.9	47.2 ± 11.2	20.5 ± 4.9	9.6 ± 2.3	4.4 ± 1.0	2.8 ± 0.7	3.0 ± 0.7
MC exp. SM events	47336.60	30212.47	10165.03	3996.23	1686.25	703.48	300.95	133.87	70.45	67.87
MC exp. Znunu events	17336.26	9828.69	4167.22	1873.42	817.73	347.09	154.27	71.52	36.57	39.74
MC exp. Wtaunu events	8956.84	6149.05	1818.99	623.75	227.31	82.83	29.35	13.19	6.39	5.98
MC exp. ttbar events	10783.33	8148.80	2016.57	477.11	105.48	25.35	7.14	1.93	0.64	0.30
MC exp. Wmunu events	2779.48	1922.80	573.16	176.39	65.99	22.68	9.30	4.36	2.16	2.65
MC exp. Wenu events	2641.03	1880.15	515.75	159.77	53.66	18.38	8.07	2.31	1.51	1.42
MC exp. Other events	3100.63	1938.56	671.68	282.76	111.65	49.72	21.64	10.34	7.09	7.18

Table 7.3.: Summary of expected and fitted background event numbers in the ≥4 jet SR for the exclusion fit in $E_{\mathrm{T}}^{\mathrm{miss}}$.

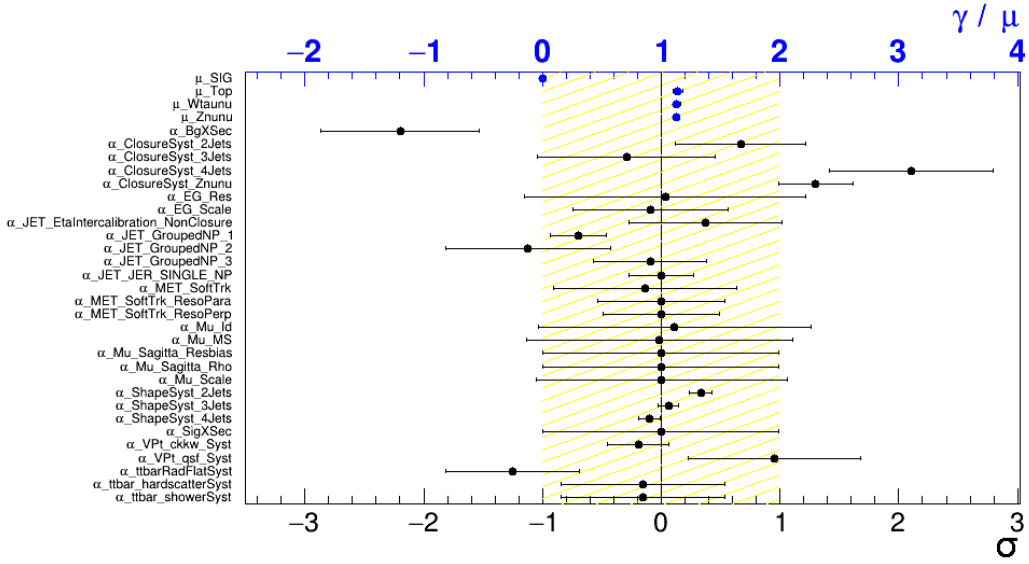

Figure 7.14.: Overview of the final fit parameter values after the exclusion fit in $E_{\mathrm{T}}^{\mathrm{miss}}$. The normalisation factors are shown on top, below the systematic uncertainties can be seen as they were pulled by the fit.

values are within the range of three sigma. A strong pulling indicates that an improved estimation of systematic uncertainties should be considered.

$M_{\mathbf{T2}}$

The normalisation factors of the backgrounds and the signal strength (for one exemplary signal with $m_{\tilde{q}} = 800\,\mathrm{GeV}$ and $m_{\tilde{\chi}_1^0} = 400\,\mathrm{GeV}$) were calculated as:

$$\begin{aligned} \mu_{Z\nu\nu}\ (\equiv \mu_{W\mu\nu}) &= 1.0327 \pm 0.0165 \\ \mu_{W\tau\nu}\ (\equiv \mu_{We\nu}) &= 1.0219 \pm 0.0191 \\ \mu_{t\bar{t}} &= 0.9536 \pm 0.0255 \\ \mu_{\mathrm{sig}} &= 2.1299 \times 10^{-5} \pm 0.0068 \end{aligned}$$

Analogously to the $E_{\mathrm{T}}^{\mathrm{miss}}$ fit, the results differ from those of the background-only fit since the SRs with high event numbers are considered as well. The distributions in the SRs before and after fit are shown in figure 7.15 and the corresponding yields per bin are shown in tables 7.7 to 7.9. It can be observed that in this case the agreement between

[SR 2Jets] Uncertainty of	Znunu	Wtaunu	ttbar	Wmunu	Wenu	Other
Total background expectation	24910.04	8420.72	672.35	3077.64	2744.66	525.49
Total statistical ($\sqrt{N_{exp}}$)	±157.83	±91.76	±25.93	±55.48	±52.39	±22.92
Total background systematic	±214.99 [0.86%]	±118.11 [1.40%]	±31.57 [4.70%]	±47.65 [1.55%]	±38.89 [1.42%]	±126.25 [24.03%]
mu_Znunu	±574.83 [2.3%]	±0.00 [0.00%]	±0.00 [0.00%]	±71.02 [2.3%]	±0.00 [0.00%]	±0.00 [0.00%]
alpha_ShapeSyst_2Jets	±438.87 [1.8%]	±157.18 [1.9%]	±0.00 [0.00%]	±57.47 [1.9%]	±51.25 [1.9%]	±0.00 [0.00%]
alpha_ClosureSyst_Znunu	±343.39 [1.4%]	±0.00 [0.00%]	±0.00 [0.00%]	±0.00 [0.00%]	±0.00 [0.00%]	±0.00 [0.00%]
alpha_JET_GroupedNP_2	±236.38 [0.95%]	±105.69 [1.3%]	±2.61 [0.39%]	±39.63 [1.3%]	±32.62 [1.2%]	±4.61 [0.88%]
alpha_JET_EtaIntercalibration	±94.53 [0.38%]	±36.13 [0.43%]	±1.71 [0.25%]	±10.06 [0.33%]	±9.11 [0.33%]	±1.29 [0.25%]
alpha_VPt_ckkw_Syst	±52.33 [0.21%]	±15.39 [0.18%]	±0.00 [0.00%]	±5.35 [0.17%]	±4.53 [0.17%]	±0.00 [0.00%]
alpha_JET_GroupedNP_3	±51.22 [0.21%]	±10.85 [0.13%]	±1.84 [0.27%]	±8.79 [0.29%]	±5.63 [0.21%]	±1.43 [0.27%]
alpha_VPt_qsf_Syst	±35.06 [0.14%]	±15.00 [0.18%]	±0.00 [0.00%]	±5.60 [0.18%]	±5.15 [0.19%]	±0.00 [0.00%]
alpha_MET_SoftTrk	±30.81 [0.12%]	±19.56 [0.23%]	±2.72 [0.40%]	±26.42 [0.86%]	±1.63 [0.06%]	±1.57 [0.30%]
alpha_JET_GroupedNP_1	±21.44 [0.09%]	±39.87 [0.47%]	±7.72 [1.1%]	±6.06 [0.20%]	±5.72 [0.21%]	±1.05 [0.20%]
alpha_Mu_MS	±0.37 [0.00%]	±0.77 [0.01%]	±0.37 [0.06%]	±0.65 [0.02%]	±0.12 [0.00%]	±0.05 [0.01%]
alpha_EG_Scale	±0.27 [0.00%]	±1.89 [0.02%]	±0.15 [0.02%]	±0.14 [0.00%]	±6.41 [0.23%]	±0.21 [0.04%]
alpha_Mu_Scale	±0.17 [0.00%]	±0.87 [0.01%]	±0.17 [0.02%]	±0.90 [0.03%]	±0.00 [0.00%]	±0.09 [0.02%]
alpha_Mu_Id	±0.05 [0.00%]	±0.81 [0.01%]	±0.29 [0.04%]	±0.24 [0.01%]	±0.01 [0.00%]	±0.09 [0.02%]
alpha_EG_Res	±0.00 [0.00%]	±1.73 [0.02%]	±0.33 [0.05%]	±0.17 [0.01%]	±2.20 [0.08%]	±0.08 [0.01%]
mu_Wtaunu	±0.00 [0.00%]	±232.53 [2.8%]	±0.00 [0.00%]	±0.00 [0.00%]	±75.79 [2.8%]	±0.00 [0.00%]
mu_Top	±0.00 [0.00%]	±0.00 [0.00%]	±25.21 [3.7%]	±0.00 [0.00%]	±0.00 [0.00%]	±0.00 [0.00%]
alpha_ClosureSyst_2Jets	±0.00 [0.00%]	±1.91 [0.02%]	±0.00 [0.00%]	±0.00 [0.00%]	±0.00 [0.00%]	±0.00 [0.00%]
alpha_BgXSec	±0.00 [0.00%]	±0.00 [0.00%]	±0.00 [0.00%]	±0.00 [0.00%]	±0.00 [0.00%]	±126.62 [24.1%]
alpha_ttbar_showerSyst	±0.00 [0.00%]	±0.00 [0.00%]	±105.69 [15.7%]	±0.00 [0.00%]	±0.00 [0.00%]	±0.00 [0.00%]
alpha_ttbarRadFlatSyst	±0.00 [0.00%]	±0.00 [0.00%]	±21.63 [3.2%]	±0.00 [0.00%]	±0.00 [0.00%]	±0.00 [0.00%]
alpha_ttbar_hardscatterSyst	±0.00 [0.00%]	±0.00 [0.00%]	±105.69 [15.7%]	±0.00 [0.00%]	±0.00 [0.00%]	±0.00 [0.00%]

Table 7.4.: Systematic uncertainties in the 2 jet SR for the exclusion fit in $E_{\mathrm{T}}^{\mathrm{miss}}$.

[SR 3Jets] Uncertainty of	Znunu	Wtaunu	ttbar	Wmunu	Wenu	Other
Total background expectation	13602.86	5613.98	2369.11	1890.49	1688.88	557.39
Total statistical ($\sqrt{N_{exp}}$)	±116.63	±74.93	±48.67	±43.48	±41.10	±23.61
Total background systematic	±136.31 [1.00%]	±91.11 [1.62%]	±79.25 [3.34%]	±34.31 [1.81%]	±28.65 [1.70%]	±133.82 [24.01%]
mu_Znunu	±313.90 [2.3%]	±0.00 [0.00%]	±0.00 [0.00%]	±43.63 [2.3%]	±0.00 [0.00%]	±0.00 [0.00%]
alpha_ClosureSyst_Znunu	±197.01 [1.4%]	±0.00 [0.00%]	±0.00 [0.00%]	±0.00 [0.00%]	±0.00 [0.00%]	±0.00 [0.00%]
alpha_JET_GroupedNP_2	±124.79 [0.92%]	±69.06 [1.2%]	±26.31 [1.1%]	±22.08 [1.2%]	±18.62 [1.1%]	±5.27 [0.94%]
alpha_JET_EtaIntercalibration	±51.68 [0.38%]	±24.57 [0.44%]	±10.49 [0.44%]	±7.10 [0.38%]	±5.23 [0.31%]	±1.20 [0.21%]
alpha_VPt_ckkw_Syst	±29.56 [0.22%]	±10.14 [0.18%]	±0.00 [0.00%]	±3.27 [0.17%]	±2.77 [0.16%]	±0.00 [0.00%]
alpha_JET_GroupedNP_3	±47.50 [0.35%]	±21.45 [0.38%]	±2.39 [0.10%]	±9.15 [0.48%]	±5.96 [0.35%]	±1.28 [0.23%]
alpha_VPt_qsf_Syst	±23.37 [0.17%]	±12.53 [0.22%]	±0.00 [0.00%]	±4.33 [0.23%]	±3.99 [0.24%]	±0.00 [0.00%]
alpha_MET_SoftTrk	±17.97 [0.13%]	±24.71 [0.44%]	±10.39 [0.44%]	±13.72 [0.73%]	±5.12 [0.30%]	±1.98 [0.36%]
alpha_JET_GroupedNP_1	±70.20 [0.52%]	±23.58 [0.42%]	±10.24 [0.43%]	±15.02 [0.79%]	±11.06 [0.65%]	±0.45 [0.08%]
alpha_Mu_MS	±0.01 [0.00%]	±0.12 [0.00%]	±0.78 [0.03%]	±0.12 [0.01%]	±0.01 [0.00%]	±0.03 [0.01%]
alpha_EG_Scale	±0.30 [0.00%]	±1.10 [0.02%]	±1.28 [0.05%]	±0.00 [0.00%]	±2.84 [0.17%]	±0.12 [0.02%]
alpha_Mu_Scale	±0.02 [0.00%]	±0.70 [0.01%]	±0.66 [0.03%]	±0.92 [0.05%]	±0.00 [0.00%]	±0.08 [0.01%]
alpha_Mu_Id	±0.13 [0.00%]	±0.63 [0.01%]	±0.02 [0.00%]	±0.14 [0.01%]	±0.00 [0.00%]	±0.02 [0.00%]
alpha_EG_Res	±0.03 [0.00%]	±0.25 [0.00%]	±0.33 [0.01%]	±0.00 [0.00%]	±0.48 [0.03%]	±0.19 [0.03%]
mu_Wtaunu	±0.00 [0.00%]	±155.02 [2.8%]	±0.00 [0.00%]	±0.00 [0.00%]	±46.64 [2.8%]	±0.00 [0.00%]
mu_Top	±0.00 [0.00%]	±0.00 [0.00%]	±88.82 [3.7%]	±0.00 [0.00%]	±0.00 [0.00%]	±0.00 [0.00%]
alpha_BgXSec	±0.00 [0.00%]	±0.00 [0.00%]	±0.00 [0.00%]	±0.00 [0.00%]	±0.00 [0.00%]	±134.31 [24.1%]
alpha_ttbar_showerSyst	±0.00 [0.00%]	±0.00 [0.00%]	±92.23 [3.9%]	±0.00 [0.00%]	±0.00 [0.00%]	±0.00 [0.00%]
alpha_ClosureSyst_3Jets	±0.00 [0.00%]	±6.13 [0.11%]	±0.00 [0.00%]	±0.00 [0.00%]	±0.00 [0.00%]	±0.00 [0.00%]
alpha_ShapeSyst_3Jets	±207.64 [1.5%]	±91.46 [1.6%]	±0.00 [0.00%]	±30.83 [1.6%]	±27.55 [1.6%]	±0.00 [0.00%]
gamma_stat_SR_3Jets_bin_7	±0.93 [0.01%]	±0.15 [0.00%]	±0.00 [0.00%]	±0.04 [0.00%]	±0.02 [0.00%]	±0.02 [0.00%]
alpha_ttbarRadFlatSyst	±0.00 [0.00%]	±0.00 [0.00%]	±73.18 [3.1%]	±0.00 [0.00%]	±0.00 [0.00%]	±0.00 [0.00%]
alpha_ttbar_hardscatterSyst	±0.00 [0.00%]	±0.00 [0.00%]	±92.23 [3.9%]	±0.00 [0.00%]	±0.00 [0.00%]	±0.00 [0.00%]

Table 7.5.: Systematic uncertainties in the 3 jet SR for the exclusion fit in $E_{\mathrm{T}}^{\mathrm{miss}}$.

[SR 4Jets] Uncertainty of	Znunu	Wtaunu	ttbar	Wmunu	Wenu	Other
Total background expectation	18865.11	9066.56	10328.56	2784.88	2651.59	1314.11
Total statistical ($\sqrt{N_{exp}}$)	±137.35	±95.22	±101.63	±52.77	±51.49	±36.25
Total background systematic	±223.54 [1.18%]	±182.48 [2.01%]	±272.24 [2.64%]	±60.35 [2.17%]	±54.33 [2.05%]	±313.43 [23.85%]
mu_Znunu	±435.34 [2.3%]	±0.00 [0.00%]	±0.00 [0.00%]	±64.26 [2.3%]	±0.00 [0.00%]	±0.00 [0.00%]
alpha_ClosureSyst_Znunu	±280.86 [1.5%]	±0.00 [0.00%]	±0.00 [0.00%]	±0.00 [0.00%]	±0.00 [0.00%]	±0.00 [0.00%]
alpha_JET_GroupedNP_2	±230.48 [1.2%]	±139.08 [1.5%]	±167.20 [1.6%]	±41.29 [1.5%]	±45.98 [1.7%]	±15.57 [1.2%]
alpha_JET_EtaIntercalibration	±84.30 [0.45%]	±42.74 [0.47%]	±62.83 [0.61%]	±16.60 [0.60%]	±14.33 [0.54%]	±6.58 [0.50%]
alpha_VPt_ckkw_Syst	±13.35 [0.07%]	±6.81 [0.08%]	±0.00 [0.00%]	±2.07 [0.07%]	±1.98 [0.07%]	±0.00 [0.00%]
alpha_JET_GroupedNP_3	±142.86 [0.76%]	±75.39 [0.83%]	±76.20 [0.74%]	±26.39 [0.95%]	±24.60 [0.93%]	±8.22 [0.63%]
alpha_VPt_qsf_Syst	±34.79 [0.18%]	±23.15 [0.26%]	±0.00 [0.00%]	±7.14 [0.26%]	±7.05 [0.27%]	±0.00 [0.00%]
alpha_MET_SoftTrk	±30.19 [0.16%]	±39.06 [0.43%]	±52.03 [0.50%]	±20.76 [0.75%]	±11.03 [0.42%]	±5.19 [0.40%]
alpha_JET_GroupedNP_1	±387.71 [2.1%]	±197.56 [2.2%]	±188.57 [1.8%]	±71.89 [2.6%]	±62.13 [2.3%]	±22.51 [1.7%]
alpha_Mu_MS	±0.16 [0.00%]	±0.89 [0.01%]	±0.02 [0.00%]	±1.34 [0.05%]	±0.10 [0.00%]	±0.01 [0.00%]
alpha_EG_Scale	±0.62 [0.00%]	±2.00 [0.02%]	±6.29 [0.06%]	±0.10 [0.00%]	±6.00 [0.23%]	±0.39 [0.03%]
alpha_Mu_Scale	±0.24 [0.00%]	±0.84 [0.01%]	±1.36 [0.01%]	±2.69 [0.10%]	±0.05 [0.00%]	±0.24 [0.02%]
alpha_Mu_Id	±0.14 [0.00%]	±0.14 [0.00%]	±1.52 [0.01%]	±1.10 [0.04%]	±0.06 [0.00%]	±0.24 [0.02%]
alpha_EG_Res	±0.04 [0.00%]	±0.65 [0.01%]	±0.42 [0.00%]	±0.03 [0.00%]	±0.28 [0.01%]	±0.26 [0.02%]
alpha_MET_SoftTrk_ResoPerp	±0.00 [0.00%]	±0.00 [0.00%]	±0.01 [0.00%]	±0.00 [0.00%]	±0.00 [0.00%]	±0.00 [0.00%]
mu_Wtaunu	±0.00 [0.00%]	±250.36 [2.8%]	±0.00 [0.00%]	±0.00 [0.00%]	±73.22 [2.8%]	±0.00 [0.00%]
mu_Top	±0.00 [0.00%]	±0.00 [0.00%]	±387.22 [3.7%]	±0.00 [0.00%]	±0.00 [0.00%]	±0.00 [0.00%]
alpha_BgXSec	±0.00 [0.00%]	±0.00 [0.00%]	±0.00 [0.00%]	±0.00 [0.00%]	±0.00 [0.00%]	±316.64 [24.1%]
alpha_ShapeSyst_4Jets	±298.82 [1.6%]	±154.66 [1.7%]	±0.00 [0.00%]	±47.48 [1.7%]	±45.27 [1.7%]	±0.00 [0.00%]
gamma_stat_SR_4Jets_bin_7	±1.85 [0.01%]	±0.29 [0.00%]	±0.02 [0.00%]	±0.11 [0.00%]	±0.07 [0.00%]	±0.14 [0.01%]
alpha_ttbar_showerSyst	±0.00 [0.00%]	±0.00 [0.00%]	±518.54 [5.0%]	±0.00 [0.00%]	±0.00 [0.00%]	±0.00 [0.00%]
alpha_ClosureSyst_4Jets	±0.00 [0.00%]	±0.41 [0.00%]	±0.00 [0.00%]	±0.00 [0.00%]	±0.00 [0.00%]	±0.00 [0.00%]
alpha_ttbarRadFlatSyst	±0.00 [0.00%]	±0.00 [0.00%]	±322.91 [3.1%]	±0.00 [0.00%]	±0.00 [0.00%]	±0.00 [0.00%]
alpha_ttbar_hardscatterSyst	±0.00 [0.00%]	±0.00 [0.00%]	±518.54 [5.0%]	±0.00 [0.00%]	±0.00 [0.00%]	±0.00 [0.00%]

Table 7.6.: Systematic uncertainties in the ≥4 jet SR for the exclusion fit in $E_{\mathrm{T}}^{\mathrm{miss}}$.

MC expectation and observed data is even better and the fit only increases the main backgrounds by 2-3% while decreasing $t\bar{t}$ by 5%. As before, the signal strength is reduced to almost 0 and no significant data excess can be found in the SRs.

The breakdowns of the highest systematic uncertainties in the SRs are presented in tables 7.10 to 7.12 and their correlations are shown in figure H.4 of appendix H. As in the $E_{\mathrm{T}}^{\mathrm{miss}}$ fit above, the highest contributions come from the theoretical uncertainties, especially from the shape and closure systematic on $Z \to \nu\nu$. The experimental uncertainties are negligible except for the jet energy resolution systematic. For $t\bar{t}$, the uncertainties on showering, radiation and hard scattering are dominant, especially in higher jet multiplicity bins. For the combined other backgrounds, the cross section uncertainty contributes most. Nevertheless, the fit is able to strongly reduce the total uncertainty which is necessary to achieve a high sensitivity. Figure 7.18 gives an overview of all normalisation factors, the signal strength and systematics after the fit. The pulled values are all within a two sigma range and the profiling (except for one systematic) is even better than in the $E_{\mathrm{T}}^{\mathrm{miss}}$ fit. This is due to the clearer pronounced bump-like shape difference between signal and background in M_{T2} compared to the $E_{\mathrm{T}}^{\mathrm{miss}}$ distributions. Thus, the systematic uncertainties can be reduced more easily and a strong profiling is not necessary.

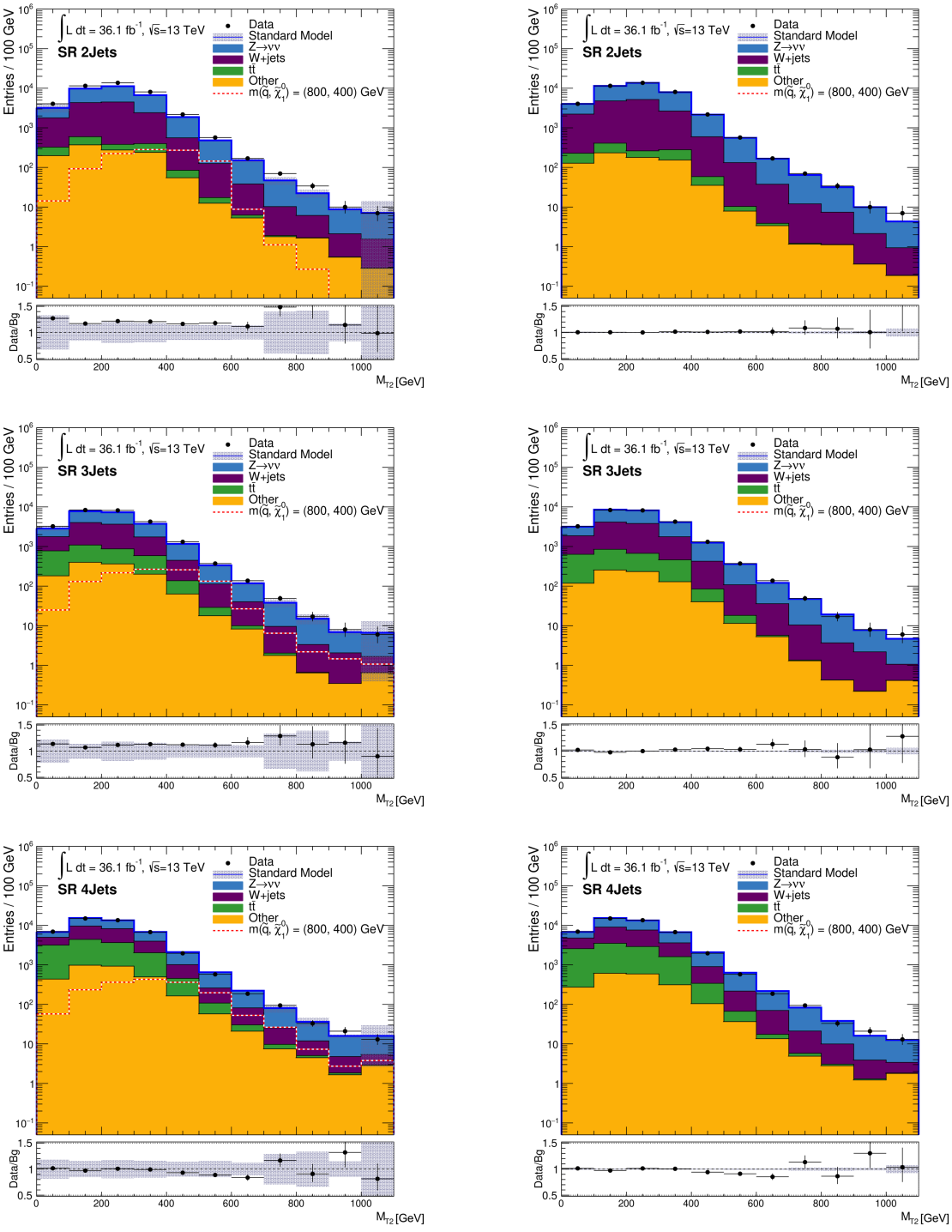

Figure 7.15.: Comparison of the M_{T2} distributions before (left) and after fit (right) for the 2jet, 3jet and $\geqslant$ 4jet SRs.

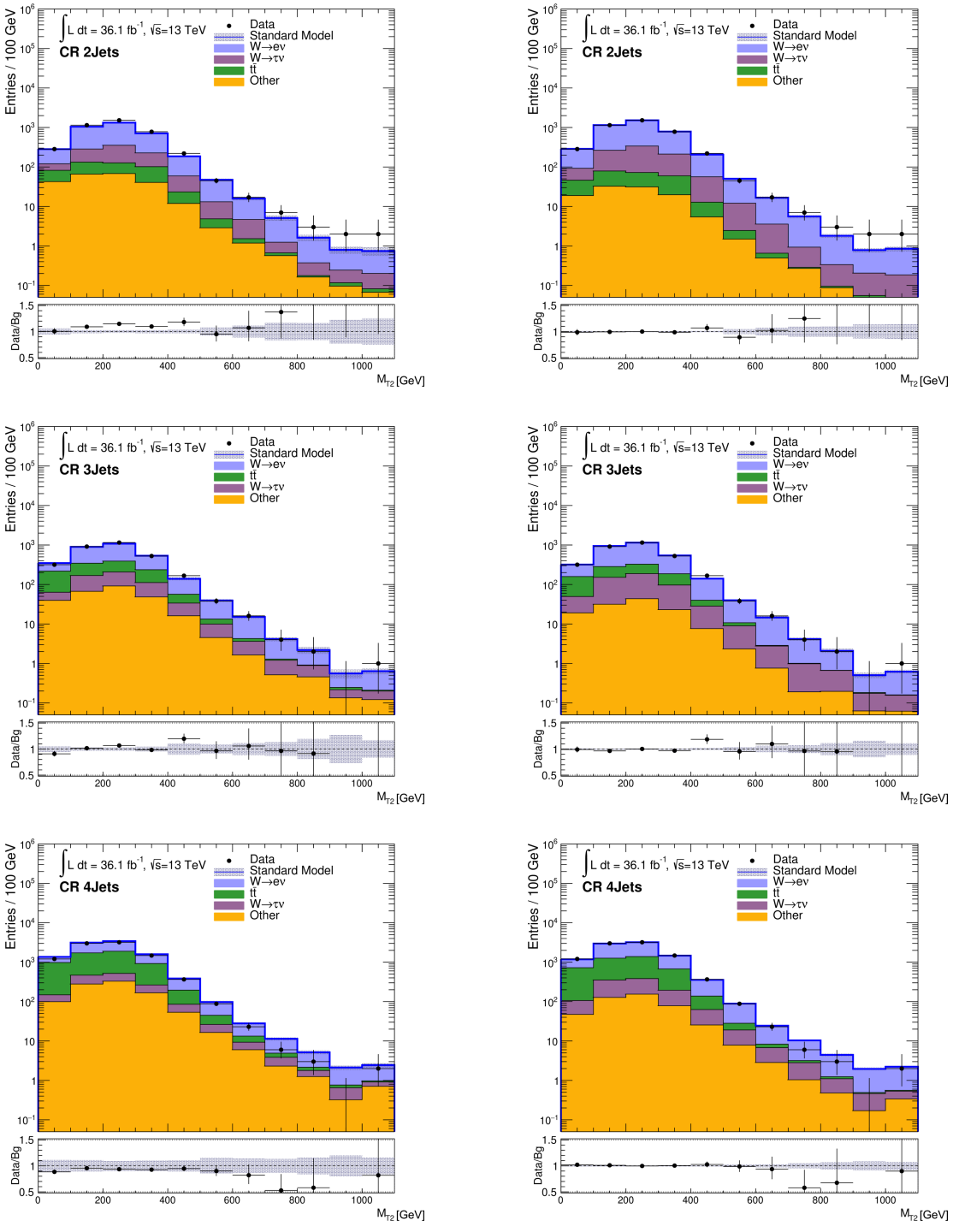

Figure 7.16.: Comparison of the M_{T2} distributions before (left) and after fit (right) for the 2jet, 3jet and $\geqslant$ 4jet electron CRs.

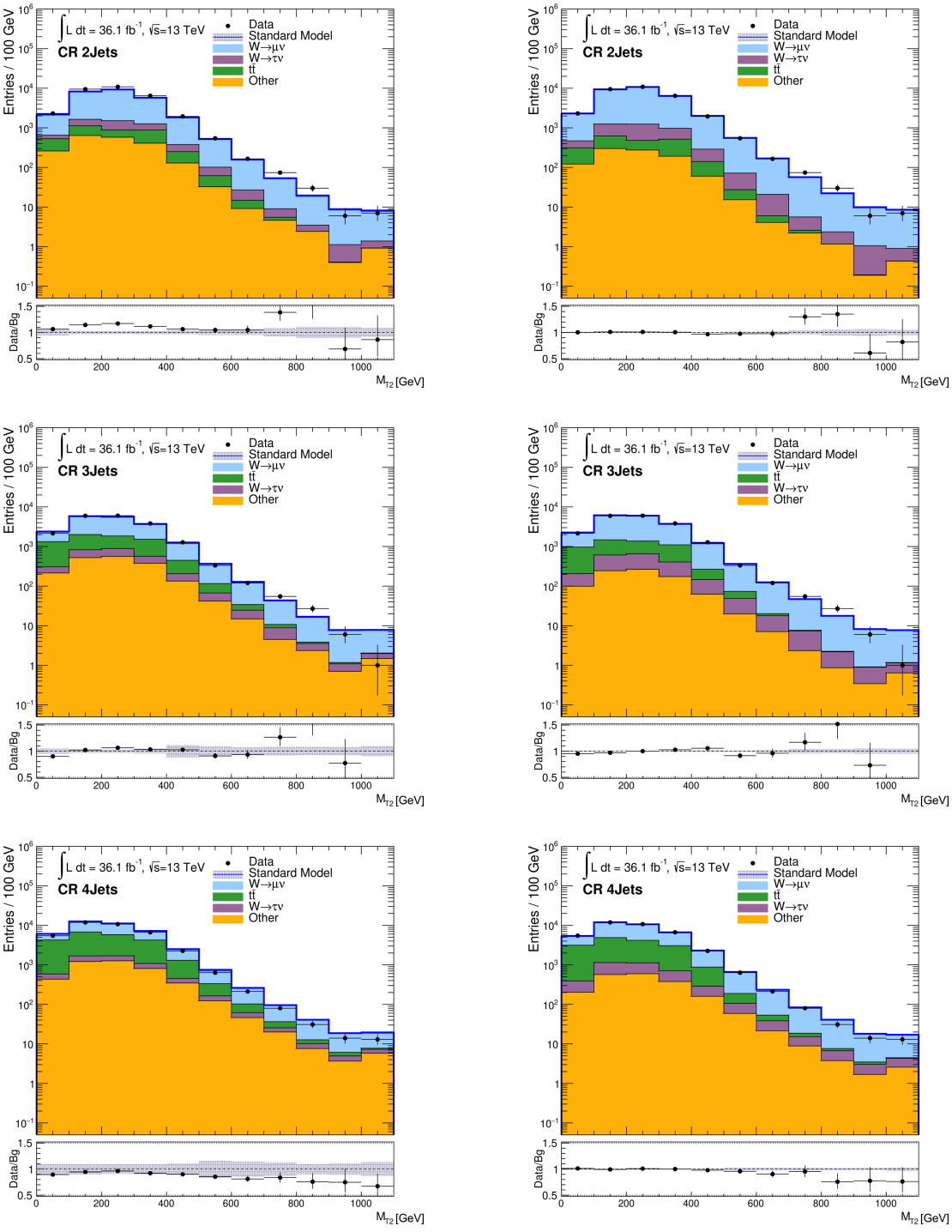

Figure 7.17.: Comparison of the M_{T2} distributions before (left) and after fit (right) for the 2jet, 3jet and $\geqslant$ 4jet muon CRs.

SR 2Jet Bin M_{T2}	total	bin0	bin1	bin2	bin3	bin4
Observed events	40332	4045	11486	13685	8078	2179
Fitted bkg events	40102.90 ± 168.75	4029.2 ± 61.4	11442.7 ± 56.5	13677.6 ± 66.5	7959.7 ± 42.2	2157.7 ± 12.8
Fitted Znunu events	24435.08 ± 175.24	1805.7 ± 14.8	6652.1 ± 50.3	8477.0 ± 61.5	5295.9 ± 40.0	1560.9 ± 12.7
Fitted Wtaunu events	8513.53 ± 98.37	1346.5 ± 62.2	2431.6 ± 30.7	2853.2 ± 40.2	1434.4 ± 20.6	337.0 ± 5.5
Fitted ttbar events	512.52 ± 23.43	101.1 ± 4.8	175.4 ± 7.9	83.2 ± 4.0	126.4 ± 5.7	23.4 ± 1.0
Fitted Wmunu events	3129.14 ± 26.49	302.0 ± 3.4	1026.1 ± 8.7	1124.5 ± 10.0	518.6 ± 5.3	118.6 ± 1.0
Fitted Wenu events	2768.43 ± 31.35	346.1 ± 4.3	923.4 ± 10.4	961.0 ± 11.3	430.3 ± 5.2	82.4 ± 1.1
Fitted Other events	744.18 ± 60.41	127.8 ± 10.4	234.0 ± 19.0	178.8 ± 14.5	154.1 ± 12.5	35.3 ± 2.9
MC exp. SM events	34558.19	3197.16	9905.92	11463.51	6972.62	2145.12
MC exp. Znunu events	19740.91	1390.20	5472.81	6753.05	4276.65	1312.82
MC exp. Wtaunu events	7034.24	945.82	2081.29	2386.45	1220.55	299.73
MC exp. ttbar events	654.57	127.32	225.93	106.50	158.99	29.84
MC exp. Wmunu events	2620.66	245.30	875.49	926.75	435.89	103.59
MC exp. Wenu events	2306.24	275.88	786.94	791.96	357.60	72.06
MC exp. Other events	1161.48	198.36	370.90	275.42	239.91	54.85

SR 2Jet Bin M_{T2}	bin5	bin6	bin7	bin8	bin9	bin10
Observed events	569	169	70	34	10	7
Fitted bkg events	559.0 ± 4.3	166.5 ± 1.7	64.5 ± 1.3	31.7 ± 0.8	9.9 ± 0.2	4.3 ± 0.3
Fitted Znunu events	426.6 ± 3.8	128.8 ± 1.4	52.4 ± 1.0	24.3 ± 0.6	7.8 ± 0.2	3.4 ± 0.3
Fitted Wtaunu events	76.1 ± 1.8	21.7 ± 0.6	7.0 ± 0.4	4.4 ± 0.1	1.3 ± 0.1	0.4 ± 0.0
Fitted ttbar events	2.5 ± 0.4	0.5 ± 0.1	0.1 ± 0.0	0.0 ± 0.0	0.0 ± 0.0	0.0 ± 0.0
Fitted Wmunu events	28.9 ± 0.5	6.7 ± 0.1	2.2 ± 0.1	1.0 ± 0.0	0.3 ± 0.0	0.3 ± 0.0
Fitted Wenu events	17.1 ± 0.2	5.4 ± 0.1	1.6 ± 0.1	0.9 ± 0.0	0.2 ± 0.0	0.1 ± 0.0
Fitted Other events	7.9 ± 0.6	3.4 ± 0.3	1.2 ± 0.1	1.1 ± 0.1	0.4 ± 0.0	0.2 ± 0.0
MC exp. SM events	627.03	160.15	48.24	22.59	8.75	7.10
MC exp. Znunu events	357.03	113.13	36.87	16.19	6.63	5.53
MC exp. Wtaunu events	68.91	20.91	5.63	3.08	1.16	0.69
MC exp. ttbar events	4.87	0.94	0.13	0.03	0.01	0.01
MC exp. Wmunu events	24.47	6.17	1.61	0.74	0.28	0.36
MC exp. Wenu events	14.81	4.90	1.11	0.62	0.12	0.23
MC exp. Other events	12.48	5.31	1.78	1.65	0.54	0.28

Table 7.7.: Summary of expected and fitted background event numbers in the 2 jet SR for the exclusion fit in M_{T2}.

SR 3Jet Bin M_{T2}	total	bin0	bin1	bin2	bin3	bin4
Observed events	25891	3239	8336	8171	4245	1311
Fitted bkg events	25798.35 ± 130.71	3165.8 ± 49.0	8529.2 ± 46.0	8163.1 ± 57.1	4126.6 ± 26.2	1253.3 ± 9.3
Fitted Znunu events	13601.64 ± 119.26	1295.6 ± 14.9	4375.0 ± 37.6	4346.5 ± 39.0	2358.4 ± 21.8	827.4 ± 7.6
Fitted Wtaunu events	5763.73 ± 72.45	807.0 ± 48.2	1921.5 ± 30.6	1903.8 ± 38.6	816.4 ± 15.4	223.7 ± 3.9
Fitted ttbar events	1938.24 ± 53.71	518.4 ± 13.7	595.4 ± 16.4	440.1 ± 12.1	332.6 ± 8.5	44.4 ± 6.0
Fitted Wmunu events	1958.61 ± 21.33	195.8 ± 2.5	743.4 ± 8.2	663.5 ± 7.7	265.2 ± 3.0	66.4 ± 1.1
Fitted Wenu events	1741.40 ± 21.62	231.0 ± 4.7	638.6 ± 7.6	576.2 ± 7.2	224.9 ± 2.9	51.2 ± 0.8
Fitted Other events	794.71 ± 64.49	118.0 ± 9.6	255.3 ± 20.7	233.1 ± 18.9	129.1 ± 10.5	40.2 ± 3.3
MC exp. SM events	24435.70	2872.12	7912.30	7523.31	4013.43	1425.31
MC exp. Znunu events	11532.93	1071.37	3752.47	3642.34	2000.97	717.87
MC exp. Wtaunu events	5066.47	627.99	1696.85	1716.66	730.75	206.40
MC exp. ttbar events	2272.79	596.41	693.40	509.00	386.89	73.83
MC exp. Wmunu events	1724.26	169.14	668.47	576.61	229.30	58.66
MC exp. Wenu events	1532.17	200.02	571.45	498.43	197.82	46.88
MC exp. Other events	1237.96	182.20	398.91	363.47	200.60	63.30

SR 3Jet Bin M_{T2}	bin5	bin6	bin7	bin8	bin9	bin10
Observed events	372	137	49	17	8	6
Fitted bkg events	360.4 ± 3.2	120.9 ± 1.4	47.4 ± 1.0	19.2 ± 0.6	7.8 ± 0.3	4.7 ± 0.3
Fitted Znunu events	252.1 ± 2.5	84.9 ± 1.0	36.9 ± 0.8	15.6 ± 0.4	5.6 ± 0.2	3.6 ± 0.2
Fitted Wtaunu events	61.1 ± 1.8	20.6 ± 0.9	5.7 ± 0.3	2.1 ± 0.2	1.5 ± 0.1	0.4 ± 0.0
Fitted ttbar events	6.8 ± 0.9	0.4 ± 0.2	0.1 ± 0.0	0.0 ± 0.0	0.0 ± 0.0	0.0 ± 0.0
Fitted Wmunu events	15.8 ± 0.2	5.4 ± 0.1	1.8 ± 0.0	0.7 ± 0.0	0.3 ± 0.0	0.2 ± 0.0
Fitted Wenu events	13.1 ± 0.2	4.3 ± 0.1	1.5 ± 0.1	0.4 ± 0.0	0.1 ± 0.0	0.0 ± 0.0
Fitted Other events	11.4 ± 0.9	5.3 ± 0.4	1.3 ± 0.1	0.4 ± 0.0	0.2 ± 0.0	0.4 ± 0.0
MC exp. SM events	467.14	144.34	44.45	17.22	8.35	7.73
MC exp. Znunu events	220.83	77.23	28.37	11.67	4.83	4.98
MC exp. Wtaunu events	57.88	21.37	4.82	1.84	1.29	0.61
MC exp. ttbar events	11.20	1.77	0.26	0.02	0.00	0.01
MC exp. Wmunu events	14.32	5.10	1.42	0.57	0.31	0.37
MC exp. Wenu events	11.88	3.92	1.33	0.29	0.12	0.03
MC exp. Other events	17.82	8.25	1.77	0.64	0.35	0.65

Table 7.8.: Summary of expected and fitted background event numbers in the 3 jet SR for the exclusion fit in M_{T2}.

SR 4Jet Bin M_{T2}	total	bin0	bin1	bin2	bin3	bin4
Observed events	45028	6931	14940	13510	6758	1965
Fitted bkg events	45349.50 ± 207.14	6837.7 ± 68.1	15363.9 ± 82.0	13336.3 ± 79.7	6721.2 ± 36.1	2088.6 ± 13.0
Fitted Znunu events	19035.78 ± 203.98	2047.0 ± 27.2	6307.5 ± 65.6	5711.7 ± 64.9	3108.7 ± 34.5	1185.2 ± 12.6
Fitted Wtaunu events	9531.41 ± 142.23	1467.4 ± 69.0	3357.2 ± 50.9	2931.8 ± 56.5	1268.6 ± 23.8	363.5 ± 6.6
Fitted ttbar events	9106.98 ± 194.67	2302.2 ± 48.7	2906.2 ± 62.2	2324.8 ± 49.1	1300.3 ± 27.5	237.7 ± 6.5
Fitted Wmunu events	2935.17 ± 39.53	369.9 ± 5.8	1127.4 ± 16.4	903.9 ± 12.1	383.0 ± 5.3	99.9 ± 1.3
Fitted Wenu events	2784.56 ± 40.35	378.9 ± 6.6	1051.8 ± 15.0	873.5 ± 13.2	346.8 ± 5.3	97.9 ± 1.5
Fitted Other events	1955.57 ± 160.48	272.3 ± 22.4	613.7 ± 50.4	590.6 ± 48.3	313.8 ± 25.7	104.3 ± 8.6
MC exp. SM events	47327.78	6883.88	15622.94	13787.61	7247.12	2474.07
MC exp. Znunu events	17325.86	1830.69	5771.23	5162.02	2832.43	1097.78
MC exp. Wtaunu events	8958.08	1125.18	3125.96	2925.30	1263.82	369.55
MC exp. ttbar events	10783.61	2728.24	3432.76	2733.34	1533.89	292.20
MC exp. Wmunu events	2779.57	344.10	1078.77	849.38	362.68	96.03
MC exp. Wenu events	2641.02	360.44	999.92	824.54	328.29	92.62
MC exp. Other events	3100.61	437.81	979.98	929.28	494.90	163.73

SR 4Jet Bin M_{T2}	bin5	bin6	bin7	bin8	bin9	bin10
Observed events	577	186	94	33	21	13
Fitted bkg events	633.7 ± 5.8	218.4 ± 2.2	83.0 ± 2.2	38.2 ± 1.2	16.1 ± 0.3	12.5 ± 1.0
Fitted Znunu events	416.4 ± 4.9	148.0 ± 1.8	61.8 ± 1.8	28.3 ± 0.9	12.2 ± 0.3	9.1 ± 0.7
Fitted Wtaunu events	94.5 ± 2.1	33.6 ± 0.6	8.6 ± 0.5	4.1 ± 0.2	1.4 ± 0.1	0.7 ± 0.1
Fitted ttbar events	30.5 ± 4.0	4.0 ± 0.8	0.9 ± 0.2	0.3 ± 0.1	0.1 ± 0.0	0.0 ± 0.0
Fitted Wmunu events	31.9 ± 0.5	11.6 ± 0.2	4.5 ± 0.1	1.7 ± 0.1	0.7 ± 0.1	0.5 ± 0.1
Fitted Wenu events	23.8 ± 0.5	7.6 ± 0.2	2.3 ± 0.1	1.1 ± 0.0	0.5 ± 0.0	0.3 ± 0.0
Fitted Other events	36.6 ± 3.0	13.5 ± 1.1	4.9 ± 0.4	2.8 ± 0.2	1.2 ± 0.1	1.8 ± 0.2
MC exp. SM events	847.59	275.37	107.11	43.66	18.65	19.78
MC exp. Znunu events	389.76	140.67	55.21	24.37	11.12	10.58
MC exp. Wtaunu events	98.57	32.62	9.35	4.43	1.80	1.51
MC exp. ttbar events	50.64	9.36	2.28	0.60	0.20	0.09
MC exp. Wmunu events	30.06	11.64	4.14	1.51	0.74	0.52
MC exp. Wenu events	23.99	7.21	2.23	0.95	0.41	0.43
MC exp. Other events	57.48	20.98	7.46	4.47	1.65	2.86

Table 7.9.: Summary of expected and fitted background event numbers in the $\geq$4 jet SR for the exclusion fit in M_{T2}.

[SR 2Jets] Uncertainty of	Znunu	Wtaunu	ttbar	Wmunu	Wenu	Other
Total background expectation	24435.08	8513.53	512.52	3129.14	2768.43	744.18
Total statistical ($\sqrt{N_{exp}}$)	±156.32	±92.27	±22.64	±55.94	±52.62	±27.28
Total background systematic	±175.24 [0.72%]	±98.37 [1.16%]	±23.43 [4.57%]	±26.49 [0.85%]	±31.35 [1.13%]	±60.41 [8.12%]
mu_Znunu	±391.11 [1.6%]	±0.00 [0.00%]	±0.00 [0.00%]	±50.09 [1.6%]	±0.00 [0.00%]	±0.00 [0.00%]
alpha_ShapeSyst_2Jets	±365.89 [1.5%]	±131.81 [1.5%]	±0.00 [0.00%]	±48.07 [1.5%]	±42.77 [1.5%]	±0.00 [0.00%]
alpha_ClosureSyst_Znunu	±192.04 [0.79%]	±0.00 [0.00%]	±0.00 [0.00%]	±0.00 [0.00%]	±0.00 [0.00%]	±0.00 [0.00%]
alpha_JET_GroupedNP_2	±88.38 [0.36%]	±34.22 [0.40%]	±1.04 [0.20%]	±19.31 [0.62%]	±11.16 [0.40%]	±2.36 [0.32%]
alpha_JET_EtaIntercalibration	±35.30 [0.14%]	±13.04 [0.15%]	±0.51 [0.10%]	±4.66 [0.15%]	±2.97 [0.11%]	±0.68 [0.09%]
alpha_VPt_ckkw_Syst	±32.36 [0.13%]	±9.18 [0.11%]	±0.00 [0.00%]	±3.34 [0.11%]	±2.72 [0.10%]	±0.00 [0.00%]
alpha_JET_GroupedNP_3	±28.07 [0.11%]	±7.57 [0.09%]	±0.78 [0.15%]	±6.83 [0.22%]	±1.63 [0.06%]	±1.07 [0.14%]
alpha_JET_GroupedNP_1	±21.09 [0.09%]	±31.86 [0.37%]	±4.76 [0.93%]	±4.37 [0.14%]	±5.41 [0.20%]	±1.39 [0.19%]
alpha_VPt_qsf_Syst	±13.69 [0.06%]	±5.30 [0.06%]	±0.00 [0.00%]	±2.01 [0.06%]	±1.80 [0.07%]	±0.00 [0.00%]
alpha_MET_SoftTrk	±8.60 [0.04%]	±6.12 [0.07%]	±0.74 [0.14%]	±7.51 [0.24%]	±0.94 [0.03%]	±0.89 [0.12%]
gamma_stat_SR_2Jets_bin_8	±0.40 [0.00%]	±0.07 [0.00%]	±0.00 [0.00%]	±0.02 [0.00%]	±0.01 [0.00%]	±0.02 [0.00%]
gamma_stat_SR_2Jets_bin_9	±0.16 [0.00%]	±0.03 [0.00%]	±0.00 [0.00%]	±0.01 [0.00%]	±0.00 [0.00%]	±0.01 [0.00%]
alpha_EG_Scale	±0.09 [0.00%]	±0.88 [0.01%]	±0.06 [0.01%]	±0.07 [0.00%]	±2.25 [0.08%]	±0.13 [0.02%]
alpha_Mu_MS	±0.08 [0.00%]	±0.15 [0.00%]	±0.08 [0.02%]	±0.15 [0.00%]	±0.03 [0.00%]	±0.02 [0.00%]
alpha_Mu_Id	±0.06 [0.00%]	±0.24 [0.00%]	±0.06 [0.01%]	±0.02 [0.00%]	±0.00 [0.00%]	±0.03 [0.00%]
alpha_Mu_Scale	±0.04 [0.00%]	±0.20 [0.00%]	±0.03 [0.01%]	±0.21 [0.01%]	±0.00 [0.00%]	±0.03 [0.00%]
alpha_EG_Res	±0.00 [0.00%]	±0.35 [0.00%]	±0.06 [0.01%]	±0.03 [0.00%]	±0.43 [0.02%]	±0.03 [0.00%]
mu_Wtaunu	±0.00 [0.00%]	±159.24 [1.9%]	±0.00 [0.00%]	±0.00 [0.00%]	±51.78 [1.9%]	±0.00 [0.00%]
alpha_ClosureSyst_2Jets	±0.00 [0.00%]	±33.16 [0.39%]	±0.00 [0.00%]	±0.00 [0.00%]	±0.00 [0.00%]	±0.00 [0.00%]
alpha_BgXSec	±0.00 [0.00%]	±0.00 [0.00%]	±0.00 [0.00%]	±0.00 [0.00%]	±0.00 [0.00%]	±60.40 [8.1%]
mu_Top	±0.00 [0.00%]	±0.00 [0.00%]	±13.71 [2.7%]	±0.00 [0.00%]	±0.00 [0.00%]	±0.00 [0.00%]
alpha_ttbar_showerSyst	±0.00 [0.00%]	±0.00 [0.00%]	±20.13 [3.9%]	±0.00 [0.00%]	±0.00 [0.00%]	±0.00 [0.00%]
alpha_ttbarRadFlatSyst	±0.00 [0.00%]	±0.00 [0.00%]	±8.06 [1.6%]	±0.00 [0.00%]	±0.00 [0.00%]	±0.00 [0.00%]
alpha_ttbar_hardscatterSyst	±0.00 [0.00%]	±0.00 [0.00%]	±20.13 [3.9%]	±0.00 [0.00%]	±0.00 [0.00%]	±0.00 [0.00%]

Table 7.10.: Systematic uncertainties in the 2 jet SR for the exclusion fit in M_{T2}.

7.4. Interpretation and Comparison

Since the conclusive fit results show a sufficient exclusion sensitivity and no consistent data excess was observed in any of the analysed regions, the method is applied to all available signal mass points of the grid (see figure 5.7) to produce expected and observed exclusion limits.

To calculate the exclusion limits at a 95% confidence level (1.64 σ), the CLs method is used as explained in chapter 7.1. The resulting expected and observed limits from both fits ($E_{\mathrm{T}}^{\mathrm{miss}}$ and M_{T2}) are shown in figure 7.19.

It can be observed that both fits show similar results: the exclusion fit in $E_{\mathrm{T}}^{\mathrm{miss}}$ performs slightly better close to the diagonal, i.e. for signals with smaller Δm while the M_{T2} limit gains a bit more towards higher Δm.

The $E_{\mathrm{T}}^{\mathrm{miss}}$ limit excludes $\tilde{\chi}_1^0$-masses up to 800 GeV, exceeding the expected value of 700 GeV and $\tilde{q}$-masses up to 1300 GeV, slightly staying behind the expected value of 1400 GeV. The M_{T2} limit, on the other hand, excludes $\tilde{\chi}_1^0$-masses up to 700 GeV (and 800 GeV at one point) and $\tilde{q}$-masses up to 1400 GeV, slightly staying behind the expected value of 1500 GeV.

To understand their behaviour, a closer look into the specific signal points is needed.

[SR 3Jets] Uncertainty of	Znunu	Wtaunu	ttbar	Wmunu	Wenu	Other
Total background expectation	13601.64	5763.73	1938.24	1958.61	1741.40	794.71
Total statistical ($\sqrt{N_{exp}}$)	±116.63	±75.92	±44.03	±44.26	±41.73	±28.19
Total background systematic	±119.26 [0.88%]	±72.45 [1.26%]	±53.71 [2.77%]	±21.33 [1.09%]	±21.62 [1.24%]	±64.49 [8.11%]
mu_Znunu	±217.71 [1.6%]	±0.00 [0.00%]	±0.00 [0.00%]	±31.35 [1.6%]	±0.00 [0.00%]	±0.00 [0.00%]
alpha_ShapeSyst_3Jets	±194.26 [1.4%]	±84.89 [1.5%]	±0.00 [0.00%]	±28.58 [1.5%]	±25.71 [1.5%]	±0.00 [0.00%]
alpha_ClosureSyst_Znunu	±111.52 [0.82%]	±0.00 [0.00%]	±0.00 [0.00%]	±0.00 [0.00%]	±0.00 [0.00%]	±0.00 [0.00%]
alpha_JET_GroupedNP_1	±48.39 [0.36%]	±14.15 [0.25%]	±6.78 [0.35%]	±11.36 [0.58%]	±7.91 [0.45%]	±0.61 [0.08%]
alpha_JET_GroupedNP_2	±44.21 [0.33%]	±19.96 [0.35%]	±7.27 [0.38%]	±9.38 [0.48%]	±6.47 [0.37%]	±2.70 [0.34%]
alpha_JET_GroupedNP_3	±23.98 [0.18%]	±8.95 [0.16%]	±0.36 [0.02%]	±5.42 [0.28%]	±3.03 [0.17%]	±0.99 [0.13%]
alpha_VPt_ckkw_Syst	±19.90 [0.15%]	±7.26 [0.13%]	±0.00 [0.00%]	±2.34 [0.12%]	±2.00 [0.11%]	±0.00 [0.00%]
alpha_JET_EtaIntercalibration	±19.14 [0.14%]	±8.30 [0.14%]	±2.91 [0.15%]	±2.53 [0.13%]	±1.99 [0.11%]	±0.61 [0.08%]
alpha_VPt_qsf_Syst	±7.06 [0.05%]	±3.36 [0.06%]	±0.00 [0.00%]	±1.18 [0.06%]	±1.06 [0.06%]	±0.00 [0.00%]
alpha_MET_SoftTrk	±5.66 [0.04%]	±10.12 [0.18%]	±1.18 [0.06%]	±4.27 [0.22%]	±1.28 [0.07%]	±0.58 [0.07%]
gamma_stat_SR_3Jets_bin_8	±0.26 [0.00%]	±0.04 [0.00%]	±0.00 [0.00%]	±0.01 [0.00%]	±0.01 [0.00%]	±0.01 [0.00%]
gamma_stat_SR_3Jets_bin_9	±0.15 [0.00%]	±0.04 [0.00%]	±0.00 [0.00%]	±0.01 [0.00%]	±0.00 [0.00%]	±0.01 [0.00%]
alpha_EG_Scale	±0.12 [0.00%]	±0.44 [0.01%]	±0.45 [0.02%]	±0.00 [0.00%]	±1.04 [0.06%]	±0.07 [0.01%]
gamma_stat_SR_3Jets_bin_10	±0.08 [0.00%]	±0.01 [0.00%]	±0.00 [0.00%]	±0.01 [0.00%]	±0.00 [0.00%]	±0.01 [0.00%]
alpha_Mu_Id	±0.02 [0.00%]	±0.12 [0.00%]	±0.05 [0.00%]	±0.02 [0.00%]	±0.00 [0.00%]	±0.01 [0.00%]
alpha_EG_Res	±0.01 [0.00%]	±0.05 [0.00%]	±0.06 [0.00%]	±0.00 [0.00%]	±0.09 [0.01%]	±0.06 [0.01%]
alpha_Mu_Scale	±0.00 [0.00%]	±0.16 [0.00%]	±0.14 [0.01%]	±0.22 [0.01%]	±0.00 [0.00%]	±0.03 [0.00%]
alpha_Mu_MS	±0.00 [0.00%]	±0.02 [0.00%]	±0.20 [0.01%]	±0.02 [0.00%]	±0.00 [0.00%]	±0.01 [0.00%]
mu_Wtaunu	±0.00 [0.00%]	±107.81 [1.9%]	±0.00 [0.00%]	±0.00 [0.00%]	±32.57 [1.9%]	±0.00 [0.00%]
alpha_BgXSec	±0.00 [0.00%]	±0.00 [0.00%]	±0.00 [0.00%]	±0.00 [0.00%]	±0.00 [0.00%]	±64.51 [8.1%]
mu_Top	±0.00 [0.00%]	±0.00 [0.00%]	±51.86 [2.7%]	±0.00 [0.00%]	±0.00 [0.00%]	±0.00 [0.00%]
alpha_ttbar_showerSyst	±0.00 [0.00%]	±0.00 [0.00%]	±29.64 [1.5%]	±0.00 [0.00%]	±0.00 [0.00%]	±0.00 [0.00%]
alpha_ClosureSyst_3Jets	±0.00 [0.00%]	±25.02 [0.43%]	±0.00 [0.00%]	±0.00 [0.00%]	±0.00 [0.00%]	±0.00 [0.00%]
alpha_ttbarRadFlatSyst	±0.00 [0.00%]	±0.00 [0.00%]	±27.01 [1.4%]	±0.00 [0.00%]	±0.00 [0.00%]	±0.00 [0.00%]
alpha_ttbar_hardscatterSyst	±0.00 [0.00%]	±0.00 [0.00%]	±29.64 [1.5%]	±0.00 [0.00%]	±0.00 [0.00%]	±0.00 [0.00%]

Table 7.11.: Systematic uncertainties in the 3 jet SR for the exclusion fit in M_{T2}.

Figure 7.20 shows a comparison of the (before fit) SR distributions of the signals with $m_{\tilde{q}} = 1000\,\mathrm{GeV}$ and $m_{\tilde{\chi}_1^0} = 800\,\mathrm{GeV}$ and $m_{\tilde{q}} = 1200\,\mathrm{GeV}$ and $m_{\tilde{\chi}_1^0} = 800\,\mathrm{GeV}$. It can be seen that the shape differences between signal and background are more pronounced in the second case, especially for higher values and in the 2 jet and 3 jet regions. This explains why it is easier for the fit to gain a high exclusion power for this mass point in contrast to the neighbouring signal point.

Both limits show a sharp decline at $m_{\tilde{q}} = 1300\,\mathrm{GeV}$ to $m_{\tilde{q}} = 1400\,\mathrm{GeV}$ which are caused by unfavourable statistic fluctuations, as shown exemplarily in figure 7.21. Since the shape of the signal is in accordance with the fluctuations in the highest bins, the fit is not able to reduce the signal strength and especially the corresponding uncertainty ($\mu_{\mathrm{sig}} = 0.01 \pm 6.15$) enough to exclude this signal point.

As described in section 6.2, the ATLAS 0-lepton group also conducted their search for SUSY signals on the complete data set of 2015 and 2016. They were able to improve the 8 TeV analysis presented in [57] and strongly enlarge the exclusion limit in the $m_{\tilde{q}}$ - $m_{\tilde{\chi}_1^0}$-mass plane as it was shown in figure 6.1. The new 13 TeV exclusion limit as published in [105] is drawn for comparison in figure 7.19.
Concluding from the comparison, the analysis of this thesis shows a higher sensitivity

[SR 4Jets] Uncertainty of	Znunu	Wtaunu	ttbar	Wmunu	Wenu	Other
Total background expectation	19035.78	9531.41	9106.98	2935.17	2784.56	1955.57
Total statistical ($\sqrt{N_{exp}}$)	±137.97	±97.63	±95.43	±54.18	±52.77	±44.22
Total background systematic	±203.98 [1.07%]	±142.23 [1.49%]	±194.67 [2.14%]	±39.53 [1.35%]	±40.35 [1.45%]	±160.48 [8.21%]
alpha_ShapeSyst_4Jets	±340.30 [1.8%]	±174.79 [1.8%]	±0.00 [0.00%]	±53.99 [1.8%]	±51.45 [1.8%]	±0.00 [0.00%]
mu_Znunu	±304.69 [1.6%]	±0.00 [0.00%]	±0.00 [0.00%]	±46.98 [1.6%]	±0.00 [0.00%]	±0.00 [0.00%]
alpha_JET_GroupedNP_1	±293.76 [1.5%]	±153.50 [1.6%]	±124.20 [1.4%]	±55.35 [1.9%]	±48.21 [1.7%]	±24.91 [1.3%]
alpha_ClosureSyst_Znunu	±165.80 [0.87%]	±0.00 [0.00%]	±0.00 [0.00%]	±0.00 [0.00%]	±0.00 [0.00%]	±0.00 [0.00%]
alpha_JET_GroupedNP_2	±88.34 [0.46%]	±50.44 [0.53%]	±54.60 [0.60%]	±17.91 [0.61%]	±16.92 [0.61%]	±9.27 [0.47%]
alpha_JET_GroupedNP_3	±74.06 [0.39%]	±38.94 [0.41%]	±33.36 [0.37%]	±13.92 [0.47%]	±13.05 [0.47%]	±6.20 [0.32%]
alpha_VPt_ckkw_Syst	±33.13 [0.17%]	±14.34 [0.15%]	±0.00 [0.00%]	±4.29 [0.15%]	±3.95 [0.14%]	±0.00 [0.00%]
alpha_JET_EtaIntercalibration	±32.33 [0.17%]	±16.13 [0.17%]	±21.01 [0.23%]	±7.25 [0.25%]	±5.23 [0.19%]	±3.92 [0.20%]
alpha_VPt_qsf_Syst	±10.25 [0.05%]	±5.97 [0.06%]	±0.00 [0.00%]	±1.87 [0.06%]	±1.82 [0.07%]	±0.00 [0.00%]
alpha_MET_SoftTrk	±7.89 [0.04%]	±12.35 [0.13%]	±11.87 [0.13%]	±6.36 [0.22%]	±3.61 [0.13%]	±2.88 [0.15%]
alpha_EG_Scale	±0.22 [0.00%]	±0.76 [0.01%]	±2.23 [0.02%]	±0.04 [0.00%]	±2.41 [0.09%]	±0.25 [0.01%]
gamma_stat_SR_4Jets_bin_10	±0.21 [0.00%]	±0.02 [0.00%]	±0.00 [0.00%]	±0.01 [0.00%]	±0.01 [0.00%]	±0.04 [0.00%]
gamma_stat_SR_4Jets_bin_9	±0.20 [0.00%]	±0.02 [0.00%]	±0.00 [0.00%]	±0.01 [0.00%]	±0.01 [0.00%]	±0.02 [0.00%]
alpha_Mu_MS	±0.06 [0.00%]	±0.21 [0.00%]	±0.03 [0.00%]	±0.35 [0.01%]	±0.03 [0.00%]	±0.01 [0.00%]
alpha_Mu_Scale	±0.06 [0.00%]	±0.20 [0.00%]	±0.31 [0.00%]	±0.66 [0.02%]	±0.01 [0.00%]	±0.09 [0.00%]
alpha_Mu_Id	±0.05 [0.00%]	±0.07 [0.00%]	±0.31 [0.00%]	±0.38 [0.01%]	±0.02 [0.00%]	±0.12 [0.01%]
alpha_EG_Res	±0.00 [0.00%]	±0.12 [0.00%]	±0.07 [0.00%]	±0.01 [0.00%]	±0.07 [0.00%]	±0.08 [0.00%]
mu_Wtaunu	±0.00 [0.00%]	±178.28 [1.9%]	±0.00 [0.00%]	±0.00 [0.00%]	±52.08 [1.9%]	±0.00 [0.00%]
alpha_BgXSec	±0.00 [0.00%]	±0.00 [0.00%]	±0.00 [0.00%]	±0.00 [0.00%]	±0.00 [0.00%]	±158.73 [8.1%]
mu_Top	±0.00 [0.00%]	±0.00 [0.00%]	±243.67 [2.7%]	±0.00 [0.00%]	±0.00 [0.00%]	±0.00 [0.00%]
alpha_ttbar_showerSyst	±0.00 [0.00%]	±0.00 [0.00%]	±116.25 [1.3%]	±0.00 [0.00%]	±0.00 [0.00%]	±0.00 [0.00%]
alpha_ClosureSyst_4Jets	±0.00 [0.00%]	±28.11 [0.29%]	±0.00 [0.00%]	±0.00 [0.00%]	±0.00 [0.00%]	±0.00 [0.00%]
alpha_ttbarRadFlatSyst	±0.00 [0.00%]	±0.00 [0.00%]	±125.53 [1.4%]	±0.00 [0.00%]	±0.00 [0.00%]	±0.00 [0.00%]
alpha_ttbar_hardscatterSyst	±0.00 [0.00%]	±0.00 [0.00%]	±116.25 [1.3%]	±0.00 [0.00%]	±0.00 [0.00%]	±0.00 [0.00%]

Table 7.12.: Systematic uncertainties in the ≥4 jet SR for the exclusion fit in M_{T2}.

and has more exclusion strength in the region of small and medium Δm signals, just as intended and described in section 6.1.

The corresponding result of the CMS 0-lepton group, obtained with a similar analysis of the 2015+2016 data set ($35.9\,\mathrm{fb}^{-1}$) at 13 TeV, see [133], is presented in figure 7.22 as second comparison. It can be concluded that their results are comparable to those of the analysis presented in this thesis: neutralino masses up to 800 GeV and squark masses up to 1400 GeV can be excluded.

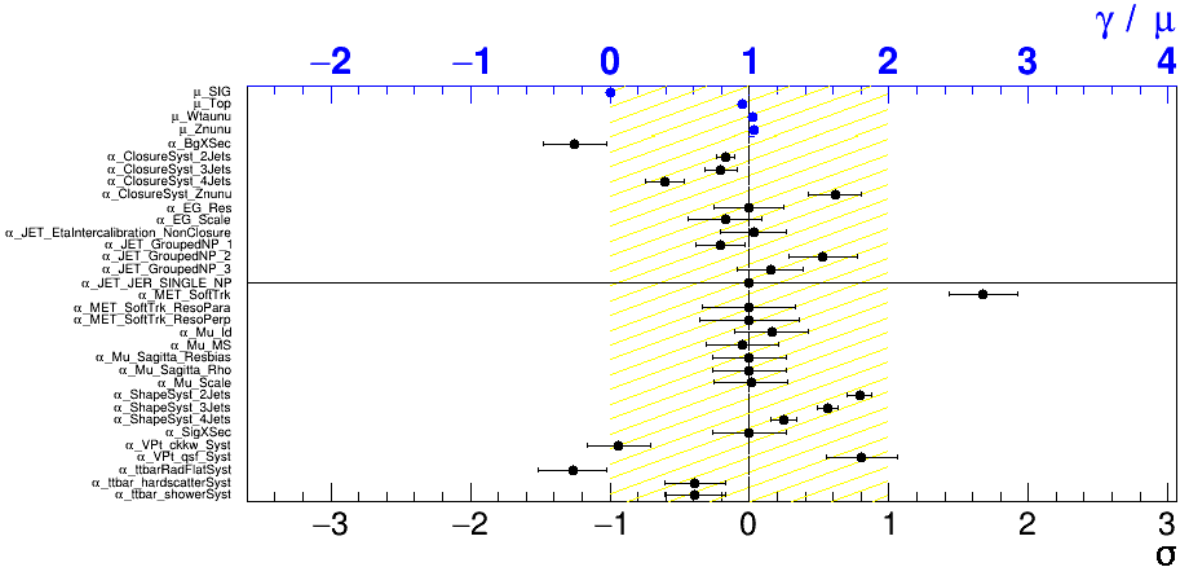

Figure 7.18.: Overview of the final fit parameter values after the exclusion fit in M_{T2}. The normalisation factors are shown on top, below the deviations from the nominal value can be seen (in units of σ) of the systematic uncertainties as they were pulled by the fit.

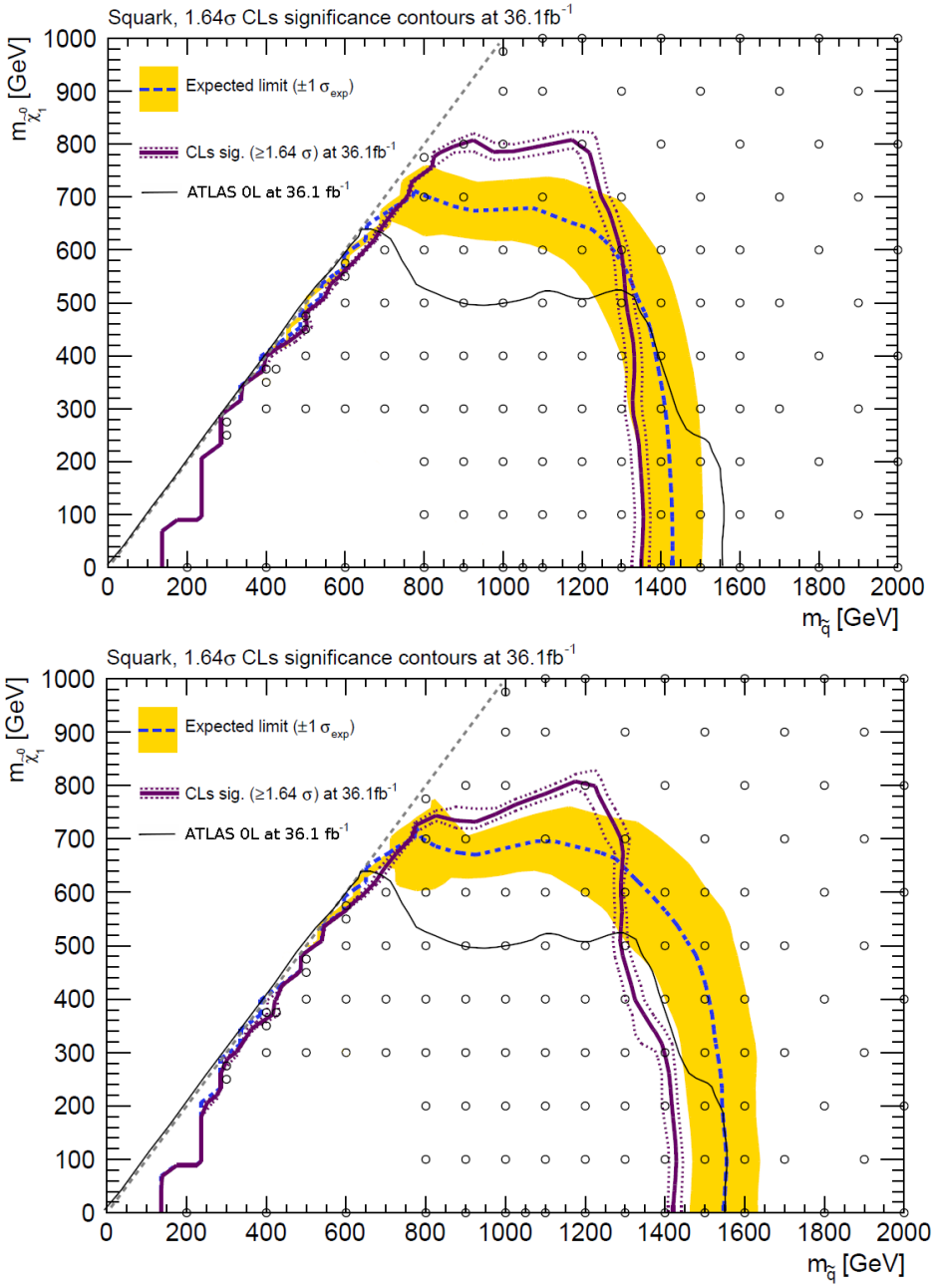

Figure 7.19.: Expected exclusion limit (blue dashed line with yellow uncertainty band) and observed exclusion limit (purple line with dashed uncertainty band) of the $E_{\mathrm{T}}^{\mathrm{miss}}$ (top) and the M_{T2} (bottom) fit. For comparison, the corresponding result of the ATLAS 0-lepton group is shown (black line) based on [105].

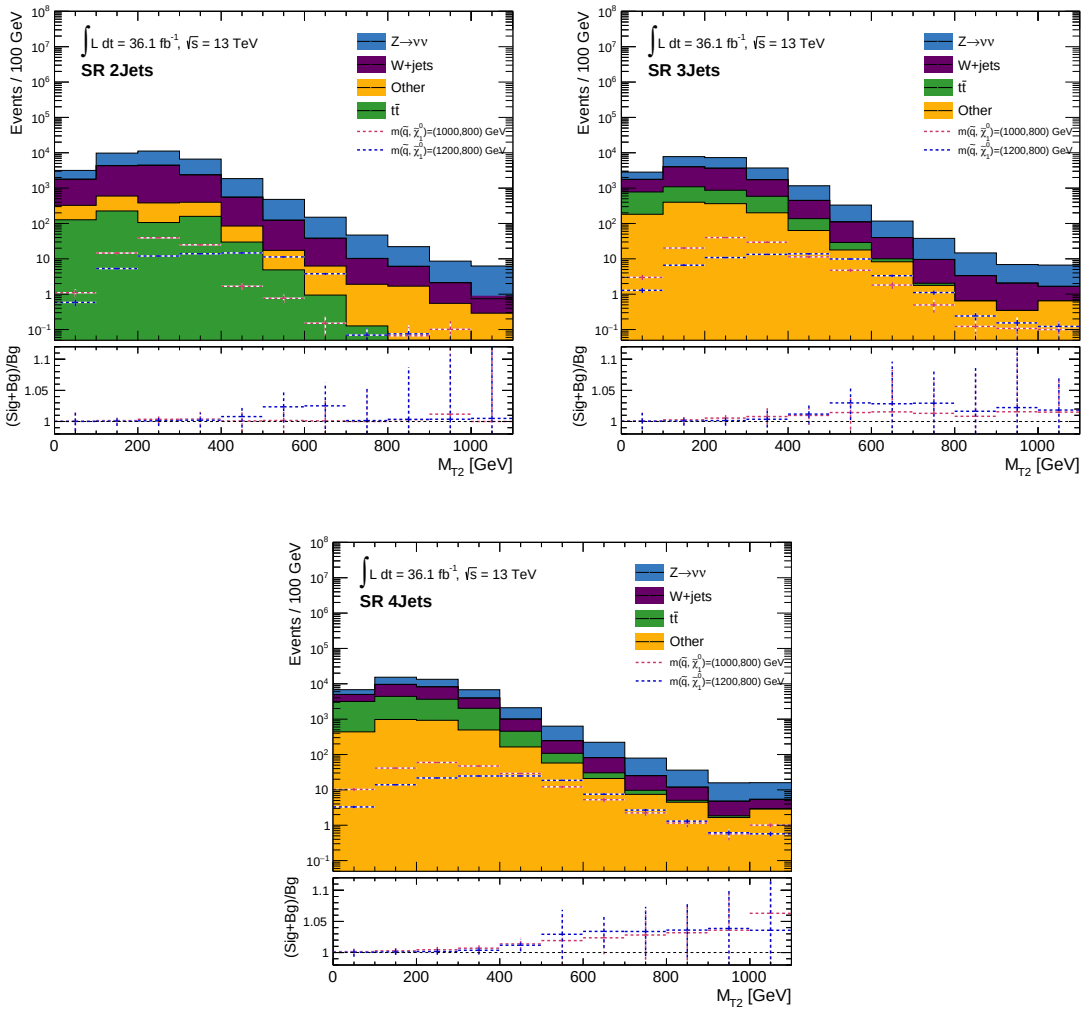

Figure 7.20.: Comparison of M_{T2} distributions in the 2 jet, 3 jet and $\geqslant$ 4 jet SR for two signal mass points with $m_{\tilde{q}} = 1000\,\mathrm{GeV}$, $m_{\tilde{\chi}_1^0} = 800\,\mathrm{GeV}$ (red) and $m_{\tilde{q}} = 1200\,\mathrm{GeV}$, $m_{\tilde{\chi}_1^0} = 800\,\mathrm{GeV}$ (blue).

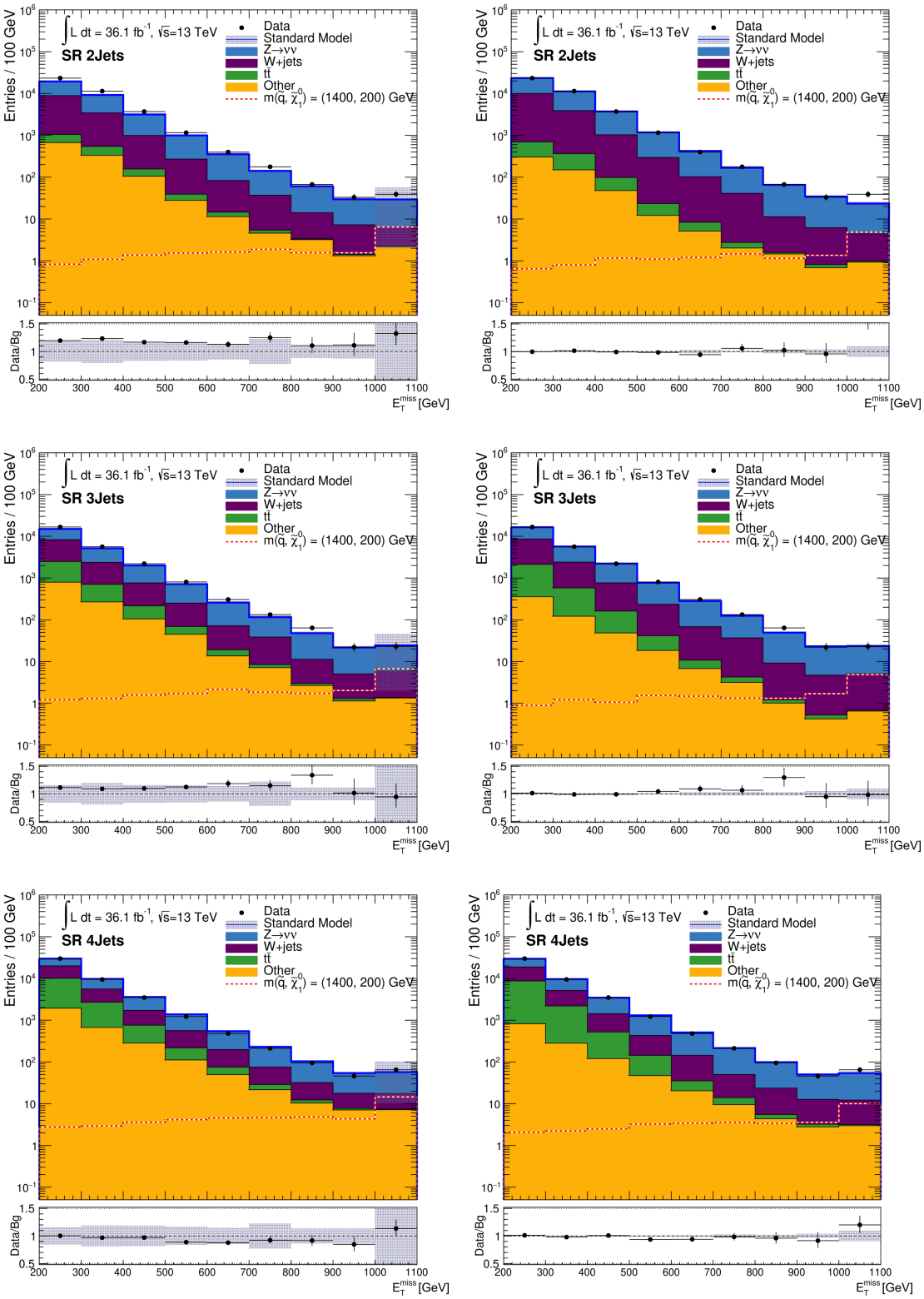

Figure 7.21.: Before and after fit $E_{\mathrm{T}}^{\mathrm{miss}}$ distributions in the 2 jet, 3 jet and $\geqslant 4$ jet SRs with the $m_{\tilde{q}} = 1400\,\mathrm{GeV}$, $m_{\tilde{\chi}_1^0} = 200\,\mathrm{GeV}$ signal point.

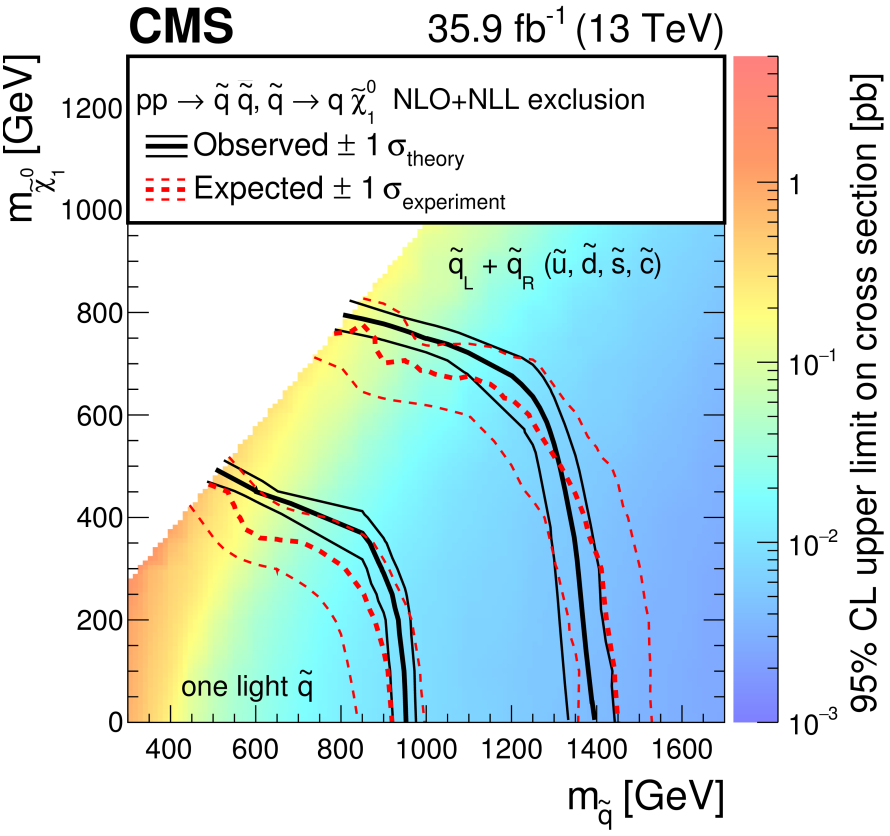

Figure 7.22.: Expected and observed exclusion limits of the CMS 0-lepton group as published in [133]. The limits indicated with "one light $\tilde{q}$" show the excluded mass points under the assumption that only one state (flavour and spin) was accessible at the LHC. The limits indicated with "$\tilde{q_L} + \tilde{q_R}(\tilde{u}, \tilde{d}, \tilde{s}, \tilde{c})$" show the excluded area under the assumption that all four flavour states are accessible at the LHC.

Chapter 8.

Summary and Outlook

8.1. Summary

In this thesis, an analysis was presented which was developed as a generic search for physics beyond the SM, focussing on final states with jets and $E_{\mathrm{T}}^{\mathrm{miss}}$. It is based on a shape sensitive method using a profile likelihood fit to determine the sensitivity especially for signals with small and medium Δm between the two BSM particles.
The analysis was applied to a SUSY model as a benchmark, describing the pair production of squarks, which decay into quarks (leading to jets) and neutralinos (causing $E_{\mathrm{T}}^{\mathrm{miss}}$).
The fit was performed in two discriminating variables, $E_{\mathrm{T}}^{\mathrm{miss}}$ and M_{T2}, which were divided into three jet multiplicity bins (2 jets, 3 jets and ≥ 4 jets) to increase the available shape information and to improve the sensitivity. Experimental and theoretical uncertainties of the Monte Carlo simulated samples for backgrounds and signal were considered. Moreover, a data-driven background estimation was applied to improve the accuracy of the Monte Carlo predictions, optimised using a replacement-method for the two main backgrounds arising from $Z \to \nu\nu$ and $W \to \tau\nu$ processes.
The analysis was conducted on the full data set of proton-proton collisions with an integrated luminosity of $36.1\,\mathrm{fb}^{-1}$, recorded by the ATLAS experiment in 2015 and 2016 at 13 TeV centre-of-mass energy.

A data excess was found in the SRs and muon CRs, indicating a potential leptoquark signal. However, further investigations of these regions in different discriminating variables, considering multiple final states, could not confirm this observation.

As the observed data showed no significant excess in the signal regions, exclusion limits were set in the mass plane of the two SUSY particles. Neutralino masses up to 800 GeV and squark masses up to 1400 GeV were excluded. The $E_{\mathrm{T}}^{\mathrm{miss}}$ variable is better suited for the regions with small and medium Δm, while M_{T2} shows better sensitivity for large Δm. Figure 8.1 shows the results in comparison with the result of the ATLAS 0-lepton group

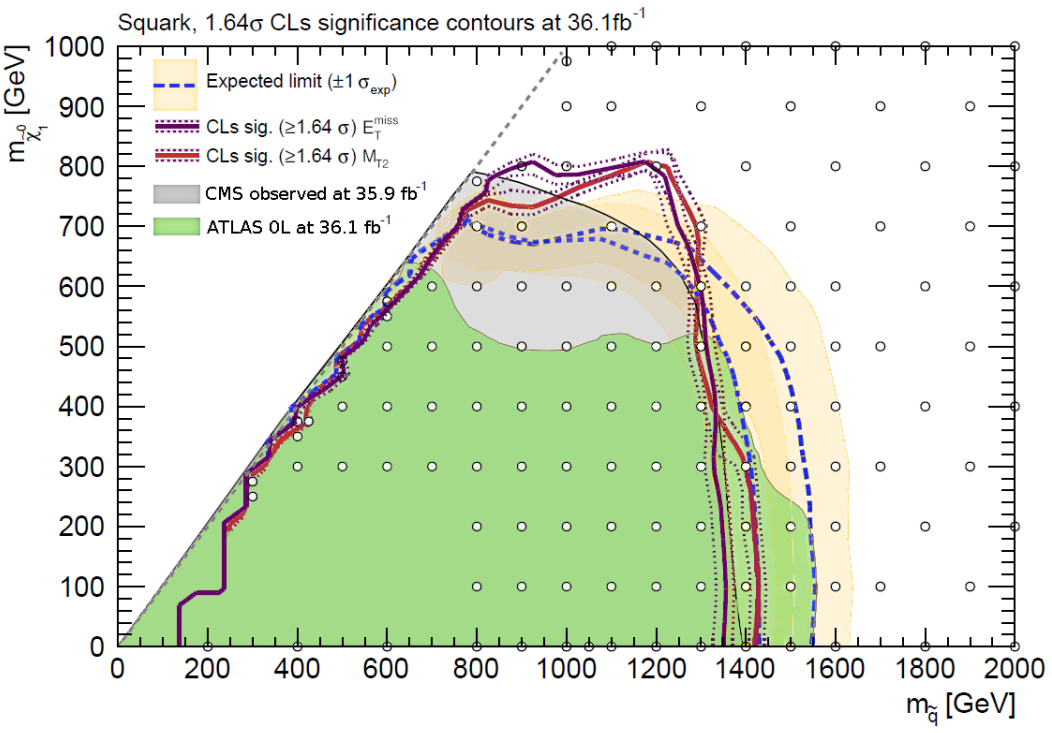

Figure 8.1.: Comparison of the resulting exclusion limits from the $E_{\mathrm{T}}^{\mathrm{miss}}$ (purple) and M_{T2} (red) shape fits and the results of the ATLAS 0-lepton and CMS groups.

and the corresponding exclusion limit set by the CMS collaboration. A clear improvement can be observed in the region of medium Δm, especially compared to the ATLAS result.

8.2. Outlook

During the completion of this thesis, the ATLAS Experiment continued taking data until the end of 2018 when the LHC commenced a long technical stop, collecting a total integrated luminosity of 147 fb^{-1} (2015-2018). The increased data statistics can improve the sensitivity for many searches, in this case the fit would gain more sensitivity especially for signals with high Δm that suffered from statistical fluctuations in the higher $E_{\mathrm{T}}^{\mathrm{miss}}$ or M_{T2} bins.

Other potential improvements could be made by optimising the replacement method and consequently reducing the corresponding systematic uncertainty. Similar to the monojet approach, other processes such as $Z \to \mu\mu$, $Z \to ee$ or $W \to e\nu$ could be used for an

improved estimation of the $Z \to \nu\nu$ background. Furthermore, using dedicated CRs for other backgrounds like $t\bar{t}$ could lead to a better prediction and reduce uncertainties. New lepton triggers are now available, which could replace the $E_{\mathrm{T}}^{\mathrm{miss}}$ triggers in the CRs. They could possibly lead to a better performance, especially for low $E_{\mathrm{T}}^{\mathrm{miss}}$ events in the electron CRs.

Since the analysis was constructed to be generic, it could also be applied to other BSM models, e.g. other MSSM channels, extra dimensions or leptoquarks, following up and completing the analysis.

The next LHC run (Run 3) is planned to start in 2021. Until then, detectors, accelerators and other components along the injector chain will receive upgrades or will be replaced. As a result, an increase to the full design energy of 14 TeV will be possible. The High-Luminosity LHC upgrade[134] [135], reaching an estimated integrated luminosity of $3000\,\mathrm{fb}^{-1}$, will be the next step towards the discovery of even heavier particles and rarer processes.
CERN has also published plans to extend the LHC's operating life: the Future Circular Collider (FCC)[136] with a circumference of 100km could take the place as the next most powerful accelerator, providing centre-of-mass energies of up to 100 TeV and pushing the boundaries for many future searches.

Appendix A.

Monte Carlo Simulations

In the following, the Monte Carlo simulations for all SM background processes considered in this analysis are listed. Subsequently the signal processes are listed, which are used as benchmark models in this analysis, covering the parameter space of $m_{\tilde{q}}$ and $m_{\tilde{\chi}_1^0}$ from 200 GeV to 2200 GeV and 0 GeV to 1100 GeV respectively.

Process	cross section	k factor
Sherpa_221_NNPDF30NNLO_Wenu_MAXHTPTV0_70_CVetoBVeto	19127.0	0.799900794
Sherpa_221_NNPDF30NNLO_Wenu_MAXHTPTV0_70_CFilterBVeto	19130.0	0.12641706
Sherpa_221_NNPDF30NNLO_Wenu_MAXHTPTV0_70_BFilter	19135.0	0.0428255982
Sherpa_221_NNPDF30NNLO_Wenu_MAXHTPTV70_140_CVetoBVeto	942.58	0.648792144
Sherpa_221_NNPDF30NNLO_Wenu_MAXHTPTV70_140_CFilterBVeto	945.67	0.221079474
Sherpa_221_NNPDF30NNLO_Wenu_MAXHTPTV70_140_BFilter	945.15	0.100328382
Sherpa_221_NNPDF30NNLO_Wenu_MAXHTPTV140_280_CVetoBVeto	339.81	0.579122082
Sherpa_221_NNPDF30NNLO_Wenu_MAXHTPTV140_280_CFilterBVeto	339.87	0.28101843
Sherpa_221_NNPDF30NNLO_Wenu_MAXHTPTV140_280_BFilter	339.48	0.105732396
Sherpa_221_NNPDF30NNLO_Wenu_MAXHTPTV280_500_CVetoBVeto	72.084	0.528186582
Sherpa_221_NNPDF30NNLO_Wenu_MAXHTPTV280_500_CFilterBVeto	72.128	0.30731085
Sherpa_221_NNPDF30NNLO_Wenu_MAXHTPTV280_500_BFilter	72.113	0.129919482
Sherpa_221_NNPDF30NNLO_Wenu_MAXHTPTV500_1000	15.224	0.9702
Sherpa_221_NNPDF30NNLO_Wenu_MAXHTPTV1000_E_CMS	1.2334	0.9702
Sherpa_221_NNPDF30NNLO_Wmunu_MAXHTPTV0_70_CVetoBVeto	19143.0	0.79925076
Sherpa_221_NNPDF30NNLO_Wmunu_MAXHTPTV0_70_CFilterBVeto	19121.0	0.12651408
Sherpa_221_NNPDF30NNLO_Wmunu_MAXHTPTV0_70_BFilter	19135.0	0.0428032836
Sherpa_221_NNPDF30NNLO_Wmunu_MAXHTPTV70_140_CVetoBVeto	944.85	0.654526026
Sherpa_221_NNPDF30NNLO_Wmunu_MAXHTPTV70_140_CFilterBVeto	937.78	0.227570112
Sherpa_221_NNPDF30NNLO_Wmunu_MAXHTPTV70_140_BFilter	944.63	0.0733936896
Sherpa_221_NNPDF30NNLO_Wmunu_MAXHTPTV140_280_CVetoBVeto	339.54	0.607354902
Sherpa_221_NNPDF30NNLO_Wmunu_MAXHTPTV140_280_CFilterBVeto	340.06	0.280843794
Sherpa_221_NNPDF30NNLO_Wmunu_MAXHTPTV140_280_BFilter	339.54	0.105480144
Sherpa_221_NNPDF30NNLO_Wmunu_MAXHTPTV280_500_CVetoBVeto	72.067	0.530185194
Sherpa_221_NNPDF30NNLO_Wmunu_MAXHTPTV280_500_CFilterBVeto	72.198	0.307970586
Sherpa_221_NNPDF30NNLO_Wmunu_MAXHTPTV280_500_BFilter	72.045	0.129395574
Sherpa_221_NNPDF30NNLO_Wmunu_MAXHTPTV500_1000	15.01	0.9702
Sherpa_221_NNPDF30NNLO_Wmunu_MAXHTPTV1000_E_CMS	1.2344	0.9702
Sherpa_221_NNPDF30NNLO_Wtaunu_MAXHTPTV0_70_CVetoBVeto	19152.0	0.80036649
Sherpa_221_NNPDF30NNLO_Wtaunu_MAXHTPTV0_70_CFilterBVeto	19153.0	0.125485668
Sherpa_221_NNPDF30NNLO_Wtaunu_MAXHTPTV0_70_BFilter	19163.0	0.0432650988
Sherpa_221_NNPDF30NNLO_Wtaunu_MAXHTPTV70_140_CVetoBVeto	947.65	0.653740164
Sherpa_221_NNPDF30NNLO_Wtaunu_MAXHTPTV70_140_CFilterBVeto	946.73	0.215597844
Sherpa_221_NNPDF30NNLO_Wtaunu_MAXHTPTV70_140_BFilter	943.30	0.100861992
Sherpa_221_NNPDF30NNLO_Wtaunu_MAXHTPTV140_280_CVetoBVeto	339.36	0.578452644
Sherpa_221_NNPDF30NNLO_Wtaunu_MAXHTPTV140_280_CFilterBVeto	339.63	0.28160055
Sherpa_221_NNPDF30NNLO_Wtaunu_MAXHTPTV140_280_BFilter	339.54	0.114473898
Sherpa_221_NNPDF30NNLO_Wtaunu_MAXHTPTV280_500_CVetoBVeto	72.065	0.502143938
Sherpa_221_NNPDF30NNLO_Wtaunu_MAXHTPTV280_500_CFilterBVeto	71.976	0.307048896
Sherpa_221_NNPDF30NNLO_Wtaunu_MAXHTPTV280_500_BFilter	72.026	0.130259052
Sherpa_221_NNPDF30NNLO_Wtaunu_MAXHTPTV500_1000	15.046	0.9702
Sherpa_221_NNPDF30NNLO_Wtaunu_MAXHTPTV1000_E_CMS	1.2339	0.9702

Table A.1.: $W \to l\nu$ (Sherpa 2.2.1)

Process	cross section	k factor
Sherpa_221_NNPDF30NNLO_Zee_MAXHTPTV0_70_CVetoBVeto	1981.8	0.800615606
Sherpa_221_NNPDF30NNLO_Zee_MAXHTPTV0_70_CFilterBVeto	1980.8	0.110137545
Sherpa_221_NNPDF30NNLO_Zee_MAXHTPTV0_70_BFilter	1981.7	0.0622201559
Sherpa_221_NNPDF30NNLO_Zee_MAXHTPTV70_140_CVetoBVeto	110.5	0.673238293
Sherpa_221_NNPDF30NNLO_Zee_MAXHTPTV70_140_CFilterBVeto	110.63	0.179242882
Sherpa_221_NNPDF30NNLO_Zee_MAXHTPTV70_140_BFilter	110.31	0.111580693
Sherpa_221_NNPDF30NNLO_Zee_MAXHTPTV140_280_CVetoBVeto	40731	0.599218452
Sherpa_221_NNPDF30NNLO_Zee_MAXHTPTV140_280_CFilterBVeto	40.67	0.224702044
Sherpa_221_NNPDF30NNLO_Zee_MAXHTPTV140_280_BFilter	40.643	0.145933466
Sherpa_221_NNPDF30NNLO_Zee_MAXHTPTV280_500_CVetoBVeto	8.6743	0.547362634
Sherpa_221_NNPDF30NNLO_Zee_MAXHTPTV280_500_CFilterBVeto	8.6711	0.256392794
Sherpa_221_NNPDF30NNLO_Zee_MAXHTPTV280_500_BFilter	8.6766	0.167941473
Sherpa_221_NNPDF30NNLO_Zee_MAXHTPTV500_1000	1.8081	0.9751
Sherpa_221_NNPDF30NNLO_Zee_MAXHTPTV1000_E_CMS	0.14857	0.9751
Sherpa_221_NNPDF30NNLO_Zmumu_MAXHTPTV0_70_CVetoBVeto	1983.0	0.80162971
Sherpa_221_NNPDF30NNLO_Zmumu_MAXHTPTV0_70_CFilterBVeto	1978.4	0.110264308
Sherpa_221_NNPDF30NNLO_Zmumu_MAXHTPTV0_70_BFilter	1982.2	0.0625633911
Sherpa_221_NNPDF30NNLO_Zmumu_MAXHTPTV70_140_CVetoBVeto	108.92	0.671580623
Sherpa_221_NNPDF30NNLO_Zmumu_MAXHTPTV70_140_CFilterBVeto	109.42	0.181329596
Sherpa_221_NNPDF30NNLO_Zmumu_MAXHTPTV70_140_BFilter	108.91	0.110917625
Sherpa_221_NNPDF30NNLO_Zmumu_MAXHTPTV140_280_CVetoBVeto	39.878	0.593826149
Sherpa_221_NNPDF30NNLO_Zmumu_MAXHTPTV140_280_CFilterBVeto	39.795	0.227276308
Sherpa_221_NNPDF30NNLO_Zmumu_MAXHTPTV140_280_BFilter	39.908	0.142540118
Sherpa_221_NNPDF30NNLO_Zmumu_MAXHTPTV280_500_CVetoBVeto	8.5375	0.545139406
Sherpa_221_NNPDF30NNLO_Zmumu_MAXHTPTV280_500_CFilterBVeto	8.5403	0.258674528
Sherpa_221_NNPDF30NNLO_Zmumu_MAXHTPTV280_500_BFilter	8.4932	0.171217809
Sherpa_221_NNPDF30NNLO_Zmumu_MAXHTPTV500_1000	1.7881	0.9751
Sherpa_221_NNPDF30NNLO_Zmumu_MAXHTPTV1000_E_CMS	0.14769	0.9751
Sherpa_221_NNPDF30NNLO_Ztautau_MAXHTPTV0_70_CVetoBVeto	1981.6	0.800966642
Sherpa_221_NNPDF30NNLO_Ztautau_MAXHTPTV0_70_CFilterBVeto	1978.8	0.110322814
Sherpa_221_NNPDF30NNLO_Ztautau_MAXHTPTV0_70_BFilter	1981.8	0.0628481203
Sherpa_221_NNPDF30NNLO_Ztautau_MAXHTPTV70_140_CVetoBVeto	110.37	0.671678133
Sherpa_221_NNPDF30NNLO_Ztautau_MAXHTPTV70_140_CFilterBVeto	110.51	0.17834579
Sherpa_221_NNPDF30NNLO_Ztautau_MAXHTPTV70_140_BFilter	110.87	0.1081249386
Sherpa_221_NNPDF30NNLO_Ztautau_MAXHTPTV140_280_CVetoBVeto	40.781	0.593065571
Sherpa_221_NNPDF30NNLO_Ztautau_MAXHTPTV140_280_CFilterBVeto	40.74	0.223268647
Sherpa_221_NNPDF30NNLO_Ztautau_MAXHTPTV140_280_BFilter	40.761	0.131072942
Sherpa_221_NNPDF30NNLO_Ztautau_MAXHTPTV280_500_CVetoBVeto	8.5502	0.546407036
Sherpa_221_NNPDF30NNLO_Ztautau_MAXHTPTV280_500_CFilterBVeto	8.6707	0.255914995
Sherpa_221_NNPDF30NNLO_Ztautau_MAXHTPTV280_500_BFilter	8.6804	0.168819063
Sherpa_221_NNPDF30NNLO_Ztautau_MAXHTPTV500_1000	1.8096	0.9751
Sherpa_221_NNPDF30NNLO_Ztautau_MAXHTPTV1000_E_CMS	0.14834	0.9751
Sherpa_221_NNPDF30NNLO_Znunu_MAXHTPTV0_70_CVetoBVeto	10700.0	0.79925248
Sherpa_221_NNPDF30NNLO_Znunu_MAXHTPTV0_70_CFilterBVeto	10702.0	0.108204544
Sherpa_221_NNPDF30NNLO_Znunu_MAXHTPTV0_70_BFilter	10709.0	0.06437504
Sherpa_221_NNPDF30NNLO_Znunu_MAXHTPTV70_140_CVetoBVeto	603.23	0.670492672
Sherpa_221_NNPDF30NNLO_Znunu_MAXHTPTV70_140_CFilterBVeto	608.15	0.177467904
Sherpa_221_NNPDF30NNLO_Znunu_MAXHTPTV70_140_BFilter	603.32	0.11629824
Sherpa_221_NNPDF30NNLO_Znunu_MAXHTPTV140_280_CVetoBVeto	222.28	0.59083008
Sherpa_221_NNPDF30NNLO_Znunu_MAXHTPTV140_280_CFilterBVeto	221.88	0.219142656
Sherpa_221_NNPDF30NNLO_Znunu_MAXHTPTV140_280_BFilter	222.47	0.14771968
Sherpa_221_NNPDF30NNLO_Znunu_MAXHTPTV280_500_CVetoBVeto	47.375	0.543668736
Sherpa_221_NNPDF30NNLO_Znunu_MAXHTPTV280_500_CFilterBVeto	47.397	0.254883328
Sherpa_221_NNPDF30NNLO_Znunu_MAXHTPTV280_500_BFilter	47.476	0.170376192
Sherpa_221_NNPDF30NNLO_Znunu_MAXHTPTV500_1000	9.9099	0.9728
Sherpa_221_NNPDF30NNLO_Znunu_MAXHTPTV1000_E_CMS	0.81809	0.9728

Table A.2.: $Z \to \nu\nu$ & $Z \to l\nu$ (Sherpa 2.2.1)

Process	cross section	k factor
Sherpa_CT10_llvvjj_ss_EW4	0.025765	0.91
Sherpa_CT10_llvvjj_ss_EW6	0.043375	0.91
Sherpa_CT10_lllvjj_EW6	0.042287	0.91
Sherpa_CT10_lllljj_EW6	0.031496	0.91
Sherpa_CT10_gglllll	0.02095	0.91
Sherpa_CT10_ggllvv	0.85492	0.91
Sherpa_221_NNPDF30NNLO_ZqqZvv	15.564	0.27976
Sherpa_221_NNPDF30NNLO_ZqqZll	15.563	0.13961
Sherpa_221_NNPDF30NNLO_WqqZvv	6.7973	1.0
Sherpa_221_NNPDF30NNLO_WqqZll	3.437	1.0
Sherpa_221_NNPDF30NNLO_WpqqWmlv	2.4717	1.0
Sherpa_221_NNPDF30NNLO_WplvWmqq	2.4725	1.0
Sherpa_221_NNPDF30NNLO_WlvZqq	11.413	1.0
Sherpa_221_NNPDF30NNLO_llll	1.2557	1.0
Sherpa_221_NNPDF30NNLO_lllv	4.5877	1.0
Sherpa_221_NNPDF30NNLO_llvv	12.465	1.0
Sherpa_221_NNPDF30NNLO_lvvv	3.2274	1.0
Sherpa_221_NNPDF30NNLO_vvvv	0.60154	1.0

Table A.3.: Diboson (Sherpa 2.2.1)

Process	cross section	k factor
PowhegPythiaEvtGen_P2012_ttbar_hdamp172p5_allhad	695.99	0.54520462
PowhegPythiaEvtGen_P2012_ttbar_hdamp172p5_nonallhad	696.11	0.6488307
PowhegPythiaEvtGen_P2012CT10_ttbarMET200_hdamp172p5_nonAH	696.22	0.0110163506775
PowhegPythiaEvtGen_P2012CT10_ttbarMET300_hdamp172p5_nonAH	696.21	0.00167023122
PowhegPythiaEvtGen_P2012CT10_ttbarMET400_hdamp172p5_nonAH	696.23	0.0003751986

Table A.4.: $t\bar{t}$ (Powheg)

Process	cross section	k factor
PowhegPythiaEvtGen_P2012_Wt_inclusive_top	34.009	1.054
PowhegPythiaEvtGen_P2012_Wt_inclusive_antitop	33.989	1.054
PowhegPythiaEvtGen_P2012CT10_Wt_inclusive_top_MET200	34.009	0.011891755
PowhegPythiaEvtGen_P2012CT10_Wt_inclusive_tbar_MET200	33.989	0.0118670914
PowhegPythiaEvtGen_P2012_singletop_tchan_lept_top	43.739	1.0094
PowhegPythiaEvtGen_P2012_singletop_tchan_lept_antitop	25.778	1.0193
PowhegPythiaEvtGen_P2012_SingleTopSchan_noAllHad_top	2.0517	1.0046
PowhegPythiaEvtGen_P2012_SingleTopSchan_noAllHad_antitop	1.2615	1.0215

Table A.5.: Single top (Powheg)

Process	cross section	k factor
MadGraphPythia8EvtGen_A14NNPDF23LO_ttW_Np0	0.17656	1.32
MadGraphPythia8EvtGen_A14NNPDF23LO_ttW_Np1	0.14062	1.32
MadGraphPythia8EvtGen_A14NNPDF23LO_ttW_Np2	0.13680	1.32
MadGraphPythia8EvtGen_A14NNPDF23LO_ttZnnqq_Np0	0.17321	1.47
MadGraphPythia8EvtGen_A14NNPDF23LO_ttZnnqq_Np1	0.16533	1.47
MadGraphPythia8EvtGen_A14NNPDF23LO_ttZnnqq_Np2	0.17427	1.47
MadGraphPythia8EvtGen_A14NNPDF23_ttbarWW	0.0080975	1.2231
MadGraph_3topSM	0.00164	1.0
MadGraphPythia8EvtGen_A14NNPDF23_4topSM	0.0091622	1.0042

Table A.6.: Other top processes (MadGraph)

Process	cross section	k factor
MadGraphPythia8EvtGen_SS_direct_200_0	518.15374755859375	1.0
MadGraphPythia8EvtGen_SS_direct_400_0	14.80424690246582	1.0
MadGraphPythia8EvtGen_SS_direct_400_375	14.80424690246582	1.0
MadGraphPythia8EvtGen_SS_direct_425_375	10.569883346557617	1.0
MadGraphPythia8EvtGen_SS_direct_400_350	14.80424690246582	1.0
MadGraphPythia8EvtGen_SS_direct_400_300	14.80424690246582	1.0
MadGraphPythia8EvtGen_SS_direct_500_475	4.1992330551147461	1.0
MadGraphPythia8EvtGen_SS_direct_500_450	4.1992330551147461	1.0
MadGraphPythia8EvtGen_SS_direct_500_400	4.1992330551147461	1.0
MadGraphPythia8EvtGen_SS_direct_600_0	1.4153077602386475	1.0
MadGraphPythia8EvtGen_SS_direct_600_500	1.4153077602386475	1.0
MadGraphPythia8EvtGen_SS_direct_600_400	1.4153077602386475	1.0
MadGraphPythia8EvtGen_SS_direct_600_575	1.4153077602386475	1.0
MadGraphPythia8EvtGen_SS_direct_600_550	1.4153077602386475	1.0
MadGraphPythia8EvtGen_SS_direct_800_100	0.2307170033454895	1.0
MadGraphPythia8EvtGen_SS_direct_800_300	0.2307170033454895	1.0
MadGraphPythia8EvtGen_SS_direct_800_500	0.2307170033454895	1.0
MadGraphPythia8EvtGen_SS_direct_800_600	0.2307170033454895	1.0
MadGraphPythia8EvtGen_SS_direct_800_700	0.2307170083	1.0
MadGraphPythia8EvtGen_SS_direct_900_0	0.10474482923746109	1.0
MadGraphPythia8EvtGen_SS_direct_900_100	0.10474482923746109	1.0
MadGraphPythia8EvtGen_SS_direct_900_200	0.10474482923746109	1.0
MadGraphPythia8EvtGen_SS_direct_900_300	0.10474482923746109	1.0
MadGraphPythia8EvtGen_SS_direct_900_400	0.10474482923746109	1.0
MadGraphPythia8EvtGen_SS_direct_800_0	0.2307170033454895	1.0
MadGraphPythia8EvtGen_SS_direct_800_200	0.2307170033454895	1.0
MadGraphPythia8EvtGen_SS_direct_800_400	0.2307170033454895	1.0
MadGraphPythia8EvtGen_SS_direct_900_500	0.10474482923746109	1.0
MadGraphPythia8EvtGen_SS_direct_900_600	0.10474482923746109	1.0
MadGraphPythia8EvtGen_SS_direct_1000_100	0.049951273947954178	1.0
MadGraphPythia8EvtGen_SS_direct_1000_300	0.049951273947954178	1.0
MadGraphPythia8EvtGen_SS_direct_1000_500	0.049951273947954178	1.0
MadGraphPythia8EvtGen_SS_direct_1000_600	0.049951273947954178	1.0
MadGraphPythia8EvtGen_SS_direct_1050_0	0.0351784553	1.0
MadGraphPythia8EvtGen_SS_direct_1100_0	0.025069791823625565	1.0
MadGraphPythia8EvtGen_SS_direct_1100_100	0.025069791823625565	1.0
MadGraphPythia8EvtGen_SS_direct_1100_200	0.025069791823625565	1.0
MadGraphPythia8EvtGen_SS_direct_1100_300	0.025069791823625565	1.0
MadGraphPythia8EvtGen_SS_direct_1000_0	0.049951273947954178	1.0
MadGraphPythia8EvtGen_SS_direct_1000_200	0.049951273947954178	1.0
MadGraphPythia8EvtGen_SS_direct_1000_400	0.049951273947954178	1.0
MadGraphPythia8EvtGen_SS_direct_1100_400	0.025069791823625565	1.0
MadGraphPythia8EvtGen_SS_direct_1100_500	0.025069791823625565	1.0
MadGraphPythia8EvtGen_SS_direct_1100_600	0.025069791823625565	1.0
MadGraphPythia8EvtGen_SS_direct_1200_100	0.013027645647525787	1.0
MadGraphPythia8EvtGen_SS_direct_1200_300	0.013027645647525787	1.0
MadGraphPythia8EvtGen_SS_direct_1200_400	0.013027645647525787	1.0
MadGraphPythia8EvtGen_SS_direct_1200_500	0.013027645647525787	1.0
MadGraphPythia8EvtGen_SS_direct_1200_600	0.013027645647525787	1.0
MadGraphPythia8EvtGen_SS_direct_1300_0	0.0069128810428082943	1.0
MadGraphPythia8EvtGen_SS_direct_1300_100	0.0069128810428082943	1.0
MadGraphPythia8EvtGen_SS_direct_1200_0	0.013027645647525787	1.0
MadGraphPythia8EvtGen_SS_direct_1200_200	0.013027645647525787	1.0
MadGraphPythia8EvtGen_SS_direct_1300_200	0.0069128810428082943	1.0
MadGraphPythia8EvtGen_SS_direct_1300_300	0.0069128810428082943	1.0
MadGraphPythia8EvtGen_SS_direct_1300_400	0.0069128810428082943	1.0
MadGraphPythia8EvtGen_SS_direct_1300_500	0.0069128810428082943	1.0
MadGraphPythia8EvtGen_SS_direct_1300_600	0.0069128810428082943	1.0
MadGraphPythia8EvtGen_SS_direct_1400_100	0.0037704464048147202	1.0
MadGraphPythia8EvtGen_SS_direct_1400_200	0.0037704464048147202	1.0
MadGraphPythia8EvtGen_SS_direct_1400_300	0.0037704464048147202	1.0
MadGraphPythia8EvtGen_SS_direct_1400_400	0.0037704464048147202	1.0
MadGraphPythia8EvtGen_SS_direct_1400_500	0.0037704464048147202	1.0
MadGraphPythia8EvtGen_SS_direct_1400_600	0.0037704464048147202	1.0
MadGraphPythia8EvtGen_SS_direct_1400_0	0.0037704464048147202	1.0
MadGraphPythia8EvtGen_SS_direct_1500_0	0.0020862654782831669	1.0
MadGraphPythia8EvtGen_SS_direct_1500_100	0.0020862654782831669	1.0
MadGraphPythia8EvtGen_SS_direct_1500_200	0.0020862654782831669	1.0
MadGraphPythia8EvtGen_SS_direct_1500_300	0.0020862654782831669	1.0
MadGraphPythia8EvtGen_SS_direct_1500_400	0.0020862654782831669	1.0
MadGraphPythia8EvtGen_SS_direct_1500_500	0.0020862654782831669	1.0
MadGraphPythia8EvtGen_SS_direct_1500_600	0.0020862654782831669	1.0
MadGraphPythia8EvtGen_SS_direct_1600_100	0.0011864259140565991	1.0
MadGraphPythia8EvtGen_SS_direct_1600_200	0.0011864259140565991	1.0
MadGraphPythia8EvtGen_SS_direct_1600_300	0.0011864259140565991	1.0
MadGraphPythia8EvtGen_SS_direct_1600_400	0.0011864259140565991	1.0
MadGraphPythia8EvtGen_SS_direct_1600_500	0.0011864259140565991	1.0
MadGraphPythia8EvtGen_SS_direct_1600_0	0.0011864259140565991	1.0
MadGraphPythia8EvtGen_SS_direct_1600_600	0.0011864259140565991	1.0

Table A.7.: Signal ($q \to \tilde{q} + \tilde{\chi}_1^0$) (MadGraph)

Process	cross section	k factor
MadGraphPythia8EvtGen_SS_direct_300_275	68.613128662109375	1.0
MadGraphPythia8EvtGen_SS_direct_300_250	68.613128662109375	1.0
MadGraphPythia8EvtGen_SS_direct_500_300	4.1992330551147461	1.0
MadGraphPythia8EvtGen_SS_direct_600_300	1.4153077602386475	1.0
MadGraphPythia8EvtGen_SS_direct_700_300	0.5421072244644165	1.0
MadGraphPythia8EvtGen_SS_direct_700_400	0.5421072244644165	1.0
MadGraphPythia8EvtGen_SS_direct_700_500	0.5421072244644165	1.0
MadGraphPythia8EvtGen_SS_direct_700_600	0.5421072244644165	1.0
MadGraphPythia8EvtGen_SS_direct_800_775	0.2307170083	1.0
MadGraphPythia8EvtGen_SS_direct_900_700	0.1047448291	1.0
MadGraphPythia8EvtGen_SS_direct_900_800	0.1047448291	1.0
MadGraphPythia8EvtGen_SS_direct_900_875	0.1047448291	1.0
MadGraphPythia8EvtGen_SS_direct_1000_800	0.0499512723	1.0
MadGraphPythia8EvtGen_SS_direct_1000_900	0.0499512723	1.0
MadGraphPythia8EvtGen_SS_direct_1000_975	0.0499512723	1.0
MadGraphPythia8EvtGen_SS_direct_1100_700	0.0250697914	1.0
MadGraphPythia8EvtGen_SS_direct_1100_900	0.0250697914	1.0
MadGraphPythia8EvtGen_SS_direct_1100_1000	0.0250697914	1.0
MadGraphPythia8EvtGen_SS_direct_1100_1075	0.0250697914	1.0
MadGraphPythia8EvtGen_SS_direct_1200_800	0.0130276452	1.0
MadGraphPythia8EvtGen_SS_direct_1200_1000	0.0130276452	1.0
MadGraphPythia8EvtGen_SS_direct_1200_1100	0.0130276452	1.0
MadGraphPythia8EvtGen_SS_direct_1300_700	0.0069128811	1.0
MadGraphPythia8EvtGen_SS_direct_1300_900	0.0069128811	1.0
MadGraphPythia8EvtGen_SS_direct_1300_1100	0.0069128811	1.0
MadGraphPythia8EvtGen_SS_direct_1400_800	0.0037704464	1.0
MadGraphPythia8EvtGen_SS_direct_1400_1000	0.0037704464	1.0
MadGraphPythia8EvtGen_SS_direct_1500_700	0.0020862655	1.0
MadGraphPythia8EvtGen_SS_direct_1500_900	0.0020862655	1.0
MadGraphPythia8EvtGen_SS_direct_1500_1100	0.0020862655	1.0
MadGraphPythia8EvtGen_SS_direct_1600_800	0.0011864259	1.0
MadGraphPythia8EvtGen_SS_direct_1600_1000	0.0011864259	1.0
MadGraphPythia8EvtGen_SS_direct_1700_100	0.0006762456	1.0
MadGraphPythia8EvtGen_SS_direct_1700_300	0.0006762456	1.0
MadGraphPythia8EvtGen_SS_direct_1700_500	0.0006762456	1.0
MadGraphPythia8EvtGen_SS_direct_1700_700	0.0006762456	1.0
MadGraphPythia8EvtGen_SS_direct_1700_900	0.0006762456	1.0
MadGraphPythia8EvtGen_SS_direct_1700_1100	0.0006762456	1.0
MadGraphPythia8EvtGen_SS_direct_1800_0	0.0003950763	1.0
MadGraphPythia8EvtGen_SS_direct_1800_200	0.0003950763	1.0
MadGraphPythia8EvtGen_SS_direct_1800_400	0.0003950763	1.0
MadGraphPythia8EvtGen_SS_direct_1800_600	0.0003950763	1.0
MadGraphPythia8EvtGen_SS_direct_1800_800	0.0003950763	1.0
MadGraphPythia8EvtGen_SS_direct_1800_1000	0.0003950763	1.0
MadGraphPythia8EvtGen_SS_direct_1900_100	0.00023164	1.0
MadGraphPythia8EvtGen_SS_direct_1900_300	0.00023164	1.0
MadGraphPythia8EvtGen_SS_direct_1900_500	0.00023164	1.0
MadGraphPythia8EvtGen_SS_direct_1900_700	0.00023164	1.0
MadGraphPythia8EvtGen_SS_direct_1900_900	0.00023164	1.0
MadGraphPythia8EvtGen_SS_direct_1900_1100	0.00023164	1.0
MadGraphPythia8EvtGen_SS_direct_2000_0	0.0001370551	1.0
MadGraphPythia8EvtGen_SS_direct_2000_200	0.0001370551	1.0
MadGraphPythia8EvtGen_SS_direct_2000_400	0.0001370551	1.0
MadGraphPythia8EvtGen_SS_direct_2000_600	0.0001370551	1.0
MadGraphPythia8EvtGen_SS_direct_2000_800	0.0001370551	1.0
MadGraphPythia8EvtGen_SS_direct_2000_1000	0.0001370551	1.0
MadGraphPythia8EvtGen_SS_direct_2100_100	8.20773E-005	1.0
MadGraphPythia8EvtGen_SS_direct_2100_300	8.20773E-005	1.0
MadGraphPythia8EvtGen_SS_direct_2100_500	8.20773E-005	1.0
MadGraphPythia8EvtGen_SS_direct_2100_700	8.20773E-005	1.0
MadGraphPythia8EvtGen_SS_direct_2100_900	8.20773E-005	1.0
MadGraphPythia8EvtGen_SS_direct_2100_1100	8.20773E-005	1.0
MadGraphPythia8EvtGen_SS_direct_2200_0	4.92552E-005	1.0
MadGraphPythia8EvtGen_SS_direct_2200_200	4.92552E-005	1.0
MadGraphPythia8EvtGen_SS_direct_2200_400	4.92552E-005	1.0
MadGraphPythia8EvtGen_SS_direct_2200_600	4.92552E-005	1.0
MadGraphPythia8EvtGen_SS_direct_2200_800	4.92552E-005	1.0
MadGraphPythia8EvtGen_SS_direct_2200_1000	4.92552E-005	1.0

Table A.8.: Signal ($q \to \tilde{q} + \tilde{\chi}_1^0$) (MadGraph) - continuation

Appendix B.

Closure Systematic

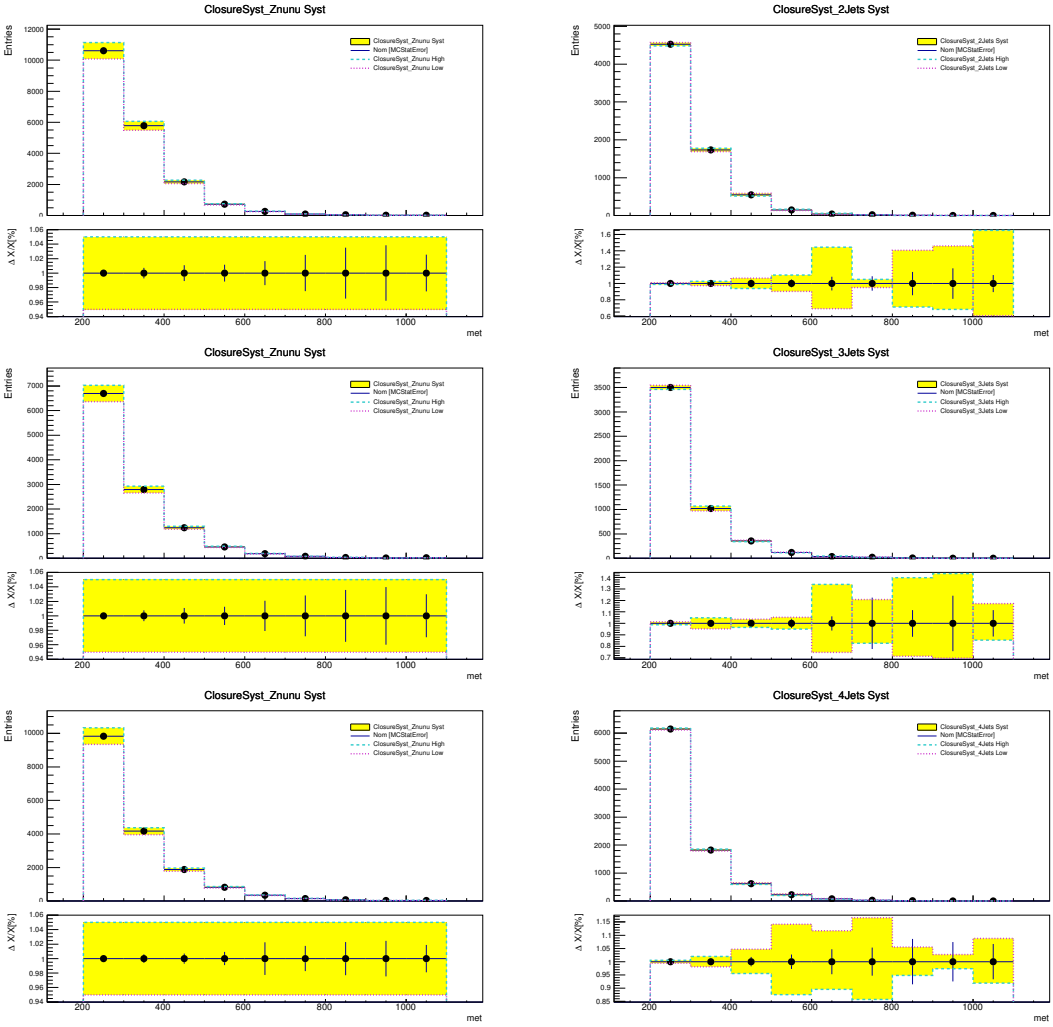

Figure B.1.: Closure systematics for the $Z \to \nu\nu$ (left) and $W \to \tau\nu$ (right) background processes, extracted from the closure test of $E_{\mathrm{T}}^{\mathrm{miss}}$ distributions in the 2 jet (top), 3 jet (middle) and ≥ 4 jet (bottom) SRs.

Appendix C.

Shape Systematic

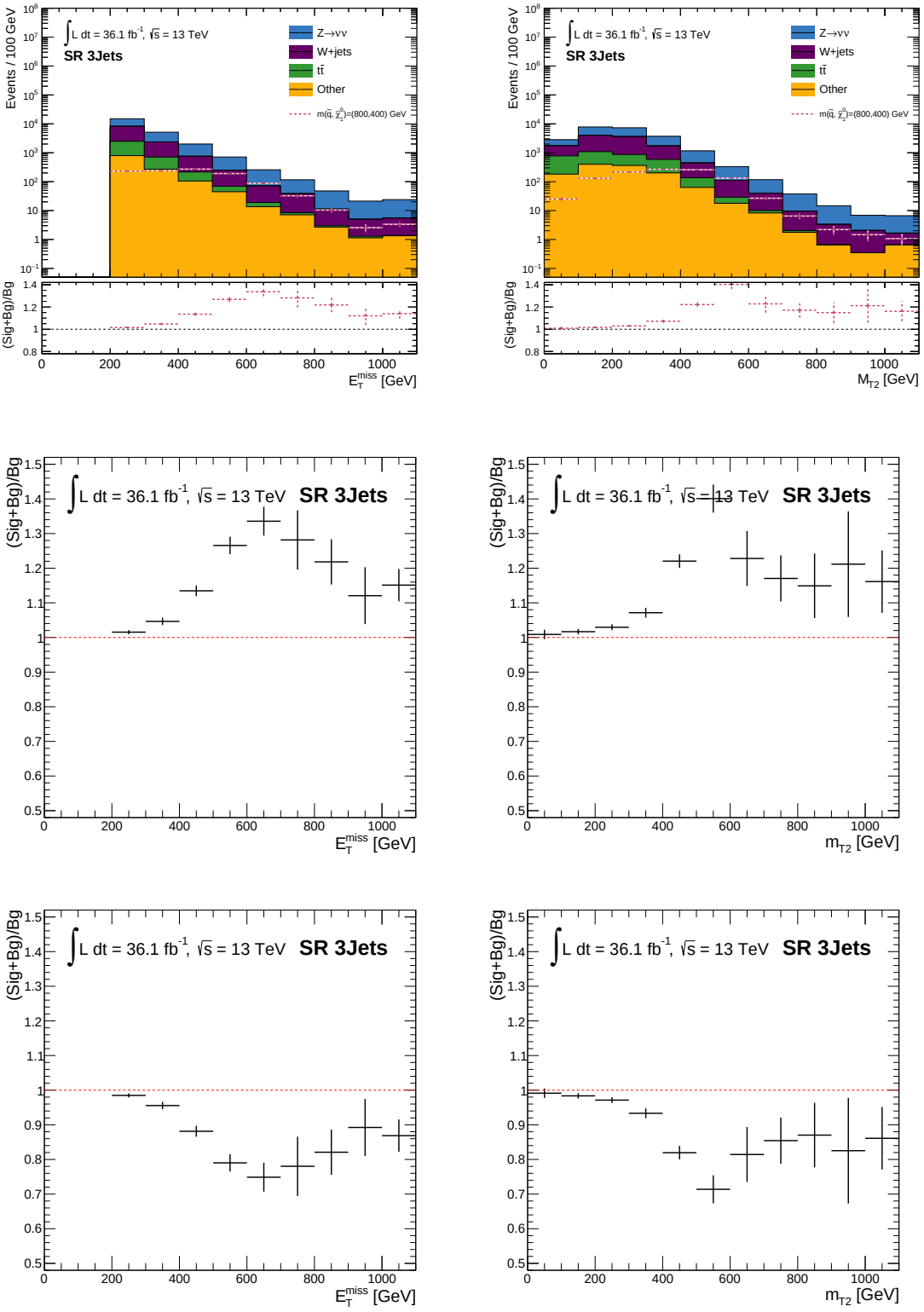

Figure C.1.: Shape systematics extracted from the 3 jet SR distributions (top row). The upward uncertainty is gained from the ratio of $\frac{\text{signal+background}}{\text{background}}$ (middle row), the downward uncertainty is produced by inverting the bin contents of the upward uncertainty (bottom row).

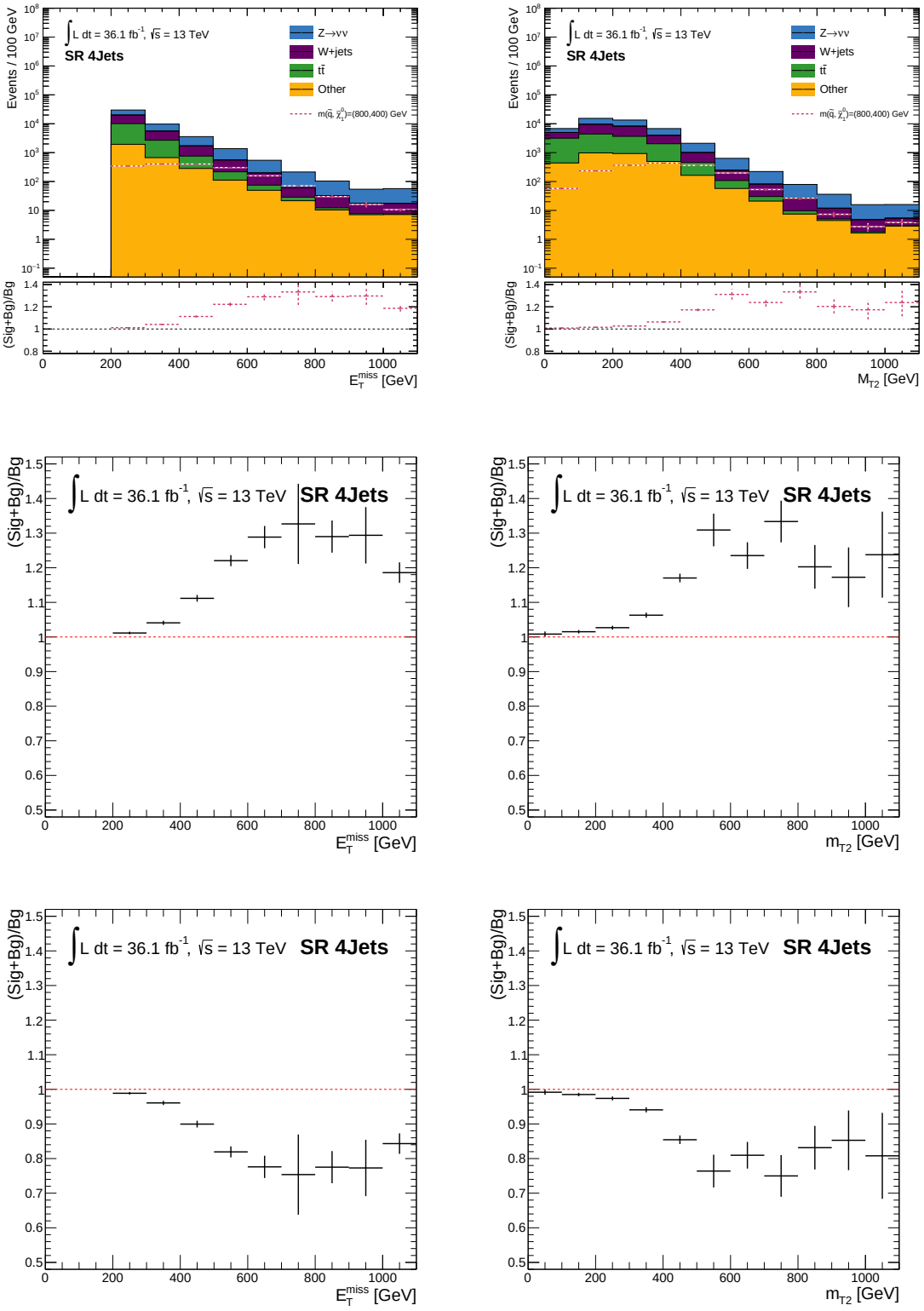

Figure C.2.: Shape systematics extracted from the 4 jet SR distributions (top row). The upward uncertainty is gained from the ratio of $\frac{\text{signal+background}}{\text{background}}$ (middle row), the downward uncertainty is produced by inverting the bin contents of the upward uncertainty (bottom row).

Appendix D.

Other Systematics

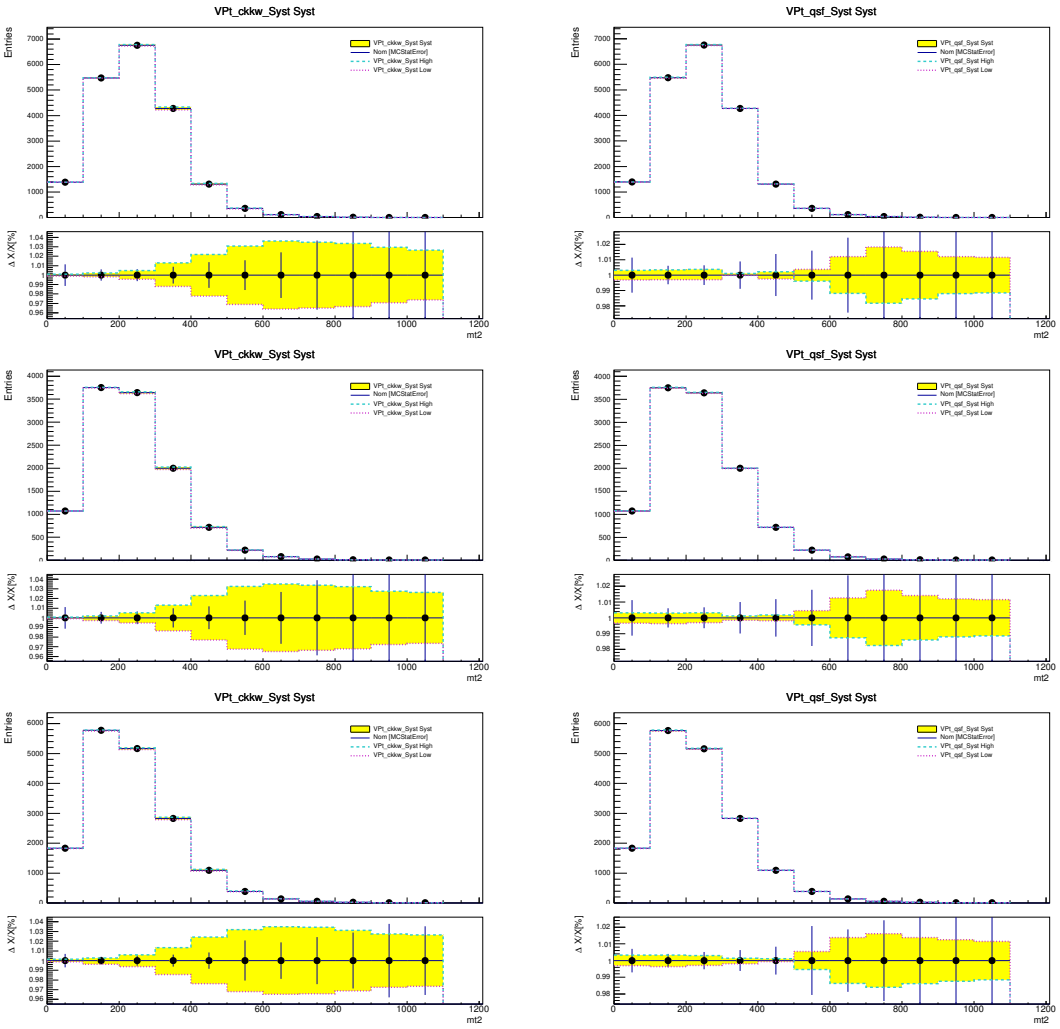

Figure D.1.: Systematics for $Z \to \nu\nu$ taking into account the CKKW matching (left) and the resummation scale (right), shown for the M_{T2} 2 distributions in the 2 jet (top), 3 jet (middle) and ≥ 4 jet (bottom) SRs.

Appendix E.

$t\bar{t}$ Theoretical Uncertainties

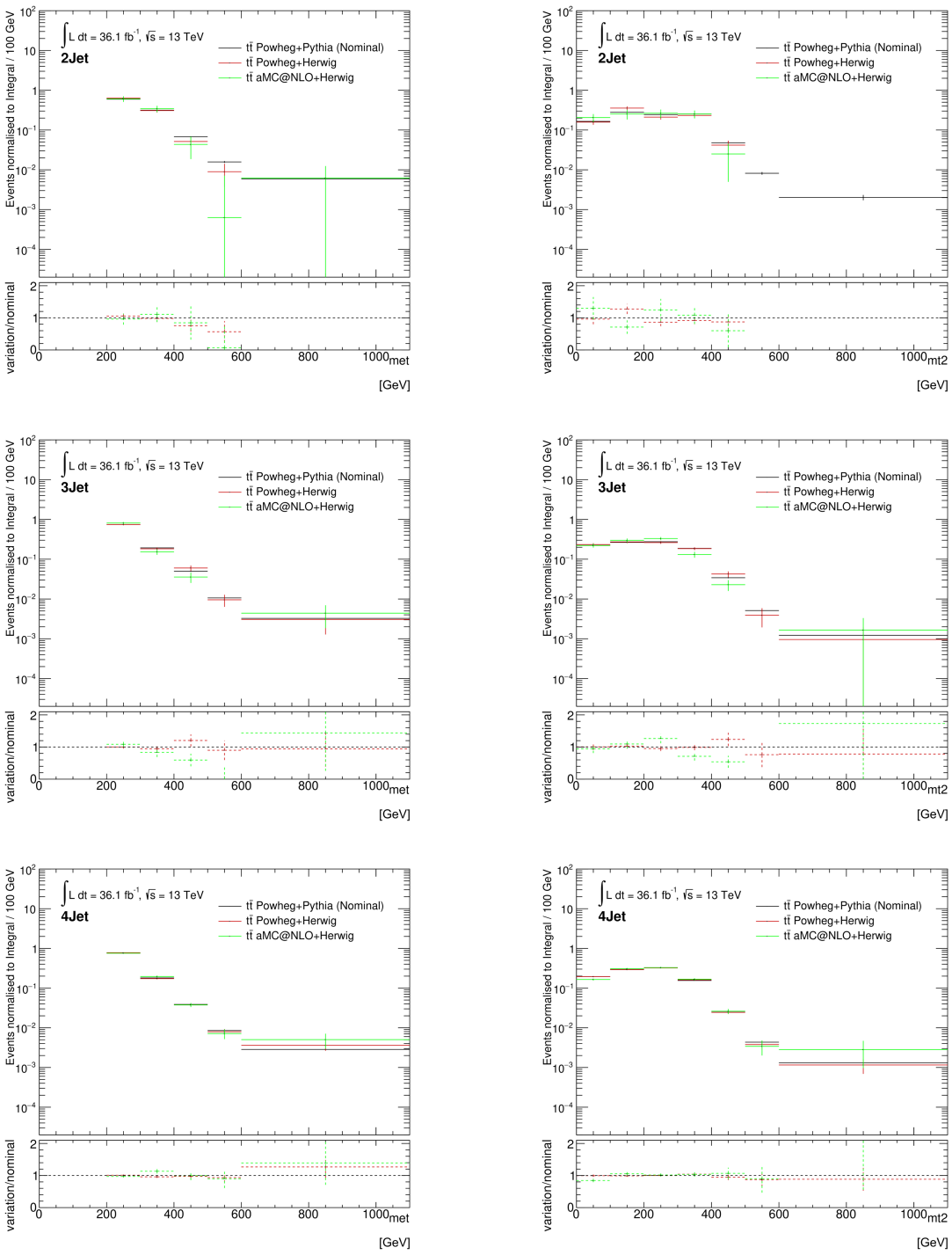

Figure E.1.: Comparison of different event generators and parton shower generators for $E_{\mathrm{T}}^{\mathrm{miss}}$ (left column) and M_{T2} (right column) in the electron CRs to estimate the theoretical uncertainties for the nominal $t\bar{t}$ sample.

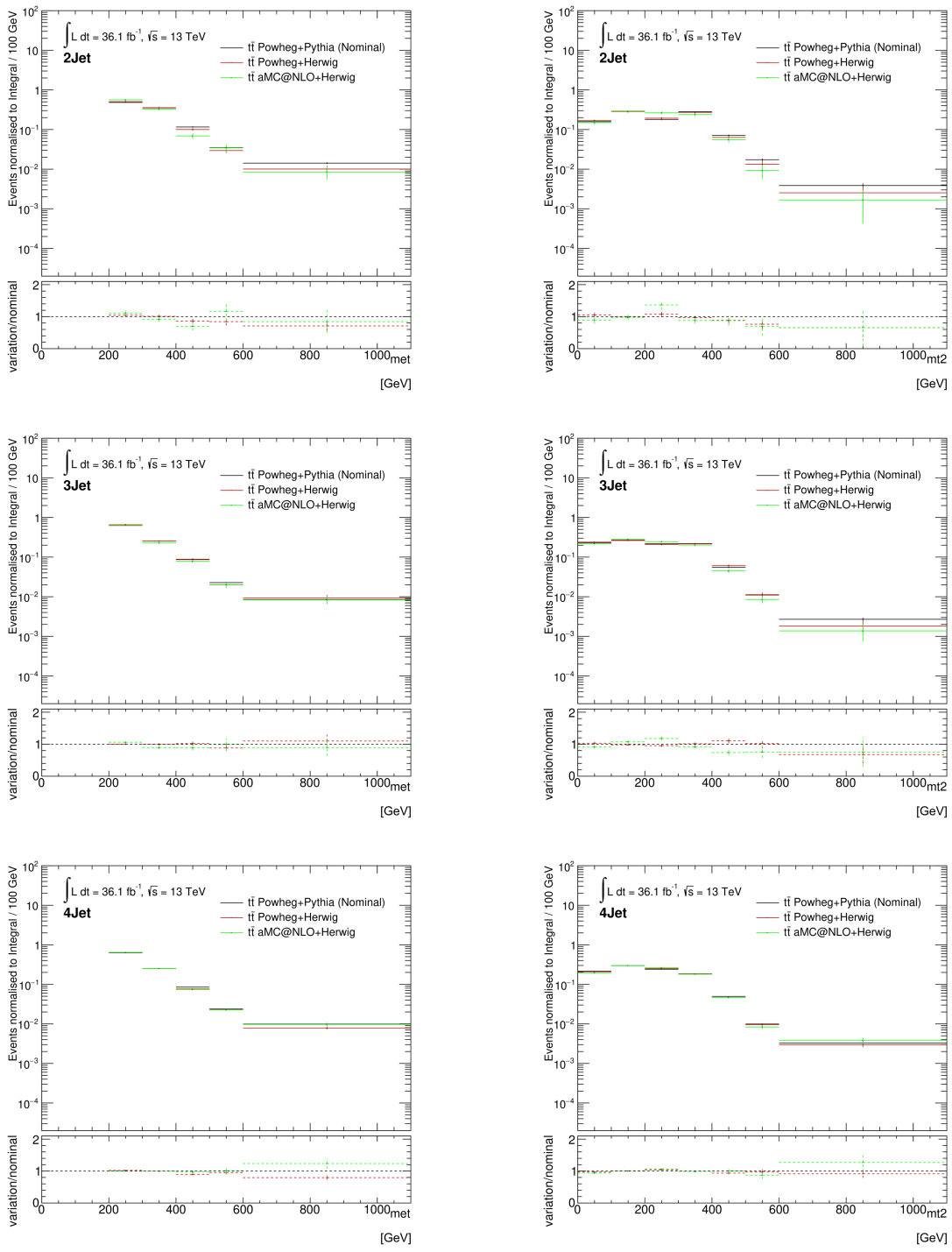

Figure E.2.: Comparison of different event generators and parton shower generators for $E_{\mathrm{T}}^{\mathrm{miss}}$ (left column) and M_{T2} (right column) in the muon CRs to estimate the theoretical uncertainties for the nominal $t\bar{t}$ sample.

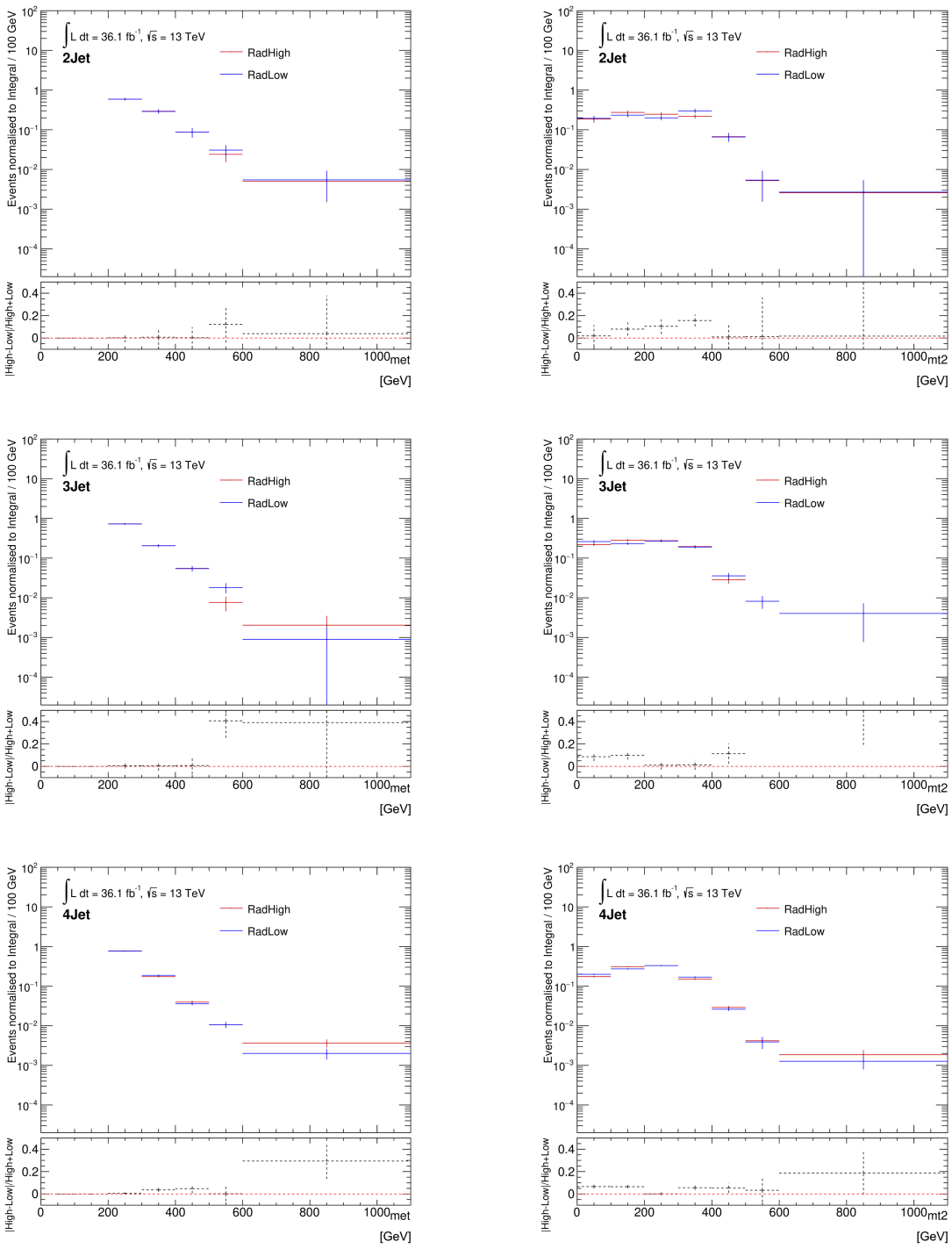

Figure E.3.: Comparison of different tunings in the Powheg+Pythia samples for $E_{\mathrm{T}}^{\mathrm{miss}}$ (left column) and M_{T2} (right column) in the electron CRs to estimate the radiation uncertainties for the nominal $t\bar{t}$ sample.

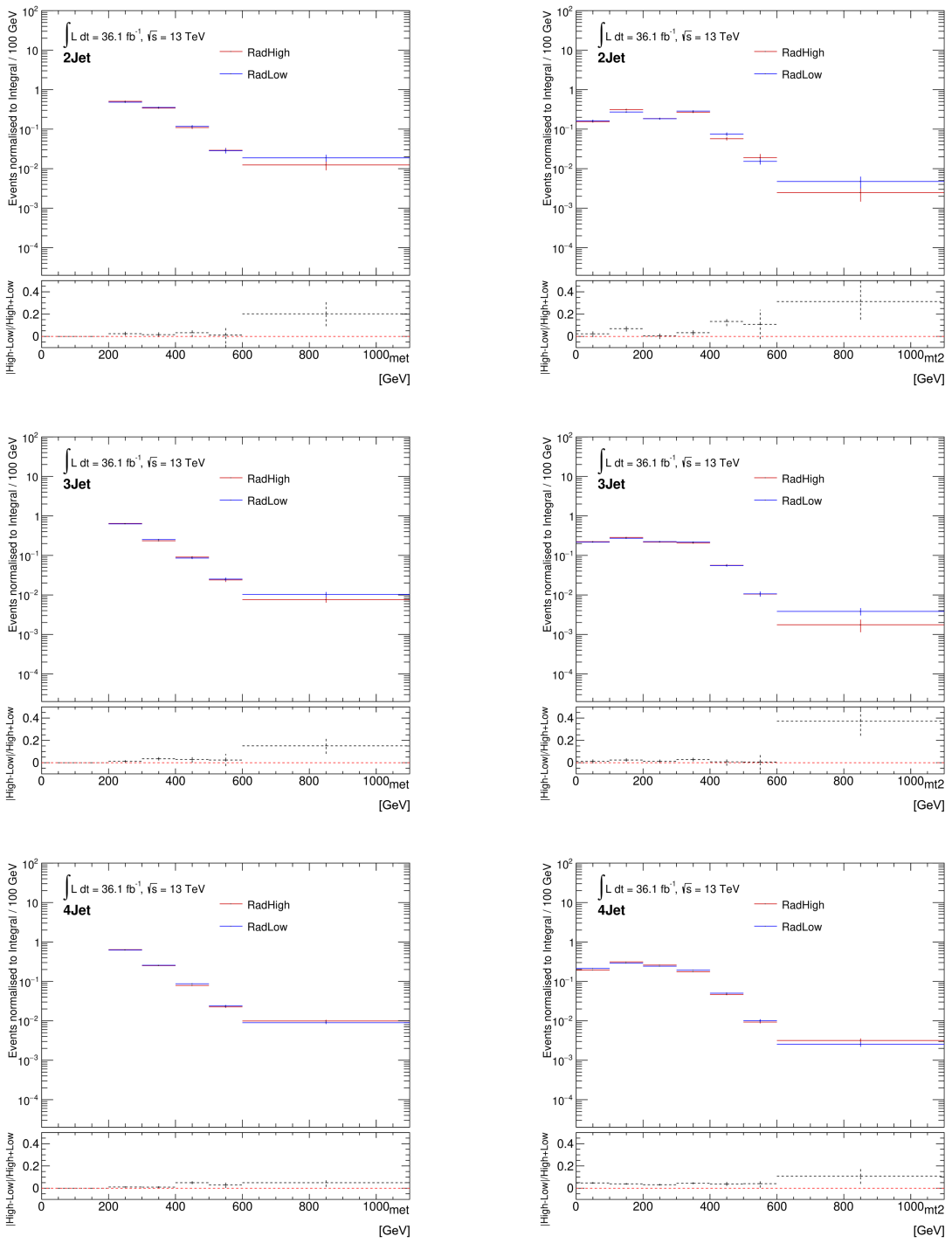

Figure E.4.: Comparison of different tunings in the Powheg+Pythia samples for $E_{\mathrm{T}}^{\mathrm{miss}}$ (left column) and M_{T2} (right column) in the muon CRs to estimate the radiation uncertainties for the nominal $t\bar{t}$ sample.

Appendix F.

Yields Tables Background Only Fit

F.1. $E_{\mathrm{T}}^{\mathrm{miss}}$

The following tables show the number of expected events from the MC prediction and the number of fitted events for each process in each bin for the SRs, the electron CRs and muon CRs with 2 jets, 3 jets and 4 or more jets, respectively. Bins 0 and 1 are not shown, since they are empty for the $E_{\mathrm{T}}^{\mathrm{miss}}$ distribution.

SR 2Jet Bin $E_{\mathrm{T}}^{\mathrm{miss}}$	total	bin2	bin3	bin4	bin5
Observed events	40332	23345	11412	3701	1159
Fitted bkg events	38847.55 ± 1219.58	22748.9 ± 662.8	10675.9 ± 359.5	3610.4 ± 141.6	1125.8 ± 49.4
Fitted Znunu events	23665.85 ± 1212.62	12798.9 ± 652.1	6906.1 ± 355.0	2585.0 ± 134.1	844.1 ± 45.3
Fitted Wtaunu events	8353.72 ± 113.32	5416.8 ± 93.4	2069.9 ± 62.1	605.8 ± 44.5	166.0 ± 18.0
Fitted ttbar events	558.39 ± 45.18	326.8 ± 26.0	177.4 ± 14.9	41.5 ± 3.4	9.1 ± 0.9
Fitted Wmunu events	3100.33 ± 43.87	2066.6 ± 31.1	752.7 ± 10.4	196.4 ± 2.3	56.0 ± 1.4
Fitted Wenu events	2733.39 ± 37.29	1887.0 ± 26.0	644.9 ± 9.1	142.2 ± 3.9	40.5 ± 0.8
Fitted Other events	435.87 ± 104.63	252.8 ± 60.7	124.9 ± 29.9	39.5 ± 9.5	10.1 ± 2.4
MC exp. SM events	33522.93	19507.91	9238.83	3164.88	996.86
MC exp. Znunu events	19746.23	10607.76	5778.39	2167.98	725.93
MC exp. Wtaunu events	7033.88	4525.98	1733.47	547.81	148.48
MC exp. ttbar events	654.57	378.95	208.92	51.11	11.22
MC exp. Wmunu events	2620.58	1742.33	638.64	164.45	48.35
MC exp. Wenu events	2306.19	1581.64	545.44	127.95	34.88
MC exp. Other events	1161.49	671.25	333.95	105.59	28.00

SR 2Jet Bin $E_{\mathrm{T}}^{\mathrm{miss}}$	bin6	bin7	bin8	bin9	bin10
Observed events	399	177	67	33	39
Fitted bkg events	401.1 ± 25.7	155.7 ± 7.2	64.9 ± 4.3	34.7 ± 2.4	30.2 ± 2.3
Fitted Znunu events	309.6 ± 17.1	116.6 ± 6.9	52.5 ± 3.0	27.9 ± 1.5	25.1 ± 1.6
Fitted Wtaunu events	56.8 ± 19.3	25.8 ± 1.5	6.1 ± 2.8	4.3 ± 1.9	2.2 ± 1.8
Fitted ttbar events	2.6 ± 0.2	0.6 ± 0.1	0.1 ± 0.0	0.1 ± 0.0	0.0 ± 0.0
Fitted Wmunu events	15.6 ± 1.0	7.3 ± 0.3	3.1 ± 0.2	1.3 ± 0.1	1.4 ± 0.1
Fitted Wenu events	12.0 ± 0.4	3.7 ± 0.3	1.9 ± 0.1	0.6 ± 0.0	0.6 ± 0.0
Fitted Other events	4.3 ± 1.0	1.7 ± 0.4	1.2 ± 0.3	0.6 ± 0.2	0.8 ± 0.2
MC exp. SM events	353.37	141.46	60.51	29.70	29.42
MC exp. Znunu events	270.19	104.37	46.31	22.44	22.87
MC exp. Wtaunu events	42.71	22.05	6.69	4.04	2.65
MC exp. ttbar events	3.21	0.83	0.14	0.11	0.08
MC exp. Wmunu events	16.18	5.56	2.69	1.36	1.02
MC exp. Wenu events	9.71	4.06	1.47	0.44	0.61
MC exp. Other events	11.37	4.59	3.21	1.32	2.19

Table F.1.: Summary of expected and fitted background event numbers in the 2 jet SR for the background only fit in $E_{\mathrm{T}}^{\mathrm{miss}}$.

SR 3Jet Bin $E_{\mathrm{T}}^{\mathrm{miss}}$	total	bin2	bin3	bin4	bin5
Observed events	25891	16706	5629	2204	804
Fitted bkg events	25908.47 ± 711.08	16654.1 ± 418.4	5736.7 ± 182.8	2233.9 ± 78.8	774.1 ± 30.5
Fitted Znunu events	13674.61 ± 715.01	8003.3 ± 416.2	3292.2 ± 174.2	1461.9 ± 77.1	536.7 ± 29.0
Fitted Wtaunu events	5926.36 ± 90.89	4096.1 ± 82.1	1214.2 ± 60.6	404.2 ± 16.9	132.8 ± 7.9
Fitted ttbar events	2031.47 ± 118.48	1518.8 ± 88.1	392.6 ± 23.1	97.6 ± 5.6	19.1 ± 1.5
Fitted Wmunu events	2023.28 ± 36.27	1433.4 ± 24.4	398.6 ± 9.7	131.8 ± 2.3	37.8 ± 0.7
Fitted Wenu events	1790.11 ± 30.85	1306.5 ± 22.9	338.1 ± 6.6	98.0 ± 1.9	32.3 ± 0.7
Fitted Other events	462.64 ± 110.94	296.0 ± 70.9	101.0 ± 24.3	40.4 ± 9.7	15.4 ± 3.6
MC exp. SM events	23363.67	15006.11	5164.88	2008.91	715.65
MC exp. Znunu events	11529.89	6694.82	2793.46	1242.23	464.19
MC exp. Wtaunu events	5066.57	3502.21	1019.85	355.96	120.50
MC exp. ttbar events	2272.81	1690.11	440.91	110.41	24.12
MC exp. Wmunu events	1724.23	1212.66	348.33	111.15	33.39
MC exp. Wenu events	1532.21	1112.40	294.26	83.94	28.64
MC exp. Other events	1237.96	793.91	268.08	105.22	44.81

SR 3Jet Bin $E_{\mathrm{T}}^{\mathrm{miss}}$	bin6	bin7	bin8	bin9	bin10
Observed events	306	133	64	22	23
Fitted bkg events	286.7 ± 16.8	122.1 ± 7.4	51.2 ± 3.3	23.7 ± 1.6	26.0 ± 1.4
Fitted Znunu events	213.8 ± 11.7	86.7 ± 5.0	40.9 ± 2.4	18.7 ± 1.1	20.4 ± 1.2
Fitted Wtaunu events	43.1 ± 12.1	23.2 ± 5.1	6.1 ± 2.2	3.3 ± 1.2	3.3 ± 0.6
Fitted ttbar events	2.5 ± 0.7	0.8 ± 0.2	0.1 ± 0.1	0.1 ± 0.0	0.0 ± 0.0
Fitted Wmunu events	12.2 ± 0.2	5.4 ± 0.2	2.0 ± 0.1	0.8 ± 0.0	1.3 ± 0.0
Fitted Wenu events	9.7 ± 0.3	3.4 ± 0.2	1.2 ± 0.1	0.5 ± 0.0	0.5 ± 0.0
Fitted Other events	5.5 ± 1.4	2.7 ± 0.6	0.8 ± 0.2	0.4 ± 0.1	0.5 ± 0.1
MC exp. SM events	258.32	115.86	47.87	21.69	24.38
MC exp. Znunu events	186.39	77.16	36.54	16.64	18.47
MC exp. Wtaunu events	34.70	22.33	5.36	2.70	2.96
MC exp. ttbar events	5.43	1.34	0.30	0.16	0.04
MC exp. Wmunu events	10.47	4.71	1.73	0.69	1.11
MC exp. Wenu events	7.70	3.20	1.26	0.37	0.45
MC exp. Other events	13.65	7.13	2.68	1.14	1.34

Table F.2.: Summary of expected and fitted background event numbers in the 3 jet SR for the background only fit in $E_{\mathrm{T}}^{\mathrm{miss}}$.

SR 4Jet Bin $E_{\mathrm{T}}^{\mathrm{miss}}$	total	bin2	bin3	bin4	bin5
Observed events	45028	29959	9459	3487	1226
Fitted bkg events	46089.62 ± 1211.34	30134.5 ± 699.3	9884.7 ± 300.3	3635.2 ± 129.5	1432.8 ± 64.8
Fitted Znunu events	19838.90 ± 1148.09	11316.3 ± 653.3	4738.4 ± 276.6	2135.1 ± 124.3	926.3 ± 53.7
Fitted Wtaunu events	10055.76 ± 293.56	6929.5 ± 206.9	2015.5 ± 74.3	703.9 ± 37.2	250.8 ± 34.5
Fitted ttbar events	9013.25 ± 356.29	6918.3 ± 260.3	1680.5 ± 63.5	321.7 ± 32.4	82.1 ± 4.6
Fitted Wmunu events	3130.50 ± 107.59	2176.7 ± 74.6	643.2 ± 23.6	191.3 ± 7.6	74.1 ± 1.7
Fitted Wenu events	2941.02 ± 88.96	2099.3 ± 63.6	567.1 ± 18.8	180.9 ± 4.8	59.8 ± 1.5
Fitted Other events	1110.19 ± 263.28	694.3 ± 164.7	240.0 ± 56.9	102.3 ± 24.3	39.7 ± 9.4
MC exp. SM events	45597.56	29868.05	9763.37	3593.20	1381.82
MC exp. Znunu events	17336.26	9828.69	4167.22	1873.42	817.73
MC exp. Wtaunu events	8956.84	6149.05	1818.99	623.75	227.31
MC exp. ttbar events	10783.33	8148.80	2016.57	477.11	105.48
MC exp. Wmunu events	2779.48	1922.80	573.16	176.39	65.99
MC exp. Wenu events	2641.03	1880.15	515.75	159.77	53.66
MC exp. Other events	3100.63	1938.56	671.68	282.76	111.65

SR 4Jet Bin $E_{\mathrm{T}}^{\mathrm{miss}}$	bin6	bin7	bin8	bin9	bin10
Observed events	479	212	95	46	65
Fitted bkg events	553.5 ± 26.0	234.0 ± 11.7	105.2 ± 4.9	53.3 ± 2.6	56.6 ± 2.8
Fitted Znunu events	387.6 ± 23.7	173.1 ± 10.2	79.4 ± 4.7	39.6 ± 2.5	43.0 ± 2.7
Fitted Wtaunu events	95.1 ± 10.5	33.3 ± 5.2	14.1 ± 0.9	6.9 ± 0.3	6.6 ± 0.6
Fitted ttbar events	7.4 ± 4.5	2.3 ± 1.3	0.6 ± 0.3	0.2 ± 0.1	0.1 ± 0.1
Fitted Wmunu events	24.8 ± 0.9	10.5 ± 0.5	4.6 ± 0.3	2.5 ± 0.1	2.8 ± 0.4
Fitted Wenu events	21.2 ± 0.7	6.8 ± 0.8	2.9 ± 0.1	1.6 ± 0.1	1.5 ± 0.1
Fitted Other events	17.4 ± 4.1	7.9 ± 1.9	3.7 ± 0.9	2.5 ± 0.6	2.5 ± 0.6
MC exp. SM events	546.06	229.77	103.65	54.36	57.28
MC exp. Znunu events	347.09	154.27	71.52	36.57	39.74
MC exp. Wtaunu events	82.83	29.35	13.19	6.39	5.98
MC exp. ttbar events	25.35	7.14	1.93	0.64	0.30
MC exp. Wmunu events	22.68	9.30	4.36	2.16	2.65
MC exp. Wenu events	18.38	8.07	2.31	1.51	1.42
MC exp. Other events	49.72	21.64	10.34	7.09	7.18

Table F.3.: Summary of expected and fitted background event numbers in the 4 jet SR for the background only fit in $E_{\mathrm{T}}^{\mathrm{miss}}$.

CR ele 2Jet Bin E_T^{miss}	total	bin2	bin3	bin4	bin5
Observed events	4025	2565	1020	300	86
Fitted bkg events	4003.32 ± 43.48	2530.3 ± 28.0	1018.3 ± 12.3	310.9 ± 4.5	92.5 ± 1.6
Fitted Znunu events	1.55 ± 0.09	1.0 ± 0.1	0.3 ± 0.0	0.2 ± 0.0	0.1 ± 0.0
Fitted Wtaunu events	708.38 ± 9.68	420.7 ± 7.5	195.8 ± 4.0	63.1 ± 1.4	18.6 ± 0.6
Fitted ttbar events	204.11 ± 16.19	124.0 ± 10.1	62.3 ± 4.8	13.5 ± 1.0	3.1 ± 0.3
Fitted Wmunu events	2.28 ± 0.10	0.3 ± 0.1	1.3 ± 0.1	0.6 ± 0.0	0.1 ± 0.0
Fitted Wenu events	3002.00 ± 44.41	1928.9 ± 29.2	738.1 ± 11.9	228.2 ± 3.5	68.2 ± 1.5
Fitted Other events	85.01 ± 20.39	55.5 ± 13.3	20.5 ± 5.0	5.3 ± 1.3	2.4 ± 0.6
MC exp. SM events	3624.66	2283.18	932.55	273.35	86.75
MC exp. Znunu events	1.25	0.78	0.22	0.16	0.08
MC exp. Wtaunu events	591.87	344.91	169.48	52.63	15.77
MC exp. ttbar events	241.01	143.69	75.72	16.36	3.81
MC exp. Wmunu events	1.75	0.20	0.98	0.50	0.07
MC exp. Wenu events	2557.85	1641.80	632.01	188.42	61.01
MC exp. Other events	230.93	151.80	54.14	15.28	6.02

CR ele 2Jet Bin E_T^{miss}	bin6	bin7	bin8	bin9	bin10
Observed events	32	10	4	4	4
Fitted bkg events	32.5 ± 2.4	11.5 ± 1.2	3.0 ± 0.8	2.0 ± 0.3	2.4 ± 0.3
Fitted Znunu events	0.0 ± 0.0	0.0 ± 0.0	0.0 ± 0.0	0.0 ± 0.0	0.0 ± 0.0
Fitted Wtaunu events	6.9 ± 0.5	2.2 ± 0.3	0.2 ± 0.1	0.4 ± 0.1	0.5 ± 0.1
Fitted ttbar events	0.8 ± 0.1	0.2 ± 0.0	0.1 ± 0.0	0.0 ± 0.0	0.0 ± 0.0
Fitted Wmunu events	0.0 ± 0.0	0.0 ± 0.0	0.0 ± 0.0	0.0 ± 0.0	0.0 ± 0.0
Fitted Wenu events	24.1 ± 1.9	8.7 ± 0.9	2.6 ± 0.7	1.4 ± 0.2	1.7 ± 0.2
Fitted Other events	0.7 ± 0.2	0.3 ± 0.1	0.1 ± 0.1	0.1 ± 0.0	0.1 ± 0.0
MC exp. SM events	31.01	11.67	2.39	1.56	2.21
MC exp. Znunu events	0.00	0.00	0.00	0.00	0.00
MC exp. Wtaunu events	6.11	2.10	0.10	0.34	0.43
MC exp. ttbar events	1.01	0.27	0.08	0.04	0.03
MC exp. Wmunu events	0.00	0.00	0.00	0.00	0.00
MC exp. Wenu events	21.78	8.52	1.75	1.02	1.53
MC exp. Other events	2.11	0.76	0.45	0.17	0.21

Table F.4.: Summary of expected and fitted background event numbers in the 2 jet electron CR for the background only fit in $E_{\mathrm{T}}^{\mathrm{miss}}$.

CR ele 3Jet Bin $E_{\mathrm{T}}^{\mathrm{miss}}$	total	bin2	bin3	bin4	bin5
Observed events	3135	2137	661	212	81
Fitted bkg events	3198.25 ± 31.68	2186.1 ± 23.2	687.6 ± 8.4	215.4 ± 3.2	68.0 ± 1.1
Fitted Znunu events	3.47 ± 0.07	2.2 ± 0.1	0.8 ± 0.0	0.3 ± 0.0	0.1 ± 0.0
Fitted Wtaunu events	392.94 ± 6.77	236.6 ± 4.2	97.6 ± 1.9	38.6 ± 0.9	13.4 ± 0.6
Fitted ttbar events	595.51 ± 33.08	445.3 ± 24.9	114.8 ± 6.2	29.0 ± 1.5	5.4 ± 0.4
Fitted Wmunu events	1.56 ± 0.08	0.6 ± 0.1	0.9 ± 0.1	$0.1^{+0.1}_{-0.1}$	0.0 ± 0.0
Fitted Wenu events	2106.03 ± 33.18	1436.8 ± 22.8	451.9 ± 7.7	139.4 ± 3.3	46.7 ± 0.9
Fitted Other events	98.74 ± 23.58	64.6 ± 15.4	21.7 ± 5.2	8.1 ± 1.9	2.3 ± 0.6
MC exp. SM events	3061.51	2091.94	652.49	208.95	65.24
MC exp. Znunu events	2.89	1.88	0.63	0.20	0.11
MC exp. Wtaunu events	331.17	201.74	80.23	31.88	10.66
MC exp. ttbar events	668.40	496.94	128.85	33.30	7.11
MC exp. Wmunu events	1.28	0.48	0.60	0.19	0.01
MC exp. Wenu events	1791.74	1217.57	384.12	121.18	40.39
MC exp. Other events	266.02	173.33	58.06	22.19	6.97

CR ele 3Jet Bin $E_{\mathrm{T}}^{\mathrm{miss}}$	bin6	bin7	bin8	bin9	bin10
Observed events	29	11	3	0	1
Fitted bkg events	24.3 ± 1.6	9.5 ± 0.9	3.6 ± 0.5	1.9 ± 0.3	1.8 ± 0.2
Fitted Znunu events	0.0 ± 0.0	0.0 ± 0.0	0.0 ± 0.0	0.0 ± 0.0	0.0 ± 0.0
Fitted Wtaunu events	3.5 ± 0.4	1.6 ± 0.2	0.8 ± 0.1	0.4 ± 0.1	0.3 ± 0.0
Fitted ttbar events	0.7 ± 0.2	0.2 ± 0.1	0.0 ± 0.0	0.0 ± 0.0	0.0 ± 0.0
Fitted Wmunu events	0.0 ± 0.0	0.0 ± 0.0	0.0 ± 0.0	0.0 ± 0.0	0.0 ± 0.0
Fitted Wenu events	18.9 ± 1.3	7.4 ± 0.7	2.5 ± 0.3	1.3 ± 0.2	1.3 ± 0.2
Fitted Other events	1.2 ± 0.3	0.4 ± 0.1	0.2 ± 0.0	0.1 ± 0.0	0.2 ± 0.0
MC exp. SM events	25.29	9.34	4.09	2.25	1.92
MC exp. Znunu events	0.04	0.01	0.00	0.00	0.01
MC exp. Wtaunu events	3.81	1.27	0.89	0.46	0.23
MC exp. ttbar events	1.68	0.33	0.09	0.05	0.06
MC exp. Wmunu events	0.01	0.00	0.00	0.00	0.00
MC exp. Wenu events	16.64	6.61	2.68	1.38	1.17
MC exp. Other events	3.11	1.11	0.43	0.36	0.45

Table F.5.: Summary of expected and fitted background event numbers in the 3 jet electron CR for the background only fit in $E_{\mathrm{T}}^{\mathrm{miss}}$.

CR ele 4Jet Bin E_T^{miss}	total	bin2	bin3	bin4	bin5
Observed events	9383	6730	1901	502	159
Fitted bkg events	9328.84 ± 68.66	6718.6 ± 48.4	1845.5 ± 18.2	509.4 ± 8.2	165.3 ± 3.0
Fitted Znunu events	5.39 ± 0.15	2.7 ± 0.1	1.8 ± 0.0	0.6 ± 0.0	0.2 ± 0.0
Fitted Wtaunu events	643.14 ± 19.48	400.3 ± 11.9	145.0 ± 4.9	60.4 ± 2.2	21.4 ± 0.7
Fitted ttbar events	3535.24 ± 132.54	2755.9 ± 98.9	636.8 ± 22.9	110.4 ± 10.9	28.7 ± 1.4
Fitted Wmunu events	2.12 ± 0.12	1.4 ± 0.1	0.4 ± 0.0	0.1 ± 0.0	0.1 ± 0.0
Fitted Wenu events	4808.03 ± 128.84	3337.4 ± 87.4	989.7 ± 29.9	312.4 ± 8.2	104.7 ± 3.3
Fitted Other events	334.93 ± 79.23	220.9 ± 52.2	71.8 ± 17.0	25.7 ± 6.1	10.1 ± 2.4
MC exp. SM events	10068.91	7213.44	1991.26	578.98	179.33
MC exp. Znunu events	4.52	2.15	1.49	0.51	0.21
MC exp. Wtaunu events	571.96	352.81	129.67	54.80	19.71
MC exp. ttbar events	4264.61	3282.75	767.93	165.35	36.36
MC exp. Wmunu events	2.10	1.47	0.41	0.08	0.10
MC exp. Wenu events	4275.64	2946.79	891.50	283.54	94.95
MC exp. Other events	950.09	627.46	200.25	74.70	28.01

CR ele 4Jet Bin $E_{\mathbf{T}}^{\mathbf{miss}}$	bin6	bin7	bin8	bin9	bin10
Observed events	61	15	8	4	3
Fitted bkg events	53.1 ± 1.6	18.5 ± 1.3	9.9 ± 0.7	4.4 ± 0.4	4.2 ± 0.4
Fitted Znunu events	0.1 ± 0.0	0.1 ± 0.0	0.0 ± 0.0	0.0 ± 0.0	0.0 ± 0.0
Fitted Wtaunu events	8.9 ± 0.3	4.0 ± 0.3	1.7 ± 0.2	0.7 ± 0.1	0.8 ± 0.1
Fitted ttbar events	2.3 ± 1.5	0.8 ± 0.4	0.2 ± 0.1	0.1 ± 0.0	0.0 ± 0.0
Fitted Wmunu events	0.0 ± 0.0	0.0 ± 0.0	0.0 ± 0.0	0.0 ± 0.0	0.0 ± 0.0
Fitted Wenu events	38.3 ± 1.2	12.2 ± 0.9	7.1 ± 0.5	3.5 ± 0.3	2.8 ± 0.3
Fitted Other events	3.5 ± 0.8	1.5 ± 0.4	0.8 ± 0.2	0.2 ± 0.1	0.5 ± 0.1
MC exp. SM events	63.19	21.94	10.35	4.96	5.46
MC exp. Znunu events	0.06	0.04	0.02	0.01	0.03
MC exp. Wtaunu events	8.44	3.40	1.72	0.56	0.84
MC exp. ttbar events	8.74	2.30	0.81	0.24	0.13
MC exp. Wmunu events	0.02	0.00	0.02	0.00	0.00
MC exp. Wenu events	35.26	11.90	5.96	2.97	2.77
MC exp. Other events	10.68	4.29	1.82	1.18	1.69

Table F.6.: Summary of expected and fitted background event numbers in the 4 jet electron CR for the background only fit in $E_{\mathrm{T}}^{\mathrm{miss}}$.

CR muon 2Jet Bin $E_{\mathrm{T}}^{\mathrm{miss}}$	total	bin2	bin3	bin4	bin5
Observed events	31854	18030	8738	3268	1102
Fitted bkg events	31521.45 ± 157.81	17780.1 ± 101.0	8614.3 ± 46.2	3314.4 ± 23.3	1124.3 ± 11.6
Fitted Znunu events	0.45 ± 0.01	0.4 ± 0.0	0.0 ± 0.0	0.0 ± 0.0	0.0 ± 0.0
Fitted Wtaunu events	2201.15 ± 34.97	1190.4 ± 22.4	625.1 ± 10.3	242.4 ± 4.5	90.9 ± 1.5
Fitted ttbar events	1446.79 ± 120.97	713.2 ± 61.9	503.2 ± 40.3	164.5 ± 13.4	46.4 ± 4.2
Fitted Wmunu events	27090.96 ± 279.09	15430.1 ± 162.4	7270.5 ± 79.9	2830.3 ± 32.1	962.0 ± 13.2
Fitted Wenu events	0.08 ± 0.00	0.1 ± 0.0	0.0 ± 0.0	0.0 ± 0.0	0.0 ± 0.0
Fitted Other events	782.01 ± 187.93	446.0 ± 107.2	215.5 ± 51.9	77.1 ± 18.5	25.0 ± 6.0
MC exp. SM events	28091.53	15714.32	7746.20	2963.69	1020.10
MC exp. Znunu events	0.38	0.30	0.00	0.03	0.04
MC exp. Wtaunu events	1839.36	990.87	511.54	212.51	78.49
MC exp. ttbar events	1697.42	818.56	598.40	196.87	59.39
MC exp. Wmunu events	22486.28	12723.02	6072.56	2348.25	815.75
MC exp. Wenu events	0.07	0.07	0.00	0.00	0.00
MC exp. Other events	2068.02	1181.51	563.69	206.02	66.44

CR muon 2Jet Bin $E_{\mathrm{T}}^{\mathrm{miss}}$	bin6	bin7	bin8	bin9	bin10
Observed events	396	180	75	31	34
Fitted bkg events	397.2 ± 6.2	158.4 ± 3.2	66.7 ± 1.9	32.2 ± 1.8	33.7 ± 0.8
Fitted Znunu events	0.0 ± 0.0	0.0 ± 0.0	0.0 ± 0.0	0.0 ± 0.0	0.0 ± 0.0
Fitted Wtaunu events	31.0 ± 0.9	10.9 ± 0.4	4.4 ± 0.1	3.3 ± 0.2	2.7 ± 0.1
Fitted ttbar events	14.0 ± 1.3	4.3 ± 0.3	0.6 ± 0.3	0.4 ± 0.0	0.2 ± 0.0
Fitted Wmunu events	342.8 ± 6.3	138.2 ± 3.3	59.1 ± 1.6	27.9 ± 1.5	30.1 ± 0.8
Fitted Wenu events	0.0 ± 0.0	0.0 ± 0.0	0.0 ± 0.0	0.0 ± 0.0	0.0 ± 0.0
Fitted Other events	9.4 ± 2.3	5.0 ± 1.2	2.6 ± 0.6	0.7 ± 0.2	0.7 ± 0.2
MC exp. SM events	370.47	151.14	64.81	29.39	31.41
MC exp. Znunu events	0.01	0.00	0.00	0.00	0.00
MC exp. Wtaunu events	26.79	10.16	3.74	2.88	2.37
MC exp. ttbar events	16.98	4.86	1.60	0.51	0.25
MC exp. Wmunu events	300.41	123.25	52.45	23.84	26.75
MC exp. Wenu events	0.00	0.00	0.00	0.00	
MC exp. Other events	26.28	12.87	7.02	2.16	2.04

Table F.7.: Summary of expected and fitted background event numbers in the 2 jet muon CR for the background only fit in $E_{\mathrm{T}}^{\mathrm{miss}}$.

CR muon 3Jet Bin $E_{\mathrm{T}}^{\mathrm{miss}}$	total	bin2	bin3	bin4	bin5
Observed events	19766	11448	4979	2087	771
Fitted bkg events	20158.04 ± 91.31	11715.5 ± 67.8	4974.8 ± 21.5	2171.9 ± 13.6	777.6 ± 7.2
Fitted Znunu events	0.18 ± 0.00	0.1 ± 0.0	0.1 ± 0.0	0.0 ± 0.0	0.0 ± 0.0
Fitted Wtaunu events	1202.20 ± 19.59	652.5 ± 10.0	308.7 ± 6.0	144.1 ± 3.2	53.5 ± 1.0
Fitted ttbar events	3945.11 ± 223.62	2518.4 ± 142.9	989.7 ± 53.7	338.5 ± 18.7	81.0 ± 6.5
Fitted Wmunu events	14309.36 ± 216.24	8152.2 ± 124.0	3502.7 ± 57.7	1611.6 ± 24.9	610.2 ± 10.2
Fitted Wenu events	0.34 ± 0.01	0.0 ± 0.0	0.3 ± 0.0	0.0 ± 0.0	0.0 ± 0.0
Fitted Other events	700.85 ± 167.85	392.5 ± 94.1	173.3 ± 41.5	77.7 ± 18.6	32.9 ± 7.9
MC exp. SM events	19389.91	11187.30	4834.13	2087.11	758.26
MC exp. Znunu events	0.14	0.09	0.05	0.00	0.00
MC exp. Wtaunu events	1022.51	553.02	262.10	120.95	47.62
MC exp. ttbar events	4437.83	2783.59	1131.02	384.53	100.85
MC exp. Wmunu events	12052.81	6803.69	2976.40	1370.24	522.03
MC exp. Wenu events	0.27	0.01	0.26	0.01	0.00
MC exp. Other events	1876.35	1046.91	464.32	211.38	87.77

CR muon 3Jet Bin $E_{\mathrm{T}}^{\mathrm{miss}}$	bin6	bin7	bin8	bin9	bin10
Observed events	263	120	46	29	23
Fitted bkg events	290.5 ± 4.6	119.8 ± 2.5	55.7 ± 1.2	24.4 ± 1.7	27.8 ± 0.5
Fitted Znunu events	0.0 ± 0.0	0.0 ± 0.0	0.0 ± 0.0	0.0 ± 0.0	0.0 ± 0.0
Fitted Wtaunu events	24.2 ± 0.6	10.9 ± 0.6	5.9 ± 0.6	$0.5^{+0.6}_{-0.5}$	2.0 ± 0.0
Fitted ttbar events	11.6 ± 3.2	4.6 ± 1.2	1.0 ± 0.2	0.2 ± 0.1	0.1 ± 0.0
Fitted Wmunu events	240.5 ± 4.7	99.3 ± 2.3	45.9 ± 1.0	22.6 ± 1.5	24.2 ± 0.5
Fitted Wenu events	0.0 ± 0.0	0.0 ± 0.0	0.0 ± 0.0	0.0 ± 0.0	0.0 ± 0.0
Fitted Other events	14.1 ± 3.4	5.0 ± 1.2	2.9 ± 0.7	1.0 ± 0.3	1.4 ± 0.3
MC exp. SM events	293.35	123.00	53.60	25.99	27.17
MC exp. Znunu events	0.00	0.00	0.00	0.00	0.00
MC exp. Wtaunu events	20.63	10.65	3.83	1.97	1.75
MC exp. ttbar events	24.80	9.98	1.82	0.95	0.29
MC exp. Wmunu events	210.03	88.38	40.51	20.23	21.30
MC exp. Wenu events	0.00	0.00	0.00	0.00	0.00
MC exp. Other events	37.88	13.99	7.45	2.84	3.82

Table F.8.: Summary of expected and fitted background event numbers in the 3 jet muon CR for the background only fit in $E_{\mathrm{T}}^{\mathrm{miss}}$.

CR muon 4Jet Bin $E_{\mathrm{T}}^{\mathrm{miss}}$	total	bin2	bin3	bin4	bin5
Observed events	38014	22495	9311	3772	1482
Fitted bkg events	37975.48 ± 179.62	22229.4 ± 118.7	9445.4 ± 53.0	3771.3 ± 58.4	1528.3 ± 19.1
Fitted Znunu events	0.47 ± 0.02	0.3 ± 0.0	0.0 ± 0.0	0.1 ± 0.0	0.0 ± 0.0
Fitted Wtaunu events	1722.00 ± 48.05	916.1 ± 26.6	427.5 ± 11.5	209.3 ± 6.6	92.3 ± 2.5
Fitted ttbar events	14358.64 ± 610.78	9328.5 ± 361.5	3639.6 ± 142.0	1015.5 ± 99.2	322.8 ± 15.4
Fitted Wmunu events	20354.85 ± 582.71	11187.8 ± 329.8	5001.1 ± 138.2	2354.2 ± 68.0	1021.8 ± 29.9
Fitted Wenu events	$0.00^{+0.00}_{-0.00}$	$0.0^{+0.0}_{-0.0}$	0.0 ± 0.0	0.0 ± 0.0	0.0 ± 0.0
Fitted Other events	1539.53 ± 365.32	796.6 ± 189.1	377.1 ± 89.6	192.0 ± 45.6	91.4 ± 21.7
MC exp. SM events	40761.75	23548.34	10128.01	4247.19	1658.65
MC exp. Znunu events	0.40	0.23	0.04	0.12	0.01
MC exp. Wtaunu events	1515.19	803.58	369.00	190.13	84.21
MC exp. ttbar events	17202.41	10822.83	4331.77	1466.47	410.05
MC exp. Wmunu events	17758.30	9707.31	4381.34	2057.99	907.00
MC exp. Wenu events	0.01	0.01	0.00	0.00	0.00
MC exp. Other events	4285.45	2214.38	1045.86	532.48	257.38

CR muon 4Jet Bin $E_{\mathrm{T}}^{\mathrm{miss}}$	bin6	bin7	bin8	bin9	bin10
Observed events	529	222	99	61	43
Fitted bkg events	540.7 ± 17.9	239.0 ± 6.0	107.8 ± 2.5	52.8 ± 1.4	60.8 ± 1.8
Fitted Znunu events	0.0 ± 0.0	0.0 ± 0.0	0.0 ± 0.0	0.0 ± 0.0	0.0 ± 0.0
Fitted Wtaunu events	39.9 ± 1.3	18.3 ± 0.7	8.8 ± 0.3	4.0 ± 0.2	5.7 ± 0.2
Fitted ttbar events	36.1 ± 21.4	10.8 ± 6.3	3.5 ± 1.9	1.2 ± 0.7	0.6 ± 0.5
Fitted Wmunu events	422.4 ± 11.4	190.3 ± 6.1	86.4 ± 2.8	42.5 ± 1.5	48.4 ± 1.6
Fitted Wenu events	0.0 ± 0.0	0.0 ± 0.0	0.0 ± 0.0	0.0 ± 0.0	0.0 ± 0.0
Fitted Other events	42.3 ± 10.0	19.6 ± 4.7	9.1 ± 2.2	5.1 ± 1.2	6.2 ± 1.5
MC exp. SM events	650.73	274.53	123.43	59.96	70.90
MC exp. Znunu events	0.00	0.00	0.00	0.01	0.00
MC exp. Wtaunu events	35.16	16.68	7.14	4.08	5.22
MC exp. ttbar events	120.14	34.42	10.63	3.66	2.43
MC exp. Wmunu events	373.51	168.08	79.13	38.91	45.03
MC exp. Wenu events	0.00	0.00	0.00	0.00	0.00
MC exp. Other events	121.93	55.35	26.53	13.30	18.23

Table F.9.: Summary of expected and fitted background event numbers in the 4 jet muon CR for the background only fit in $E_{\mathrm{T}}^{\mathrm{miss}}$.

F.2. M_{T2}

The following tables show the number of expected events from the MC prediction and the number of fitted events for each process in each bin for the SRs, the electron CRs and muon CRs with 2 jets, 3 jets and 4 or more jets, respectively.

SR 2Jet Bin M_{T2}	total	bin0	bin1	bin2	bin3	bin4	bin5	bin6	bin7	bin8	bin9	bin10
Observed events	40332	4045	11486	13685	8078	2179	569	169	70	34	10	7
Fitted bkg events	39138.66 ± 1282.70	3642.3 ± 912.61	1454.4 ± 343.31	3368.3 ± 513.27	701.9 ± 314.62	168.6 ± 97.75	42.7 ± 34.81	66.6 ± 12.25	1.7 ± 5.12	4.8 ± 1.89	8 ± 0.97	6 ± 0.4
Fitted Znunu events	23891.96 ± 1223.44	1704.8 ± 86.2	6640.9 ± 340.0	8222.0 ± 418.35	148.3 ± 265.51	563.5 ± 82.54	10.5 ± 22.9	127.0 ± 7.44	2.3 ± 2.41	9.0 ± 1.57	6 ± 0.76	1 ± 0.4
Fitted Wtaunu events	8363.74 ± 376.96	1129.0 ± 908.5	2486.3 ± 32.8	2882.8 ± 294.91	393.6 ± 168.0	358.3 ± 51.7	79.0 ± 26.0	23.8 ± 9.7	5.3 ± 4.5	3.7 ± 0.41	3 ± 0.40	8 ± 0.0
Fitted ttbar events	441.81 ± 34.86	90.0 ± 7.3	151.1 ± 11.9	70.4 ± 5.8	108.1 ± 8.4	19.5 ± 1.6	2.2 ± 0.7	0.4 ± 0.1	0.1 ± 0.0	0.0 ± 0.00	0 ± 0.00	0 ± 0.0
Fitted Wmunu events	3143.38 ± 38.55	293.0 ± 5.3	1056.3 ± 13.4	1116.3 ± 13.0	516.9 ± 7.0	121.6 ± 2.0	28.5 ± 0.5	7.3 ± 0.2	1.9 ± 0.1	0.7 ± 0.10	4 ± 0.00	4 ± 0.0
Fitted Wenu events	2756.41 ± 35.84	332.4 ± 4.6	949.1 ± 12.4	946.3 ± 12.8	423.8 ± 6.3	80.2 ± 2.1	16.8 ± 0.4	5.6 ± 0.1	1.2 ± 0.0	0.6 ± 0.10	2 ± 0.00	3 ± 0.0
Fitted Other events	541.35 ± 93.26	93.0 ± 16.0	170.8 ± 29.4	130.6 ± 22.6	111.3 ± 19.2	25.5 ± 4.4	5.7 ± 1.0	2.4 ± 0.4	0.9 ± 0.2	0.8 ± 0.10	3 ± 0.10	1 ± 0.0
MC exp. SM events	33518.10	3182.88	9813.38	11240.13	6689.59	1872.89	482.57	151.36	47.13	22.32	8.75	7.10
MC exp. Znunu events	19740.91	1390.20	5472.81	6753.05	4276.65	1312.82	357.03	113.13	36.87	16.19	6.63	5.53
MC exp. Wtaunu events	7034.24	945.82	2081.29	2386.45	1220.55	299.73	68.91	20.91	5.63	3.08	1.16	0.69
MC exp. ttbar events	654.57	127.32	225.93	106.50	158.99	29.84	4.87	0.94	0.13	0.03	0.01	0.01
MC exp. Wmunu events	2620.66	245.30	875.49	926.75	435.89	103.59	24.47	6.17	1.61	0.74	0.28	0.36
MC exp. Wenu events	2306.24	275.88	786.94	791.96	357.60	72.06	14.81	4.90	1.11	0.62	0.12	0.23
MC exp. Other events	1161.48	198.36	370.90	275.42	239.91	54.85	12.48	5.31	1.78	1.65	0.54	0.28

Table F.10.: Summary of expected and fitted background event numbers in the 2 jet SR for the background only fit in M_{T2}.

SR 3Jet Bin M_{T2}	total	bin0	bin1	bin2	bin3	bin4	bin5	bin6	bin7	bin8	bin9	bin10
Observed events	40332	4045	11486	13685	8078	2179	569	169	70	34	10	7
Fitted bkg events	39138.66 ± 1282.70	3642.3 ± 912.61	1454.4 ± 343.31	3368.3 ± 513.27	701.9 ± 314.62	168.6 ± 97.75	42.7 ± 34.81	66.6 ± 12.25	1.7 ± 5.12	4.8 ± 1.89	8 ± 0.9	7.6 ± 0.4
Fitted Znunu events	23891.96 ± 1223.44	1704.8 ± 86.2	6640.9 ± 340.0	8222.0 ± 418.35	148.3 ± 265.51	563.5 ± 82.54	10.5 ± 22.9	127.0 ± 7.44	2.3 ± 2.41	9.0 ± 1.57	6 ± 0.76	1 ± 0.4
Fitted Wtaunu events	8363.74 ± 376.96	1129.0 ± 908.5	2486.3 ± 32.8	2882.8 ± 294.91	393.6 ± 168.0	358.3 ± 51.7	79.0 ± 26.0	23.8 ± 9.7	5.3 ± 4.5	3.7 ± 0.41	3 ± 0.40	8 ± 0.0
Fitted ttbar events	441.81 ± 34.86	90.0 ± 7.3	151.1 ± 11.9	70.4 ± 5.8	108.1 ± 8.4	19.5 ± 1.6	2.2 ± 0.7	0.4 ± 0.1	0.1 ± 0.0	0.0 ± 0.00	0 ± 0.00	0 ± 0.0
Fitted Wmunu events	3143.38 ± 38.55	293.0 ± 5.3	1056.3 ± 13.4	1116.3 ± 13.0	516.9 ± 7.0	121.6 ± 2.0	28.5 ± 0.5	7.3 ± 0.2	1.9 ± 0.1	0.7 ± 0.10	4 ± 0.00	4 ± 0.0
Fitted Wenu events	2756.41 ± 35.84	332.4 ± 4.6	949.1 ± 12.4	946.3 ± 12.8	423.8 ± 6.3	80.2 ± 2.1	16.8 ± 0.4	5.6 ± 0.1	1.2 ± 0.0	0.6 ± 0.10	2 ± 0.00	3 ± 0.0
Fitted Other events	541.35 ± 93.26	93.0 ± 16.0	170.8 ± 29.4	130.6 ± 22.6	111.3 ± 19.2	25.5 ± 4.4	5.7 ± 1.0	2.4 ± 0.4	0.9 ± 0.2	0.8 ± 0.10	3 ± 0.10	1 ± 0.0
MC exp. SM events	33518.10	3182.88	9813.38	11240.13	6689.59	1872.89	482.57	151.36	47.13	22.32	8.75	7.10
MC exp. Znunu events	19740.91	1390.20	5472.81	6753.05	4276.65	1312.82	357.03	113.13	36.87	16.19	6.63	5.53
MC exp. Wtaunu events	7034.24	945.82	2081.29	2386.45	1220.55	299.73	68.91	20.91	5.63	3.08	1.16	0.69
MC exp. ttbar events	654.57	127.32	225.93	106.50	158.99	29.84	4.87	0.94	0.13	0.03	0.01	0.01
MC exp. Wmunu events	2620.66	245.30	875.49	926.75	435.89	103.59	24.47	6.17	1.61	0.74	0.28	0.36
MC exp. Wenu events	2306.24	275.88	786.94	791.96	357.60	72.06	14.81	4.90	1.11	0.62	0.12	0.23
MC exp. Other events	1161.48	198.36	370.90	275.42	239.91	54.85	12.48	5.31	1.78	1.65	0.54	0.28

Table F.11.: Summary of expected and fitted background event numbers in the 3 jet SR for the background only fit in M_{T2}.

SR 4Jet Bin M_{T2}	total	bin0	bin1	bin2	bin3	bin4	bin5	bin6	bin7	bin8	bin9	bin10
Observed events	40332	4045	11486	13685	8078	2179	569	169	70	34	10	7
Fitted bkg events	39138.66 ± 1282.70	3642.3 ± 912.61	11454.4 ± 343.31	3368.3 ± 513.27	701.9 ± 314.62	168.6 ± 97.75	42.7 ± 34.81	66.6 ± 12.25	1.7 ± 5.12	4.8 ± 1.89	8 ± 0.9	7.6 ± 0.4
Fitted Znunu events	23891.96 ± 1223.44	1704.8 ± 86.2	6640.9 ± 340.0	8222.0 ± 418.35	148.3 ± 265.51	563.5 ± 82.54	10.5 ± 22.9	127.0 ± 7.44	2.3 ± 2.41	9.0 ± 1.57	6 ± 0.7	6.1 ± 0.4
Fitted Wtaunu events	8363.74 ± 376.96	1129.0 ± 908.5	2486.3 ± 32.8	2882.8 ± 294.91	393.6 ± 168.0	358.3 ± 51.7	79.0 ± 26.0	23.8 ± 9.7	5.3 ± 4.5	3.7 ± 0.4	1.3 ± 0.4	0.8 ± 0.0
Fitted ttbar events	441.81 ± 34.86	90.0 ± 7.3	151.1 ± 11.9	70.4 ± 5.8	108.1 ± 8.4	19.5 ± 1.6	2.2 ± 0.7	0.4 ± 0.1	0.1 ± 0.0	0.0 ± 0.0	0.0 ± 0.0	0.0 ± 0.0
Fitted Wmunu events	3143.38 ± 38.55	293.0 ± 5.3	1056.3 ± 13.4	1116.3 ± 13.0	516.9 ± 7.0	121.6 ± 2.0	28.5 ± 0.5	7.3 ± 0.2	1.9 ± 0.1	0.7 ± 0.1	0.4 ± 0.0	0.4 ± 0.0
Fitted Wenu events	2756.41 ± 35.84	332.4 ± 4.6	949.1 ± 12.4	946.3 ± 12.8	423.8 ± 6.3	80.2 ± 2.1	16.8 ± 0.4	5.6 ± 0.1	1.2 ± 0.0	0.6 ± 0.1	0.2 ± 0.0	0.3 ± 0.0
Fitted Other events	541.35 ± 93.26	93.0 ± 16.0	170.8 ± 29.4	130.6 ± 22.6	111.3 ± 19.2	25.5 ± 4.4	5.7 ± 1.0	2.4 ± 0.4	0.9 ± 0.2	0.8 ± 0.1	0.3 ± 0.1	0.1 ± 0.0
MC exp. SM events	33518.10	3182.88	9813.38	11240.13	6689.59	1872.89	482.57	151.36	47.13	22.32	8.75	7.10
MC exp. Znunu events	19740.91	1390.20	5472.81	6753.05	4276.65	1312.82	357.03	113.13	36.87	16.19	6.63	5.53
MC exp. Wtaunu events	7034.24	945.82	2081.29	2386.45	1220.55	299.73	68.91	20.91	5.63	3.08	1.16	0.69
MC exp. ttbar events	654.57	127.32	225.93	106.50	158.99	29.84	4.87	0.94	0.13	0.03	0.01	0.01
MC exp. Wmunu events	2620.66	245.30	875.49	926.75	435.89	103.59	24.47	6.17	1.61	0.74	0.28	0.36
MC exp. Wenu events	2306.24	275.88	786.94	791.96	357.60	72.06	14.81	4.90	1.11	0.62	0.12	0.23
MC exp. Other events	1161.48	198.36	370.90	275.42	239.91	54.85	12.48	5.31	1.78	1.65	0.54	0.28

Table F.12.: Summary of expected and fitted background event numbers in the 4 jet SR for the background only fit in M_{T2}.

CR ele 2Jet Bin M_{T2}	total	bin0	bin1	bin2	bin3	bin4	bin5	bin6	bin7	bin8	bin9	bin10
Observed events	4025	284	1144	1521	780	220	45	17	7	3	2	2
Fitted bkg events	4083.94 ± 41.30	305.2 ± 3.5	1155.2 ± 11.6	1541.3 ± 16.2	799.6 ± 8.4	205.0 ± 2.3	51.2 ± 1.2	16.3 ± 0.5	6.8 ± 0.3	2.1 ± 0.1	0.9 ± 0.1	0.5 ± 0.0
Fitted Znunu events	1.50 ± 0.02	0.2 ± 0.0	0.7 ± 0.0	0.3 ± 0.0	0.1 ± 0.0	0.1 ± 0.0	0.0 ± 0.0	0.0 ± 0.0	0.0 ± 0.0	0.0 ± 0.0	0.0 ± 0.0	0.0 ± 0.0
Fitted Wtaunu events	708.50 ± 8.39	46.8 ± 0.7	178.8 ± 2.6	276.2 ± 3.5	150.9 ± 1.8	41.6 ± 0.5	9.5 ± 0.2	3.2 ± 0.1	0.8 ± 0.0	0.3 ± 0.0	0.2 ± 0.0	0.1 ± 0.0
Fitted ttbar events	190.96 ± 8.51	31.7 ± 1.7	53.9 ± 2.2	48.2 ± 2.1	46.7 ± 2.1	9.2 ± 0.4	1.0 ± 0.1	0.2 ± 0.0	0.0 ± 0.0	0.0 ± 0.0	0.0 ± 0.0	0.0 ± 0.0
Fitted Wmunu events	2.23 ± 0.07	$0.0^{+0.0}_{-0.0}$	0.2 ± 0.0	0.7 ± 0.0	1.3 ± 0.1	0.0 ± 0.0	0.1 ± 0.0	0.0 ± 0.0	0.0 ± 0.0	0.0 ± 0.0	0.0 ± 0.0	0.0 ± 0.0
Fitted Wenu events	3031.51 ± 34.68	200.4 ± 2.7	878.3 ± 10.0	1172.6 ± 13.5	574.6 ± 7.2	146.4 ± 1.8	38.8 ± 0.9	12.1 ± 0.4	5.6 ± 0.3	1.7 ± 0.1	0.7 ± 0.0	0.4 ± 0.0
Fitted Other events	149.24 ± 12.13	26.0 ± 2.1	43.2 ± 3.5	43.4 ± 3.5	25.8 ± 2.1	7.7 ± 0.6	1.8 ± 0.2	0.7 ± 0.1	0.4 ± 0.0	0.1 ± 0.0	0.1 ± 0.0	0.1 ± 0.0
MC exp. SM events	3624.66	282.67	1048.14	1325.43	710.77	186.19	47.34	15.88	5.09	1.62	0.80	0.74
MC exp. Znunu events	1.25	0.18	0.62	0.20	0.13	0.05	0.05	0.01	0.00	0.00	0.00	0.00
MC exp. Wtaunu events	591.87	38.15	152.64	227.36	125.29	35.97	8.30	3.15	0.57	0.20	0.13	0.12
MC exp. ttbar events	241.01	39.73	67.21	59.01	61.07	11.52	1.97	0.35	0.10	0.01	0.02	0.02
MC exp. Wmunu events	1.75	0.00	0.14	0.54	0.93	0.07	0.07	0.00	0.00	0.00	0.00	0.00
MC exp. Wenu events	2557.85	162.23	762.39	971.05	483.80	126.79	34.19	11.20	3.85	1.25	0.55	0.54
MC exp. Other events	230.93	42.37	65.14	67.26	39.53	11.80	2.76	1.17	0.57	0.16	0.10	0.07

Table F.13.: Summary of expected and fitted background event numbers in the 2 jet electron CR for the background only fit in M_{T2}.

CR ele 3Jet Bin M_{T2}	total	bin0	bin1	bin2	bin3	bin4	bin5	bin6	bin7	bin8	bin9	bin10
Observed events	3135	317	912	1152	526	167	38	16	4	2	0	1
Fitted bkg events	3140.88 ± 28.08	340.7 ± 3.4	921.1 ± 8.5	1131.2 ± 10.9	549.1 ± 5.0	136.8 ± 2.1	39.0 ± 0.8	14.8 ± 0.4	4.9 ± 0.2	2.4 ± 0.1	0.6 ± 0.0	0.4 ± 0.0
Fitted Znunu events	3.36 ± 0.04	0.2 ± 0.0	0.5 ± 0.1	2.0 ± 0.1	0.4 ± 0.0	0.1 ± 0.0	0.1 ± 0.0	0.0 ± 0.0	0.0 ± 0.0	0.0 ± 0.0	0.0 ± 0.0	0.0 ± 0.0
Fitted Wtaunu events	376.27 ± 4.68	29.1 ± 0.4	112.8 ± 1.5	134.3 ± 2.1	70.6 ± 1.4	19.9 ± 0.4	6.0 ± 0.1	2.1 ± 0.1	0.9 ± 0.0	0.5 ± 0.0	0.1 ± 0.0	0.1 ± 0.0
Fitted ttbar events	562.93 ± 15.03	130.4 ± 3.2	151.5 ± 3.8	159.6 ± 4.7	105.4 ± 2.5	13.8 ± 1.8	2.0 ± 0.3	0.2 ± 0.1	0.0 ± 0.0	0.0 ± 0.0	0.0 ± 0.0	0.0 ± 0.0
Fitted Wmunu events	1.47 ± 0.02	0.4 ± 0.0	0.2 ± 0.0	0.2 ± 0.0	0.5 ± 0.0	0.1 ± 0.0	0.1 ± 0.0	0.0 ± 0.0	0.0 ± 0.0	0.0 ± 0.0	0.0 ± 0.0	0.0 ± 0.0
Fitted Wenu events	2029.46 ± 24.68	155.9 ± 2.2	613.7 ± 7.4	780.1 ± 9.8	341.9 ± 4.5	92.6 ± 1.2	28.0 ± 0.6	11.5 ± 0.3	3.6 ± 0.1	1.6 ± 0.1	0.3 ± 0.0	0.3 ± 0.0
Fitted Other events	167.39 ± 13.60	24.7 ± 2.0	42.6 ± 3.5	55.0 ± 4.5	30.2 ± 2.5	10.3 ± 0.8	2.8 ± 0.2	1.1 ± 0.1	0.3 ± 0.0	0.3 ± 0.0	0.1 ± 0.0	0.1 ± 0.0
MC exp. SM events	3062.25	348.89	896.95	1079.29	535.46	139.66	39.35	15.11	4.15	2.19	0.56	0.64
MC exp. Znunu events	2.89	0.15	0.29	1.80	0.39	0.12	0.11	0.00	0.00	0.00	0.00	0.00
MC exp. Wtaunu events	331.17	24.08	101.55	115.60	63.58	17.68	5.41	1.99	0.69	0.43	0.08	0.08
MC exp. ttbar events	668.40	155.08	177.37	183.88	124.96	22.88	3.42	0.66	0.09	0.03	0.03	0.01
MC exp. Wmunu events	1.28	0.32	0.18	0.16	0.43	0.09	0.10	0.00	0.00	0.00	0.00	0.00
MC exp. Wenu events	1791.74	130.13	550.93	687.86	298.38	82.76	25.99	10.83	2.85	1.27	0.31	0.43
MC exp. Other events	266.02	39.12	66.63	89.71	47.49	15.90	4.32	1.63	0.51	0.46	0.13	0.12

Table F.14.: Summary of expected and fitted background event numbers in the 3 jet electron CR for the background only fit in M_{T2}.

CR ele 4Jet Bin M_{T2}	total	bin0	bin1	bin2	bin3	bin4	bin5	bin6	bin7	bin8	bin9	bin10
Observed events	9383	1208	3005	3206	1476	366	88	23	6	3	0	2
Fitted bkg events	9279.59 ± 62.95	1217.8 ± 11.2	2918.7 ± 21.1	3193.7 ± 21.5	1469.2 ± 10.1	351.1 ± 3.0	85.8 ± 1.5	24.1 ± 0.4	10.7 ± 0.4	4.8 ± 0.2	2.0 ± 0.1	1.9 ± 0.1
Fitted Znunu events	4.81 ± 0.07	0.5 ± 0.0	0.7 ± 0.0	1.5 ± 0.0	1.5 ± 0.0	0.4 ± 0.0	0.1 ± 0.0	0.0 ± 0.0	0.0 ± 0.0	0.0 ± 0.0	0.0 ± 0.0	0.0 ± 0.0
Fitted Wtaunu events	598.96 ± 8.76	51.4 ± 1.0	196.0 ± 2.7	200.1 ± 3.1	102.1 ± 1.5	33.0 ± 0.5	10.2 ± 0.2	3.4 ± 0.1	1.7 ± 0.1	0.6 ± 0.0	0.4 ± 0.0	0.2 ± 0.0
Fitted ttbar events	3583.78 ± 77.04	695.6 ± 15.1	1055.2 ± 22.6	1169.2 ± 24.8	561.3 ± 12.0	89.1 ± 2.4	10.8 ± 1.5	2.0 ± 0.4	0.5 ± 0.1	0.2 ± 0.0	0.0 ± 0.0	0.0 ± 0.0
Fitted Wmunu events	2.28 ± 0.04	0.1 ± 0.0	1.3 ± 0.0	0.5 ± 0.0	0.2 ± 0.0	0.2 ± 0.0	0.0 ± 0.0	0.0 ± 0.0	0.0 ± 0.0	0.0 ± 0.0	0.0 ± 0.0	0.0 ± 0.0
Fitted Wenu events	4492.16 ± 65.74	405.8 ± 7.1	1492.4 ± 20.5	1616.5 ± 25.2	700.6 ± 10.6	194.9 ± 2.9	54.2 ± 0.9	14.8 ± 0.3	7.1 ± 0.3	3.2 ± 0.1	1.4 ± 0.1	1.2 ± 0.1
Fitted Other events	597.59 ± 49.17	64.5 ± 5.4	173.1 ± 14.3	205.9 ± 16.9	103.5 ± 8.5	33.4 ± 2.8	10.5 ± 0.9	3.8 ± 0.3	1.4 ± 0.1	0.8 ± 0.1	0.2 ± 0.0	0.5 ± 0.0
MC exp. SM events	10070.75	1366.57	3147.38	3428.52	1593.59	386.65	98.86	28.05	11.39	5.17	2.12	2.45
MC exp. Znunu events	4.52	0.42	0.68	1.45	1.39	0.35	0.12	0.05	0.04	0.00	0.01	0.00
MC exp. Wtaunu events	571.96	49.17	187.94	189.30	97.77	31.91	9.93	3.31	1.55	0.54	0.33	0.20
MC exp. ttbar events	4264.62	833.66	1255.09	1379.70	661.98	110.07	18.50	4.01	1.06	0.37	0.11	0.06
MC exp. Wmunu events	2.10	0.05	1.09	0.51	0.19	0.22	0.02	0.00	0.01	0.01	0.00	0.00
MC exp. Wenu events	4275.60	384.32	1424.55	1529.88	666.25	190.82	52.76	14.72	6.47	3.01	1.36	1.47
MC exp. Other events	950.08	98.95	278.03	327.68	165.56	53.04	16.34	5.97	2.27	1.24	0.31	0.70

Table F.15.: Summary of expected and fitted background event numbers in the 4 jet electron CR for the background only fit in M_{T2}.

CR ele 2Jet Bin M_{T2}	total	bin0	bin1	bin2	bin3	bin4	bin5	bin6	bin7	bin8	bin9	bin10
Observed events	31854	2310	9468	10876	6431	1943	544	165	74	30	6	7
Fitted bkg events	31956.88 ± 144.65	2436.5 ± 16.1	9254.7 ± 44.9	10883.1 ± 54.7	6522.0 ± 31.5	2016.9 ± 11.1	566.5 ± 4.3	164.5 ± 1.6	71.3 ± 1.7	26.8 ± 0.8	9.7 ± 0.3	4.8 ± 0.4
Fitted Znunu events	0.46 ± 0.00	0.0 ± 0.0	0.1 ± 0.0	0.2 ± 0.0	0.0 ± 0.0	0.0 ± 0.0	0.0 ± 0.0	0.0 ± 0.0	0.0 ± 0.0	0.0 ± 0.0	0.0 ± 0.0	0.0 ± 0.0
Fitted Wtaunu events	2200.67 ± 24.95	156.4 ± 1.9	610.2 ± 7.1	765.9 ± 8.9	453.0 ± 5.3	148.0 ± 1.8	46.5 ± 0.7	13.4 ± 0.2	4.6 ± 0.2	1.5 ± 0.1	0.8 ± 0.0	0.3 ± 0.0
Fitted ttbar events	1340.12 ± 62.10	216.5 ± 10.8	389.2 ± 17.5	242.4 ± 11.9	380.9 ± 16.7	95.1 ± 4.5	13.0 ± 2.1	2.6 ± 0.4	0.4 ± 0.1	$0.0^{+0.0}_{-0.0}$	0.0 ± 0.0	0.0 ± 0.0
Fitted Wmunu events	27086.99 ± 180.28	1897.2 ± 15.9	7844.9 ± 53.3	9501.3 ± 63.7	5426.1 ± 40.3	1689.6 ± 12.7	486.0 ± 4.3	142.5 ± 1.6	63.4 ± 1.6	23.5 ± 0.7	8.6 ± 0.3	3.9 ± 0.3
Fitted Wenu events	0.08 ± 0.00	0.0 ± 0.0	0.1 ± 0.0	0.0 ± 0.0	0.0 ± 0.0	0.0 ± 0.0	0.0 ± 0.0	0.0 ± 0.0	0.0 ± 0.0	0.0 ± 0.0	0.0 ± 0.0	0.0 ± 0.0
Fitted Other events	1328.57 ± 107.84	166.3 ± 13.5	410.1 ± 33.3	373.3 ± 30.3	262.0 ± 21.3	84.3 ± 6.8	21.1 ± 1.7	6.0 ± 0.5	2.9 ± 0.2	1.7 ± 0.2	0.3 ± 0.0	0.6 ± 0.0
MC exp. SM events	28091.31	2171.02	8276.96	9288.46	5759.77	1827.77	520.01	157.57	53.43	19.45	8.77	8.11
MC exp. Znunu events	0.38	0.03	0.13	0.15	0.00	0.04	0.03	0.00	0.00	0.00	0.00	0.00
MC exp. Wtaunu events	1839.36	125.17	514.37	635.69	377.73	128.65	39.68	12.25	3.55	1.08	0.72	0.46
MC exp. ttbar events	1697.42	268.78	489.35	305.02	477.10	121.19	29.43	5.66	0.89	0.00	0.01	0.01
MC exp. Wmunu events	22486.07	1516.62	6633.07	7768.42	4495.83	1448.50	418.44	130.50	44.37	15.95	7.65	6.72
MC exp. Wenu events	0.07	0.00	0.07	0.00	0.00	0.00	0.00	0.00	0.00	0.00	0.00	0.00
MC exp. Other events	2068.01	260.43	639.97	579.17	409.10	129.39	32.42	9.16	4.62	2.42	0.40	0.92

Table F.16.: Summary of expected and fitted background event numbers in the 2 jet muon CR for the background only fit in M_{T2}.

CR mu 3Jet Bin M_{T2}	total	bin0	bin1	bin2	bin3	bin4	bin5	bin6	bin7	bin8	bin9	bin10
Observed events	19766	2152	5960	6007	3828	1277	333	120	55	27	6	1
Fitted bkg events	19937.24 ± 98.00	2371.3 ± 17.5	6023.3 ± 29.7	5974.7 ± 33.4	3797.0 ± 19.9	1200.8 ± 17.4	362.9 ± 3.8	121.8 ± 1.5	51.6 ± 1.4	20.3 ± 0.6	8.2 ± 0.2	5.2 ± 0.3
Fitted Znunu events	0.16 ± 0.00	0.0 ± 0.0	0.0 ± 0.0	0.1 ± 0.0	0.0 ± 0.0	0.0 ± 0.0	0.0 ± 0.0	0.0 ± 0.0	0.0 ± 0.0	$0.0^{+0.0}_{-0.0}$	0.0 ± 0.0	0.0 ± 0.0
Fitted Wtaunu events	1159.13 ± 14.41	106.4 ± 1.6	338.5 ± 4.3	368.9 ± 4.8	219.6 ± 2.8	79.2 ± 1.0	28.3 ± 0.4	10.4 ± 0.2	5.6 ± 0.2	1.5 ± 0.1	0.4 ± 0.0	0.3 ± 0.0
Fitted ttbar events	3744.40 ± 104.91	876.1 ± 22.9	1020.3 ± 26.1	841.0 ± 23.6	830.8 ± 20.6	143.3 ± 19.7	29.9 ± 3.9	2.1 ± 1.1	0.7 ± 0.2	0.1 ± 0.0	$0.0^{+0.0}_{-0.0}$	0.0 ± 0.0
Fitted Wmunu events	13835.08 ± 132.53	1254.0 ± 15.4	4329.5 ± 39.8	4405.8 ± 42.9	2505.1 ± 25.0	892.2 ± 9.6	278.1 ± 3.0	99.6 ± 1.3	42.3 ± 1.2	17.2 ± 0.5	7.3 ± 0.1	4.0 ± 0.3
Fitted Wenu events	0.31 ± 0.01	0.0 ± 0.0	$0.0^{+0.0}_{-0.0}$	0.3 ± 0.0	0.0 ± 0.0	0.0 ± 0.0	0.0 ± 0.0	0.0 ± 0.0	0.0 ± 0.0	0.0 ± 0.0	0.0 ± 0.0	0.0 ± 0.0
Fitted Other events	1198.16 ± 97.21	134.8 ± 11.0	334.9 ± 27.2	358.6 ± 29.1	241.5 ± 19.6	86.1 ± 7.0	26.6 ± 2.2	9.8 ± 0.8	3.0 ± 0.3	1.5 ± 0.1	0.5 ± 0.0	0.9 ± 0.1
MC exp. SM events	19390.37	2390.84	5832.72	5645.04	3706.48	1244.29	366.57	128.60	43.43	16.80	7.78	7.84
MC exp. Znunu events	0.14	0.00	0.03	0.06	0.04	0.00	0.00	0.00	0.00	0.00	0.00	0.00
MC exp. Wtaunu events	1022.51	91.23	304.15	322.41	191.32	71.77	25.38	9.85	4.34	1.20	0.38	0.50
MC exp. ttbar events	4437.81	1026.26	1182.47	964.58	960.37	243.11	49.05	9.62	1.91	0.29	0.09	0.06
MC exp. Wmunu events	12052.98	1058.84	3821.82	3795.73	2178.88	795.11	250.31	94.28	32.67	12.95	6.60	5.79
MC exp. Wenu events	0.27	0.00	0.00	0.27	0.00	0.00	0.01	0.00	0.00	0.00	0.00	0.00
MC exp. Other events	1876.36	214.51	524.25	562.00	375.56	134.30	41.83	14.85	4.50	2.36	0.71	1.48

Table F.17.: Summary of expected and fitted background event numbers in the 3 jet muon CR for the background only fit in M_{T2}.

CR ele 2Jet Bin M_{T2}	total	bin0	bin1	bin2	bin3	bin4	bin5	bin6	bin7	bin8	bin9	bin10
Observed events	38014	5459	11899	10744	6667	2260	635	212	80	31	14	13
Fitted bkg events	37780.21 ± 166.13	5543.8 ± 43.4	11717.2 ± 57.3	10506.8 ± 46.3	6695.4 ± 32.6	2283.7 ± 13.5	646.8 ± 11.9	225.7 ± 3.5	87.2 ± 2.3	41.7 ± 1.2	17.1 ± 0.2	14.8 ± 0.9
Fitted Znunu events	0.42 ± 0.01	0.0 ± 0.0	0.0 ± 0.0	0.2 ± 0.0	0.1 ± 0.0	0.0 ± 0.0	0.0 ± 0.0	0.0 ± 0.0	0.0 ± 0.0	0.0 ± 0.0	0.0 ± 0.0	0.0 ± 0.0
Fitted Wtaunu events	1600.70 ± 24.06	165.9 ± 3.0	500.5 ± 7.1	462.2 ± 7.3	290.0 ± 4.6	112.6 ± 1.7	42.6 ± 0.7	15.7 ± 0.3	5.9 ± 0.2	2.8 ± 0.1	1.3 ± 0.0	1.2 ± 0.1
Fitted ttbar events	14521.18 ± 313.00	3136.8 ± 66.0	4317.0 ± 91.4	3539.1 ± 75.4	2711.7 ± 57.4	692.4 ± 18.8	101.1 ± 13.4	17.1 ± 3.6	4.2 ± 1.0	1.1 ± 0.2	0.5 ± 0.1	0.2 ± 0.0
Fitted Wmunu events	18946.97 ± 241.80	1970.1 ± 30.7	6134.0 ± 74.2	5699.3 ± 76.1	3177.8 ± 42.7	1259.9 ± 15.7	423.1 ± 5.7	163.0 ± 2.4	64.5 ± 2.1	32.7 ± 1.1	13.0 ± 0.2	9.6 ± 0.8
Fitted Wenu events	0.04 ± 0.04	0.0 ± 0.0	0.0 ± 0.0	$0.0^{+0.0}_{-0.0}$	0.0 ± 0.0	0.0 ± 0.0	0.0 ± 0.0	0.0 ± 0.0	0.0 ± 0.0	0.0 ± 0.0	0.0 ± 0.0	0.0 ± 0.0
Fitted Other events	2710.91 ± 222.10	271.0 ± 22.3	765.7 ± 62.7	806.0 ± 66.0	515.7 ± 42.2	218.8 ± 18.0	80.0 ± 6.6	29.9 ± 2.4	12.6 ± 1.0	5.1 ± 0.4	2.3 ± 0.2	3.7 ± 0.3
MC exp. SM events	40763.29	6104.42	12581.70	11150.77	7236.63	2509.50	744.15	261.46	95.67	40.89	18.73	19.36
MC exp. Znunu events	0.40	0.03	0.04	0.19	0.12	0.00	0.00	0.00	0.00	0.01	0.00	0.00
MC exp. Wtaunu events	1515.19	154.69	474.27	432.75	278.06	108.39	40.70	15.50	5.52	2.52	1.29	1.52
MC exp. ttbar events	17202.41	3698.96	5113.08	4140.07	3170.95	852.28	170.66	41.17	11.01	2.56	1.20	0.48
MC exp. Wmunu events	17759.56	1814.73	5776.36	5310.40	2977.73	1200.92	409.53	158.45	59.12	28.17	12.57	11.58
MC exp. Wenu events	0.01	0.00	0.01	0.00	0.00	0.00	0.00	0.00	0.00	0.00	0.00	0.00
MC exp. Other events	4285.46	436.01	1217.93	1267.37	809.77	347.64	123.27	46.35	20.03	7.63	3.67	5.80

Table F.18.: Summary of expected and fitted background event numbers in the 4 jet muon CR for the background only fit in M_{T2}.

Appendix G.

Systematics Tables Background Only Fit

G.1. $E_{\mathbf{T}}^{\mathbf{miss}}$

The following tables show the systematic uncertainties considered in the background only fit performed with the $E_{\mathrm{T}}^{\mathrm{miss}}$ distributions with 2 jets, 3 jets and 4 or more jets respectively. The given values are the mean of the uncertainties in each bin of the distribution.

[SR 2Jets] Uncertainty of	Znunu	Wtaunu	ttbar	Wmunu	Wenu	Other
Total background expectation	23665.85	8353.72	558.39	3100.33	2733.39	435.87
Total statistical ($\sqrt{N_{exp}}$)	±153.84	±91.40	±23.63	±55.68	±52.28	±20.88
Total background systematic	±1212.62 [5.12%]	±113.32 [1.36%]	±45.18 [8.09%]	±43.87 [1.42%]	±37.29 [1.36%]	±104.63 [24.01%]
alpha_ClosureSyst_Znunu	±1185.86 [5.0%]	±0.00 [0.00%]	±0.00 [0.00%]	±0.00 [0.00%]	±0.00 [0.00%]	±0.00 [0.00%]
mu_Znunu	±371.12 [1.6%]	±0.00 [0.00%]	±0.00 [0.00%]	±48.62 [1.6%]	±0.00 [0.00%]	±0.00 [0.00%]
alpha_JET_GroupedNP_2	±251.46 [1.1%]	±116.65 [1.4%]	±2.46 [0.44%]	±45.16 [1.5%]	±36.22 [1.3%]	±4.27 [0.98%]
alpha_JET_EtaIntercalibration	±90.17 [0.38%]	±35.91 [0.43%]	±1.43 [0.26%]	±10.24 [0.33%]	±9.07 [0.33%]	±1.07 [0.25%]
alpha_VPt_ckkw_Syst	±85.74 [0.36%]	±24.79 [0.30%]	±0.00 [0.00%]	±8.75 [0.28%]	±7.33 [0.27%]	±0.00 [0.00%]
alpha_JET_GroupedNP_3	±47.08 [0.20%]	±10.35 [0.12%]	±1.48 [0.26%]	±8.49 [0.27%]	±5.49 [0.20%]	±1.15 [0.26%]
alpha_VPt_qsf_Syst	±43.51 [0.18%]	±18.33 [0.22%]	±0.00 [0.00%]	±6.94 [0.22%]	±6.32 [0.23%]	±0.00 [0.00%]
alpha_JET_GroupedNP_1	±24.66 [0.10%]	±45.80 [0.55%]	±7.45 [1.3%]	±6.95 [0.22%]	±6.81 [0.25%]	±1.04 [0.24%]
alpha_MET_SoftTrk	±19.83 [0.08%]	±13.41 [0.16%]	±1.62 [0.29%]	±17.95 [0.58%]	±1.35 [0.05%]	±0.96 [0.22%]
alpha_Mu_MS	±0.39 [0.00%]	±0.79 [0.01%]	±0.33 [0.06%]	±0.69 [0.02%]	±0.13 [0.00%]	±0.04 [0.01%]
alpha_EG_Scale	±0.30 [0.00%]	±1.83 [0.02%]	±0.12 [0.02%]	±0.13 [0.00%]	±7.01 [0.26%]	±0.17 [0.04%]
alpha_Mu_Scale	±0.18 [0.00%]	±0.93 [0.01%]	±0.15 [0.03%]	±0.98 [0.03%]	±0.00 [0.00%]	±0.08 [0.02%]
alpha_EG_Res	±0.01 [0.00%]	±1.65 [0.02%]	±0.28 [0.05%]	±0.17 [0.01%]	±2.16 [0.08%]	±0.06 [0.01%]
alpha_Mu_Id	±0.01 [0.00%]	±0.79 [0.01%]	±0.25 [0.04%]	±0.31 [0.01%]	±0.01 [0.00%]	±0.07 [0.02%]
mu_Wtaunu	±0.00 [0.00%]	±167.98 [2.0%]	±0.00 [0.00%]	±0.00 [0.00%]	±54.96 [2.0%]	±0.00 [0.00%]
mu_Top	±0.00 [0.00%]	±0.00 [0.00%]	±27.24 [4.9%]	±0.00 [0.00%]	±0.00 [0.00%]	±0.00 [0.00%]
alpha_ClosureSyst_2Jets	±0.00 [0.00%]	±4.87 [0.06%]	±0.00 [0.00%]	±0.00 [0.00%]	±0.00 [0.00%]	±0.00 [0.00%]
alpha_ttbar_showerSyst	±0.00 [0.00%]	±0.00 [0.00%]	±96.56 [17.3%]	±0.00 [0.00%]	±0.00 [0.00%]	±0.00 [0.00%]
alpha_ttbarRadFlatSyst	±0.00 [0.00%]	±0.00 [0.00%]	±21.52 [3.9%]	±0.00 [0.00%]	±0.00 [0.00%]	±0.00 [0.00%]
alpha_BgXSec	±0.00 [0.00%]	±0.00 [0.00%]	±0.00 [0.00%]	±0.00 [0.00%]	±0.00 [0.00%]	±104.80 [24.0%]
alpha_ttbar_hardscatterSyst	±0.00 [0.00%]	±0.00 [0.00%]	±96.56 [17.3%]	±0.00 [0.00%]	±0.00 [0.00%]	±0.00 [0.00%]

Table G.1.: Breakdown of the systematic uncertainties in the 2 jet SR for the background only fit in $E_{\mathrm{T}}^{\mathrm{miss}}$.

[SR 3Jets] Uncertainty of	Znunu	Wtaunu	ttbar	Wmunu	Wenu	Other
Total background expectation	13674.61	5926.36	2031.47	2023.28	1790.11	462.64
Total statistical ($\sqrt{N_{exp}}$)	±116.94	±76.98	±45.07	±44.98	±42.31	±21.51
Total background systematic	±715.01 [5.23%]	±90.89 [1.53%]	±118.48 [5.83%]	±36.27 [1.79%]	±30.85 [1.72%]	±110.94 [23.98%]
alpha_ClosureSyst_Znunu	±684.96 [5.0%]	±0.00 [0.00%]	±0.00 [0.00%]	±0.00 [0.00%]	±0.00 [0.00%]	±0.00 [0.00%]
mu_Znunu	±0.00 [0.00%]	±0.00 [0.00%]	±31.73 [1.6%]	±0.00 [0.00%]	±0.00 [0.00%]	±311.11 [1.6%]
alpha_JET_GroupedNP_2	±140.08 [1.0%]	±80.78 [1.4%]	±25.15 [1.2%]	±26.54 [1.3%]	±22.00 [1.2%]	±4.88 [1.1%]
alpha_JET_EtaIntercalibration	±52.12 [0.38%]	±25.92 [0.44%]	±8.99 [0.44%]	±7.61 [0.38%]	±5.56 [0.31%]	±1.00 [0.22%]
alpha_VPt_ckkw_Syst	±47.97 [0.35%]	±16.01 [0.27%]	±0.00 [0.00%]	±5.22 [0.26%]	±4.36 [0.24%]	±0.00 [0.00%]
alpha_JET_GroupedNP_3	±46.31 [0.34%]	±22.06 [0.37%]	±2.01 [0.10%]	±9.47 [0.47%]	±6.13 [0.34%]	±1.03 [0.22%]
alpha_VPt_qsf_Syst	±29.03 [0.21%]	±15.35 [0.26%]	±0.00 [0.00%]	±5.38 [0.27%]	±4.91 [0.27%]	±0.00 [0.00%]
alpha_JET_GroupedNP_1	±79.97 [0.58%]	±27.54 [0.46%]	±10.20 [0.50%]	±18.38 [0.91%]	±13.29 [0.74%]	±0.45 [0.10%]
alpha_MET_SoftTrk	±12.54 [0.09%]	±19.32 [0.33%]	±5.32 [0.26%]	±10.08 [0.50%]	±3.55 [0.20%]	±1.04 [0.23%]
alpha_Mu_MS	±0.01 [0.00%]	±0.12 [0.00%]	±0.70 [0.03%]	±0.13 [0.01%]	±0.01 [0.00%]	±0.02 [0.01%]
alpha_EG_Scale	±0.32 [0.00%]	±1.16 [0.02%]	±1.15 [0.06%]	±0.00 [0.00%]	±3.11 [0.17%]	±0.10 [0.02%]
alpha_Mu_Scale	±0.01 [0.00%]	±0.75 [0.01%]	±0.60 [0.03%]	±1.01 [0.05%]	±0.00 [0.00%]	±0.07 [0.01%]
alpha_EG_Res	±0.04 [0.00%]	±0.24 [0.00%]	±0.26 [0.01%]	±0.00 [0.00%]	±0.49 [0.03%]	±0.14 [0.03%]
alpha_Mu_Id	±0.15 [0.00%]	±0.68 [0.01%]	±0.06 [0.00%]	±0.19 [0.01%]	±0.01 [0.00%]	±0.03 [0.01%]
mu_Wtaunu	±0.00 [0.00%]	±119.17 [2.0%]	±0.00 [0.00%]	±0.00 [0.00%]	±36.00 [2.0%]	±0.00 [0.00%]
mu_Top	±0.00 [0.00%]	±0.00 [0.00%]	±99.11 [4.9%]	±0.00 [0.00%]	±0.00 [0.00%]	±0.00 [0.00%]
alpha_ClosureSyst_3Jets	±0.00 [0.00%]	±6.45 [0.11%]	±0.00 [0.00%]	±0.00 [0.00%]	±0.00 [0.00%]	±0.00 [0.00%]
alpha_ttbar_showerSyst	±0.00 [0.00%]	±0.00 [0.00%]	±84.48 [4.2%]	±0.00 [0.00%]	±0.00 [0.00%]	±0.00 [0.00%]
alpha_ttbarRadFlatSyst	±0.00 [0.00%]	±0.00 [0.00%]	±73.00 [3.6%]	±0.00 [0.00%]	±0.00 [0.00%]	±0.00 [0.00%]
alpha_BgXSec	±0.00 [0.00%]	±0.00 [0.00%]	±0.00 [0.00%]	±0.00 [0.00%]	±0.00 [0.00%]	±111.24 [24.0%]
alpha_ttbar_hardscatterSyst	±0.00 [0.00%]	±0.00 [0.00%]	±84.48 [4.2%]	±0.00 [0.00%]	±0.00 [0.00%]	±0.00 [0.00%]

Table G.2.: Breakdown of the systematic uncertainties in the 3 jet SR for the background only fit in $E_{\mathrm{T}}^{\mathrm{miss}}$.

[SR 4Jets] Uncertainty of	Znunu	Wtaunu	ttbar	Wmunu	Wenu	Other
Total background expectation	19838.90	10055.76	9013.25	3130.50	2941.02	1110.19
Total statistical ($\sqrt{N_{exp}}$)	±140.85	±100.28	±94.94	±55.95	±54.23	±33.32
Total background systematic	±1148.09 [5.79%]	±293.56 [2.92%]	±356.29 [3.95%]	±107.59 [3.44%]	±88.96 [3.02%]	±263.28 [23.71%]
alpha_ClosureSyst_Znunu	±990.69 [5.0%]	±0.00 [0.00%]	±0.00 [0.00%]	±0.00 [0.00%]	±0.00 [0.00%]	±0.00 [0.00%]
mu_Znunu	±311.11 [1.6%]	±0.00 [0.00%]	±0.00 [0.00%]	±49.09 [1.6%]	±0.00 [0.00%]	±0.00 [0.00%]
alpha_JET_GroupedNP_2	±271.35 [1.4%]	±172.06 [1.7%]	±163.19 [1.8%]	±52.14 [1.7%]	±56.92 [1.9%]	±14.76 [1.3%]
alpha_JET_EtaIntercalibration	±89.01 [0.45%]	±47.50 [0.47%]	±55.04 [0.61%]	±18.79 [0.60%]	±15.91 [0.54%]	±5.59 [0.50%]
alpha_VPt_ckkw_Syst	±6.31 [0.03%]	±5.19 [0.05%]	±0.00 [0.00%]	±1.62 [0.05%]	±1.61 [0.05%]	±0.00 [0.00%]
alpha_JET_GroupedNP_3	±145.65 [0.73%]	±81.14 [0.81%]	±64.52 [0.72%]	±28.78 [0.92%]	±26.47 [0.90%]	±6.74 [0.61%]
alpha_VPt_qsf_Syst	±43.52 [0.22%]	±28.68 [0.29%]	±0.00 [0.00%]	±8.96 [0.29%]	±8.74 [0.30%]	±0.00 [0.00%]
alpha_JET_GroupedNP_1	±468.49 [2.4%]	±251.03 [2.5%]	±188.87 [2.1%]	±92.39 [3.0%]	±78.95 [2.7%]	±21.81 [2.0%]
alpha_MET_SoftTrk	±21.06 [0.11%]	±29.74 [0.30%]	±30.11 [0.33%]	±15.89 [0.51%]	±8.47 [0.29%]	±3.18 [0.29%]
alpha_Mu_MS	±0.18 [0.00%]	±0.95 [0.01%]	±0.01 [0.00%]	±1.46 [0.05%]	±0.11 [0.00%]	±0.01 [0.00%]
alpha_EG_Scale	±0.71 [0.00%]	±2.22 [0.02%]	±5.87 [0.07%]	±0.12 [0.00%]	±6.57 [0.22%]	±0.33 [0.03%]
alpha_Mu_Scale	±0.27 [0.00%]	±0.92 [0.01%]	±1.25 [0.01%]	±2.98 [0.10%]	±0.05 [0.00%]	±0.20 [0.02%]
alpha_EG_Res	±0.05 [0.00%]	±0.68 [0.01%]	±0.39 [0.00%]	±0.03 [0.00%]	±0.26 [0.01%]	±0.21 [0.02%]
alpha_Mu_Id	±0.14 [0.00%]	±0.12 [0.00%]	±1.37 [0.02%]	±1.09 [0.03%]	±0.06 [0.00%]	±0.18 [0.02%]
mu_Wtaunu	±0.00 [0.00%]	±202.20 [2.0%]	±0.00 [0.00%]	±0.00 [0.00%]	±59.14 [2.0%]	±0.00 [0.00%]
mu_Top	±0.00 [0.00%]	±0.00 [0.00%]	±439.73 [4.9%]	±0.00 [0.00%]	±0.00 [0.00%]	±0.00 [0.00%]
alpha_ttbar_showerSyst	±0.00 [0.00%]	±0.00 [0.00%]	±484.88 [5.4%]	±0.00 [0.00%]	±0.00 [0.00%]	±0.00 [0.00%]
alpha_ClosureSyst_4Jets	±0.00 [0.00%]	±5.14 [0.05%]	±0.00 [0.00%]	±0.00 [0.00%]	±0.00 [0.00%]	±0.00 [0.00%]
alpha_ttbarRadFlatSyst	±0.00 [0.00%]	±0.00 [0.00%]	±328.84 [3.6%]	±0.00 [0.00%]	±0.00 [0.00%]	±0.00 [0.00%]
alpha_BgXSec	±0.00 [0.00%]	±0.00 [0.00%]	±0.00 [0.00%]	±0.00 [0.00%]	±0.00 [0.00%]	±266.94 [24.0%]
alpha_ttbar_hardscatterSyst	±0.00 [0.00%]	±0.00 [0.00%]	±484.88 [5.4%]	±0.00 [0.00%]	±0.00 [0.00%]	±0.00 [0.00%]

Table G.3.: Breakdown of the systematic uncertainties in the 4 jet SR for the background only fit in $E_{\mathrm{T}}^{\mathrm{miss}}$.

[CRele 2Jets] Uncertainty of	Znunu	Wtaunu	ttbar	Wmunu	Wenu	Other
Total background expectation	1.55	708.38	204.11	2.28	3002.00	85.01
Total statistical ($\sqrt{N_{exp}}$)	±1.25	±26.62	±14.29	±1.51	±54.79	±9.22
Total background systematic	±0.09 [5.47%]	±9.68 [1.37%]	±16.19 [7.93%]	±0.10 [4.34%]	±44.41 [1.48%]	±20.39 [23.98%]
alpha_EG_Res	±0.08 [5.3%]	±0.36 [0.05%]	±0.11 [0.05%]	±0.04 [1.9%]	±0.36 [0.01%]	±0.39 [0.46%]
alpha_JET_GroupedNP_1	±0.03 [1.9%]	±4.77 [0.67%]	±2.14 [1.0%]	±0.09 [3.8%]	±11.12 [0.37%]	±0.17 [0.19%]
mu_Znunu	±0.02 [1.6%]	±0.00 [0.00%]	±0.00 [0.00%]	±0.04 [1.6%]	±0.00 [0.00%]	±0.00 [0.00%]
alpha_EG_Scale	±0.01 [0.48%]	±0.13 [0.02%]	±0.49 [0.24%]	±0.06 [2.7%]	±1.52 [0.05%]	±0.02 [0.03%]
alpha_JET_EtaIntercalibration	±0.01 [0.46%]	±3.58 [0.51%]	±0.03 [0.01%]	±0.02 [0.66%]	±7.20 [0.24%]	±0.27 [0.32%]
alpha_VPt_ckkw_Syst	±0.01 [0.35%]	±2.31 [0.33%]	±0.00 [0.00%]	±0.01 [0.53%]	±9.01 [0.30%]	±0.00 [0.00%]
alpha_JET_GroupedNP_3	±0.01 [0.34%]	±0.03 [0.00%]	±0.40 [0.20%]	±0.01 [0.23%]	±7.26 [0.24%]	±0.54 [0.64%]
alpha_VPt_qsf_Syst	±0.00 [0.22%]	±1.43 [0.20%]	±0.00 [0.00%]	±0.00 [0.13%]	±6.49 [0.22%]	±0.00 [0.00%]
alpha_JET_GroupedNP_2	±0.00 [0.19%]	±7.35 [1.0%]	±1.27 [0.62%]	±0.01 [0.39%]	±39.98 [1.3%]	±1.50 [1.8%]
gamma_stat_CRele_2Jets_bin_6	±0.00 [0.09%]	±0.04 [0.01%]	±0.02 [0.01%]	±0.00 [0.00%]	±0.66 [0.02%]	±0.04 [0.04%]
gamma_stat_CRele_2Jets_bin_8	±0.00 [0.04%]	±0.06 [0.01%]	±0.00 [0.00%]	±0.00 [0.00%]	±0.19 [0.01%]	±0.01 [0.01%]
gamma_stat_CRele_2Jets_bin_5	±0.00 [0.03%]	±0.23 [0.03%]	±0.02 [0.01%]	±0.00 [0.00%]	±0.88 [0.03%]	±0.03 [0.04%]
alpha_MET_SoftTrk	±0.00 [0.00%]	±0.58 [0.08%]	±0.12 [0.06%]	±0.01 [0.27%]	±5.31 [0.18%]	±0.09 [0.11%]
gamma_stat_CRele_2Jets_bin_7	±0.00 [0.00%]	±0.06 [0.01%]	±0.00 [0.00%]	±0.00 [0.00%]	±0.21 [0.01%]	±0.01 [0.01%]
mu_Wtaunu	±0.00 [0.00%]	±14.24 [2.0%]	±0.00 [0.00%]	±0.00 [0.00%]	±60.37 [2.0%]	±0.00 [0.00%]
gamma_stat_CRele_2Jets_bin_4	±0.00 [0.00%]	±0.50 [0.07%]	±0.06 [0.03%]	±0.00 [0.00%]	±1.76 [0.06%]	±0.05 [0.06%]
mu_Top	±0.00 [0.00%]	±0.00 [0.00%]	±9.96 [4.9%]	±0.00 [0.00%]	±0.00 [0.00%]	±0.00 [0.00%]
alpha_ttbar_showerSyst	±0.00 [0.00%]	±0.00 [0.00%]	±35.30 [17.3%]	±0.00 [0.00%]	±0.00 [0.00%]	±0.00 [0.00%]
alpha_Mu_MS	±0.00 [0.00%]	±0.00 [0.00%]	±0.01 [0.00%]	±0.00 [0.00%]	±0.06 [0.00%]	±0.00 [0.00%]
alpha_Mu_Scale	±0.00 [0.00%]	±0.00 [0.00%]	±0.21 [0.10%]	±0.00 [0.00%]	±0.06 [0.00%]	±0.00 [0.00%]
alpha_Mu_Id	±0.00 [0.00%]	±0.00 [0.00%]	±0.04 [0.02%]	±0.00 [0.00%]	±0.02 [0.00%]	±0.00 [0.00%]
alpha_ttbarRadFlatSyst	±0.00 [0.00%]	±0.00 [0.00%]	±7.87 [3.9%]	±0.00 [0.00%]	±0.00 [0.00%]	±0.00 [0.00%]
alpha_BgXSec	±0.00 [0.00%]	±0.00 [0.00%]	±0.00 [0.00%]	±0.00 [0.00%]	±0.00 [0.00%]	±20.44 [24.0%]
alpha_ttbar_hardscatterSyst	±0.00 [0.00%]	±0.00 [0.00%]	±35.30 [17.3%]	±0.00 [0.00%]	±0.00 [0.00%]	±0.00 [0.00%]

Table G.4.: Breakdown of the systematic uncertainties in the 2 jet electron CR for the background only fit in $E_{\mathrm{T}}^{\mathrm{miss}}$.

[CRele 3Jets] Uncertainty of	Znunu	Wtaunu	ttbar	Wmunu	Wenu	Other
Total background expectation	3.47	392.94	595.51	1.56	2106.03	98.74
Total statistical ($\sqrt{N_{exp}}$)	±1.86	±19.82	±24.40	±1.25	±45.89	±9.94
Total background systematic	±0.07 [2.01%]	±6.77 [1.72%]	±33.08 [5.56%]	±0.08 [5.41%]	±33.18 [1.58%]	±23.58 [23.88%]
mu_Znunu	±0.05 [1.6%]	±0.00 [0.00%]	±0.00 [0.00%]	±0.02 [1.6%]	±0.00 [0.00%]	±0.00 [0.00%]
alpha_JET_GroupedNP_2	±0.05 [1.4%]	±2.98 [0.76%]	±7.16 [1.2%]	±0.01 [0.47%]	±22.84 [1.1%]	±1.01 [1.0%]
alpha_EG_Res	±0.05 [1.3%]	±0.57 [0.14%]	±0.49 [0.08%]	±0.02 [1.3%]	±1.32 [0.06%]	±0.09 [0.09%]
alpha_JET_EtaIntercalibration	±0.03 [0.83%]	±1.36 [0.35%]	±1.10 [0.18%]	±0.00 [0.00%]	±8.31 [0.39%]	±0.10 [0.10%]
alpha_EG_Scale	±0.03 [0.77%]	±0.06 [0.02%]	±0.21 [0.04%]	±0.08 [5.0%]	±3.10 [0.15%]	±0.02 [0.02%]
alpha_JET_GroupedNP_1	±0.02 [0.60%]	±1.57 [0.40%]	±1.19 [0.20%]	±0.00 [0.31%]	±8.42 [0.40%]	±0.64 [0.65%]
alpha_JET_GroupedNP_3	±0.01 [0.32%]	±0.33 [0.08%]	±1.20 [0.20%]	±0.00 [0.04%]	±7.56 [0.36%]	±0.27 [0.27%]
alpha_VPt_ckkw_Syst	±0.01 [0.30%]	±1.27 [0.32%]	±0.00 [0.00%]	±0.01 [0.40%]	±5.80 [0.28%]	±0.00 [0.00%]
alpha_VPt_qsf_Syst	±0.01 [0.24%]	±0.90 [0.23%]	±0.00 [0.00%]	±0.00 [0.18%]	±5.32 [0.25%]	±0.00 [0.00%]
gamma_stat_CRele_3Jets_bin_4	±0.00 [0.08%]	±0.21 [0.05%]	±0.04 [0.01%]	±0.00 [0.04%]	±1.15 [0.05%]	±0.08 [0.08%]
gamma_stat_CRele_3Jets_bin_8	±0.00 [0.06%]	±0.04 [0.01%]	±0.00 [0.00%]	±0.00 [0.00%]	±0.16 [0.01%]	±0.02 [0.02%]
alpha_MET_SoftTrk	±0.00 [0.03%]	±0.25 [0.06%]	±2.43 [0.41%]	±0.01 [0.38%]	±8.94 [0.42%]	±0.55 [0.56%]
gamma_stat_CRele_3Jets_bin_5	±0.00 [0.03%]	±0.15 [0.04%]	±0.02 [0.00%]	±0.00 [0.00%]	±0.69 [0.03%]	±0.04 [0.04%]
gamma_stat_CRele_3Jets_bin_6	±0.00 [0.02%]	±0.09 [0.02%]	±0.01 [0.00%]	±0.00 [0.00%]	±0.28 [0.01%]	±0.02 [0.02%]
mu_Wtaunu	±0.00 [0.00%]	±7.90 [2.0%]	±0.00 [0.00%]	±0.00 [0.00%]	±42.35 [2.0%]	±0.00 [0.00%]
mu_Top	±0.00 [0.00%]	±0.00 [0.00%]	±29.05 [4.9%]	±0.00 [0.00%]	±0.00 [0.00%]	±0.00 [0.00%]
alpha_ttbar_showerSyst	±0.00 [0.00%]	±0.00 [0.00%]	±24.78 [4.2%]	±0.00 [0.00%]	±0.00 [0.00%]	±0.00 [0.00%]
alpha_Mu_MS	±0.00 [0.00%]	±0.11 [0.03%]	±0.03 [0.01%]	±0.00 [0.00%]	±0.20 [0.01%]	±0.00 [0.00%]
alpha_Mu_Scale	±0.00 [0.00%]	±0.00 [0.00%]	±0.03 [0.01%]	±0.00 [0.00%]	±0.01 [0.00%]	±0.00 [0.00%]
alpha_Mu_Id	±0.00 [0.00%]	±0.01 [0.00%]	±0.04 [0.01%]	±0.00 [0.00%]	±1.30 [0.06%]	±0.00 [0.00%]
alpha_ttbarRadFlatSyst	±0.00 [0.00%]	±0.00 [0.00%]	±21.41 [3.6%]	±0.00 [0.00%]	±0.00 [0.00%]	±0.00 [0.00%]
alpha_BgXSec	±0.00 [0.00%]	±0.00 [0.00%]	±0.00 [0.00%]	±0.00 [0.00%]	±0.00 [0.00%]	±23.74 [24.0%]
gamma_stat_CRele_3Jets_bin_7	±0.00 [0.00%]	±0.07 [0.02%]	±0.00 [0.00%]	±0.00 [0.00%]	±0.19 [0.01%]	±0.02 [0.02%]
alpha_ttbar_hardscatterSyst	±0.00 [0.00%]	±0.00 [0.00%]	±24.78 [4.2%]	±0.00 [0.00%]	±0.00 [0.00%]	±0.00 [0.00%]

Table G.5.: Breakdown of the systematic uncertainties in the 3 jet electron CR for the background only fit in $E_{\mathrm{T}}^{\mathrm{miss}}$.

[CRele 4Jets] Uncertainty of	Znunu	Wtaunu	ttbar	Wmunu	Wenu	Other
Total background expectation	5.39	643.14	3535.24	2.12	4808.03	334.93
Total statistical ($\sqrt{N_{exp}}$)	±2.32	±25.36	±59.46	±1.46	±69.34	±18.30
Total background systematic	±0.15 [2.72%]	±19.48 [3.03%]	±132.54 [3.75%]	±0.12 [5.82%]	±128.84 [2.68%]	±79.23 [23.66%]
mu_Znunu	±0.08 [1.6%]	±0.00 [0.00%]	±0.00 [0.00%]	±0.03 [1.6%]	±0.00 [0.00%]	±0.00 [0.00%]
alpha_JET_GroupedNP_1	±0.08 [1.5%]	±16.59 [2.6%]	±85.78 [2.4%]	±0.08 [3.7%]	±106.95 [2.2%]	±7.38 [2.2%]
alpha_EG_Scale	±0.03 [0.54%]	±0.14 [0.02%]	±0.84 [0.02%]	±0.00 [0.16%]	±3.39 [0.07%]	±0.09 [0.03%]
alpha_JET_GroupedNP_3	±0.02 [0.36%]	±5.00 [0.78%]	±30.22 [0.85%]	±0.06 [3.0%]	±36.78 [0.76%]	±2.49 [0.74%]
alpha_JET_EtaIntercalibration	±0.02 [0.28%]	±2.42 [0.38%]	±22.03 [0.62%]	±0.02 [0.80%]	±26.12 [0.54%]	±2.05 [0.61%]
alpha_VPt_qsf_Syst	±0.01 [0.19%]	±1.61 [0.25%]	±0.00 [0.00%]	±0.01 [0.27%]	±13.84 [0.29%]	±0.00 [0.00%]
alpha_EG_Res	±0.01 [0.14%]	±0.74 [0.12%]	±0.92 [0.03%]	±0.00 [0.20%]	±4.48 [0.09%]	±0.54 [0.16%]
alpha_JET_GroupedNP_2	±0.01 [0.14%]	±10.18 [1.6%]	±71.45 [2.0%]	±0.14 [6.6%]	±85.93 [1.8%]	±6.28 [1.9%]
gamma_stat_CRele_4Jets_bin_5	±0.00 [0.07%]	±0.26 [0.04%]	±0.05 [0.00%]	±0.00 [0.00%]	±0.80 [0.02%]	±0.10 [0.03%]
alpha_Mu_Id	±0.00 [0.06%]	±0.02 [0.00%]	±0.43 [0.01%]	±0.00 [0.00%]	±0.03 [0.00%]	±0.01 [0.00%]
gamma_stat_CRele_4Jets_bin_8	±0.00 [0.05%]	±0.08 [0.01%]	±0.00 [0.00%]	±0.00 [0.00%]	±0.27 [0.01%]	±0.05 [0.02%]
alpha_VPt_ckkw_Syst	±0.00 [0.03%]	±0.27 [0.04%]	±0.00 [0.00%]	±0.00 [0.05%]	±2.54 [0.05%]	±0.00 [0.00%]
gamma_stat_CRele_4Jets_bin_7	±0.00 [0.01%]	±0.05 [0.01%]	±0.00 [0.00%]	±0.00 [0.00%]	±0.28 [0.01%]	±0.01 [0.00%]
gamma_stat_CRele_4Jets_bin_6	±0.00 [0.01%]	±0.10 [0.02%]	±0.01 [0.00%]	±0.00 [0.07%]	±0.44 [0.01%]	±0.05 [0.02%]
alpha_MET_SoftTrk	±0.00 [0.01%]	±2.05 [0.32%]	±12.95 [0.37%]	±0.00 [0.15%]	±17.94 [0.37%]	±1.48 [0.44%]
mu_Wtaunu	±0.00 [0.00%]	±12.93 [2.0%]	±0.00 [0.00%]	±0.00 [0.00%]	±96.68 [2.0%]	±0.00 [0.00%]
mu_Top	±0.00 [0.00%]	±0.00 [0.00%]	±172.47 [4.9%]	±0.00 [0.00%]	±0.00 [0.00%]	±0.00 [0.00%]
alpha_ttbar_showerSyst	±0.00 [0.00%]	±0.00 [0.00%]	±184.01 [5.2%]	±0.00 [0.00%]	±0.00 [0.00%]	±0.00 [0.00%]
alpha_Mu_MS	±0.00 [0.00%]	±0.00 [0.00%]	±0.12 [0.00%]	±0.00 [0.00%]	±0.08 [0.00%]	±0.00 [0.00%]
alpha_Mu_Scale	±0.00 [0.00%]	±0.00 [0.00%]	±0.47 [0.01%]	±0.00 [0.00%]	±0.02 [0.00%]	±0.01 [0.00%]
alpha_ttbarRadFlatSyst	±0.00 [0.00%]	±0.00 [0.00%]	±128.54 [3.6%]	±0.00 [0.00%]	±0.00 [0.00%]	±0.00 [0.00%]
alpha_BgXSec	±0.00 [0.00%]	±0.00 [0.00%]	±0.00 [0.00%]	±0.00 [0.00%]	±0.00 [0.00%]	±80.53 [24.0%]
alpha_ttbar_hardscatterSyst	±0.00 [0.00%]	±0.00 [0.00%]	±184.01 [5.2%]	±0.00 [0.00%]	±0.00 [0.00%]	±0.00 [0.00%]

Table G.6.: Breakdown of the systematic uncertainties in the 4 jet electron CR for the background only fit in $E_{\mathrm{T}}^{\mathrm{miss}}$.

[CRmu 2Jets] Uncertainty of	Znunu	Wtaunu	ttbar	Wmunu	Wenu	Other
Total background expectation	0.45	2201.15	1446.79	27090.96	0.08	782.01
Total statistical ($\sqrt{N_{exp}}$)	±0.67	±46.92	±38.04	±164.59	±0.29	±27.96
Total background systematic	±0.01 [1.76%]	±34.97 [1.59%]	±120.97 [8.36%]	±279.09 [1.03%]	±0.00 [1.96%]	±187.93 [24.03%]
mu_Znunu	±0.01 [1.6%]	±0.00 [0.00%]	±0.00 [0.00%]	±424.83 [1.6%]	±0.00 [0.00%]	±0.00 [0.00%]
alpha_JET_GroupedNP_2	±0.01 [1.2%]	±14.06 [0.64%]	±8.51 [0.59%]	±241.33 [0.89%]	±0.00 [0.00%]	±4.84 [0.62%]
alpha_Mu_Id	±0.00 [0.67%]	±1.51 [0.07%]	±0.40 [0.03%]	±1.65 [0.01%]	±0.00 [0.00%]	±0.08 [0.01%]
alpha_Mu_MS	±0.00 [0.67%]	±1.27 [0.06%]	±0.40 [0.03%]	±5.53 [0.02%]	±0.00 [0.00%]	±0.12 [0.02%]
alpha_JET_GroupedNP_1	±0.00 [0.49%]	±0.80 [0.04%]	±22.97 [1.6%]	±45.83 [0.17%]	±0.00 [0.00%]	±2.20 [0.28%]
alpha_VPt_ckkw_Syst	±0.00 [0.32%]	±8.14 [0.37%]	±0.00 [0.00%]	±95.28 [0.35%]	±0.00 [0.14%]	±0.00 [0.00%]
alpha_VPt_qsf_Syst	±0.00 [0.25%]	±4.03 [0.18%]	±0.00 [0.00%]	±51.52 [0.19%]	±0.00 [0.31%]	±0.00 [0.00%]
alpha_MET_SoftTrk	±0.00 [0.11%]	±0.78 [0.04%]	±0.57 [0.04%]	±14.95 [0.06%]	±0.00 [0.00%]	±1.29 [0.16%]
alpha_JET_GroupedNP_3	±0.00 [0.04%]	±1.34 [0.06%]	±1.43 [0.10%]	±42.53 [0.16%]	±0.00 [0.00%]	±0.75 [0.10%]
alpha_JET_EtaIntercalibration	±0.00 [0.00%]	±7.09 [0.32%]	±4.38 [0.30%]	±79.37 [0.29%]	±0.00 [0.00%]	±1.93 [0.25%]
mu_Wtaunu	±0.00 [0.00%]	±44.26 [2.0%]	±0.00 [0.00%]	±0.00 [0.00%]	±0.00 [2.0%]	±0.00 [0.00%]
mu_Top	±0.00 [0.00%]	±0.00 [0.00%]	±70.59 [4.9%]	±0.00 [0.00%]	±0.00 [0.00%]	±0.00 [0.00%]
alpha_ttbar_showerSyst	±0.00 [0.00%]	±0.00 [0.00%]	±250.19 [17.3%]	±0.00 [0.00%]	±0.00 [0.00%]	±0.00 [0.00%]
alpha_EG_Scale	±0.00 [0.00%]	±0.00 [0.00%]	±0.14 [0.01%]	±0.62 [0.00%]	±0.00 [0.00%]	±0.06 [0.01%]
alpha_Mu_Scale	±0.00 [0.00%]	±0.29 [0.01%]	±0.08 [0.01%]	±2.27 [0.01%]	±0.00 [0.00%]	±0.08 [0.01%]
alpha_EG_Res	±0.00 [0.00%]	±0.00 [0.00%]	±0.22 [0.02%]	±1.59 [0.01%]	±0.00 [0.00%]	±0.05 [0.01%]
gamma_stat_CRmu_2Jets_bin_7	±0.00 [0.00%]	±0.17 [0.01%]	±0.02 [0.00%]	±1.46 [0.01%]	±0.00 [0.00%]	±0.04 [0.00%]
alpha_ttbarRadFlatSyst	±0.00 [0.00%]	±0.00 [0.00%]	±55.75 [3.9%]	±0.00 [0.00%]	±0.00 [0.00%]	±0.00 [0.00%]
alpha_BgXSec	±0.00 [0.00%]	±0.00 [0.00%]	±0.00 [0.00%]	±0.00 [0.00%]	±0.00 [0.00%]	±188.03 [24.0%]
alpha_ttbar_hardscatterSyst	±0.00 [0.00%]	±0.00 [0.00%]	±250.19 [17.3%]	±0.00 [0.00%]	±0.00 [0.00%]	±0.00 [0.00%]

Table G.7.: Breakdown of the systematic uncertainties in the 2 jet muon CR for the background only fit in $E_{\mathrm{T}}^{\mathrm{miss}}$.

[CRmu 3Jets] Uncertainty of	Znunu	Wtaunu	ttbar	Wmunu	Wenu	Other
Total background expectation	0.18	1202.20	3945.11	14309.36	0.34	700.85
Total statistical ($\sqrt{N_{exp}}$)	±0.42	±34.67	±62.81	±119.62	±0.58	±26.47
Total background systematic	±0.00 [1.51%]	±19.59 [1.63%]	±223.62 [5.67%]	±216.24 [1.51%]	±0.01 [2.33%]	±167.85 [23.95%]
alpha_JET_GroupedNP_1	±0.00 [2.2%]	±6.03 [0.50%]	±12.11 [0.31%]	±82.96 [0.58%]	±0.00 [0.81%]	±1.14 [0.16%]
mu_Znunu	±0.00 [1.6%]	±0.00 [0.00%]	±0.00 [0.00%]	±224.40 [1.6%]	±0.00 [0.00%]	±0.00 [0.00%]
alpha_VPt_ckkw_Syst	±0.00 [0.27%]	±4.60 [0.38%]	±0.00 [0.00%]	±52.00 [0.36%]	±0.00 [0.48%]	±0.00 [0.00%]
alpha_VPt_qsf_Syst	±0.00 [0.22%]	±2.28 [0.19%]	±0.00 [0.00%]	±29.35 [0.21%]	±0.00 [0.03%]	±0.00 [0.00%]
gamma_stat_CRmu_3Jets_bin_7	±0.00 [0.11%]	±0.03 [0.00%]	±0.01 [0.00%]	±1.35 [0.01%]	±0.00 [0.00%]	±0.06 [0.01%]
alpha_JET_EtaIntercalibration	±0.00 [0.00%]	±3.11 [0.26%]	±19.37 [0.49%]	±66.36 [0.46%]	±0.00 [0.00%]	±2.21 [0.32%]
mu_Wtaunu	±0.00 [0.00%]	±24.17 [2.0%]	±0.00 [0.00%]	±0.00 [0.00%]	±0.01 [2.0%]	±0.00 [0.00%]
alpha_JET_GroupedNP_3	±0.00 [0.00%]	±3.21 [0.27%]	±4.82 [0.12%]	±39.11 [0.27%]	±0.01 [1.6%]	±1.60 [0.23%]
alpha_JET_GroupedNP_2	±0.00 [0.00%]	±12.93 [1.1%]	±45.67 [1.2%]	±138.50 [0.97%]	±0.00 [0.01%]	±6.18 [0.88%]
mu_Top	±0.00 [0.00%]	±0.00 [0.00%]	±192.47 [4.9%]	±0.00 [0.00%]	±0.00 [0.00%]	±0.00 [0.00%]
alpha_ttbar_showerSyst	±0.00 [0.00%]	±0.00 [0.00%]	±172.85 [4.4%]	±0.00 [0.00%]	±0.00 [0.00%]	±0.00 [0.00%]
alpha_MET_SoftTrk	±0.00 [0.00%]	±0.71 [0.06%]	±5.47 [0.14%]	±10.35 [0.07%]	±0.00 [0.06%]	±1.28 [0.18%]
alpha_Mu_MS	±0.00 [0.00%]	±0.17 [0.01%]	±0.72 [0.02%]	±1.16 [0.01%]	±0.00 [0.00%]	±0.02 [0.00%]
alpha_EG_Scale	±0.00 [0.00%]	±0.03 [0.00%]	±0.31 [0.01%]	±0.07 [0.00%]	±0.00 [0.00%]	±0.03 [0.00%]
alpha_Mu_Scale	±0.00 [0.00%]	±0.51 [0.04%]	±0.51 [0.01%]	±1.90 [0.01%]	±0.00 [0.00%]	±0.05 [0.01%]
gamma_stat_CRele_3Jets_bin_8	±0.00 [0.00%]	±0.00 [0.00%]	±0.00 [0.00%]	±0.00 [0.00%]	±0.00 [0.00%]	±0.00 [0.00%]
alpha_EG_Res	±0.00 [0.00%]	±0.02 [0.00%]	±0.12 [0.00%]	±0.12 [0.00%]	±0.00 [0.00%]	±0.33 [0.05%]
alpha_Mu_Id	±0.00 [0.00%]	±0.64 [0.05%]	±0.48 [0.01%]	±1.47 [0.01%]	±0.00 [0.00%]	±0.04 [0.01%]
alpha_ttbarRadFlatSyst	±0.00 [0.00%]	±0.00 [0.00%]	±144.46 [3.7%]	±0.00 [0.00%]	±0.00 [0.00%]	±0.00 [0.00%]
alpha_BgXSec	±0.00 [0.00%]	±0.00 [0.00%]	±0.00 [0.00%]	±0.00 [0.00%]	±0.00 [0.00%]	±168.52 [24.0%]
alpha_ttbar_hardscatterSyst	±0.00 [0.00%]	±0.00 [0.00%]	±172.85 [4.4%]	±0.00 [0.00%]	±0.00 [0.00%]	±0.00 [0.00%]

Table G.8.: Breakdown of the systematic uncertainties in the 3 jet muon CR for the background only fit in $E_{\mathrm{T}}^{\mathrm{miss}}$.

[CRmu 4Jets] Uncertainty of	Znunu	Wtaunu	ttbar	Wmunu	Wenu	Other
Total background expectation	0.47	1722.00	14358.64	20354.85	0.00	1539.53
Total statistical ($\sqrt{N_{exp}}$)	±0.68	±41.50	±119.83	±142.67	±0.00	±39.24
Total background systematic	±0.02 [4.40%]	±48.05 [2.79%]	±610.78 [4.25%]	±582.71 [2.86%]	±0.00 [2163.29%]	±365.32 [23.73%]
alpha_JET_GroupedNP_1	±0.01 [3.1%]	±37.63 [2.2%]	±267.66 [1.9%]	±465.25 [2.3%]	±0.00 [28.6%]	±28.14 [1.8%]
mu_Znunu	±0.01 [1.6%]	±0.00 [0.00%]	±0.00 [0.00%]	±319.20 [1.6%]	±0.00 [0.00%]	±0.00 [0.00%]
alpha_Mu_Id	±0.00 [0.69%]	±0.22 [0.01%]	±1.57 [0.01%]	±0.46 [0.00%]	±0.00 [0.00%]	±0.15 [0.01%]
alpha_VPt_qsf_Syst	±0.00 [0.29%]	±3.43 [0.20%]	±0.00 [0.00%]	±42.77 [0.21%]	±0.00 [0.41%]	±0.00 [0.00%]
alpha_VPt_ckkw_Syst	±0.00 [0.06%]	±0.44 [0.03%]	±0.00 [0.00%]	±5.98 [0.03%]	±0.00 [0.08%]	±0.00 [0.00%]
alpha_JET_GroupedNP_3	±0.00 [0.01%]	±10.31 [0.60%]	±97.35 [0.68%]	±147.71 [0.73%]	±0.00 [141.2%]	±9.70 [0.63%]
alpha_Mu_MS	±0.00 [0.00%]	±0.77 [0.04%]	±1.93 [0.01%]	±0.60 [0.00%]	±0.00 [0.00%]	±0.02 [0.00%]
alpha_JET_GroupedNP_2	±0.00 [0.00%]	±23.10 [1.3%]	±215.51 [1.5%]	±273.61 [1.3%]	±0.00 [2138.7%]	±19.91 [1.3%]
mu_Wtaunu	±0.00 [0.00%]	±34.63 [2.0%]	±0.00 [0.00%]	±0.00 [0.00%]	±0.00 [2.0%]	±0.00 [0.00%]
mu_Top	±0.00 [0.00%]	±0.00 [0.00%]	±700.52 [4.9%]	±0.00 [0.00%]	±0.00 [0.00%]	±0.00 [0.00%]
alpha_JET_EtaIntercalibration	±0.00 [0.00%]	±8.68 [0.50%]	±76.65 [0.53%]	±102.65 [0.50%]	±0.00 [201.5%]	±6.57 [0.43%]
alpha_ttbar_showerSyst	±0.00 [0.00%]	±0.00 [0.00%]	±974.48 [6.8%]	±0.00 [0.00%]	±0.00 [0.00%]	±0.00 [0.00%]
alpha_MET_SoftTrk	±0.00 [0.00%]	±0.41 [0.02%]	±20.48 [0.14%]	±18.05 [0.09%]	±0.00 [0.00%]	±2.09 [0.14%]
alpha_EG_Scale	±0.00 [0.00%]	±0.03 [0.00%]	±0.94 [0.01%]	±0.90 [0.00%]	±0.00 [0.00%]	±0.09 [0.01%]
alpha_Mu_Scale	±0.00 [0.00%]	±0.13 [0.01%]	±1.07 [0.01%]	±2.12 [0.01%]	±0.00 [0.00%]	±0.06 [0.00%]
alpha_EG_Res	±0.00 [0.00%]	±0.05 [0.00%]	±0.05 [0.00%]	±0.31 [0.00%]	±0.00 [0.00%]	±0.01 [0.00%]
alpha_ttbarRadFlatSyst	±0.00 [0.00%]	±0.00 [0.00%]	±547.86 [3.8%]	±0.00 [0.00%]	±0.00 [0.00%]	±0.00 [0.00%]
alpha_BgXSec	±0.00 [0.00%]	±0.00 [0.00%]	±0.00 [0.00%]	±0.00 [0.00%]	±0.00 [0.00%]	±370.18 [24.0%]
alpha_ttbar_hardscatterSyst	±0.00 [0.00%]	±0.00 [0.00%]	±974.48 [6.8%]	±0.00 [0.00%]	±0.00 [0.00%]	±0.00 [0.00%]

Table G.9.: Breakdown of the systematic uncertainties in the 4 jet muon CR for the background only fit in $E_{\mathrm{T}}^{\mathrm{miss}}$.

G.2. M_{T2}

The following tables show the systematic uncertainties considered in the background only fit performed with the M_{T2} distributions with 2 jets, 3 jets and 4 or more jets respectively. The given values are the mean of the uncertainties in each bin of the distribution.

[SR 2Jets] Uncertainty of	Znunu	Wtaunu	ttbar	Wmunu	Wenu	Other
Total background expectation	24435.08	8513.53	512.52	3129.14	2768.43	744.18
Total statistical ($\sqrt{N_{exp}}$)	±156.32	±92.27	±22.64	±55.94	±52.62	±27.28
Total background systematic	±175.24 [0.72%]	±98.37 [1.16%]	±23.43 [4.57%]	±26.49 [0.85%]	±31.35 [1.13%]	±60.41 [8.12%]
mu_Znunu	±391.11 [1.6%]	±0.00 [0.00%]	±0.00 [0.00%]	±50.09 [1.6%]	±0.00 [0.00%]	±0.00 [0.00%]
alpha_ShapeSyst_2Jets	±365.89 [1.5%]	±131.81 [1.5%]	±0.00 [0.00%]	±48.07 [1.5%]	±42.77 [1.5%]	±0.00 [0.00%]
alpha_ClosureSyst_Znunu	±192.04 [0.79%]	±0.00 [0.00%]	±0.00 [0.00%]	±0.00 [0.00%]	±0.00 [0.00%]	±0.00 [0.00%]
alpha_JET_GroupedNP_2	±88.38 [0.36%]	±34.22 [0.40%]	±1.04 [0.20%]	±19.31 [0.62%]	±11.16 [0.40%]	±2.36 [0.32%]
alpha_JET_EtaIntercalibration	±35.30 [0.14%]	±13.04 [0.15%]	±0.51 [0.10%]	±4.66 [0.15%]	±2.97 [0.11%]	±0.68 [0.09%]
alpha_VPt_ckkw_Syst	±32.36 [0.13%]	±9.18 [0.11%]	±0.00 [0.00%]	±3.34 [0.11%]	±2.72 [0.10%]	±0.00 [0.00%]
alpha_JET_GroupedNP_3	±28.07 [0.11%]	±7.57 [0.09%]	±0.78 [0.15%]	±6.83 [0.22%]	±1.63 [0.06%]	±1.07 [0.14%]
alpha_JET_GroupedNP_1	±21.09 [0.09%]	±31.86 [0.37%]	±4.76 [0.93%]	±4.37 [0.14%]	±5.41 [0.20%]	±1.39 [0.19%]
alpha_VPt_qsf_Syst	±13.69 [0.06%]	±5.30 [0.06%]	±0.00 [0.00%]	±2.01 [0.06%]	±1.80 [0.07%]	±0.00 [0.00%]
alpha_MET_SoftTrk	±8.60 [0.04%]	±6.12 [0.07%]	±0.74 [0.14%]	±7.51 [0.24%]	±0.94 [0.03%]	±0.89 [0.12%]
gamma_stat_SR_2JetBin_bin_8	±0.40 [0.00%]	±0.07 [0.00%]	±0.00 [0.00%]	±0.02 [0.00%]	±0.01 [0.00%]	±0.02 [0.00%]
gamma_stat_SR_2JetBin_bin_9	±0.16 [0.00%]	±0.03 [0.00%]	±0.00 [0.00%]	±0.01 [0.00%]	±0.00 [0.00%]	±0.01 [0.00%]
alpha_EG_Scale	±0.09 [0.00%]	±0.88 [0.01%]	±0.06 [0.01%]	±0.07 [0.00%]	±2.25 [0.08%]	±0.13 [0.02%]
alpha_Mu_MS	±0.08 [0.00%]	±0.15 [0.00%]	±0.08 [0.02%]	±0.15 [0.00%]	±0.03 [0.00%]	±0.02 [0.00%]
alpha_Mu_Id	±0.06 [0.00%]	±0.24 [0.00%]	±0.06 [0.01%]	±0.02 [0.00%]	±0.00 [0.00%]	±0.03 [0.00%]
alpha_Mu_Scale	±0.04 [0.00%]	±0.20 [0.00%]	±0.03 [0.01%]	±0.21 [0.01%]	±0.00 [0.00%]	±0.03 [0.00%]
alpha_EG_Res	±0.00 [0.00%]	±0.35 [0.00%]	±0.06 [0.01%]	±0.03 [0.00%]	±0.43 [0.02%]	±0.03 [0.00%]
mu_Wtaunu	±0.00 [0.00%]	±159.24 [1.9%]	±0.00 [0.00%]	±0.00 [0.00%]	±51.78 [1.9%]	±0.00 [0.00%]
alpha_ClosureSyst_2Jets	±0.00 [0.00%]	±33.16 [0.39%]	±0.00 [0.00%]	±0.00 [0.00%]	±0.00 [0.00%]	±0.00 [0.00%]
alpha_BgXSec	±0.00 [0.00%]	±0.00 [0.00%]	±0.00 [0.00%]	±0.00 [0.00%]	±0.00 [0.00%]	±60.40 [8.1%]
mu_Top	±0.00 [0.00%]	±0.00 [0.00%]	±13.71 [2.7%]	±0.00 [0.00%]	±0.00 [0.00%]	±0.00 [0.00%]
alpha_ttbar_showerSyst	±0.00 [0.00%]	±0.00 [0.00%]	±20.13 [3.9%]	±0.00 [0.00%]	±0.00 [0.00%]	±0.00 [0.00%]
alpha_ttbarRadFlatSyst	±0.00 [0.00%]	±0.00 [0.00%]	±8.06 [1.6%]	±0.00 [0.00%]	±0.00 [0.00%]	±0.00 [0.00%]
alpha_ttbar_hardscatterSyst	±0.00 [0.00%]	±0.00 [0.00%]	±20.13 [3.9%]	±0.00 [0.00%]	±0.00 [0.00%]	±0.00 [0.00%]

Table G.10.: Breakdown of the systematic uncertainties in the 2 jet SR for the background only fit in M_{T2}.

[SR 3Jets] Uncertainty of	Znunu	Wtaunu	ttbar	Wmunu	Wenu	Other
Total background expectation	13601.64	5763.73	1938.24	1958.61	1741.40	794.71
Total statistical ($\sqrt{N_{exp}}$)	±116.63	±75.92	±44.03	±44.26	±41.73	±28.19
Total background systematic	±119.26 [0.88%]	±72.45 [1.26%]	±53.71 [2.77%]	±21.33 [1.09%]	±21.62 [1.24%]	±64.49 [8.11%]
mu_Znunu	±217.71 [1.6%]	±0.00 [0.00%]	±0.00 [0.00%]	±31.35 [1.6%]	±0.00 [0.00%]	±0.00 [0.00%]
alpha_ShapeSyst_3Jets	±194.26 [1.4%]	±84.89 [1.5%]	±0.00 [0.00%]	±28.58 [1.5%]	±25.71 [1.5%]	±0.00 [0.00%]
alpha_ClosureSyst_Znunu	±111.52 [0.82%]	±0.00 [0.00%]	±0.00 [0.00%]	±0.00 [0.00%]	±0.00 [0.00%]	±0.00 [0.00%]
alpha_JET_GroupedNP_1	±48.39 [0.36%]	±14.15 [0.25%]	±6.78 [0.35%]	±11.36 [0.58%]	±7.91 [0.45%]	±0.61 [0.08%]
alpha_JET_GroupedNP_2	±44.21 [0.33%]	±19.96 [0.35%]	±7.27 [0.38%]	±9.38 [0.48%]	±6.47 [0.37%]	±2.70 [0.34%]
alpha_JET_GroupedNP_3	±23.98 [0.18%]	±8.95 [0.16%]	±0.36 [0.02%]	±5.42 [0.28%]	±3.03 [0.17%]	±0.99 [0.13%]
alpha_VPt_ckkw_Syst	±19.90 [0.15%]	±7.26 [0.13%]	±0.00 [0.00%]	±2.34 [0.12%]	±2.00 [0.11%]	±0.00 [0.00%]
alpha_JET_EtaIntercalibration	±19.14 [0.14%]	±8.30 [0.14%]	±2.91 [0.15%]	±2.53 [0.13%]	±1.99 [0.11%]	±0.61 [0.08%]
alpha_VPt_qsf_Syst	±7.06 [0.05%]	±3.36 [0.06%]	±0.00 [0.00%]	±1.18 [0.06%]	±1.06 [0.06%]	±0.00 [0.00%]
alpha_MET_SoftTrk	±5.66 [0.04%]	±10.12 [0.18%]	±1.18 [0.06%]	±4.27 [0.22%]	±1.28 [0.07%]	±0.58 [0.07%]
gamma_stat_SR_3JetBin_bin_8	±0.26 [0.00%]	±0.04 [0.00%]	±0.00 [0.00%]	±0.01 [0.00%]	±0.01 [0.00%]	±0.01 [0.00%]
gamma_stat_SR_3JetBin_bin_9	±0.15 [0.00%]	±0.04 [0.00%]	±0.00 [0.00%]	±0.01 [0.00%]	±0.00 [0.00%]	±0.01 [0.00%]
alpha_EG_Scale	±0.12 [0.00%]	±0.44 [0.01%]	±0.45 [0.02%]	±0.00 [0.00%]	±1.04 [0.06%]	±0.07 [0.01%]
gamma_stat_SR_3JetBin_bin_10	±0.08 [0.00%]	±0.01 [0.00%]	±0.00 [0.00%]	±0.01 [0.00%]	±0.00 [0.00%]	±0.01 [0.00%]
alpha_Mu_Id	±0.02 [0.00%]	±0.12 [0.00%]	±0.05 [0.00%]	±0.02 [0.00%]	±0.00 [0.00%]	±0.01 [0.00%]
alpha_EG_Res	±0.01 [0.00%]	±0.05 [0.00%]	±0.06 [0.00%]	±0.00 [0.00%]	±0.09 [0.01%]	±0.06 [0.01%]
alpha_Mu_Scale	±0.00 [0.00%]	±0.16 [0.00%]	±0.14 [0.01%]	±0.22 [0.01%]	±0.00 [0.00%]	±0.03 [0.00%]
alpha_Mu_MS	±0.00 [0.00%]	±0.02 [0.00%]	±0.20 [0.01%]	±0.02 [0.00%]	±0.00 [0.00%]	±0.01 [0.00%]
mu_Wtaunu	±0.00 [0.00%]	±107.81 [1.9%]	±0.00 [0.00%]	±0.00 [0.00%]	±32.57 [1.9%]	±0.00 [0.00%]
alpha_BgXSec	±0.00 [0.00%]	±0.00 [0.00%]	±0.00 [0.00%]	±0.00 [0.00%]	±0.00 [0.00%]	±64.51 [8.1%]
mu_Top	±0.00 [0.00%]	±0.00 [0.00%]	±51.86 [2.7%]	±0.00 [0.00%]	±0.00 [0.00%]	±0.00 [0.00%]
alpha_ttbar_showerSyst	±0.00 [0.00%]	±0.00 [0.00%]	±29.64 [1.5%]	±0.00 [0.00%]	±0.00 [0.00%]	±0.00 [0.00%]
alpha_ClosureSyst_3Jets	±0.00 [0.00%]	±25.02 [0.43%]	±0.00 [0.00%]	±0.00 [0.00%]	±0.00 [0.00%]	±0.00 [0.00%]
alpha_ttbarRadFlatSyst	±0.00 [0.00%]	±0.00 [0.00%]	±27.01 [1.4%]	±0.00 [0.00%]	±0.00 [0.00%]	±0.00 [0.00%]
alpha_ttbar_hardscatterSyst	±0.00 [0.00%]	±0.00 [0.00%]	±29.64 [1.5%]	±0.00 [0.00%]	±0.00 [0.00%]	±0.00 [0.00%]

Table G.11.: Breakdown of the systematic uncertainties in the 3 jet SR for the background only fit in M_{T2}.

[SR 4Jets] Uncertainty of	Znunu	Wtaunu	ttbar	Wmunu	Wenu	Other
Total background expectation	19035.78	9531.41	9106.98	2935.17	2784.56	1955.57
Total statistical ($\sqrt{N_{exp}}$)	±137.97	±97.63	±95.43	±54.18	±52.77	±44.22
Total background systematic	±203.98 [1.07%]	±142.23 [1.49%]	±194.67 [2.14%]	±39.53 [1.35%]	±40.35 [1.45%]	±160.48 [8.21%]
alpha_ShapeSyst_4Jets	±340.30 [1.8%]	±174.79 [1.8%]	±0.00 [0.00%]	±53.99 [1.8%]	±51.45 [1.8%]	±0.00 [0.00%]
mu_Znunu	±304.69 [1.6%]	±0.00 [0.00%]	±0.00 [0.00%]	±46.98 [1.6%]	±0.00 [0.00%]	±0.00 [0.00%]
alpha_JET_GroupedNP_1	±293.76 [1.5%]	±153.50 [1.6%]	±124.20 [1.4%]	±55.35 [1.9%]	±48.21 [1.7%]	±24.91 [1.3%]
alpha_ClosureSyst_Znunu	±165.80 [0.87%]	±0.00 [0.00%]	±0.00 [0.00%]	±0.00 [0.00%]	±0.00 [0.00%]	±0.00 [0.00%]
alpha_JET_GroupedNP_2	±88.34 [0.46%]	±50.44 [0.53%]	±54.60 [0.60%]	±17.91 [0.61%]	±16.92 [0.61%]	±9.27 [0.47%]
alpha_JET_GroupedNP_3	±74.06 [0.39%]	±38.94 [0.41%]	±33.36 [0.37%]	±13.92 [0.47%]	±13.05 [0.47%]	±6.20 [0.32%]
alpha_VPt_ckkw_Syst	±33.13 [0.17%]	±14.34 [0.15%]	±0.00 [0.00%]	±4.29 [0.15%]	±3.95 [0.14%]	±0.00 [0.00%]
alpha_JET_EtaIntercalibration	±32.33 [0.17%]	±16.13 [0.17%]	±21.01 [0.23%]	±7.25 [0.25%]	±5.23 [0.19%]	±3.92 [0.20%]
alpha_VPt_qsf_Syst	±10.25 [0.05%]	±5.97 [0.06%]	±0.00 [0.00%]	±1.87 [0.06%]	±1.82 [0.07%]	±0.00 [0.00%]
alpha_MET_SoftTrk	±7.89 [0.04%]	±12.35 [0.13%]	±11.87 [0.13%]	±6.36 [0.22%]	±3.61 [0.13%]	±2.88 [0.15%]
alpha_EG_Scale	±0.22 [0.00%]	±0.76 [0.01%]	±2.23 [0.02%]	±0.04 [0.00%]	±2.41 [0.09%]	±0.25 [0.01%]
gamma_stat_SR_4JetBin_bin_10	±0.21 [0.00%]	±0.02 [0.00%]	±0.00 [0.00%]	±0.01 [0.00%]	±0.01 [0.00%]	±0.04 [0.00%]
gamma_stat_SR_4JetBin_bin_9	±0.20 [0.00%]	±0.02 [0.00%]	±0.00 [0.00%]	±0.01 [0.00%]	±0.01 [0.00%]	±0.02 [0.00%]
alpha_Mu_MS	±0.06 [0.00%]	±0.21 [0.00%]	±0.03 [0.00%]	±0.35 [0.01%]	±0.03 [0.00%]	±0.01 [0.00%]
alpha_Mu_Scale	±0.06 [0.00%]	±0.20 [0.00%]	±0.31 [0.00%]	±0.66 [0.02%]	±0.01 [0.00%]	±0.09 [0.00%]
alpha_Mu_Id	±0.05 [0.00%]	±0.07 [0.00%]	±0.31 [0.00%]	±0.38 [0.01%]	±0.02 [0.00%]	±0.12 [0.01%]
alpha_EG_Res	±0.00 [0.00%]	±0.12 [0.00%]	±0.07 [0.00%]	±0.01 [0.00%]	±0.07 [0.00%]	±0.08 [0.00%]
mu_Wtaunu	±0.00 [0.00%]	±178.28 [1.9%]	±0.00 [0.00%]	±0.00 [0.00%]	±52.08 [1.9%]	±0.00 [0.00%]
alpha_BgXSec	±0.00 [0.00%]	±0.00 [0.00%]	±0.00 [0.00%]	±0.00 [0.00%]	±0.00 [0.00%]	±158.73 [8.1%]
mu_Top	±0.00 [0.00%]	±0.00 [0.00%]	±243.67 [2.7%]	±0.00 [0.00%]	±0.00 [0.00%]	±0.00 [0.00%]
alpha_ttbar_showerSyst	±0.00 [0.00%]	±0.00 [0.00%]	±116.25 [1.3%]	±0.00 [0.00%]	±0.00 [0.00%]	±0.00 [0.00%]
alpha_ClosureSyst_4Jets	±0.00 [0.00%]	±28.11 [0.29%]	±0.00 [0.00%]	±0.00 [0.00%]	±0.00 [0.00%]	±0.00 [0.00%]
alpha_ttbarRadFlatSyst	±0.00 [0.00%]	±0.00 [0.00%]	±125.53 [1.4%]	±0.00 [0.00%]	±0.00 [0.00%]	±0.00 [0.00%]
alpha_ttbar_hardscatterSyst	±0.00 [0.00%]	±0.00 [0.00%]	±116.25 [1.3%]	±0.00 [0.00%]	±0.00 [0.00%]	±0.00 [0.00%]

Table G.12.: Breakdown of the systematic uncertainties in the 4 jet SR for the background only fit in M_{T2}.

[CRele 2Jets] Uncertainty of	Znunu	Wtaunu	ttbar	Wmunu	Wenu	Other
Total background expectation	1.50	708.50	190.96	2.23	3031.51	149.24
Total statistical ($\sqrt{N_{exp}}$)	±1.23	±26.62	±13.82	±1.49	±55.06	±12.22
Total background systematic	±0.02 [1.54%]	±8.39 [1.18%]	±8.51 [4.45%]	±0.07 [2.99%]	±34.68 [1.14%]	±12.13 [8.13%]
mu_Znunu	±0.02 [1.6%]	±0.00 [0.00%]	±0.00 [0.00%]	±0.04 [1.6%]	±0.00 [0.00%]	±0.00 [0.00%]
alpha_ShapeSyst_2Jets	±0.02 [1.5%]	±10.92 [1.5%]	±0.00 [0.00%]	±0.03 [1.5%]	±46.50 [1.5%]	±0.00 [0.00%]
alpha_EG_Res	±0.02 [1.2%]	±0.07 [0.01%]	±0.01 [0.01%]	±0.00 [0.05%]	±0.08 [0.00%]	±0.15 [0.10%]
alpha_JET_GroupedNP_1	±0.01 [0.84%]	±2.88 [0.41%]	±1.41 [0.74%]	±0.07 [2.9%]	±5.07 [0.17%]	±0.18 [0.12%]
alpha_EG_Scale	±0.00 [0.31%]	±0.03 [0.00%]	±0.13 [0.07%]	±0.01 [0.41%]	±0.40 [0.01%]	±0.05 [0.03%]
alpha_JET_EtaIntercalibration	±0.00 [0.18%]	±1.52 [0.22%]	±0.09 [0.05%]	±0.01 [0.25%]	±3.25 [0.11%]	±0.29 [0.20%]
alpha_JET_GroupedNP_2	±0.00 [0.12%]	±2.19 [0.31%]	±0.81 [0.42%]	±0.01 [0.39%]	±12.04 [0.40%]	±0.77 [0.51%]
alpha_VPt_ckkw_Syst	±0.00 [0.11%]	±0.93 [0.13%]	±0.00 [0.00%]	±0.00 [0.17%]	±3.68 [0.12%]	±0.00 [0.00%]
alpha_JET_GroupedNP_3	±0.00 [0.09%]	±0.03 [0.00%]	±0.29 [0.15%]	±0.01 [0.43%]	±4.56 [0.15%]	±0.60 [0.40%]
alpha_VPt_qsf_Syst	±0.00 [0.06%]	±0.42 [0.06%]	±0.00 [0.00%]	±0.00 [0.04%]	±1.86 [0.06%]	±0.00 [0.00%]
gamma_stat_CRele_2Jets_bin_5	±0.00 [0.06%]	±0.17 [0.02%]	±0.02 [0.01%]	±0.00 [0.06%]	±0.69 [0.02%]	±0.03 [0.02%]
gamma_stat_CRele_2Jets_bin_6	±0.00 [0.02%]	±0.09 [0.01%]	±0.01 [0.00%]	±0.00 [0.00%]	±0.34 [0.01%]	±0.02 [0.01%]
gamma_stat_CRele_2Jets_bin_8	±0.00 [0.02%]	±0.01 [0.00%]	±0.00 [0.00%]	±0.00 [0.00%]	±0.06 [0.00%]	±0.00 [0.00%]
alpha_MET_SoftTrk	±0.00 [0.00%]	±0.16 [0.02%]	±0.04 [0.02%]	±0.02 [1.0%]	±3.63 [0.12%]	±0.08 [0.06%]
mu_Wtaunu	±0.00 [0.00%]	±13.25 [1.9%]	±0.00 [0.00%]	±0.00 [0.00%]	±56.70 [1.9%]	±0.00 [0.00%]
alpha_BgXSec	±0.00 [0.00%]	±0.00 [0.00%]	±0.00 [0.00%]	±0.00 [0.00%]	±0.00 [0.00%]	±12.11 [8.1%]
gamma_stat_CRele_2Jets_bin_7	±0.00 [0.00%]	±0.03 [0.00%]	±0.00 [0.00%]	±0.00 [0.00%]	±0.22 [0.01%]	±0.01 [0.01%]
mu_Top	±0.00 [0.00%]	±0.00 [0.00%]	±5.11 [2.7%]	±0.00 [0.00%]	±0.00 [0.00%]	±0.00 [0.00%]
alpha_ttbar_showerSyst	±0.00 [0.00%]	±0.00 [0.00%]	±7.50 [3.9%]	±0.00 [0.00%]	±0.00 [0.00%]	±0.00 [0.00%]
alpha_Mu_MS	±0.00 [0.00%]	±0.00 [0.00%]	±0.01 [0.01%]	±0.00 [0.00%]	±0.01 [0.00%]	±0.00 [0.00%]
alpha_Mu_Scale	±0.00 [0.00%]	±0.00 [0.00%]	±0.05 [0.03%]	±0.00 [0.00%]	±0.01 [0.00%]	±0.00 [0.00%]
alpha_Mu_Id	±0.00 [0.00%]	±0.00 [0.00%]	±0.01 [0.01%]	±0.00 [0.00%]	±0.00 [0.00%]	±0.00 [0.00%]
alpha_ttbarRadFlatSyst	±0.00 [0.00%]	±0.00 [0.00%]	±3.02 [1.6%]	±0.00 [0.00%]	±0.00 [0.00%]	±0.00 [0.00%]
alpha_ttbar_hardscatterSyst	±0.00 [0.00%]	±0.00 [0.00%]	±7.50 [3.9%]	±0.00 [0.00%]	±0.00 [0.00%]	±0.00 [0.00%]

Table G.13.: Breakdown of the systematic uncertainties in the 2 jet electron CR for the background only fit in M_{T2}.

[CRele 3Jets] Uncertainty of	Znunu	Wtaunu	ttbar	Wmunu	Wenu	Other
Total background expectation	3.36	376.27	562.93	1.47	2029.46	167.39
Total statistical ($\sqrt{N_{exp}}$)	±1.83	±19.40	±23.73	±1.21	±45.05	±12.94
Total background systematic	±0.04 [1.15%]	±4.68 [1.24%]	±15.03 [2.67%]	±0.02 [1.47%]	±24.68 [1.22%]	±13.60 [8.12%]
mu_Znunu	±0.05 [1.6%]	±0.00 [0.00%]	±0.00 [0.00%]	±0.02 [1.6%]	±0.00 [0.00%]	±0.00 [0.00%]
alpha_ShapeSyst_3Jets	±0.05 [1.5%]	±5.54 [1.5%]	±0.00 [0.00%]	±0.02 [1.5%]	±29.88 [1.5%]	±0.00 [0.00%]
alpha_JET_GroupedNP_1	±0.02 [0.52%]	±0.76 [0.20%]	±0.95 [0.17%]	±0.00 [0.25%]	±5.92 [0.29%]	±0.46 [0.27%]
alpha_EG_Res	±0.01 [0.27%]	±0.10 [0.03%]	±0.12 [0.02%]	±0.01 [0.51%]	±0.31 [0.02%]	±0.04 [0.02%]
alpha_EG_Scale	±0.01 [0.23%]	±0.04 [0.01%]	±0.03 [0.01%]	±0.01 [0.70%]	±0.89 [0.04%]	±0.00 [0.00%]
alpha_JET_EtaIntercalibration	±0.01 [0.22%]	±0.34 [0.09%]	±0.47 [0.08%]	±0.00 [0.00%]	±3.38 [0.17%]	±0.11 [0.07%]
alpha_VPt_ckkw_Syst	±0.01 [0.16%]	±0.57 [0.15%]	±0.00 [0.00%]	±0.00 [0.20%]	±2.88 [0.14%]	±0.00 [0.00%]
gamma_stat_CRele_3Jets_bin_5	±0.00 [0.06%]	±0.09 [0.02%]	±0.03 [0.01%]	±0.00 [0.10%]	±0.43 [0.02%]	±0.04 [0.03%]
alpha_VPt_qsf_Syst	±0.00 [0.06%]	±0.20 [0.05%]	±0.00 [0.00%]	±0.00 [0.04%]	±1.14 [0.06%]	±0.00 [0.00%]
alpha_JET_GroupedNP_3	±0.00 [0.04%]	±0.30 [0.08%]	±0.78 [0.14%]	±0.00 [0.02%]	±4.92 [0.24%]	±0.31 [0.18%]
alpha_MET_SoftTrk	±0.00 [0.04%]	±0.09 [0.02%]	±1.22 [0.22%]	±0.00 [0.17%]	±2.76 [0.14%]	±0.51 [0.31%]
alpha_JET_GroupedNP_2	±0.00 [0.01%]	±0.74 [0.20%]	±2.22 [0.40%]	±0.01 [0.37%]	±9.76 [0.48%]	±0.45 [0.27%]
gamma_stat_CRele_3Jets_bin_7	±0.00 [0.01%]	±0.03 [0.01%]	±0.00 [0.00%]	±0.00 [0.00%]	±0.11 [0.01%]	±0.01 [0.01%]
gamma_stat_CRele_3Jets_bin_6	±0.00 [0.00%]	±0.04 [0.01%]	±0.00 [0.00%]	±0.00 [0.00%]	±0.24 [0.01%]	±0.02 [0.01%]
gamma_stat_CRele_3Jets_bin_10	±0.00 [0.00%]	±0.00 [0.00%]	±0.00 [0.00%]	±0.00 [0.00%]	±0.01 [0.00%]	±0.00 [0.00%]
mu_Wtaunu	±0.00 [0.00%]	±7.04 [1.9%]	±0.00 [0.00%]	±0.00 [0.00%]	±37.96 [1.9%]	±0.00 [0.00%]
alpha_BgXSec	±0.00 [0.00%]	±0.00 [0.00%]	±0.00 [0.00%]	±0.00 [0.00%]	±0.00 [0.00%]	±13.59 [8.1%]
mu_Top	±0.00 [0.00%]	±0.00 [0.00%]	±15.06 [2.7%]	±0.00 [0.00%]	±0.00 [0.00%]	±0.00 [0.00%]
alpha_ttbar_showerSyst	±0.00 [0.00%]	±0.00 [0.00%]	±8.72 [1.5%]	±0.00 [0.00%]	±0.00 [0.00%]	±0.00 [0.00%]
alpha_Mu_MS	±0.00 [0.00%]	±0.03 [0.01%]	±0.01 [0.00%]	±0.00 [0.00%]	±0.04 [0.00%]	±0.00 [0.00%]
alpha_Mu_Scale	±0.00 [0.00%]	±0.00 [0.00%]	±0.01 [0.00%]	±0.00 [0.00%]	±0.00 [0.00%]	±0.00 [0.00%]
alpha_Mu_Id	±0.00 [0.00%]	±0.00 [0.00%]	±0.01 [0.00%]	±0.00 [0.00%]	±0.10 [0.01%]	±0.00 [0.00%]
alpha_ttbarRadFlatSyst	±0.00 [0.00%]	±0.00 [0.00%]	±7.87 [1.4%]	±0.00 [0.00%]	±0.00 [0.00%]	±0.00 [0.00%]
gamma_stat_CRele_3Jets_bin_9	±0.00 [0.00%]	±0.01 [0.00%]	±0.00 [0.00%]	±0.00 [0.00%]	±0.02 [0.00%]	±0.00 [0.00%]
gamma_stat_CRele_3Jets_bin_8	±0.00 [0.00%]	±0.02 [0.01%]	±0.00 [0.00%]	±0.00 [0.00%]	±0.07 [0.00%]	±0.01 [0.01%]
alpha_ttbar_hardscatterSyst	±0.00 [0.00%]	±0.00 [0.00%]	±8.72 [1.5%]	±0.00 [0.00%]	±0.00 [0.00%]	±0.00 [0.00%]

Table G.14.: Breakdown of the systematic uncertainties in the 3 jet electron CR for the background only fit in M_{T2}.

[CRele 4Jets] Uncertainty of	Znunu	Wtaunu	ttbar	Wmunu	Wenu	Other
Total background expectation	4.81	598.96	3583.78	2.28	4492.16	597.59
Total statistical ($\sqrt{N_{exp}}$)	±2.19	±24.47	±59.86	±1.51	±67.02	±24.45
Total background systematic	±0.07 [1.52%]	±8.76 [1.46%]	±77.04 [2.15%]	±0.04 [1.81%]	±65.74 [1.46%]	±49.17 [8.23%]
alpha_ShapeSyst_4Jets	±0.09 [1.9%]	±11.02 [1.8%]	±0.00 [0.00%]	±0.04 [1.7%]	±82.83 [1.8%]	±0.00 [0.00%]
mu_Znunu	±0.08 [1.6%]	±0.00 [0.00%]	±0.00 [0.00%]	±0.04 [1.6%]	±0.00 [0.00%]	±0.00 [0.00%]
alpha_JET_GroupedNP_1	±0.05 [0.98%]	±9.94 [1.7%]	±55.58 [1.6%]	±0.05 [2.3%]	±66.22 [1.5%]	±8.32 [1.4%]
alpha_VPt_ckkw_Syst	±0.01 [0.23%]	±1.05 [0.17%]	±0.00 [0.00%]	±0.00 [0.17%]	±7.28 [0.16%]	±0.00 [0.00%]
alpha_EG_Scale	±0.01 [0.12%]	±0.01 [0.00%]	±0.03 [0.00%]	±0.00 [0.03%]	±0.82 [0.02%]	±0.11 [0.02%]
alpha_JET_GroupedNP_3	±0.00 [0.05%]	±2.29 [0.38%]	±14.24 [0.40%]	±0.02 [1.1%]	±16.99 [0.38%]	±2.17 [0.36%]
alpha_VPt_qsf_Syst	±0.00 [0.04%]	±0.35 [0.06%]	±0.00 [0.00%]	±0.00 [0.06%]	±2.77 [0.06%]	±0.00 [0.00%]
alpha_JET_GroupedNP_2	±0.00 [0.04%]	±2.58 [0.43%]	±21.89 [0.61%]	±0.02 [0.73%]	±24.52 [0.55%]	±3.35 [0.56%]
alpha_JET_EtaIntercalibration	±0.00 [0.03%]	±0.98 [0.16%]	±7.91 [0.22%]	±0.01 [0.60%]	±8.40 [0.19%]	±1.20 [0.20%]
alpha_EG_Res	±0.00 [0.02%]	±0.16 [0.03%]	±0.16 [0.00%]	±0.00 [0.04%]	±1.04 [0.02%]	±0.23 [0.04%]
alpha_Mu_Id	±0.00 [0.02%]	±0.00 [0.00%]	±0.11 [0.00%]	±0.00 [0.00%]	±0.04 [0.00%]	±0.00 [0.00%]
gamma_stat_CRele_4Jets_bin_7	±0.00 [0.01%]	±0.03 [0.00%]	±0.01 [0.00%]	±0.00 [0.01%]	±0.12 [0.00%]	±0.02 [0.00%]
alpha_MET_SoftTrk	±0.00 [0.01%]	±0.87 [0.15%]	±6.55 [0.18%]	±0.00 [0.12%]	±7.50 [0.17%]	±1.22 [0.20%]
gamma_stat_CRele_4Jets_bin_9	±0.00 [0.01%]	±0.01 [0.00%]	±0.00 [0.00%]	±0.00 [0.00%]	±0.05 [0.00%]	±0.01 [0.00%]
gamma_stat_CRele_4Jets_bin_10	±0.00 [0.00%]	±0.01 [0.00%]	±0.00 [0.00%]	±0.00 [0.00%]	±0.04 [0.00%]	±0.01 [0.00%]
gamma_stat_CRele_4Jets_bin_8	±0.00 [0.00%]	±0.01 [0.00%]	±0.00 [0.00%]	±0.00 [0.01%]	±0.08 [0.00%]	±0.02 [0.00%]
mu_Wtaunu	±0.00 [0.00%]	±11.20 [1.9%]	±0.00 [0.00%]	±0.00 [0.00%]	±84.02 [1.9%]	±0.00 [0.00%]
alpha_BgXSec	±0.00 [0.00%]	±0.00 [0.00%]	±0.00 [0.00%]	±0.00 [0.00%]	±0.00 [0.00%]	±48.51 [8.1%]
mu_Top	±0.00 [0.00%]	±0.00 [0.00%]	±95.89 [2.7%]	±0.00 [0.00%]	±0.00 [0.00%]	±0.00 [0.00%]
alpha_ttbar_showerSyst	±0.00 [0.00%]	±0.00 [0.00%]	±45.63 [1.3%]	±0.00 [0.00%]	±0.00 [0.00%]	±0.00 [0.00%]
alpha_Mu_MS	±0.00 [0.00%]	±0.00 [0.00%]	±0.01 [0.00%]	±0.00 [0.00%]	±0.03 [0.00%]	±0.00 [0.00%]
alpha_Mu_Scale	±0.00 [0.00%]	±0.00 [0.00%]	±0.13 [0.00%]	±0.00 [0.00%]	±0.00 [0.00%]	±0.01 [0.00%]
alpha_ttbarRadFlatSyst	±0.00 [0.00%]	±0.00 [0.00%]	±49.42 [1.4%]	±0.00 [0.00%]	±0.00 [0.00%]	±0.00 [0.00%]
alpha_ttbar_hardscatterSyst	±0.00 [0.00%]	±0.00 [0.00%]	±45.63 [1.3%]	±0.00 [0.00%]	±0.00 [0.00%]	±0.00 [0.00%]

Table G.15.: Breakdown of the systematic uncertainties in the 4 jet electron CR for the background only fit in M_{T2}.

[CRmu 2Jets] Uncertainty of	Znunu	Wtaunu	ttbar	Wmunu	Wenu	Other
Total background expectation	0.46	2200.67	1340.12	27086.99	0.08	1328.57
Total statistical ($\sqrt{N_{exp}}$)	±0.67	±46.91	±36.61	±164.58	±0.28	±36.45
Total background systematic	±0.00 [0.85%]	±24.95 [1.13%]	±62.10 [4.63%]	±180.28 [0.67%]	±0.00 [1.22%]	±107.84 [8.12%]
mu_Znunu	±0.01 [1.6%]	±0.00 [0.00%]	±0.00 [0.00%]	±433.56 [1.6%]	±0.00 [0.00%]	±0.00 [0.00%]
alpha_ShapeSyst_2Jets	±0.01 [1.5%]	±33.74 [1.5%]	±0.00 [0.00%]	±414.66 [1.5%]	±0.00 [1.3%]	±0.00 [0.00%]
alpha_JET_GroupedNP_2	±0.00 [0.36%]	±8.19 [0.37%]	±4.21 [0.31%]	±82.83 [0.31%]	±0.00 [0.00%]	±5.00 [0.38%]
alpha_Mu_Id	±0.00 [0.24%]	±0.38 [0.02%]	±0.06 [0.00%]	±0.64 [0.00%]	±0.00 [0.00%]	±0.03 [0.00%]
alpha_Mu_MS	±0.00 [0.18%]	±0.27 [0.01%]	±0.11 [0.01%]	±1.11 [0.00%]	±0.00 [0.00%]	±0.06 [0.00%]
alpha_JET_GroupedNP_1	±0.00 [0.18%]	±1.66 [0.08%]	±13.82 [1.0%]	±32.49 [0.12%]	±0.00 [0.00%]	±2.38 [0.18%]
alpha_VPt_ckkw_Syst	±0.00 [0.14%]	±3.03 [0.14%]	±0.00 [0.00%]	±35.88 [0.13%]	±0.00 [0.04%]	±0.00 [0.00%]
alpha_VPt_qsf_Syst	±0.00 [0.06%]	±1.26 [0.06%]	±0.00 [0.00%]	±15.80 [0.06%]	±0.00 [0.08%]	±0.00 [0.00%]
gamma_stat_CRmu_2Jets_bin_9	±0.00 [0.00%]	±0.02 [0.00%]	±0.00 [0.00%]	±0.22 [0.00%]	±0.00 [0.00%]	±0.01 [0.00%]
mu_Wtaunu	±0.00 [0.00%]	±41.16 [1.9%]	±0.00 [0.00%]	±0.00 [0.00%]	±0.00 [1.9%]	±0.00 [0.00%]
alpha_JET_GroupedNP_3	±0.00 [0.00%]	±1.33 [0.06%]	±0.32 [0.02%]	±27.35 [0.10%]	±0.00 [0.00%]	±1.40 [0.11%]
gamma_stat_CRmu_2Jets_bin_8	±0.00 [0.00%]	±0.04 [0.00%]	±0.00 [0.00%]	±0.56 [0.00%]	±0.00 [0.00%]	±0.04 [0.00%]
alpha_BgXSec	±0.00 [0.00%]	±0.00 [0.00%]	±0.00 [0.00%]	±0.00 [0.00%]	±0.00 [0.00%]	±107.84 [8.1%]
alpha_MET_SoftTrk	±0.00 [0.00%]	±0.30 [0.01%]	±0.12 [0.01%]	±8.43 [0.03%]	±0.00 [0.00%]	±1.00 [0.08%]
gamma_stat_CRmu_2Jets_bin_7	±0.00 [0.00%]	±0.07 [0.00%]	±0.01 [0.00%]	±0.89 [0.00%]	±0.00 [0.00%]	±0.04 [0.00%]
gamma_stat_CRmu_2Jets_bin_10	±0.00 [0.00%]	±0.00 [0.00%]	±0.00 [0.00%]	±0.07 [0.00%]	±0.00 [0.00%]	±0.01 [0.00%]
mu_Top	±0.00 [0.00%]	±0.00 [0.00%]	±35.86 [2.7%]	±0.00 [0.00%]	±0.00 [0.00%]	±0.00 [0.00%]
alpha_JET_EtaIntercalibration	±0.00 [0.00%]	±2.87 [0.13%]	±1.98 [0.15%]	±32.39 [0.12%]	±0.00 [0.00%]	±1.67 [0.13%]
alpha_ttbar_showerSyst	±0.00 [0.00%]	±0.00 [0.00%]	±52.88 [3.9%]	±0.00 [0.00%]	±0.00 [0.00%]	±0.00 [0.00%]
alpha_EG_Scale	±0.00 [0.00%]	±0.00 [0.00%]	±0.03 [0.00%]	±0.26 [0.00%]	±0.00 [0.00%]	±0.04 [0.00%]
alpha_Mu_Scale	±0.00 [0.00%]	±0.06 [0.00%]	±0.02 [0.00%]	±0.50 [0.00%]	±0.00 [0.00%]	±0.03 [0.00%]
alpha_EG_Res	±0.00 [0.00%]	±0.00 [0.00%]	±0.04 [0.00%]	±0.35 [0.00%]	±0.00 [0.00%]	±0.02 [0.00%]
alpha_ttbarRadFlatSyst	±0.00 [0.00%]	±0.00 [0.00%]	±22.41 [1.7%]	±0.00 [0.00%]	±0.00 [0.00%]	±0.00 [0.00%]
alpha_ttbar_hardscatterSyst	±0.00 [0.00%]	±0.00 [0.00%]	±52.88 [3.9%]	±0.00 [0.00%]	±0.00 [0.00%]	±0.00 [0.00%]

Table G.16.: Breakdown of the systematic uncertainties in the 2 jet muon CR for the background only fit in M_{T2}.

[CRmu 3Jets] Uncertainty of	Znunu	Wtaunu	ttbar	Wmunu	Wenu	Other
Total background expectation	0.16	1159.13	3744.40	13835.08	0.31	1198.16
Total statistical ($\sqrt{N_{exp}}$)	±0.40	±34.05	±61.19	±117.62	±0.56	±34.61
Total background systematic	±0.00 [1.75%]	±14.41 [1.24%]	±104.91 [2.80%]	±132.53 [0.96%]	±0.01 [1.62%]	±97.21 [8.11%]
mu_Znunu	±0.00 [1.6%]	±0.00 [0.00%]	±0.00 [0.00%]	±221.45 [1.6%]	±0.00 [0.00%]	±0.00 [0.00%]
alpha_ShapeSyst_3Jets	±0.00 [1.5%]	±17.08 [1.5%]	±0.00 [0.00%]	±202.96 [1.5%]	±0.00 [1.6%]	±0.00 [0.00%]
alpha_JET_GroupedNP_1	±0.00 [1.5%]	±2.92 [0.25%]	±8.31 [0.22%]	±47.24 [0.34%]	±0.00 [0.09%]	±0.78 [0.06%]
alpha_VPt_ckkw_Syst	±0.00 [0.17%]	±1.89 [0.16%]	±0.00 [0.00%]	±21.55 [0.16%]	±0.00 [0.12%]	±0.00 [0.00%]
gamma_stat_CRmu_3Jets_bin_7	±0.00 [0.05%]	±0.09 [0.01%]	±0.01 [0.00%]	±0.65 [0.00%]	±0.00 [0.00%]	±0.05 [0.00%]
alpha_VPt_qsf_Syst	±0.00 [0.04%]	±0.58 [0.05%]	±0.00 [0.00%]	±7.20 [0.05%]	±0.00 [0.07%]	±0.00 [0.00%]
gamma_stat_CRmu_3Jets_bin_8	±0.00 [0.01%]	±0.02 [0.00%]	±0.00 [0.00%]	±0.27 [0.00%]	±0.00 [0.00%]	±0.02 [0.00%]
mu_Wtaunu	±0.00 [0.00%]	±21.68 [1.9%]	±0.00 [0.00%]	±0.00 [0.00%]	±0.01 [1.9%]	±0.00 [0.00%]
gamma_stat_CRmu_3Jets_bin_10	±0.00 [0.00%]	±0.01 [0.00%]	±0.00 [0.00%]	±0.07 [0.00%]	±0.00 [0.00%]	±0.02 [0.00%]
alpha_JET_GroupedNP_3	±0.00 [0.00%]	±1.55 [0.13%]	±3.29 [0.09%]	±22.24 [0.16%]	±0.00 [0.79%]	±1.55 [0.13%]
alpha_JET_GroupedNP_2	±0.00 [0.00%]	±2.16 [0.19%]	±12.80 [0.34%]	±45.07 [0.33%]	±0.00 [0.00%]	±3.16 [0.26%]
alpha_BgXSec	±0.00 [0.00%]	±0.00 [0.00%]	±0.00 [0.00%]	±0.00 [0.00%]	±0.00 [0.00%]	±97.25 [8.1%]
alpha_MET_SoftTrk	±0.00 [0.00%]	±0.59 [0.05%]	±1.62 [0.04%]	±4.89 [0.04%]	±0.00 [0.00%]	±1.27 [0.11%]
mu_Top	±0.00 [0.00%]	±0.00 [0.00%]	±100.18 [2.7%]	±0.00 [0.00%]	±0.00 [0.00%]	±0.00 [0.00%]
alpha_JET_EtaIntercalibration	±0.00 [0.00%]	±0.92 [0.08%]	±7.06 [0.19%]	±24.23 [0.18%]	±0.00 [0.00%]	±1.55 [0.13%]
alpha_ttbar_showerSyst	±0.00 [0.00%]	±0.00 [0.00%]	±67.50 [1.8%]	±0.00 [0.00%]	±0.00 [0.00%]	±0.00 [0.00%]
alpha_Mu_MS	±0.00 [0.00%]	±0.03 [0.00%]	±0.14 [0.00%]	±0.24 [0.00%]	±0.00 [0.00%]	±0.01 [0.00%]
alpha_EG_Scale	±0.00 [0.00%]	±0.01 [0.00%]	±0.10 [0.00%]	±0.01 [0.00%]	±0.00 [0.00%]	±0.00 [0.00%]
alpha_Mu_Scale	±0.00 [0.00%]	±0.10 [0.01%]	±0.13 [0.00%]	±0.41 [0.00%]	±0.00 [0.00%]	±0.02 [0.00%]
alpha_EG_Res	±0.00 [0.00%]	±0.00 [0.00%]	±0.02 [0.00%]	±0.02 [0.00%]	±0.00 [0.00%]	±0.14 [0.01%]
alpha_Mu_Id	±0.00 [0.00%]	±0.12 [0.01%]	±0.33 [0.01%]	±0.22 [0.00%]	±0.00 [0.00%]	±0.06 [0.00%]
alpha_ttbarRadFlatSyst	±0.00 [0.00%]	±0.00 [0.00%]	±53.28 [1.4%]	±0.00 [0.00%]	±0.00 [0.00%]	±0.00 [0.00%]
gamma_stat_CRmu_3Jets_bin_9	±0.00 [0.00%]	±0.01 [0.00%]	±0.00 [0.00%]	±0.12 [0.00%]	±0.00 [0.00%]	±0.01 [0.00%]
alpha_ttbar_hardscatterSyst	±0.00 [0.00%]	±0.00 [0.00%]	±67.50 [1.8%]	±0.00 [0.00%]	±0.00 [0.00%]	±0.00 [0.00%]

Table G.17.: Breakdown of the systematic uncertainties in the 3 jet muon CR for the background only fit in M_{T2}.

[CRmu 4Jets] Uncertainty of	Znunu	Wtaunu	ttbar	Wmunu	Wenu	Other
Total background expectation	0.42	1600.70	14521.18	18946.97	0.04	2710.91
Total statistical ($\sqrt{N_{exp}}$)	±0.65	±40.01	±120.50	±137.65	±0.21	±52.07
Total background systematic	±0.01 [1.53%]	±24.06 [1.50%]	±313.00 [2.16%]	±241.80 [1.28%]	±0.04 [99.33%]	±222.10 [8.19%]
alpha_ShapeSyst_4Jets	±0.01 [2.0%]	±29.45 [1.8%]	±0.00 [0.00%]	±348.63 [1.8%]	±0.00 [1.5%]	±0.00 [0.00%]
alpha_JET_GroupedNP_1	±0.01 [1.7%]	±22.74 [1.4%]	±175.57 [1.2%]	±281.57 [1.5%]	±0.00 [4.9%]	±32.41 [1.2%]
mu_Znunu	±0.01 [1.6%]	±0.00 [0.00%]	±0.00 [0.00%]	±303.27 [1.6%]	±0.00 [0.00%]	±0.00 [0.00%]
alpha_Mu_Id	±0.00 [0.23%]	±0.05 [0.00%]	±0.51 [0.00%]	±0.18 [0.00%]	±0.00 [0.00%]	±0.10 [0.00%]
alpha_VPt_ckkw_Syst	±0.00 [0.19%]	±3.07 [0.19%]	±0.00 [0.00%]	±34.75 [0.18%]	±0.00 [0.08%]	±0.00 [0.00%]
alpha_VPt_qsf_Syst	±0.00 [0.05%]	±0.83 [0.05%]	±0.00 [0.00%]	±10.31 [0.05%]	±0.00 [0.08%]	±0.00 [0.00%]
alpha_JET_GroupedNP_3	±0.00 [0.00%]	±4.74 [0.30%]	±47.95 [0.33%]	±70.59 [0.37%]	±0.02 [56.7%]	±8.00 [0.30%]
alpha_Mu_MS	±0.00 [0.00%]	±0.18 [0.01%]	±0.44 [0.00%]	±0.09 [0.00%]	±0.00 [0.00%]	±0.02 [0.00%]
mu_Wtaunu	±0.00 [0.00%]	±29.94 [1.9%]	±0.00 [0.00%]	±0.00 [0.00%]	±0.00 [1.9%]	±0.00 [0.00%]
alpha_JET_GroupedNP_2	±0.00 [0.00%]	±5.90 [0.37%]	±69.90 [0.48%]	±82.59 [0.44%]	±0.02 [57.4%]	±9.61 [0.35%]
alpha_BgXSec	±0.00 [0.00%]	±0.00 [0.00%]	±0.00 [0.00%]	±0.00 [0.00%]	±0.00 [0.00%]	±220.04 [8.1%]
alpha_MET_SoftTrk	±0.00 [0.00%]	±0.28 [0.02%]	±10.31 [0.07%]	±8.86 [0.05%]	±0.00 [0.00%]	±2.29 [0.08%]
mu_Top	±0.00 [0.00%]	±0.00 [0.00%]	±388.53 [2.7%]	±0.00 [0.00%]	±0.00 [0.00%]	±0.00 [0.00%]
alpha_JET_EtaIntercalibration	±0.00 [0.00%]	±2.87 [0.18%]	±27.07 [0.19%]	±34.63 [0.18%]	±0.03 [59.7%]	±4.26 [0.16%]
alpha_ttbar_showerSyst	±0.00 [0.00%]	±0.00 [0.00%]	±198.95 [1.4%]	±0.00 [0.00%]	±0.00 [0.00%]	±0.00 [0.00%]
alpha_EG_Scale	±0.00 [0.00%]	±0.01 [0.00%]	±0.35 [0.00%]	±0.30 [0.00%]	±0.00 [0.00%]	±0.05 [0.00%]
alpha_Mu_Scale	±0.00 [0.00%]	±0.03 [0.00%]	±0.25 [0.00%]	±0.48 [0.00%]	±0.00 [0.00%]	±0.02 [0.00%]
alpha_EG_Res	±0.00 [0.00%]	±0.01 [0.00%]	±0.00 [0.00%]	±0.06 [0.00%]	±0.00 [0.00%]	±0.00 [0.00%]
alpha_ttbarRadFlatSyst	±0.00 [0.00%]	±0.00 [0.00%]	±202.21 [1.4%]	±0.00 [0.00%]	±0.00 [0.00%]	±0.00 [0.00%]
alpha_ttbar_hardscatterSyst	±0.00 [0.00%]	±0.00 [0.00%]	±198.95 [1.4%]	±0.00 [0.00%]	±0.00 [0.00%]	±0.00 [0.00%]

Table G.18.: Breakdown of the systematic uncertainties in the 4 jet muon CR for the background only fit in M_{T2}.

Appendix H.

Correlation Matrix

These matrices show the correlations between all systematic uncertainties for the $E_{\mathrm{T}}^{\mathrm{miss}}$ and the M_{T2} background only fit, respectively.
The following matrices show the correlations between all systematic uncertainties for the $E_{\mathrm{T}}^{\mathrm{miss}}$ and the M_{T2} exclusion fit, respectively.

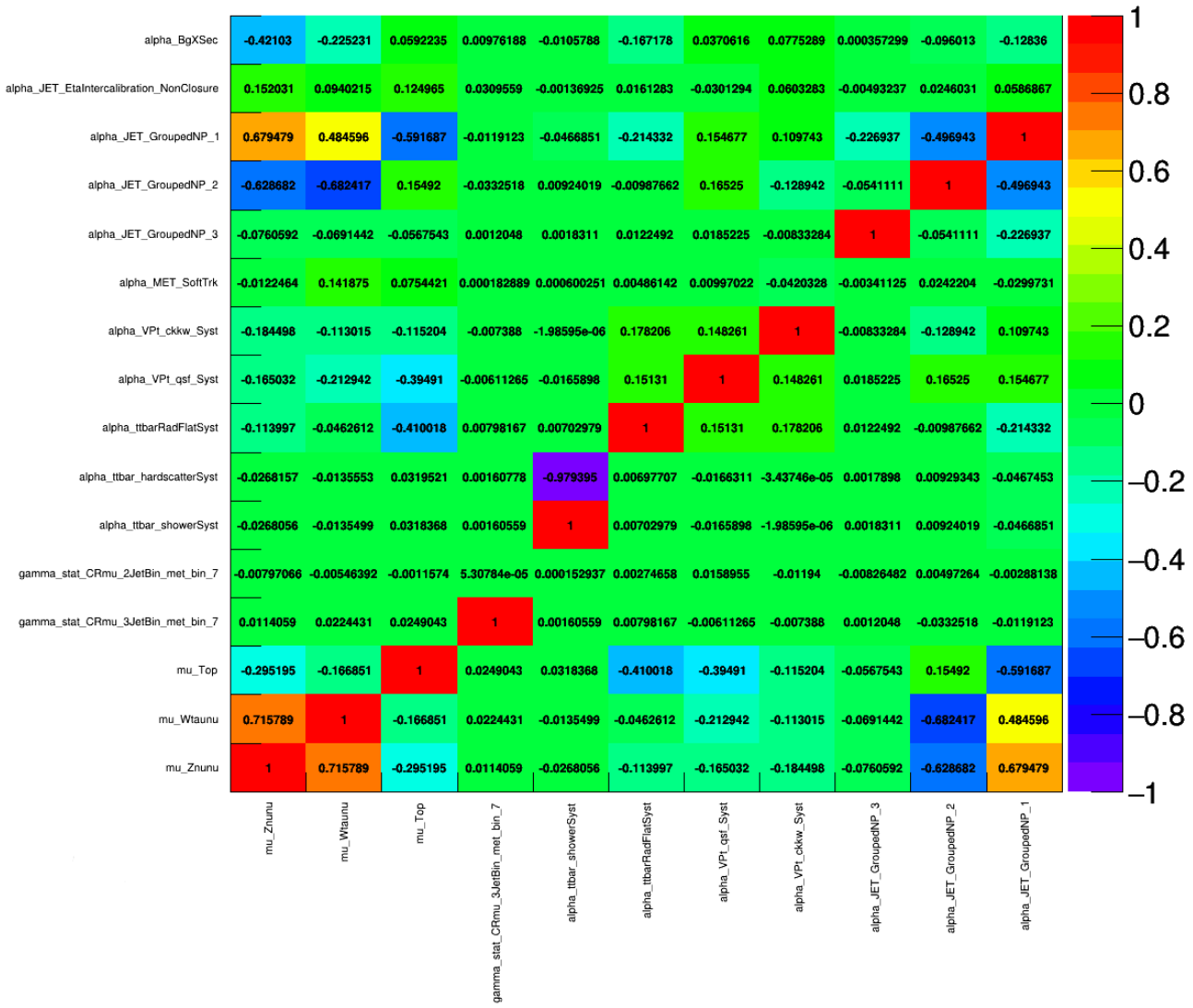

Figure H.1.: Correlations between systematic uncertainties used in the $E_{\mathrm{T}}^{\mathrm{miss}}$ fit.

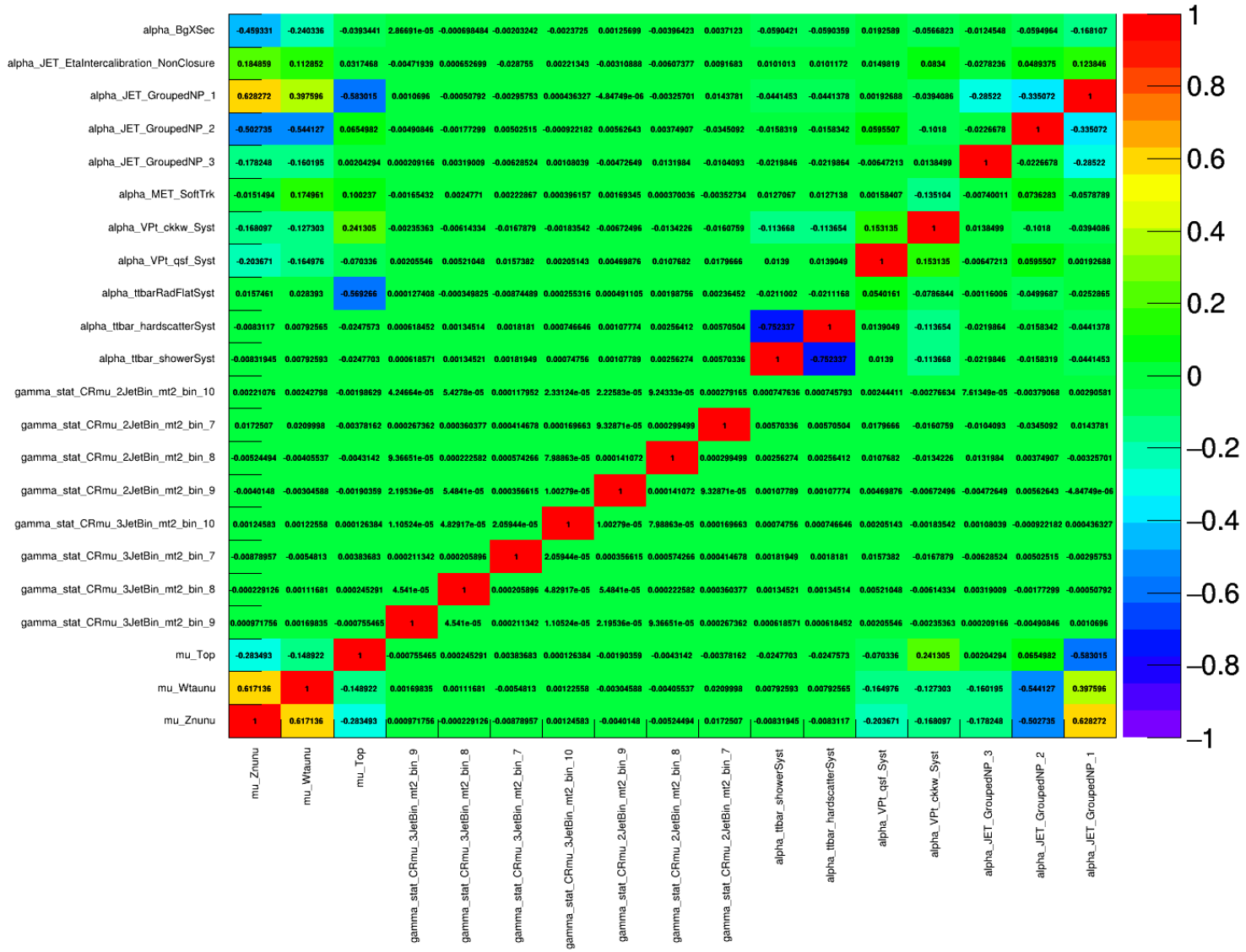

Figure H.2.: Correlations between systematic uncertainties used in the M_{T2} fit.

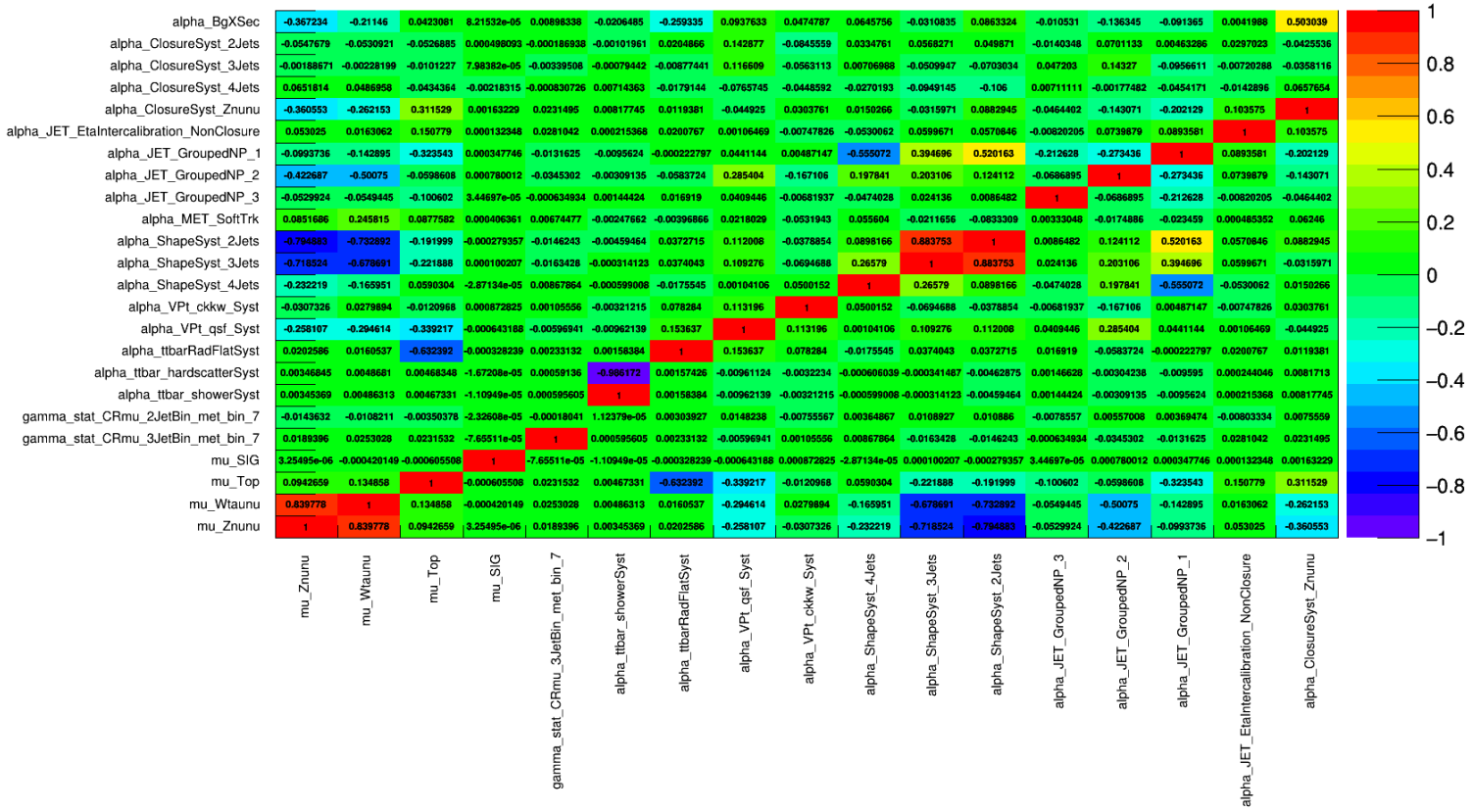

Figure H.3.: Correlations between systematic uncertainties used in the $E_{\mathrm{T}}^{\mathrm{miss}}$ fit.

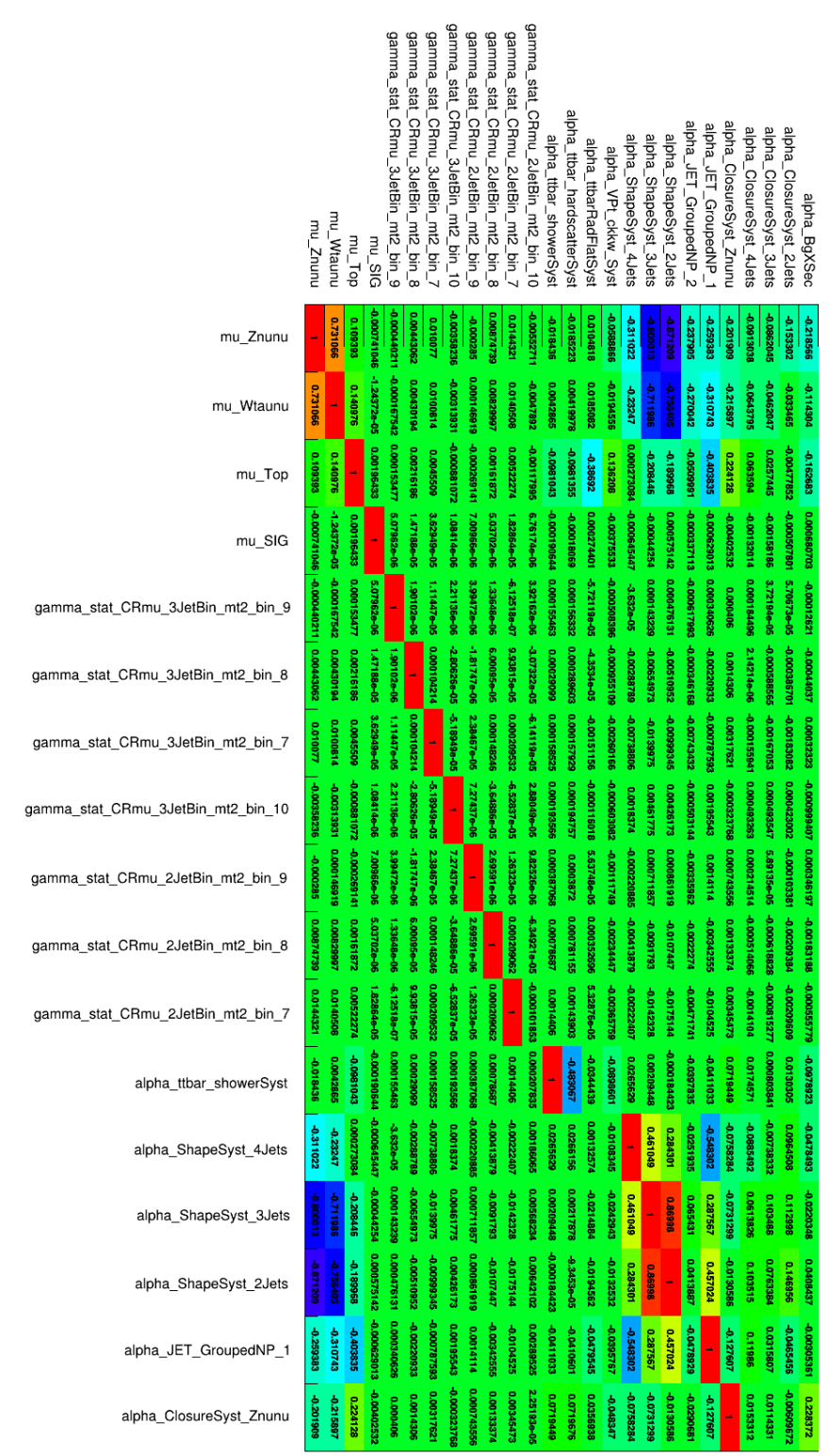

Figure H.4.: Correlations between systematic uncertainties used in the M_{T2} fit.

Bibliography

1. Copernicus, N. *De Revolutionibus orbium coelestium* (Roskam's Boeken Verkoop Kantoor, 1543).
2. Kepler, J. *Epitome astronomiae copernicanae* (Jo. Plancus, 1618).
3. Galilei, G. *Dialogo di Galileo Galilei sopra i due massimi sistemi del mondo, tolemaico, e copernicano* (Culture et Civilisation, 1632).
4. Newton, I. *Philosophiae naturalis principia mathematica* (J. Societatis Regiae ac Typis J. Streater, 1687).
5. Einstein, A. Die Grundlage der allgemeinen Relativitätstheorie. *Annalen der Physik* **354:** 769–822 (1916).
6. Thomson, J. J. XL. Cathode Rays. *Philosophical Magazine* **44:** 293–316 (1897).
7. Curie, P., Curie, M. & Bémont, M. Sur une nouvelle substance fortement redio-active, contenue dans la pechblende. *Comptes Rendus de l'Académie des Sciences, Paris, France* (Dec. 1898).
8. Becquerel, H. Sur les Radiations Invisibles Émises par les Corps Phosphorescents. *Comptes rendus Acad, des Sciences, Paris, France* **122** (Jan. 1895).
9. Rutherford, E. *Radio-activity* (Cambridge [Eng.] University Press, 1905).
10. YUKAWA, H. On the Interaction of Elementary Particles. I. *Proceedings of the Physico-Mathematical Society of Japan. 3rd Series* **17:** 48–57 (1935).
11. Petermann, A. Propriétés de l'étrangeté et une formule de masse pour les mésons vectoriels. *Nuclear Physics* **63:** 349–352 (1965).
12. Gell-Mann, M. A Schematic Model of Baryons and Mesons. *Phys. Lett.* **8:** 214–215 (1964).
13. Zweig, G. *An SU3 model for strong interaction symmetry and its breaking Version 1* tech. rep. CERN-TH-401 (CERN, Geneva, Jan. 1964). <`http://cds.cern.ch/record/352337`>.
14. Glashow, S. L. The renormalizability of vector meson interactions. *Nucl. Phys.* **10:** 107–117 (1959).
15. Salam, A. & Ward, J. C. Weak and electromagnetic interactions. *Il Nuovo Cimento (1955-1965)* **11:** 568–577 (Feb. 1959).
16. Weinberg, S. A Model of Leptons. *Phys. Rev. Lett.* **19:** 1264–1266 (21 Nov. 1967).
17. Englert, F. & Brout, R. Broken Symmetry and the Mass of Gauge Vector Mesons. *Phys. Rev. Lett.* **13:** 321–323 (9 Aug. 1964).
18. Higgs, P. W. Broken Symmetries and the Masses of Gauge Bosons. *Phys. Rev. Lett.* **13:** 508–509 (16 Oct. 1964).
19. The ATLAS Collaboration. Observation of a new particle in the search for the Standard Model Higgs boson with the ATLAS detector at the LHC. *Physics Letters B* **716:** 1–29 (Sept. 2012).

20. The CMS Collaboration. Observation of a new boson at a mass of 125 GeV with the CMS experiment at the LHC. *Physics Letters B* **716:** 30–61 (2012).

21. Sakharov, A. D. Violation ofCPin variance,Casymmetry, and baryon asymmetry of the universe. *Soviet Physics Uspekhi* **34:** 392–393 (May 1991).

22. Bennett, C. L., Banday, A. J., Górski, K. M., Hinshaw, G., Jackson, P., Keegstra, P., Kogut, A., Smoot, G. F., Wilkinson, D. T. & Wright, E. L. Four-Year [ITAL]COBE[/ITAL] DMR Cosmic Microwave Background Observations: Maps and Basic Results. *The Astrophysical Journal* **464:** L1–L4 (June 1996).

23. Barbieri, R. & Strumia, A. *The 'LEP paradox'* in *4th Rencontres du Vietnam: Physics at Extreme Energies (Particle Physics and Astrophysics) Hanoi, Vietnam, July 19-25, 2000* (2000). arXiv: hep-ph/0007265 [hep-ph].

24. Patrignani, C. & others (Particle Data Group). Review of Particle Physics. *Chin. Phys.* **C40:** 100001 (2016).

25. Povh, B., Rith, K., Scholz, C. & Zetsche, F. *Teilchen und Kerne: Eine Einführung in die physikalischen Konzepte* (Springer, London, 2008).

26. Griffiths, D. *Introduction to Elementary Particles* (John Wiley & Sons, New York, 1987).

27. Martin, B. & Shaw, G. *Particle Physics* 3rd ed. (John Wiley & Sons, Chichester, 2008).

28. Martin, S. P. *A Supersymmetry Primer* tech. rep. (2016). eprint: arXiv:hep-ph/9709356v7.

29. Higgs, P. W. Broken Symmetries and the Masses of Gauge Bosons. *Phys. Rev. Lett.* **13:** 508–509 (16 Oct. 1964).

30. Langacker, P. *Introduction to the Standard Model and Electroweak Physics* in *The Dawn of the LHC Era: TASI 2008* (ed Han, T.) (Aug. 2010): 3–48. doi:10.1142/9789812838360_0001. arXiv: 0901.0241 [hep-ph].

31. Kazakov, D. I. *Beyond the standard model: In search of supersymmetry* in (2000): 125–199. arXiv: hep-ph/0012288 [hep-ph].

32. Bernal, T., Fernández-Hernández, L. M., Matos, T. & Rodríguez-Meza, M. A. Rotation Curves of High-Resolution LSB and SPARC Galaxies in Wave (Fuzzy) and Multistate (Ultra-light Boson) Scalar Field Dark Matter. *ArXiv e-prints.* arXiv: 1701.00912 (Jan. 2017).

33. <http://hubblesite.org/newscenter/archive/releases/2012/10/image/a/>.

34. Planck Collaboration. Planck 2015 results - I. Overview of products and scientific results. *A&A* **594:** A1 (2016).

35. ESA. *Cosmic microwave background seen by Planck* <http://sci.esa.int/jump.cfm?oid=51553> (2013).

36. Penzias, A. A. & Wilson, R. W. A Measurement of Excess Antenna Temperature at 4080 Mc/s. *Astrophysical Journal* **142:** 419–421 (July 1965).

37. Boggess, N. W. *et al.* The COBE mission - Its design and performance two years after launch. *Astrophysical Journal* **397:** 420–429 (Oct. 1992).

38. Bennett, C. L. *et al.* Nine-year Wilkinson Microwave Anisotropy Probe (WMAP) Observations: Final Maps and Results. *The Astrophysical Journal Supplement Series* **208:** 20 (2013).

39. Planck Collaboration. Planck 2013 results. XVI. Cosmological parameters. *A&A* **571:** A16 (2014).

40. Nagashima, Y. *Beyond the Standard Model of Elementary Particle Physics* (Wiley, 2014).

41. Pati, J. C. & Salam, A. Unified Lepton-Hadron Symmetry and a Gauge Theory of theBasic Interactions. *Phys. Rev.* **D8:** 1240–1251 (1973).

42. Cheng, H.-C. & Low, I. TeV symmetry and the little hierarchy problem. *Journal of High Energy Physics* **2003:** 051 (2003).

43. Peccei, R. D. & Quinn, H. R. CP Conservation in the Presence of Pseudoparticles. *Phys. Rev. Lett.* **38:** 1440–1443 (25 June 1977).

44. Dodelson, S. & Widrow, L. M. Sterile-neutrinos as dark matter. *Phys. Rev. Lett.* **72:** 17–20 (1994).

45. Kaluza, T. Zum Unitätsproblem in der Physik. *Sitzungsber. Preuss. Akad. Wiss. Berlin (Math. Phys.)* 966 (1921).

46. Klein, O. Quantentheorie und fünfdimensionale Relativitätstheorie. **37:** 895–906 (Dec. 1926).

47. The ATLAS Collaboration. Search for dark matter and other new phenomena in events with an energetic jet and large missing transverse momentum using the ATLAS detector. arXiv: `1711.03301 [hep-ex]` (2017).

48. Diaz, B., Schmaltz, M. & Zhong, Y.-M. The leptoquark Hunter's guide: Pair production. *JHEP* **10:** 097 (2017).

49. The ATLAS Collaboration. Search for scalar leptoquarks in pp collisions at $\sqrt{s} = 13$ TeV with the ATLAS experiment. *New J. Phys.* **18:** 093016 (2016).

50. Coleman, S. & Mandula, J. All Possible Symmetries of the S Matrix. *Phys. Rev.* **159:** 1251–1256 (5 July 1967).

51. Haag, R., Lopuszanski, J. T. & Sohnius, M. All possible generators of supersymmetries of the S-matrix. *Nuclear Physics B* **88:** 257–274 (Mar. 1975).

52. d'Enterria, D. CMS physics highlights in the LHC Run 1. *PoS* **Bormio2015:** 027 (2015).

53. <`https://atlas.web.cern.ch/Atlas/GROUPS/PHYSICS/CombinedSummaryPlots/EXOTICS/ATLAS_Exotics_Summary/history.html`>.

54. Joint LEP 2 SUSY Working Group. *LEPSUSYWG, ALEPH, DELPHI, L3 and OPAL experiments* LEPSUSYWG/04-02.1. <`http://lepsusy.web.cern.ch/lepsusy/`> (2004).

55. <`https://twiki.cern.ch/twiki/pub/AtlasPublic/CombinedSummaryPlots/AtlasSearchesSUSY_SUSY2013.pdf`>.

56. <`https://twiki.cern.ch/twiki/bin/view/CMSPublic/SUSYSMSSummaryPlots8TeV`>.

57. The ATLAS Collaboration. Summary of the searches for squarks and gluinos using $\sqrt{s} = 8$ TeV pp collisions with the ATLAS experiment at the LHC. *Journal of High Energy Physics* **2015:** 54 (Oct. 2015).

58. <`https://twiki.cern.ch/twiki/bin/view/CMSPublic/SUSYSMSSummaryPlots8TeV`>.

59. <`https://home.cern/`>.

60. <`https://atlas.cern/`>.

61. Brüning, O. S., Collier, P., Lebrun, P., Myers, S., Ostojic, R., Poole, J. & Proudlock, P. *LHC Design Report* <`https://cds.cern.ch/record/782076`> (CERN, Geneva, 2004).

62. *LHC Guide* Mar. 2017. <`http://cds.cern.ch/record/2255762`>.

63. Mobs, E. The CERN accelerator complex. Complexe des accélérateurs du CERN. General Photo. <`http://cds.cern.ch/record/2197559`> (July 2016).

64. <`https://twiki.cern.ch/twiki/bin/view/AtlasPublic/LuminosityPublicResultsRun2`>.

65. Drell, S. D. & Yan, T.-M. Massive Lepton-Pair Production in Hadron-Hadron Collisions at High Energies. *Phys. Rev. Lett.* **25:** 316–320 (5 Aug. 1970).

66. Campbell, J. M., Huston, J. W. & Stirling, W. J. Hard Interactions of Quarks and Gluons: A Primer for LHC Physics. *Rept. Prog. Phys.* **70:** 89 (2007).

67. Borschensky, C., Krämer, M., Kulesza, A., Mangano, M., Padhi, S., Plehn, T. & Portell, X. Squark and gluino production cross sections in pp collisions at $\sqrt{s}$ = 13, 14, 33 and 100 TeV. *Eur. Phys. J.* **C74:** 3174 (2014).

68. Pequenao, J. *Computer generated image of the whole ATLAS detector* Mar. 2008. <http://cds.cern.ch/record/1095924>.

69. The ATLAS Collaboration. *ATLAS detector and physics performance: Technical Design Report 1* <https://cds.cern.ch/record/391176> (CERN, Geneva, 1999).

70. The ATLAS Collaboration. *ATLAS detector and physics performance: Technical Design Report 2* <https://cds.cern.ch/record/391177> (CERN, Geneva, 1999).

71. The ATLAS Collaboration. *The ATLAS Experiment at the CERN Large Hadron Collider* **08:** S08003. <http://stacks.iop.org/1748-0221/3/i=08/a=S08003> (2008).

72. Pequenao, J. *Computer generated image of the ATLAS inner detector* Mar. 2008. <http://cds.cern.ch/record/1095926>.

73. Potamianos, K. The upgraded Pixel detector and the commissioning of the Inner Detector tracking of the ATLAS experiment for Run-2 at the Large Hadron Collider. *PoS* **EPS-HEP2015:** 261 (2015).

74. Pequenao, J. *Computer Generated image of the ATLAS calorimeter* Mar. 2008. <https://cds.cern.ch/record/1095927>.

75. The ATLAS Collaboration. Jet energy resolution in proton-proton collisions at $\sqrt{s}$ = 7 TeV recorded in 2010 with the ATLAS detector. *Eur. Phys. J.* **C73:** 2306 (2013).

76. The ATLAS Collaboration. The ATLAS Experiment at the CERN Large Hadron Collider. *JINST* **3.** Also published by CERN Geneva in 2010: S08003. 437 p (2008).

77. Pequenao, J. *Computer generated image of the ATLAS Muons subsystem* Mar. 2008. <http://cds.cern.ch/record/1095929>.

78. Panduro Vazquez, J. G. *The ATLAS Data Acquisition System: from Run 1 to Run 2* tech. rep. ATL-COM-DAQ-2014-118. Proceedings deadline 15th October 2014. (CERN, Geneva, Oct. 2014). <https://cds.cern.ch/record/1951428>.

79. <https://royalsocietypublishing.org/doi/10.1098/rsta.2011.0459>.

80. <https://twiki.cern.ch/twiki/bin/view/AtlasProtected/InDetTrackingPerformanceGuidelines>.

81. *Vertex Reconstruction Performance of the ATLAS Detector at $\sqrt{s}$ = 13 TeV* tech. rep. ATL-PHYS-PUB-2015-026 (CERN, Geneva, July 2015). <http://cds.cern.ch/record/2037717>.

82. The ATLAS Collaboration. Measurements of b-jet tagging efficiency with the ATLAS detector using $t\bar{t}$ events at $\sqrt{s}$ = 13 TeV. *JHEP* **08:** 089 (2018).

83. The ATLAS Collaboration. Performance of the ATLAS Track Reconstruction Algorithms in Dense Environments in LHC Run 2. *Eur. Phys. J.* **C77:** 673 (2017).

84. <https://twiki.cern.ch/twiki/bin/view/AtlasPublic/EventDisplayStandAlone#2012_Z_mu_mu_event_with_high_pil>.

85. Lampl, W., Laplace, S., Lelas, D., Loch, P., Ma H and Menke, S., Rajagopalan, S., Rousseau, D., Snyder, S. & Unal, G. *Calorimeter Clustering Algorithms: Description and Performance* tech. rep. ATL-LARG-PUB-2008-002. ATL-COM-LARG-2008-003 (CERN, Geneva, Apr. 2008). <https://cds.cern.ch/record/1099735>.

86. The ATLAS Collaboration. Electron reconstruction and identification in the ATLAS experiment using the 2015 and 2016 LHC proton-proton collision data at $\sqrt{s} = 13$ TeV. *Submitted to: Eur. Phys. J.* arXiv: 1902.04655 [physics.ins-det] (2019).

87. <https://twiki.cern.ch/twiki/bin/view/AtlasProtected/EGammaIdentificationRun2>.

88. *Electron efficiency measurements with the ATLAS detector using the 2015 LHC proton-proton collision data* tech. rep. ATLAS-CONF-2016-024 (CERN, Geneva, June 2016). <https://cds.cern.ch/record/2157687>.

89. <https://atlas.web.cern.ch/Atlas/GROUPS/PHYSICS/PLOTS/EGAM-2016-002/index.html>.

90. <https://twiki.cern.ch/twiki/bin/view/AtlasProtected/MCPAnalysisGuidelinesMC15>.

91. The ATLAS Collaboration. Muon reconstruction performance of the ATLAS detector in proton–proton collision data at $\sqrt{s}$ =13 TeV. *Eur. Phys. J.* **C76:** 292 (2016).

92. *Measurement of the tau lepton reconstruction and identification performance in the ATLAS experiment using pp collisions at $\sqrt{s} = 13$ TeV* tech. rep. ATLAS-CONF-2017-029 (CERN, Geneva, May 2017). <https://cds.cern.ch/record/2261772>.

93. The ATLAS Collaboration. Topological cell clustering in the ATLAS calorimeters and its performance in LHC Run 1. *Eur. Phys. J.* **C77:** 490 (2017).

94. Cacciari, M., Salam, G. P. & Soyez, G. The anti-k_t jet clustering algorithm. *JHEP* **04:** 063 (2008).

95. The ATLAS Collaboration. Jet energy scale measurements and their systematic uncertainties in proton-proton ollisions at $\sqrt{s} = 13$ TeV with the ATLAS detector. *Phys. Rev.* **D96:** 072002 (2017).

96. *Pile-up subtraction and suppression for jets in ATLAS* tech. rep. ATLAS-CONF-2013-083 (CERN, Geneva, Aug. 2013). <https://cds.cern.ch/record/1570994>.

97. *Jet Calibration and Systematic Uncertainties for Jets Reconstructed in the ATLAS Detector at $\sqrt{s} = 13$ TeV* tech. rep. ATL-PHYS-PUB-2015-015 (CERN, Geneva, July 2015). <http://cds.cern.ch/record/2037613>.

98. *Jet Calibration and Systematic Uncertainties for Jets Reconstructed in the ATLAS Detector at $\sqrt{s} = 13$ TeV* tech. rep. ATL-PHYS-PUB-2015-015 (CERN, Geneva, July 2015). <https://cds.cern.ch/record/2037613>.

99. *Tagging and suppression of pileup jets with the ATLAS detector* tech. rep. ATLAS-CONF-2014-018 (CERN, Geneva, May 2014). <https://cds.cern.ch/record/1700870>.

100. *Pile-up subtraction and suppression for jets in ATLAS* tech. rep. ATLAS-CONF-2013-083 (CERN, Geneva, Aug. 2013). <http://cds.cern.ch/record/1570994>.

101. <https://twiki.cern.ch/twiki/bin/view/AtlasProtected/JVTCalibration>.

102. *Selection of jets produced in 13TeV proton-proton collisions with the ATLAS detector* tech. rep. ATLAS-CONF-2015-029 (CERN, Geneva, July 2015). <https://cds.cern.ch/record/2037702>.

103. <https://twiki.cern.ch/twiki/bin/view/AtlasProtected/SusyObjectDefinitionsr2013TeV#Overlap_Removals>.

104. The ATLAS Collaboration. Performance of missing transverse momentum reconstruction with the ATLAS detector using proton-proton collisions at $\sqrt{s} = 13$ TeV. *Eur. Phys. J.* **C78:** 903 (2018).

105. The ATLAS Collaboration. Search for squarks and gluinos in final states with jets and missing transverse momentum using 36 fb^{-1} of $\sqrt{s}$=13 TeV pp collision data with the ATLAS detector. arXiv: 1712.02332 [hep-ex] (2017).

106. Aad, G. *et al.* The ATLAS Simulation Infrastructure. *Eur. Phys. J.* **C70:** 823–874 (2010).

107. Et al., S. A. Geant4—a simulation toolkit. *Nuclear Instruments and Methods in Physics Research Section A: Accelerators, Spectrometers, Detectors and Associated Equipment* **506:** 250–303 (2003).

108. Asai, M., Dotti, A., Verderi, M. & Wright, D. H. Recent developments in Geant4. *Annals of Nuclear Energy* **82.** Joint International Conference on Supercomputing in Nuclear Applications and Monte Carlo 2013, SNA + MC 2013. Pluri- and Trans-disciplinarity, Towards New Modeling and Numerical Simulation Paradigms: 19–28 (2015).

109. Gleisberg, T., Hoeche, S., Krauss F. and Schonherr, M., Schumann, S., Siegert, F. & Winter, J. Event generation with SHERPA 1.1. *JHEP* **02:** 007 (2009).

110. Frixione, S., Nason, P. & Oleari, C. Matching NLO QCD computations with Parton Shower simulations: the POWHEG method. *JHEP* **11:** 070 (2007).

111. Sjostrand, T., Mrenna, S. & Skands, P. Z. PYTHIA 6.4 Physics and Manual. *JHEP* **05:** 026 (2006).

112. Alwall, J., Frederix, R., Frixione, S., Hirschi, V., Maltoni, F., Mattelaer, O., Shao H. -S. and Stelzer, T., Torrielli, P. & Zaro, M. The automated computation of tree-level and next-to-leading order differential cross sections, and their matching to parton shower simulations. *JHEP* **07:** 079 (2014).

113. Sjostrand, T., Mrenna, S. & Skands, P. Z. A Brief Introduction to PYTHIA 8.1. *Comput. Phys. Commun.* **178:** 852–867 (2008).

114. Jakobi, K. *Suche nach dem supersymmetrischen Partner des Top-Quarks mit einer formsensitiven Analyse* Apr. 2013.

115. Barr, A., Lester, C. & Stephens, P. m(T2): The Truth behind the glamour. *J. Phys.* **G29:** 2343–2363 (2003).

116. <https://twiki.cern.ch/twiki/bin/view/AtlasPublic/MissingEtTriggerPublicResults>.

117. <https://svnweb.cern.ch/trac/atlasoff/browser/PhysicsAnalysis/SUSYPhys/SUSYTools/tags/SUSYTools-00-08-60>.

118. <https://twiki.cern.ch/twiki/bin/view/AtlasProtected/SusyObjectDefinitionsr2013TeV#SUSYTools>.

119. <https://root.cern.ch/root/html526/RooStats__NumberCountingUtils.html>.

120. *Electron efficiency measurements with the ATLAS detector using the 2015 LHC proton-proton collision data* tech. rep. ATLAS-CONF-2016-024 (CERN, Geneva, June 2016). <https://cds.cern.ch/record/2157687>.

121. Aad, G. *et al.* Muon reconstruction performance of the ATLAS detector in proton–proton collision data at $\sqrt{s}$ =13 TeV. *Eur. Phys. J.* **C76:** 292 (2016).

122. Buttinger, W. *Using Event Weights to account for differences in Instantaneous Luminosity and Trigger Prescale in Monte Carlo and Data* tech. rep. ATL-COM-SOFT-2015-119 (CERN, Geneva, May 2015). <https://cds.cern.ch/record/2014726>.

123. Aaboud, M. *et al.* Luminosity determination in pp collisions at $\sqrt{s}$= 8 TeV using the ATLAS detector at the LHC. *Eur. Phys. J.* **C76:** 653 (2016).

124. <https://twiki.cern.ch/twiki/bin/view/AtlasProtected/MC15SystematicUncertainties>.

125. <https://twiki.cern.ch/twiki/bin/view/AtlasProtected/TopSystematics2015>.

126. <https://twiki.cern.ch/twiki/bin/viewauth/AtlasProtected/MC15SystematicUncertainties#V_jets_and_gamma_jets_Sherpa>.

127. Baak, M., Besjes, G. J., Côte, D., Koutsman, A., Lorenz, J. & Short, D. HistFitter software framework for statistical data analysis. *Eur. Phys. J.* **C75:** 153 (2015).

128. Moneta, L., Belasco, K., Cranmer, K. S., Kreiss, S., Lazzaro, A., Piparo, D., Schott, G., Verkerke, W. & Wolf, M. The RooStats Project. *PoS* **ACAT2010:** 057 (2010).

129. Cranmer, K., Lewis, G., Moneta, L., Shibata, A. & Verkerke, W. *HistFactory: A tool for creating statistical models for use with RooFit and RooStats* tech. rep. CERN-OPEN-2012-016 (New York U., New York, Jan. 2012). <https://cds.cern.ch/record/1456844>.

130. Cowan, G., Cranmer, K., Gross, E. & Vitells, O. Asymptotic formulae for likelihood-based tests of new physics. *Eur. Phys. J.* **C71.** [Erratum: Eur. Phys. J.C73,2501(2013)]: 1554 (2011).

131. <https://twiki.cern.ch/twiki/bin/view/Main/HistFitterTutorialOutsideAtlas#Introduction>.

132. Schäffer, J. *LQ distributions* Kindly provided by Jan Schäffer. Dec. 2018.

133. The CMS Collaboration. Search for supersymmetry in multijet events with missing transverse momentum in proton-proton collisions at 13 TeV. *Phys. Rev.* **D96:** 032003 (2017).

134. Apollinari, G., Béjar Alonso, I., Brüning, O., Lamont, M. & Rossi, L. *High-Luminosity Large Hadron Collider (HL-LHC): Preliminary Design Report* <https://cds.cern.ch/record/2116337> (CERN, Geneva, 2015).

135. <http://hilumilhc.web.cern.ch/about/hl-lhc-project>.

136. <https://fcc-cdr.web.cern.ch/>.